

Copyright

by

Joshua Max Katzenstein

2013

The Dissertation Committee for Joshua Max Katzenstein Certifies that this is the approved version of the following dissertation:

Mobility in Polymer Thin Films: Diffusion and Marangoni Driven Patterning

Committee:

Christopher J. Ellison, Supervisor

C. Grant Willson

Benny D. Freeman

Venkat Ganesan

Katherine A. Willets

**Mobility in Polymer Thin Films: Diffusion and Marangoni Driven
Patterning**

by

Joshua Max Katzenstein, B.S.E., in Ch.E.

Dissertation

Presented to the Faculty of the Graduate School of

The University of Texas at Austin

in Partial Fulfillment

of the Requirements

for the Degree of

Doctor of Philosophy

The University of Texas at Austin

May 2013

Dedication

For Sarah

In the hope that the work contained within will allow us to have a wonderful life together

And for Opa

Who took me to my first chemistry lab when I was 6 years old

Acknowledgements

First, and most obviously, I would like to thank my advisor Dr. Chris Ellison. From a brief exchange of e-mails in the summer of 2008 before moving to Austin, to a meeting in his office the first week I was on campus in which he laid out his plans for a research group, to now, he has provided me with support, guidance, advice, and friendship. I feel like we both took a chance on each other back when there were no papers, no other students to talk to, and not even a lab to look at, and it's worked out incredibly well for me. We've been through a lot of ups and downs and growing pains as a research group and I think the experience of us starting from nothing together has been invaluable for me and my career.

I would like to also thank all of my Ellison Group lab-mates for their technical expertise and friendship. I would like to especially thank Julie Cushen, who has been there with me from my second year onward for useful scientific conversations and unwavering personal support. Dr. Dustin Janes has also been an invaluable editor, sounding board, friend, and voice of reason through all of my work. My papers wouldn't have been half as good without him. I would also like to thank and give my best wishes to Reika Katsumata and Chaebin Kim who will be taking over my projects after I leave. I think I leave both in very capable and motivated hands and am excited to see the work that comes next. I also have had a string of very talented undergrads that have been phenomenally helpful including Haley Hocker, Justin Chandler, Nikhil Hira, Dana McGuffin, and Nathan Prisco.

I also wish to express my gratitude to Dr. Grant Willson for being the one to e-mail me out of the blue and convince me to come to The University of Texas. Since I got here he has been supportive and kind to me at every opportunity. Some of the members

of his group (current and former) as well were instrumental to my research, specifically Ryan Deschner, Chris Bates, Dr. Jeff Strahan, Dr. Brandon Rawlings, and Dr. Xinyu Gu. The people in this list helped me learn a lot about doing research and always were quick to jump in with advice and support.

I have had several mentors before coming to graduate school who deserve recognition for guiding me to where I am today. First is Mrs. Marla Fallucca, my high school chemistry teacher for helping me decide to be a chemical engineer. Second, my undergraduate advisor, Dr. Susan Montgomery, deserves thanks for reminding me that I would never be happy until I was in control of my own ideas. Finally, thanks to my undergraduate research advisor Dr. Richard Laine, who exposed me to research for the first time.

I think it goes without saying that a significant amount of the credit for my Ph.D. goes to my family and my wonderful fiancée, Sarah. They read my papers when they didn't understand them, listened to me complain when I needed to, and supported me emotionally every step of the way. Sarah's dedication and encouragement have gotten me through and provided constant light and happiness to my life for the last three years and hopefully will for many more to come. My parents, grandparents, and sisters, who are incredibly excited that I am moving back to Michigan, have also been there for me my whole life. Even if they never knew exactly what it was I did, always made sure that I was happy doing it.

Mobility in Polymer Thin Films: Diffusion and Marangoni Driven Patterning

Joshua Max Katzenstein, Ph.D.

The University of Texas at Austin, 2013

Supervisor: Christopher J. Ellison

Polymer thin films are ubiquitous in a variety of everyday applications from cookware to packaging. Light can be used to both probe and manipulate the mobility of polymers in thin films. The first project involves the self-diffusion of poly(isobutyl methacrylate) (PiBMA) in thin films using fluorescence recovery after patterned photobleaching (FRAPP). PiBMA is an ideal polymer for this study because it exhibits a film thickness-independent glass transition temperature (T_g) on silicon oxide substrates in film thicknesses down to 14 nm. Since the diffusion coefficient of a polymer depends on the proximity of the experimental temperature to its T_g , nanoconfined diffusion can be measured without superimposed influence from T_g nanoconfinement effects. In this study, self-diffusion of PiBMA parallel to the confining interfaces was found to be film thickness independent to ~ 30 nm. The reason for the film thickness independence of the T_g of PiBMA is the balance between enhanced mobility at the free interface and hydrogen bonding with the substrate. However, when hydroxyls on the substrate are masked, the T_g of PiBMA decreases with decreasing film thickness. In this case, the diffusion coefficient increases with decreasing film thickness in a way consistent with additional distance from T_g .

The second project involves a new approach for creating topographic patterns in thin films via the Marangoni effect, which describes how small variations in surface energy can promote dramatic movement of fluids. Topographic patterns created using this method are potentially useful in a variety of applications, such as the creation of soft lithography stamps. Using a photomask, surface energy gradients can be patterned into solid polymer films. Upon heating the polymer film to a liquid state the Marangoni effect causes the polymer to flow creating three-dimensional topography. This technique was first demonstrated in polystyrene, which undergoes a partial dehydrogenation of the polymer backbone upon photoexposure. However, as exposed and unexposed regions inter-diffuse the topographic features decay. A solution to this problem is to use two orthogonally acting photosensitizers in the polymer film, one for topography creation, and the other for cross-linking which stabilizes the topography at high temperature.

Table of Contents

List of Tables	xv
List of Figures	xvi
List of Schemes	xxxii
DIFFUSION IN POLYMER THIN FILMS	1
Chapter 1: Diffusion in Polymer Thin Films	1
1.1 Introduction - Polymer Thin Films and Their Applications	1
1.2 General Diffusion Theory	2
1.3 Polymer Diffusion.....	3
1.4 Nanoconfined Diffusion.....	5
1.4.1 Diffusion Components	6
1.4.1.1 Diffusion Parallel to Interfaces	7
1.4.1.2 Diffusion Perpendicular to Interfaces	9
1.4.2 Measurement Methods.....	10
1.4.2.1 Isotopic	10
1.4.2.2 Fluorescence.....	11
1.5 Nanoconfined T_g	14
1.6 Summary and Objective.....	18
1.7 References.....	19
Chapter 2: Diffusion in Poly(isobutyl methacrylate) (PiBMA) Thin Films Parallel to Interfaces.....	26
2.1 Introduction.....	26
2.2 T_g in PiBMA Films	27
2.3 Self-Quenching Effects.....	29
2.4 Fluorescence Recovery After Patterned Photobleaching (FRAPP).....	31
2.5 Single-Spot Diffusion	33
2.6 Diffusion in Photobleached Arrays.....	36
2.7 Discussion of Diffusion Results.....	44

2.8	Conclusions.....	47
2.9	Experimental.....	48
2.9.1	Materials.....	48
2.9.1.1	Initiator Synthesis.....	48
2.9.1.2	Polymerization.....	50
2.9.2	Methods.....	52
2.9.2.1	Film Preparation.....	52
2.9.2.2	Thin Film T_g Determination.....	53
2.9.2.3	FRAPP.....	53
2.10	References.....	56
Chapter 3: Self-Diffusion of Poly(isobutyl methacrylate) in Multi-layer thin films		59
3.1	Motivation.....	59
3.2	Multi-Layer Films.....	60
3.3	Preliminary Results.....	61
3.3.1	High Temperature Diffusion Results.....	61
3.3.2	Low Temperature Diffusion Measurements.....	62
3.4	Discussion of Diffusion Results.....	64
3.5	Experimental.....	66
3.5.1	Materials.....	66
3.5.1.1	Purification of iBMA Monomer.....	67
3.5.1.2	Purification of Tetrahydrofuran.....	68
3.5.1.3	Polymerization.....	68
3.5.1.4	Fluorophore Attachment.....	70
3.5.2	Methods.....	71
3.5.2.1	Film Preparation.....	71
3.5.2.2	Determination of Thin Film T_g	72
3.5.2.3	FRAPP.....	73
3.6	References.....	74

MARANGONI EFFECT DRIVEN TOPOGRAPHIC PATTERNING IN THIN POLYMER FILMS	76
Chapter 4: Directing Convection to Pattern Thin Polymer Films	76
4.1 Introduction.....	76
4.2 Patterning Using Evaporative Self-Organization.....	77
4.3 Patterning by Temperature-Induced Instabilities.....	80
4.4 Electrohydrodynamic Patterning	83
4.5 Conclusions.....	86
4.6 References.....	87
Chapter 5: Patterning by Photochemically Directing the Marangoni Effect	92
5.1 Introduction - The Marangoni Effect.....	92
5.1.1 Patterning via the Marangoni Effect.....	92
5.2 Polystyrene (PS) Photochemistry	95
5.2.1 Fluorimetry.....	95
5.2.2 Quantification of Backbone Conversion.....	97
5.2.3 Contact Angle Measurements	100
5.3 Topographic Pattern Variety.....	101
5.3.1 Controlled Directionality of Feature Formation	104
5.4 Repeatability of Topography Formation.....	105
5.5 Topographic Pattern Transfer and Overlayers.....	107
5.6 Marangoni Number Calculations.....	108
5.7 Kinetics of Marangoni Driven Topography Formation.....	111
5.7.1 Exposure Dose	111
5.7.2 Initial Film Thickness	112
5.7.3 Temperature	114
5.8 Control Experiments	116
5.8.1 Light Filtering and Fluorescently Labeled PS	116
5.8.2 X-ray Photoelectron Spectroscopy (XPS)	117
5.8.3 Gel Permeation Chromatography (GPC).....	119
5.8.4 Infrared Camera	120

5.8.5 Mask Sink-In.....	122
5.9 Conclusions.....	123
5.10 Experimental.....	123
5.10.1 Materials.....	123
5.10.2 Methods.....	126
5.10.2.2 Topographic Feature Formation.....	127
5.10.2.3 Other Experimental Techniques.....	128
5.11 References.....	130
Chapter 6: Cross-linkable Topographic Features Created via Orthogonal Photochemistry and the Marangoni Effect.....	133
6.1 Introduction.....	133
6.2 Orthogonal Photochemistry.....	133
6.2.1 Host Polymer.....	135
6.2.2 Photoactive Compounds.....	136
6.3 Feature Formation and Cross-Linking.....	138
6.4 Quantification of Photo-Conversion.....	141
6.4.1 Michler's Ketone.....	141
6.4.2 Bis-Benzophenone.....	148
6.5 PiBMA Plasticization.....	150
6.6 Conclusion.....	151
6.7 Experimental.....	152
6.7.1 Materials and Material Characterization.....	152
6.7.2 Methods.....	154
6.7.2.1 Film preparation.....	154
6.7.2.2 Topography Formation, Characterization, and Other Equipment.....	155
6.8 References.....	156
Chapter 7: Future Work.....	157
7.1 Introduction.....	157
7.2 Nanoconfined Diffusion.....	157

7.2.1 Symmetric Interfaces	157
7.2.2 Nanocomposites	158
7.2.3 Molecular Weight Effects	159
7.3 Marangoni Driven Topographic Patterning	160
7.3.1 Simulations and Theory	160
7.3.2 Sub-Micron Patterning	161
7.3.2.1 Laser Induced Periodic Structures (LIPS)	162
7.3.2.2 Direct Write	163
7.3.3 Larger Surface Energy Gradients	163
7.3.4 Alignment of Block Co-Polymers	164
7.4 References	166
Appendices	168
Appendix A: Determination of the Diffusion Coefficient in a Polymer Thin Film by FRAPP	168
A.1 Introduction	168
A.2 Sample Preparation and Photobleaching	168
A.3 Data Collection	169
A.3.1 Equipment Setup	170
A.4 Data Analysis	189
A.5 References	199
Appendix B: Fluorescently Labeled Polymers	200
B.1 Introduction	200
B.2 NBD Incorporated Into Polymerization	200
B.3 Post-Polymerization Functionalization	203
B.3.1 Click Chemistry	203
B.3.2 ATRP	206
B.3.3 Anionic Polymerization	207
B.4 Other Potential Routes	209
B.4.1 Protected Anionic Initiators	209
B.4.2 Functional Monomers	210

B.5 References.....	211
References.....	212
Vita.....	230

List of Tables

Table 2.1: Table of diffusion results from single-spot FRAPP experiments, error is from repeated measurements. (1) Value estimated from the Rouse model (eq. 2.3). ²⁰ (2) Extrapolated from data using scaling theory for 12 kg/mol material. ²²	36
Table 6.1: Percent of polymer film dissolved as a function of both wt% BB (balance is PiBMA) and exposure dose through the 254 nm bandpass filter. Solubility is defined as percentage reduction in film thickness after the film is soaked in THF and dried as characterized by spectroscopy ellipsometry.....	150
Table 6.2: T_g of various compositions used in this study showing plasticization effect of small molecules on PiBMA.....	151

List of Figures

Figure 1.1: Illustrations of some applications where diffusion of polymers in thin films is important: a) hard drive lubrication (www.phi.com), b) polymer nanocomposite intercalation (reprinted with permission of the National Research Council of Canada, www.nrc-cnrc.gc.ca), c) lipid bilayers (reprinted with permission from “Organization and Dynamics of NBD-Labeled Lipids in Membranes Analyzed by Fluorescence Recovery after Photobleaching” Pucadyil, T. J.; Mukherjee, S.; Chattopadhyay, A. *The Journal of Physical Chemistry B* **2007**, *111*, 1975-1983, copyright 2007 American Chemical Society), and d) molecular transfer printing (reprinted with permission from “Molecular Transfer Printing Using Block Copolymers” Ji, S. X.; Liu, C. C.; Liu, G. L.; Nealey, P. F. *ACS Nano* **2010**, *4*, 599-609, copyright 2010 American Chemical Society).
.....6

Figure 1.2: Previous studies of nano-confined diffusion parallel to interfaces of polystyrene⁴⁸ (\diamond) and poly(dimethyl siloxane)⁵⁰ (\square). Diffusion coefficients are normalized by the bulk diffusion coefficient and plotted against film thickness.....8

Figure 1.3: Summary of diffusion perpendicular to interfaces on polystyrene from previous studies. a) The diffusion coefficient decreases as dark (deuterated) layer is closer to supporting substrate (decrease in X_w , adapted from ref. ⁶⁵). b) A decrease in diffusion coefficient is observed at the air interface surface relative to the bulk diffusion coefficient as the ratio of the deuterated film thickness (d) to the R_g is decreased.(adapted from ref. ⁵⁷).10

Figure 1.4: Photobleaching and recovery of a fluorescently labeled protein in untreated cells. Time-lapse micrographs of the bleached area before (pre-bleach), at the time of bleaching (laser spot), and at intervals during the recovery. Elapsed time, in seconds, is shown in each micrograph. Reproduced with permission from ref. ⁸³14

Figure 1.5: T_g of polystyrene in supported thin films measured by a variety of technique showing wide agreement amongst researchers. Reprinted with permission from ref. ⁹⁰16

Figure 2.1: Representative ellipsometric scan for a 50 nm thick film of PiBMA. Every sixth data point collected is shown here for clarity. The linear regressions above and below the T_g uses a span of data more than 15 °C wide.....27

Figure 2.2: T_g data for PiBMA (\square) and PiBMA-NBD (\circ) as a function of film thickness taken at 25 °C. The error bars indicate the error in ellipsometric measurements of T_g (± 1 °C).⁴ The bulk T_g for these materials is 51 °C, as measured by DSC and ellipsometry.....29

Figure 2.3: Fluorescence intensity per fluorophore at $\lambda_{\text{ex}} = 461 \text{ nm}$ and $\lambda_{\text{em}} = 520 \text{ nm}$ plotted against the amount of fluorophore in PiBMA-NBD films. The vertical line indicates the maximum amount of fluorophore that can be loaded into a PiBMA thin film without observing self-quenching effects. The amount of fluorophore was controlled by blending NBD labeled PiBMA with unlabeled PiBMA.31

Figure 2.4: Cartoon of a generic FRAPP experiment.32

Figure 2.5: a) Fluorescence micrographs from a typical single-spot FRAPP experiment in a 150 nm thick film of PiBMA-NBD at 140 °C. The white rectangle indicates the region over which diffusion was measured and the photobleached spot is 30 μm x 33 μm . b) Plot of recovery M_t/M_∞ against time for the experiment. Solid line is fit to eq. 2.2 where D is the only fitted parameter.34

Figure 2.6: Schematic of the periodic array FRAPP experiment. a) Spin coating and annealing of a polymer film with a uniform fluorophore distribution. b) Photobleaching with a high intensity broadband light source through a mask to initially create a periodic array of fluorescent and non-fluorescent regions. c) Redistribution of fluorophores from the initial condition ($t=0$) to long times ($t=t_{\text{long}}$) as diffusion occurs over time causes a relaxation in the pattern monitored by an epifluorescence microscope. Light areas indicate regions of high fluorescent intensity and dark regions indicate regions of low fluorescent intensity.....37

Figure 2.7: Fluorescence micrographs a) before photobleaching (\triangle) b) at the start of the diffusion experiment after patterned photobleaching and annealing (\diamond) and c) after significant recovery (\square) of a 127 nm film of PiBMA-NBD. Plot shows the normalized intensity as function of position (x) from a 300 pixel wide (in y) line integral perpendicular to the bleached pattern over several periods. ‘ A ’ indicates the amplitude of the sinusoid and ‘ λ ’ indicates the wavelength.....39

Figure 2.8: Results of a typical FRAPP experiment for a 127 nm film. The left axis shows the negative natural log of the amplitude normalized by the amplitude of the initial condition (A_0) (\circ), and the right axis contains the wavelength (\square) of the best fit sinusoid against time. The solid line through the amplitude data indicates best fit line that is then used with eq 2 to calculate the diffusion coefficient. The error in the amplitude is smaller than the symbols and is less than 4% for each data point. ...41

Figure 2.9: Diffusion coefficient at 80 °C of PiBMA-NBD (\square) and PiBMA-NBD-PiBMA (\circ) as a function of film thickness recorded at 25 °C. The dashed line indicates the bulk diffusion coefficient estimated using the Rouse model for this molecular weight and temperature (1.05×10^{-12} cm²/sec). Error bars indicate the uncertainty as calculated from eq 2.6.43

Figure 2.10: Photobleaching of PiBMA-NBD at room temperature (thin line) and 80 °C (thick line) at $\lambda_{ex} = 465$ and $\lambda_{em} = 520$. Inset shows first minute of photobleaching which is typical total amount of exposure time during a diffusion experiment showing <5% photobleaching occurs at 80 °C.55

Figure 3.1: a) Structure of PCHE b) Schematic of multi-layer film.....60

Figure 3.2: Diffusion coefficient as a function of film thickness for PiBMA multi-layer films at 78 °C. Solid line indicates bulk diffusion coefficient calculated from the Rouse model. Dashed line indicates the diffusion coefficient if the sample is 2 °C further from T_g . Error bars represent a 95% confidence interval.	62
Figure 3.3: Diffusion coefficient as a function of film thickness for PiBMA multi-layer films at 66 °C. Solid line indicates the bulk diffusion coefficient calculated from the Rouse model. Error bars represent a 95% confidence interval.	63
Figure 3.4: Diffusion coefficient of PiBMA as a function of $T-T_g$	65
Figure 4.1: a) Top view and b) side view schematic illustrations of the parallel-plate geometry in which the upper plate slides over the lower stationary plate at a fixed speed with a polymer solution confined between the plates. c) Optical micrographs of patterns produced from different PS in chloroform solution concentrations at a constant sliding speed of 50 $\mu\text{m/s}$. Reproduced from ref. ²⁴ with permission from John Wiley and Sons, © 2005.....	78

Figure 4.2: a) AFM topographical image of the honeycomb patterns resulting from co-casting PS ($M_w = 220$ kDa) and PVP ($M_w = 11$ kDa) from ethylbenzene solution (4 wt.% polymer, 4:1 weight ratio of PS to PVP) onto a mica substrate with an applied $1 \text{ L}\cdot\text{min}^{-1}$ airflow. The inset is a fast-Fourier transform of the AFM image. b) Schematic of the drying process the authors proposed to explain the phenomenological results. Adapted with permission from “Honeycomb pattern formation via polystyrene/poly(2-vinylpyridine) phase separation” Cui, L.; Han, Y. C. *Langmuir* **2005**, 21, 11085-11091. Copyright 2005, American Chemical Society.....80

Figure 4.3: a) A schematic representation of lithographically induced self-assembly (LISA) as demonstrated by Chou and Zhuang.¹² A 95 nm thick supported film of poly(methyl methacrylate) (PMMA, $M_w = 2$ kDa) is brought in close contact with a mask. After heating the film to $130 \text{ }^\circ\text{C}$, the polymer flows into pillars that span the mask/substrate gap, which are subsequently preserved by cooling below T_g . b) shows an example AFM image of pillars which formed against a mask with a protruding rectangle. The pillars are 440 nm tall and $2 \text{ }\mu\text{m}$ in diameter. Reprinted with permission from “Lithographically induced self-assembly of periodic polymer micropillar arrays” Chou, S. Y.; Zhuang, L. *J. Vac. Sci. Technol. B* **1999**, 17, 3197-3202. Copyright 1999, American Vacuum Society.....81

Figure 4.4: a) A schematic representation of electrohydrodynamic patterning (EHP) as demonstrated by Schäffer et al.¹³. A 45 nm thick film of brominated PS is placed 80 nm from a mask patterned by lines that had a width of 200 nm and a height of 170 nm. A voltage of 42 V was applied. After heating the film to 170 °C for 14h, the polymer flows toward the mask protrusions, which are subsequently preserved by cooling below T_g . b) An example top down AFM image and height profile of the 140 nm wide lines that resulted. Reprinted by permission from Macmillan Publishers Ltd: *Nature* (ref. ¹³), copyright 2000. c) An example AFM image of an EHP pattern formed by employing a mask with a protruding triangular grid that directed the pillar size and placement. Reproduced from ref. ⁵³ with permission from John Wiley and Sons © 2006. d) An example SEM micrograph of PMMA structures that resulted after EHP patterning of a PS/PMMA bilayer film and selective rinsing of PS. Reprinted by permission from Macmillan Publishers Ltd: *Nature Materials* (ref. ⁵⁴), copyright 2002.....84

Figure 5.1: SEM image of a top view of the silica colloidal (1 μm diameter) crystal films demonstrating the high degree of long-range ordering created via isothermal evaporation-induced self-assembly. This technique utilizes thermal Marangoni convective currents to deposit the colloidal particles. Reprinted with permission from “Colloidal crystal films: Advances in universality and perfection” Wong, S.; Kitaev, V.; Ozin, G. A. *J. Am. Chem. Soc.* **2003**, *125*, 15589-15598. Copyright 2003, American Chemical Society.....93

Figure 5.2: Schematic illustration of the steps involved in feature formation in a PS thin film. a) A brightfield micrograph of a glassy polymer film (~150 nm thick) after exposure to light through a photomask which induces a photochemical reaction in exposed regions and an associated patterned surface energy. For the PS films employed here, there is higher surface energy in the exposed regions. No topography can be detected by atomic force microscopy after this stage. b) After heating the same film to 110 °C, where the polymer becomes a liquid, the patterned surface energy drives formation of topographic features via the Marangoni Effect. 95

Figure 5.3: Fluorescence spectra of PS precursor (solid line) and PS exposed to UV light for two minutes (dashed line), both in THF solutions at 0.05 mg/mL. For both samples $\lambda_{ex} = 310$ nm.97

Figure 5.4: a) Full and b) selected region of interest [indicated by rectangle in a)] FTIR spectra for PS as a function of exposure dose. All spectra are normalized to tallest peak in the phenyl ring region (2926 cm^{-1}). The dashed arrow indicates the direction of increasing exposure dose. ...98

Figure 5.5: Percent conversion of PS backbone to carbon-carbon double bonds as a function of exposure dose by infrared spectroscopy. The filled data point represents the typical dose and conversion used in this study.99

Figure 5.6: Contact angle of PS as a function of exposure dose for water (Δ), glycerol (\square), and poly(ethylene glycol) (\diamond). Error bars indicate standard deviation from ten measurements. Changes are all statistically significant ($p < 0.01$).101

Figure 5.7: Various line pattern periods created in ~150 nm thick PS films with overlaid profilometry traces showing topography formed by using photomasks with different line spacing of a) 100 μm chrome lines with a 200 μm pitch b) 12.5 μm chrome lines on a 25 μm pitch and c) 5 μm chrome lines on a 10 μm pitch. For part c), the profilometer stylus is too large for accurate characterization of the topography. Panel a) highlights that Marangoni-driven patterning is sensitive to the local gradient in surface energy, which occurs only near interfaces of exposed and unexposed regions which are a smaller portion of the overall image in a) than b) or c).....102

Figure 5.8: Various patterns formed by photochemically directed Marangoni flow.

Patterns shown in a) triangular pillars with triangular area exposed to light, that rise up above the film and b) ‘longhorn’ patterns which sink into the film, both are 1:1 replications of patterns on the photomask. Patterned c) large (formed by the 12.5 μm chrome lines on a 25 μm pitch photomask) and d) small (formed by the 5 μm lines on a 10 μm pitch photomask) mounds are formed by exposure through the same line-and-space mask twice with the mask turned 90° between exposures. Pattern e) lines-in-lines is the result of two exposures of different line-and-space periods parallel to each other and f) ‘dogbones’ by the same method with the second mask turned 90° between exposures. For e) and f) one exposure utilized a 12.5 μm chrome lines on a 25 μm pitch photomask while the second exposure used a 5 μm lines on a 10 μm pitch photomask. Colors are interference patterns caused by changes in film height. All films are 100-300 nm thick before patterning and have scale bars of 30 μm103

Figure 5.9: Brightfield micrographs (top) and corresponding profilometry traces (bottom) of topographic features a) that sink into the film and b) that rise out of the film. Dark lines on micrographs indicate region where profilometry trace was collected105

- Figure 5.10: Repeated topographic feature formation using the photochemically directed Marangoni process in a single PS film with an initial film thickness of ~ 140 nm. The left column contains optical micrographs of topographic features formed after exposure through a photomask with $12.5 \mu\text{m}$ chrome lines on a $25 \mu\text{m}$ pitch and annealing at 120°C for 60 minutes. The right column contains optical micrographs of the same film after 60 minutes of annealing at 145°C , where features have completely dissipated. Scale bars are $50 \mu\text{m}$106
- Figure 5.11: Optical micrographs of a) PS film ‘master’ with topography formed by photochemically directing Marangoni-driven flow and b) pattern transferred into Sylgard® 184 after curing at room temperature for 24 hours and subsequent heating to 100°C for 2 hours to complete crosslinking. Scale bars are $100 \mu\text{m}$107
- Figure 5.12: Optical micrographs of Marangoni driven topography formation in 150 nm thick PS films with various overlayers placed on top before photoexposure and thermal annealing. Topography was generated with a a) 95 nm PMMA overlayer, a glassy polymer, b) 52 nm sputter deposited gold overlayer, a metal, and c) 300 g/mol PEG overlayer, a liquid polymer (washed off with water before imaging). Scale bars are $50 \mu\text{m}$. Similar topography can also be formed by first photoexposing the PS film and then depositing the over-layer prior to heating the film to develop topography.....108
- Figure 5.13: Peak to valley height as a function of heating time at 136°C with exposure doses of 840 J/cm^2 (Δ), 420 J/cm^2 (\square), and 210 J/cm^2 (\diamond) on films with an initial thickness of 130 nm.....112

Figure 5.14: Peak to valley height as a function of heating time at 136 °C with exposure doses of 840 J/cm² at film thicknesses of 300 nm (Δ), 130 nm (□), and 60 nm (◇). Inset shows peak to valley heights normalized by the initial thickness of the film.....114

Figure 5.15: Peak to valley height as a function of heating time at 120 °C (Δ), 130 °C (□), and 140 °C (◇) with exposure doses of 840 J/cm² at film thicknesses of 145 nm. Inset is 140 °C data with a vertical dashed line at the characteristic diffusion time for PS at this temperature.....116

Figure 5.16: Micrographs showing the effect of blocking all wavelengths absorbed by a PS film with a 385 nm long pass filter during light exposure. a) Bright field micrograph immediately after exposure. b) Fluorescence micrograph showing photobleaching of NBD-labeled PS after exposure with the long pass filter in place; light areas indicate high fluorophore concentrations in regions protected by the photo mask. c) Bright field micrograph of the same region after 1 hour at 110 °C showing no topography117

Figure 5.17: XPS spectra of unexposed (dashed line) and exposed (solid line) PS films. No peak is observed at 531 eV which is characteristic of the presence of oxygen.118

Figure 5.18: Plot of refractive index vs. time collected by GPC for neat PS (Δ) and PS exposed to the light source (○).....120

Figure 5.19: Temperature of clean quartz (dotted line), PS film (dashed line) and chrome on quartz photomask (solid line) during photoexposure as a function of time. Horizontal line indicates the T_g of the PS used for these experiments121

Figure 5.20: Bright field micrographs of a PS film a) immediately after UV exposure for 45 seconds at -100 °C and following b) 1 hour of heating at 110 °C to develop the topography.....	122
Figure 6.1: Schematic of orthogonal photochemistry used for a) topographic feature formation via the Marangoni effect and subsequent cross-linking in the second exposure. b) Generic attachment of benzophenone to a carbon atom via hydrogen abstraction.....	135
Figure 6.2: a) Structure of Michler's ketone (MK). b) Structure of bis-benzophenone (BB). c) UV/Vis absorption spectra of PiBMA (solid line), PiBMA with 10 wt% MK (dashed line), and PiBMA with 10 wt% BB (dotted line). Films were all approximately 400 nm thick on quartz. Shaded regions indicate bandpass filters used to activate MK (365 nm, 10 nm FWHM) and the BB (254 nm, 40 nm FWHM).	137
Figure 6.3: Films with only 2% MK a) immediately after features formed by heating and b) after the features decay with continued heating. Films containing 2% MK and 10% BB c) immediately after features formed by heating and d) after the features decay after continued heating without exposure at 254 nm. Films containing 2% MK and 10% BB e) immediately after features formed by heating and f) after exposure at 254 nm to cross-link and continued heating showing topographic feature stabilization. Scale bars are 30 μm. Colors are formed from interference due to changes in film thickness. All films are roughly 100 nm thick before patterning.	140

Figure 6.4: Film of PiBMA with 2% MK and 10 wt% BB a) after 5 seconds of photoexposure and b) topographic features formed after 5 minutes of subsequent heating at 125 °C. Topography is roughly 15 nm in peak to valley height at this point. Scale bars are 30 μm.141

Figure 6.5: Representative IR spectra, inset shows MK carbonyl peak with an arrow indicating the direction of increasing photoexposure. In the direction of the arrow the photoexposure doses for each spectrum are 0 J/cm², 4 J/cm², and 125 J/cm². Data are normalized to the tallest carbonyl peak.143

Figure 6.6: Conversion of MK by FTIR. Inset is on a logarithmic scale with best fit line to guide the eye.144

Figure 6.7: Contact angle of poly(ethylene glycol) on PiBMA films with 2 wt% MK as a function of exposure dose. Error bars represent standard deviations from 10 measurements.145

Figure 6.8: Gel permeation chromatography of PiBMA + 2 wt% MK. a) Before photoexposure showing a peak in the refractive index detector (broken line) no fluorescence peak (solid line). b) After photoexposure showing coincident refractive index and fluorescence peaks indicating covalent attachment of MK to the polymer. The fluorescence signal has been vertically shifted for clarity.147

Figure 6.9: Representative IR spectra, inset shows the BB carbonyl peak with an arrow indicating the direction of increasing photoexposure. In the direction of the arrow the photoexposure doses for each spectrum are 0 J/cm², 0.5 J/cm², and 4 J/cm². Data are normalized to the tallest carbonyl peak.148

Figure 6.10: Conversion of BB by FTIR. Inset is on a logarithmic scale with best fit line to guide the eye.	149
Figure A.2: QuantaMaster 40 Fluorimeter.....	170
Figure A.4: Inside of the fluorimeter set up to serve as the microscope light source. The lens that must be installed is indicated with a red arrow.	172
Figure A.5: Microscope light source power switch	173
Figure A.6: Controller and camera power switches (outlined in red) and shutter control toggles (outlined in yellow).....	174
Figure A.7: Location of excitation slit micrometers.....	175
Figure A.8: Hot stage setup with sample in center	176
Figure A.9: PTI Felix login screen	177
Figure A.11: Micro-Manager startup screen.....	179
Figure A.13: Filter wheel with shutter switch in red box.	181
Figure A.14: Location of focus knobs	182
Figure A.15: Example of an acceptable fluorescence intensity profile before heating the thin film. Note the peaks and valleys roughly line up.	183
Figure A.16: Linkham hot stage control panel.	185
Figure A.17: Micro-Manager device/property browser.....	187
Figure A.18: Micro-Manager Multi-dimensional acquisition window.....	189
Figure A.20: Diffusion image with correctly drawn line, inset shows angle is $\sim 1.3^\circ$	191
Figure A.21: Intensity vs. position plot for one time point.....	192
Figure A.22: Completed Excel spreadsheet for one time point in a diffusion experiment.....	193
Figure A.23: Solver window setup for parameter calculation	194

Figure A.24: Example curve fitting. Open symbols represent data points and the solid line is the best fit curve.195

Figure A.25: a) Data table for diffusion experiment. b) Plot of data (open symbols) and best fit line (solid line), the slope is used to calculate the diffusion coefficient.196

Figure A.26: Linear regression setup.....197

List of Schemes

Scheme 2.1: a) Synthesis of mono-functional NBD bearing one ATRP initiator site for chain-end labeled polymers. b) Synthesis of di-functional NBD bearing two ATRP initiator sites for mid-chain labeled polymers.	50
Scheme 2.2: Synthesis of a) chain-end labeled PiBMA-NBD and b) mid-chain labeled PiBMA-NBD-PiBMA by ARGET ATRP.	52
Scheme 3.1: Anionic polymerization of azide terminated PiBMA	69
Scheme 3.2: Synthesis of alkyne-bearing NBD fluorophore.	70
Scheme 3.3: Attachment of NBD-Aminyne to PiBMA-Az via click reaction	71
Scheme 5.1: Dehydrogenation of PS by exposure to UV light.	96
Scheme 5.2: Synthesis of alkyne-bearing NBD fluorophore.	125
Scheme 5.3: 'Click' reaction of NBD fluorophore with PS polymer	126
Scheme 6.1: Synthesis of bis-benzophenone, adapted from Ref. ³	154
Scheme B.1: a) Structure of PiBMA b) Structure of NBD-Cl.	200
Scheme B.2: a) Synthesis of mono-functional NBD bearing one ATRP initiator site for chain-end labeled polymers. b) Synthesis of di-functional NBD bearing two ATRP initiator sites for mid-chain labeled polymers.	201
Scheme B.3: Synthesis of a) chain-end labeled PiBMA-NBD and b) mid-chain labeled PiBMA-NBD-PiBMA by ARGET ATRP.	203
Scheme B.4: Synthesis of NBD-Alkyne	204
Scheme B.5: Click reaction of NBD-Alkyne with an azide containing polymer	206
Scheme B.6: Synthesis of azide ATRP initiator	207
Scheme B.7: 'Simple' anionic polymerization of PiBMA-NBD.	208

Scheme B.8: Halide end-capped anionic polymerization of PiBMA and azide attachment.....	209
Scheme B.9: Protected amine containing anionic polymerization initiators	210
Scheme B.10: Functional monomers: a) amine methacrylate b) azide methacrylate	210

DIFFUSION IN POLYMER THIN FILMS

Chapter 1: Diffusion in Polymer Thin Films *

1.1 INTRODUCTION - POLYMER THIN FILMS AND THEIR APPLICATIONS

Synthetic polymers have been a part of everyday life since 1907 when Bakelite was invented by Leo Baekeland in an attempt to find a synthetic replacement for shellac.¹ One of the next major innovations that led to the acceleration of polymer science was the invention of nylon by Wallace Carothers at Dupont in 1935. This material became very popular during World War II when it was used in everything from parachute lines to pantyhose as a replacement for silk.² Since then, synthetic polymers are found in everything from food packaging to computers to carpeting and have enabled a wide variety of technological enhancements that are integral to modern life.

Many modern applications of polymers rely on polymers cast into thin films. For example, most non-stick cookware is covered with a thin film of polytetrafluoroethylene (Teflon)³ and many lithium ion batteries use solid polymer electrolyte thin films.⁴ Polymer thin films are critical to the \$300 billion microelectronics industry and have also been used in a wide variety of biomedical applications as protein-repellant coatings, antibacterial coatings, and for other uses.⁵ Polymers can be easily cast into films on the order of tens of nanometers to several microns thick by spin coating, solvent casting, spray coating, or any of several other technologies. These films have become ubiquitous

* Sections of this chapter reproduced in part with permission from “Nanoconfined Self-Diffusion of Poly(isobutyl methacrylate) in Films with a Thickness Independent Glass Transition” Katzenstein, J. M.; Janes, D. W.; Hocker, H. E.; Chandler, J. K.; Ellison, C. J. *Macromolecules* **2011**, *45*, 1544-1552. Copyright 2011 American Chemical Society.

in a wide variety of applications, in many instances going unnoticed, but they are critical to functions most people take for granted.

1.2 GENERAL DIFFUSION THEORY

Before diffusion in polymer thin films can be discussed, it is important to review the physical foundation on which these principles are built. A colloidal particle in a liquid collides randomly with molecules around it over time. This can cause the particle to jump or diffuse to adjacent available positions by Brownian (thermal) motion. In three-dimensions, the mean-square displacement ($\langle [r(t)-r(0)]^2 \rangle$) of the particle diffusing in a random walk over a time interval (t) is proportional to the diffusion coefficient (D) (eq. 1.1).⁶

$$\langle [r(t)-r(0)]^2 \rangle = 6Dt \quad (1.1)$$

Eq. 1.1 comes from the central limit theorem which shows that after a period of time the spatial distribution of endpoints follows a normal distribution.⁷ The collisions of liquid molecules with the particle exert an average force on the particle, which moves with an average velocity. The force and velocity are related by a constant of proportionality called the friction coefficient (ζ). Einstein showed⁸ that this friction coefficient is related to the thermal energy of the particle by the diffusion coefficient (eq. 1.2, where k_B is the Boltzmann constant and T is absolute temperature).

$$D = k_B T / \zeta \quad (1.2)$$

There are several systems in which the friction coefficient is known. For example, in 1851 Stokes determined an equation for the friction coefficient of a sphere as a function of solution viscosity (η) and the radius of the particle (R) (eq. 1.3).⁹

$$\zeta = 6\pi\eta R \quad (1.3)$$

Combining eqs. 1.2 and 1.3 leads to the Stokes-Einstein relationship for the diffusion coefficient of a spherical particle in a liquid (eq. 1.4).

$$D = \frac{k_B T}{6\pi\eta R_B} \quad (1.4)$$

1.3 POLYMER DIFFUSION

Using the ideas described in the previous section, in 1953 Rouse developed a model of a diffusing unentangled polymer that represents the chain as a series of N spherical beads connected by springs of average size b , which is equivalent to the statistical segment length for that polymer.¹⁰ In this model, individual beads make a frictional contribution. The diffusion coefficient (eq. 1.5) is simply the sum of the contributions from each of N total beads; therefore D scales as N^{-1} (or similarly M^{-1} where M is the polymer molecular weight).

$$D = k_B T / N\zeta \quad (1.5)$$

In practice, it is useful to relate D to directly measurable quantities. The zero-shear viscosity (η_0) of a polymer melt is related to the characteristic time for a molecule to diffuse a distance equivalent to its size (τ_R , the Rouse time) and therefore directly related to ζ by eq. 1.6 (where ρ is the mass density of the polymer, and N_A is Avogadro's number).

$$\eta_0 = (\rho N^2 N_A / 36M) * b^2 \zeta \quad (1.6)$$

This relationship allows for the calculation of D by (eq. 1.7) in which R is the ideal gas constant, and $\langle R^2 \rangle$ is the mean-squared end-to-end length of the polymer.^{10,11}

$$D = \frac{\rho R T \langle R^2 \rangle}{36M\eta_0} \quad (1.7)$$

Diffusion in an entangled, moderate to high molecular weight, bulk polymer melt takes place by chain reptation, in which the chain diffuses by “threading” through a field of molecular obstacles, known as entanglements, in addition to the frictional

contributions discussed above. According to the original reptation theory, the diffusion coefficient in these systems scales according to M^{-2} .¹¹⁻¹³ However, more detailed experimental studies show that diffusion scales as $M^{-2.3}$ due to constraint release and tube length fluctuation.¹⁴

The other major parameter that influences the diffusion coefficient is temperature. While it appears in eq. 1.7 that the diffusion coefficient scales linearly with temperature, η_0 and ρ also depend on temperature. Therefore, the overall temperature dependence is more complex. Most studies of the temperature dependence of diffusion fit either simulation or experimental results to an empirical relationship for the diffusion coefficient or friction coefficient. Two commonly used equations are the Vogel-Fulcher-Tammann (or equivalently Williams-Landel-Ferry) model (eq. 1.8)¹⁵⁻¹⁷ or, over a smaller temperature range, an Arrhenius relationship (eq. 1.9)^{18,19} in which D_∞ , A , B , C , and E_D are empirically determined constants for a specific polymer.

$$D = D_\infty \exp\left[A + \frac{B}{T-T_0}\right] \quad (1.8)$$

$$D = C * \exp\left[\frac{E_D}{RT}\right] \quad (1.9)$$

Using these relationships, there have been many studies, both theoretical and experimental, of bulk polymer diffusion. One of the primary techniques used to directly measure diffusion in polymer melts is Pulsed Field Gradient – Nuclear Magnetic Resonance (PFG-NMR). A review of this technique was published in 1983 by von Meerwall, one of the pioneers of this approach.²⁰ Much of the focus in these studies has been concentrated in two areas. First, many studies have investigated the relationship between the diffusion coefficient and molecular weight or temperature for a specific polymer.^{17,21} Second, the crossover from un-entangled (Rouse) to entangled (reptation) systems has received significant attention both experimentally^{22,23} and theoretically.^{24,25}

1.4 NANOCONFINED DIFFUSION

Physical properties of polymers, including physical aging,²⁶⁻²⁹ viscosity,³⁰⁻³² elastic modulus,³³⁻³⁵ polymer blend stability,³⁶ creep compliance,³⁷ polymer wrinkling,³⁸ adhesion,³⁹ and other molecular motions in glassy polymers^{40,41} are often different compared to bulk when the polymer is constrained to the ~1-100 nanometer size scale, or nanoconfined. Considerable research has been devoted to studying polymers in thin films as a convenient means of examining interfacial effects; because as film thickness decreases, the surface or interfacial area to volume ratio increases.

Unfortunately, nanoconfined polymer diffusion has not received significant experimental attention but is highly relevant to several important properties such as adhesion⁴² and friction.⁴³ Nanoconfined diffusion is also important in many existing polymer technologies such as in the exfoliation of clay nanoparticles in nanocomposites, where exfoliation processes require diffusion of polymers along sheet-like filler particles and in between inter-particle galleries.⁴⁴ Exfoliation of nanoparticles is key to achieving the desired property enhancement that makes nanocomposites attractive, such as increased modulus and degree of crystallinity.⁴⁵ In addition, newly emerging technologies, such as molecular transfer printing (MTP), rely on nanoconfined polymer diffusion processes in their function.⁴⁶ In MTP, substrate-reactive polymer ‘inks’ diffuse along polymer/polymer interfaces whose separation distance is defined by a self-assembled block co-polymer. Figure 1.1 shows some illustrations of some of these and other applications where diffusion of polymers in thin films is important.

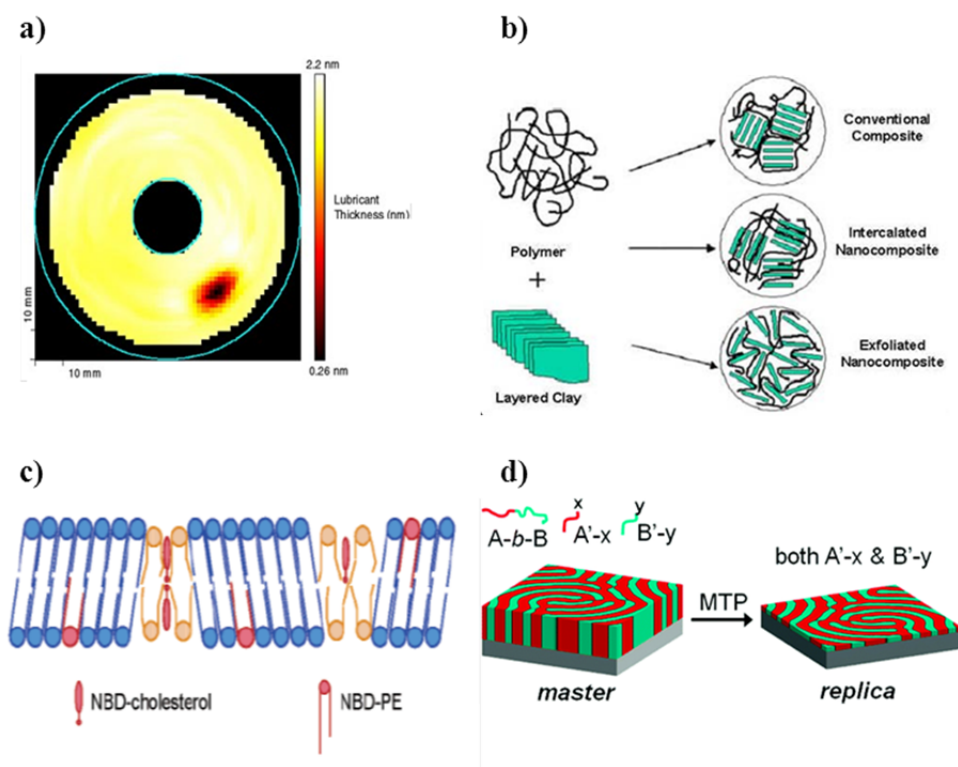


Figure 1.1: Illustrations of some applications where diffusion of polymers in thin films is important: a) hard drive lubrication (www.phi.com), b) polymer nanocomposite intercalation (reprinted with permission of the National Research Council of Canada, www.nrc-cnrc.gc.ca), c) lipid bilayers (reprinted with permission from “Organization and Dynamics of NBD-Labeled Lipids in Membranes Analyzed by Fluorescence Recovery after Photobleaching” Pucadyil, T. J.; Mukherjee, S.; Chattopadhyay, A. *The Journal of Physical Chemistry B* **2007**, *111*, 1975-1983, copyright 2007 American Chemical Society), and d) molecular transfer printing (reprinted with permission from “Molecular Transfer Printing Using Block Copolymers” Ji, S. X.; Liu, C. C.; Liu, G. L.; Nealey, P. F. *ACS Nano* **2010**, *4*, 599-609, copyright 2010 American Chemical Society).

1.4.1 Diffusion Components

Monte Carlo simulations of polymers of varying chain length confined between hard wall interfaces have revealed anisotropy to the center of mass mobility.⁴⁷ The results suggest that the center of mass displacement parallel and perpendicular to the confining interfaces scaled differently with time. Such diffusion anisotropy exemplifies that studies

of diffusion parallel and perpendicular to interfaces are crucial for assembling a complete understanding of nanoconfined diffusion. This is especially true given that diffusion in some applications, such as in nanocomposite exfoliation, could reflect contributions from both components.

1.4.1.1 Diffusion Parallel to Interfaces

While polymer diffusion parallel to nanoconfining interfaces has important implications for a variety of applications, such as those shown in Figure 1.1, relatively few experimental studies have been reported to date. An early study by Frank and coworkers⁴⁸ examined the diffusion of a single molecular weight of polystyrene at a single temperature. This study determined that the diffusion coefficient was reduced by a factor of two as the film thickness was reduced below approximately 150 nm (about $50xR_g$). Another study of diffusion parallel to interfaces by Bae et al.,⁴⁹ subsequently extended by Wong et al.,⁵⁰ was conducted using poly(dimethyl siloxane) nanoconfined between mica sheets in a surface forces apparatus. They found, relative to bulk diffusion coefficients, a reduction in diffusion coefficients by a factor of ~ 2 at a film thickness of 10 nm, and a reduction by a factor of ~ 4 at a film thickness of 2 nm. The key results of these two studies are shown in Figure 1.2 below.

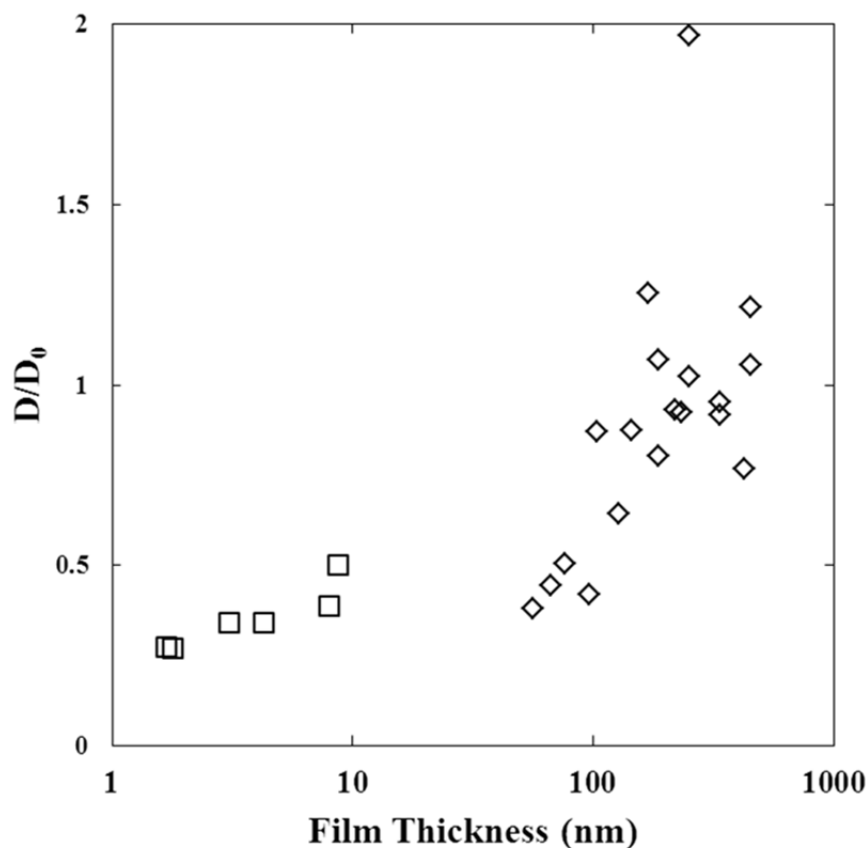


Figure 1.2: Previous studies of nano-confined diffusion parallel to interfaces of polystyrene⁴⁸ (◇) and poly(dimethyl siloxane)⁵⁰ (□). Diffusion coefficients are normalized by the bulk diffusion coefficient and plotted against film thickness.

The same group that studied poly(dimethyl siloxane) above also studied diffusion of adsorbed poly(ethylene glycol) chains at dilute surface coverage along the interface of a self-assembled monolayer of octadecyltriethoxysilane and water.⁵¹ They observed the molecular weight dependence of the diffusion coefficient was much stronger ($M^{-1.5}$) for adsorbed polymers diffusing along a surface than for the same polymer in solution ($M^{0.5}$). Additionally, Manias et al.⁵² examined diffusion of polystyrene in a 2 nm gap between atomically smooth mica sheets modified with alkyl chains of varying length on the surface. They found that not only do longer alkyl chains increase the rate of diffusion,

a 10 fold increase in D resulted when going from 12 to 18 carbons, but the molecular weight dependence of the effective diffusion coefficient in these systems scaled as $M^{-1.09}$, rather than the expected $M^{-2.0}$ for bulk entangled polystyrene.

1.4.1.2 Diffusion Perpendicular to Interfaces

Nano-confined diffusion has been relatively well studied perpendicular to interfaces.⁵³⁻⁶² Van Alsten and collaborators in 1992 performed one early study in which they measured the mobility of deuterated poly(methyl methacrylate) (PMMA) to show that the center of mass diffusion near a solid substrate was significantly reduced compared to a deuterated layer within a bulk film.⁵⁸ This was the first direct experimental evidence that interfaces do impact diffusion, confirming earlier simulation studies.^{63,64}

Studies of entangled polystyrene films on a silicon wafer with native oxide showed changes in M dependence of the D from that of bulk polymer ($D \sim M^{-2.0}$) at both interfaces. Within a distance of ~ 4 times the radius of gyration (R_g) from the free interface (polymer/air), D scaled as $M^{-2.5}$.⁵⁷ In contrast, at the supported interface (polymer/substrate) D scaled as $M^{-1.5}$ for entangled polystyrene with dramatically slowed diffusion in films up to $10 \times R_g$.⁶⁵ This indicates that different interfaces, at least in the case of this specific polymer film/substrate system, can have an impact on the translational mobility of the chain. See Figure 1.3 for a summary the results of these studies.

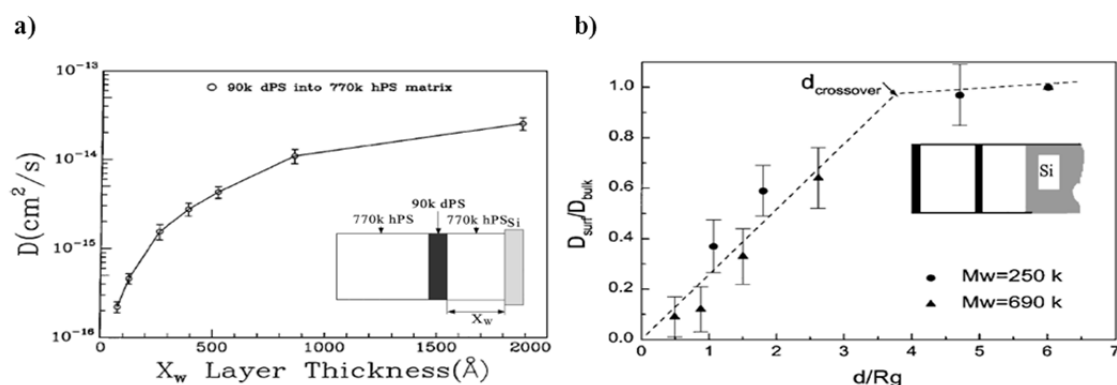


Figure 1.3: Summary of diffusion perpendicular to interfaces on polystyrene from previous studies. a) The diffusion coefficient decreases as dark (deuterated) layer is closer to supporting substrate (decrease in X_w , adapted from ref. ⁶⁵). b) A decrease in diffusion coefficient is observed at the air interface surface relative to the bulk diffusion coefficient as the ratio of the deuterated film thickness (d) to the R_g is decreased.(adapted from ref. ⁵⁷).

1.4.2 Measurement Methods

Characterizing diffusion of nanoconfined polymers has been accomplished by a variety of techniques. However, there are two distinct types of methods, isotopic and fluorescence. Isotopic techniques, using (most commonly) deuterated versions of polymers, examine the concentration profiles of individual isotopes. However, these materials are fairly expensive and cannot be readily made in some instances. The second, and more common, type of method is fluorescence based which relies on a fluorescent tag or label to track the position of polymer chains.

1.4.2.1 Isotopic

Isotopic techniques for measuring diffusion take advantage of the difference between deuterium atoms and hydrogen atoms on polymers that are otherwise chemically identical. The leading isotopic technique for studying diffusion of nanoconfined polymers is secondary ion mass spectroscopy (SIMS), which uses layered hydrogenated and deuterated versions of a polymer and measures the concentration profile of deuterium

atoms as a function of depth into the film. The diffusion coefficient can be calculated by annealing films at a specific diffusion temperature for various times.

There are three main reasons that SIMS is not a suitable method for diffusion studies parallel to interfaces. First, it requires a fairly large lateral area (around 80 μm in diameter⁴²) to obtain sufficient signal for accurate concentration profiles. Second, while construction of vertically layered films by floating techniques and other methods is common, construction of horizontally layered films to study diffusion across an interface is more difficult. Finally, SIMS is a destructive method, tunneling into the film to collect time of flight mass spectroscopy as a function of depth which means that for each time point a separate film has to be used.

Another isotopic technique used to characterize diffusion in nanoconfined polymers is specular neutron reflectivity (SNR). This method, like SIMS, uses layered hydrogenated and deuterated polymers. However, rather than using mass spectrometry to calculate a concentration profile, SNR measures momentum transfer over a range of neutron momenta. The reflectivity of the neutrons with varying momenta can be fit to a model for layered polymers and the diffusion coefficient can be calculated.⁵⁸ The major disadvantage to both isotopic techniques is fabrication of the nanoconfined system. SIMS and SNR requires starting with two distinct layers, one with the hydrogenated version of a polymer, the other with the deuterated version. Like SIMS there can be fabrication challenges in creating two distinct horizontal regions on a planar substrate.

1.4.2.2 Fluorescence

Fluorescence techniques used to measure diffusion were first developed using small molecule dyes or ‘probes’ in polymer matrices, and at first it was the mobility of the probe, not the polymer itself, that could be characterized. Any fluorescence based

technique, however, can be adapted for use with polymers by covalently attaching the fluorescent label. One of the first techniques was fluorescence correlation spectroscopy (FCS), developed by Madge, Elson and Webb in 1972 to study binding of ethidium bromide to DNA.⁶⁶ The basic principle of FCS is the use of a fluorophore at a sufficiently dilute concentration such that only a small number (1-100) are in the viewing volume at any given time. Raw data from this experiment is the fluorescence intensity plotted against time, which is fit to an autocorrelation function that can be used to extract meaningful physical information, such as diffusion coefficients or relaxation times. A variety of studies have been performed using FCS on polymer systems.⁶⁷⁻⁷² However, as Van Keuren and Schrof pointed out, FCS is only suitable for materials with diffusion coefficients larger than 10^{-8} cm²/sec,⁷³ so other techniques are necessary for study of systems with smaller diffusion coefficients.

Fluorescence non-radiative energy transfer (FRET or NRET) was pioneered in doped and labeled polymers by Deppe, Dhinojwala, and Torkelson in 1996^{61,62} based on a technique first mathematically described by Tirrell.⁷⁴ This technique uses a donor/acceptor pair in which fluorescence intensity decreases when they come into close proximity, the rate of which can be correlated to diffusion. A significant advantage to this technique is that it has the sensitivity to measure very small diffusion coefficients, measurements on the order of 10^{-16} cm²/sec have been reported.⁷⁵ A drawback to FRET is the necessity of fabricating two layers, one with the donor and one with the acceptor. This is the same difficulty presented by both isotopic techniques discussed previous section.

Another technique called forced Rayleigh scattering (FRS) was developed in 1973 at IBM for the study of thermodynamic fluctuations in solids.⁷⁶ In this technique a diffraction pattern is written into a sample containing a light sensitive molecule, which is

often a fluorescent dye, by utilizing two coherent lasers to create a holographic grating. To 'read' the pattern a probe beam is directed at the sample at the first order Bragg angle and the intensity of the diffracted light decreases as a function of time. This rate of decrease can be correlated to the diffusion coefficient of the probe molecules.⁷⁷ This technique is very sensitive and has been used to measure the diffusion of probe molecules in a polymer matrix below the glass transition temperature (T_g) of the polymer.⁷⁸ A few studies of self-diffusion parallel to self-assembled block copolymer interfaces have been performed by FRS for both lamellar⁷⁹ and cylinder forming⁸⁰ block copolymers. An interesting result from the lamellar block copolymer study was a clear anisotropy of diffusion where polymers moved parallel to phase boundaries much faster than perpendicular to phase boundaries.

Fluorescence recovery after patterned photobleaching (FRAPP) is the technique used for the studies in later chapters. FRAPP was originally developed by Axelrod in 1976 for the study of two-dimensional lateral mobility in regions of a cell.⁸¹ This technique is widely used in quantitative biology to measure protein mobility, to determine the percentage of protein that is mobile (as opposed to bound),⁸² to characterize microtubule binding (see Figure 1.4),⁸³ and to measure transport within membranes.⁸⁴ Details of this experiment, including theory and mathematics, will be described in Chapter 2. Briefly, a fluorophore is incorporated into the system of interest and irreversibly chemically changed by high intensity light (photobleached) to a permanently non-fluorescent state. Then, the recovery of intensity into the photobleached region is monitored as a function of time with lower intensity light. The rate of recovery can be directly related to the diffusion coefficient of either the doped fluorophore or the species the fluorophore is covalently attached to.

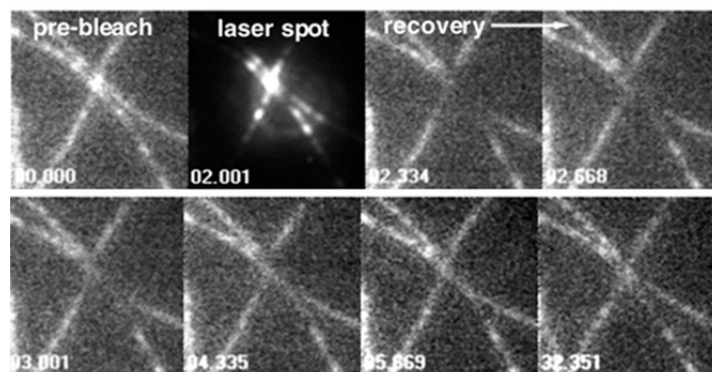


Figure 1.4: Photobleaching and recovery of a fluorescently labeled protein in untreated cells. Time-lapse micrographs of the bleached area before (pre-bleach), at the time of bleaching (laser spot), and at intervals during the recovery. Elapsed time, in seconds, is shown in each micrograph. Reproduced with permission from ref. ⁸³

A significant advantage to FRAPP is that its sensitivity is equal to that of FRET and the film begins with a uniform composition, thereby avoiding fabrication challenges inherent to FRET or SIMS. The first application of this technique to polymers was in 1982 by Smith who demonstrated this technique using fluorophore-doped thick films by photobleaching through a mask with chrome lines.⁸⁵ Several other studies have been performed using FRAPP to examine polymer systems, the results of which will be discussed later.^{48-50,86,87} A comparison study between FRS and FRAPP for covalently labeled polymers in solution concluded that the results from each were similar.⁸⁸ The most significant drawback of FRS is that the photobleached product of the fluorophore can create anomalous diffraction intensity, but this does not occur in FRAPP because the photobleached molecule does not fluoresce.

1.5 NANOCONFINED T_g

The T_g of a polymer is “the single most important characteristic in choosing a polymer for a given application”⁸⁹ and has significant implications for nanoconfined

diffusion. This is the temperature at which molecular motion becomes so slow that the polymer does not flow over relevant timescales, but the system is not in equilibrium. A review by Forrest and Dalnoki-Veress in 2001 discussed the history of T_g studies in supported polymer films.⁹⁰ The somewhat surprising result of this review was the extensive agreement on the thickness dependence of T_g for substrate supported polystyrene films throughout the literature about the effect of nano-confinement on the T_g . This agreement has been seen using a variety of different techniques to measure T_g including ellipsometry, positron annihilation, two dielectric spectroscopy studies, Brillouin light scattering, and two X-ray reflectivity studies on polystyrene supported thin films (Figure 1.5).

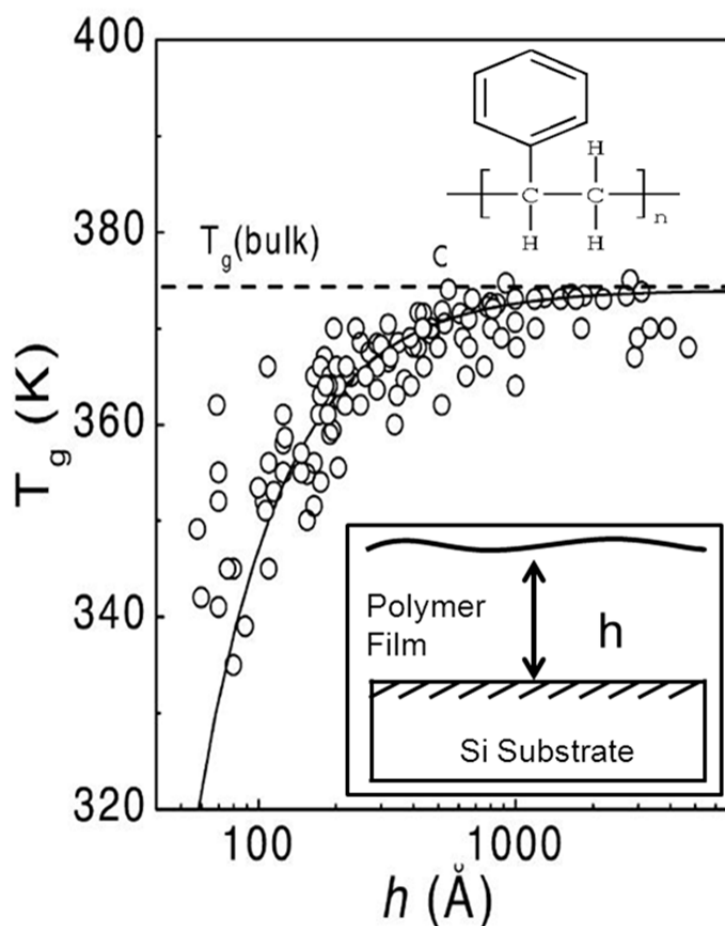


Figure 1.5: T_g of polystyrene in supported thin films measured by a variety of technique showing wide agreement amongst researchers. Reprinted with permission from ref.⁹⁰

De Gennes suggested that it might be more appropriate to characterize a distribution of T_g s in a thin film rather than a single T_g .⁹¹ Consequently, a later study characterizing the role of individual interfaces (polymer/air or polymer/substrate) on T_g showed the polymer/air interface to have the more significant effect in the overall T_g of polystyrene thin films. The study also found changes in T_g due to the free surface permeated several tens of nanometers into the film.⁹² However, for polymers that strongly

interact with the substrate, such as poly(2-vinylpyridine), the polymer/substrate interaction is predominant and the T_g increases with decreased film thickness.⁹³

It is important to consider the effect of nanoconfinement on the T_g of the polymer when studying nanoconfined diffusion. The reason is that bulk diffusion, according to the Rouse model, is dependent on the proximity of the diffusion temperature to T_g . If the T_g of the nanoconfined polymer film is different from its bulk value, nanoconfined diffusion processes could be influenced both by the effect of nanoconfinement on T_g and other factors resulting from nanoconfinement. In fact, one commentary⁹⁴ on a previous study⁴⁸ pointed out that the change in thin film diffusion coefficient might be attributed to T_g changes of 7 °C.

Several techniques have been used in the past to study the T_g of polymer thin films, such as fluorescence^{92,95,96} and dielectric spectroscopy.^{97,98} However, here the focus is going to be on the one by which nanoconfinement effects on T_g were discovered, ellipsometry.^{99,100} Since this is the technique used in studies presented in subsequent chapters, the experimental details will be provided in depth later. Briefly, ellipsometry measures the change in the ellipticity and orientation of reflected polarized light and these results are compared to a model to calculate the thickness of a film. Since the thermal expansion coefficients of the glassy and rubbery states of the same polymer are distinct, the T_g can be identified as the inflection point of a plot of thickness against temperature.

Ellipsometry is a powerful technique because it is sensitive and fairly quick. Additionally, unlike other techniques for measuring diffusion or T_g , the polymer film does not need to have any special characteristics or be modified in any way, such as the inclusion of a fluorophore. It can simply be spin-coated onto a reflective surface such as a silicon wafer. This makes it an ideal technique for a wide range of polymers. Many

studies have been performed using this technique to characterize the effect of tacticity, chain conformation, film thickness, heating rate,¹⁰¹ adsorbed water,¹⁰² molecular weight,¹⁰³ and various substrates¹⁰⁴ on thin film T_g .

1.6 SUMMARY AND OBJECTIVE

For about the past two decades studies on thin films have shown that a wide range of the properties depend on the film thickness due to interfacial interactions becoming more important at these length scales. Even though polymer thin films can be found in many products encountered every day, there are still significant open questions about the diffusion at interfaces in these systems.¹⁰⁵ While several different techniques have been developed for the study of diffusion in thin films, many have shortcomings, such as a lower bound on diffusion coefficients in the case of FCS, that have limited experimental work to date. The goal of the next few chapters is to try to address some of the weaknesses in existing techniques through the refinement of FRAPP and to look at some specific cases of single and multi-layer polymer films. It will also be important to examine how diffusion relates to nanoconfinement effects on the T_g of these polymer systems since the Rouse model predicts that diffusion depends on the proximity of the diffusion temperature to T_g .

1.7 REFERENCES

1. American Chemical Society National Historic Chemical Landmarks. Bakelite: The World's First Synthetic Plastic. <http://portal.acs.org/portal/PublicWebSite/education/whatischemistry/landmarks/bakelite/index.htm> (Accessed February 11, 2013).
2. History - DuPont Heritage Timeline: Nylon. http://www2.dupont.com/Phoenix_Heritage/en_US/1939_c_detail.html (Accessed February 11, 2013).
3. How Stuff Works: How Nonstick Cookware Works. <http://home.howstuffworks.com/nonstick-cookware.htm> (Accessed February 8, 2013).
4. Gaston Narada: What is a Lithium Battery? <http://www.gaston-lithium.com/> (Accessed February 8, 2013).
5. Vendra, V. K.; Wu, L.; Krishnan, S. *Nanomaterials for the Life Sciences Vol.5: Nanostructured Thin Films and Surfaces.*; WILEY-VCH Verlag GmbH & Co. KGaA: Weinheim, 2010.
6. Rubinstein, M.; Colby, R. H. *Polymer Physics*; Oxford University Press: Oxford, 2003.
7. Einstein, A. *Ann. Phys. (Weinheim, Ger.)* **1906**, *19*, 371-381.
8. Einstein, A. *Ann. Phys. (Weinheim, Ger.)* **1905**, *17*, 549-560.
9. Stokes, G. G. *Trans. Cambridge. Phil. Soci.* **1851**, *9*, 8-106.
10. Rouse, P. E., Jr. *Journal of Chemical Physics* **1953**, *21*, 1272-80.
11. Doi, M.; Edwards, S. F. *The Theory of Polymer Dynamics*; Clarendon Press: Oxford, 1986.
12. de Gennes, P. G. *Journal of Chemical Physics* **1971**, *55*, 572-579.
13. Jones, R. A. L.; Richards, R. W. *Polymers at Surfaces and Interfaces*; Cambridge University Press: Cambridge, 1999.
14. Lodge, T. P. *Physical Review Letters* **1999**, *83*, 3218-3221.

15. Bytner, O.; Smith, G. D. *J. Polym. Sci. Pt. B-Polym. Phys.* **2001**, *39*, 3067-3071.
16. Fleischer, G.; Appel, M. *Macromolecules* **1995**, *28*, 7281-7283.
17. Pearson, D. S.; Fetters, L. J.; Graessley, W. W.; Strate, G. V.; Vonmeerwall, E. *Macromolecules* **1994**, *27*, 711-719.
18. Bartels, C. R.; Crist, B.; Graessley, W. W. *Macromolecules* **1984**, *17*, 2702-2708.
19. Tao, H.; Lodge, T. P.; von Meerwall, E. D. *Macromolecules* **2000**, *33*, 1747-1758.
20. von Meerwall, E. D. *Advances in Polymer Science* **1984**, *54*, 1-29.
21. Appel, M.; Fleischer, G. *Macromolecules* **1993**, *26*, 5520-5525.
22. Kubo, T.; Nose, T. *Polym. J.* **1992**, *24*, 1351-1361.
23. Richter, D.; Willner, L.; Zirkel, A.; Farago, B.; Fetters, L. J.; Huang, J. S. *Macromolecules* **1994**, *27*, 7437-7446.
24. Drzewinski, A.; van Leeuwen, J. M. J. *Phys. Rev. E* **2008**, *77*, 8.
25. Sun, Q.; Faller, R. *Macromolecules* **2006**, *39*, 812-820.
26. Huang, Y.; Paul, D. R. *Macromolecules* **2006**, *39*, 1554-1559.
27. Pfromm, P. H.; Koros, W. J. *Polymer* **1995**, *36*, 2379-2387.
28. Priestley, R. D.; Ellison, C. J.; Broadbelt, L. J.; Torkelson, J. M. *Science* **2005**, *309*, 456-459.
29. Kawana, S.; Jones, R. A. L. *Eur. Phys. J. E* **2003**, *10*, 223-230.
30. Khare, R.; dePablo, J. J.; Yethiraj, A. *Macromolecules* **1996**, *29*, 7910-7918.
31. Luengo, G.; Schmitt, F. J.; Hill, R.; Israelachvili, J. *Macromolecules* **1997**, *30*, 2482-2494.
32. Yang, Z.; Fujii, Y.; Lee, F. K.; Lam, C.-H.; Tsui, O. K. C. *Science* **2010**, *328*, 1676-1679.
33. Stafford, C. M.; Vogt, B. D.; Harrison, C.; Julthongpiput, D.; Huang, R. *Macromolecules* **2006**, *39*, 5095-5099.

34. Torres, J. M.; Stafford, C. M.; Vogt, B. D. *Polymer* **2010**, *51*, 4211-4217.
35. Torres, J. M.; Stafford, C. M.; Vogt, B. D. *ACS Nano* **2009**, *3*, 2677-2685.
36. Zhang Newby, B.-m.; Wakabayashi, K.; Composto, R. J. *Polymer* **2001**, *42*, 9155-9162.
37. O'Connell, P. A.; McKenna, G. B. *Science* **2005**, *307*, 1760-1763.
38. Huang, R.; Stafford, C. M.; Vogt, B. D. *J. Aerosp. Eng.* **2007**, *20*, 38-44.
39. Wang, X. P.; Xiao, X.; Tsui, O. K. C. *Macromolecules* **2001**, *34*, 4180-4185.
40. Paeng, K.; Ediger, M. D. *Macromolecules* **2011**, *44*, 7034-7042.
41. Paeng, K.; Swallen, S. F.; Ediger, M. D. *J. Am. Chem. Soc.* **2011**, *133*, 8444-8447.
42. Russell, T. P. *Annu. Rev. Mater. Sci.* **1991**, *21*, 249-268.
43. Green, P. F.; Palmstrom, C. J.; Mayer, J. W.; Kramer, E. J. *Macromolecules* **1985**, *18*, 501-507.
44. Vaia, R. A.; Giannelis, E. P. *MRS Bull.* **2001**, *26*, 394-401.
45. Gopakumar, T. G.; Lee, J. A.; Kontopoulou, M.; Parent, J. S. *Polymer* **2002**, *43*, 5483-5491.
46. Ji, S. X.; Liu, C. C.; Liu, G. L.; Nealey, P. F. *ACS Nano* **2010**, *4*, 599-609.
47. Binder, K.; Milchev, A.; Baschnagel, J. *Annu. Rev. Mater. Sci.* **1996**, *26*, 107-134.
48. Frank, B.; Gast, A. P.; Russell, T. P.; Brown, H. R.; Hawker, C. *Macromolecules* **1996**, *29*, 6531-6534.
49. Bae, S. C.; Wong, J. S.; Kim, M.; Jiang, S.; Hong, L.; Granick, S. *Philos. Trans. R. Soc. A-Math. Phys. Eng. Sci.* **2008**, *366*, 1443-1454.
50. Wong, J. S. S.; Hong, L.; Bae, S. C.; Granick, S. *Journal of Polymer Science Part B: Polymer Physics* **2010**, *48*, 2582-2588.
51. Sukhishvili, S. A.; Chen, Y.; Muller, J. D.; Gratton, E.; Schweizer, K. S.; Granick, S. *Macromolecules* **2002**, *35*, 1776-1784.

52. Manias, E.; Chen, H.; Krishnamoorti, R.; Genzer, J.; Kramer, E. J.; Giannelis, E. *P. Macromolecules* **2000**, *33*, 7955-7966.
53. Composto, R. J.; Mayer, J. W.; Kramer, E. J.; White, D. M. *Phys. Rev. Lett.* **1986**, *57*, 1312-1315.
54. Green, P. F.; Doyle, B. L. *Macromolecules* **1987**, *20*, 2471-2474.
55. Green, P. F.; Kramer, E. J. *Macromolecules* **1986**, *19*, 1108-1114.
56. Mills, P. J.; Green, P. F.; Palmstrom, C. J.; Mayer, J. W.; Kramer, E. J. *Applied Physics Letters* **1984**, *45*, 957-959.
57. Pu, Y.; Rafailovich, M. H.; Sokolov, J.; Gersappe, D.; Peterson, T.; Wu, W. L.; Schwarz, S. A. *Phys. Rev. Lett.* **2001**, *87*, 4.
58. van Alsten, J. G.; Sauer, B. B.; Walsh, D. J. *Macromolecules* **1992**, *25*, 4046-4048.
59. Yokoyama, H.; Kramer, E. J.; Rafailovich, M. H.; Sokolov, J.; Schwarz, S. A. *Macromolecules* **1998**, *31*, 8826-8830.
60. Zheng, X.; Sauer, B. B.; Vanalsten, J. G.; Schwarz, S. A.; Rafailovich, M. H.; Sokolov, J.; Rubinstein, M. *Phys. Rev. Lett.* **1995**, *74*, 407-410.
61. Deppe, D. D.; Dhinojwala, A.; Torkelson, J. M. *Macromolecules* **1996**, *29*, 3898-3908.
62. Dhinojwala, A.; Torkelson, J. M. *Macromolecules* **1994**, *27*, 4817-4824.
63. Kumar, S. K.; Vacatello, M.; Yoon, D. Y. *Journal of Chemical Physics* **1988**, *89*, 5206-5215.
64. Madden, W. G. *Journal of Chemical Physics* **1988**, *88*, 3934-3943.
65. Zheng, X.; Rafailovich, M. H.; Sokolov, J.; Strzhemechny, Y.; Schwarz, S. A.; Sauer, B. B.; Rubinstein, M. *Phys. Rev. Lett.* **1997**, *79*, 241-244.
66. Magde, D.; Webb, W. W.; Elson, E. *Physical Review Letters* **1972**, *29*, 705-&.
67. Casoli, A.; Schonhoff, M. *Biol. Chem.* **2001**, *382*, 363-369.

68. Cherdhirankorn, T.; Floudas, G.; Butt, H. J.; Koynov, K. *Macromolecules* **2009**, *42*, 9183-9189.
69. Cherdhirankorn, T.; Harmandaris, V.; Juhari, A.; Voudouris, P.; Fytas, G.; Kremer, K.; Koynov, K. *Macromolecules* **2009**, *42*, 4858-4866.
70. Masuda, A.; Ushida, K.; Okamoto, T. *J. Photochem. Photobiol. A-Chem.* **2006**, *183*, 304-308.
71. Zettl, H.; Hafner, W.; Boker, A.; Schmalz, H.; Lanzendorfer, M.; Muller, A. H. E.; Krausch, G. *Macromolecules* **2004**, *37*, 1917-1920.
72. Zhao, J.; Granick, S. *Macromolecules* **2007**, *40*, 1243-1247.
73. Van Keuren, E.; Schrof, W. *Macromolecules* **2003**, *36*, 5002-5007.
74. Tirrell, M.; Adolf, D.; Prager, S. *Lecture Notes in Mathematics* **1984**, *1063*, 37-45.
75. Hall, D. B.; Torkelson, J. M. *Macromolecules* **1998**, *31*, 8817-8825.
76. Pohl, D. W.; Schwarz, S. E.; Irniger, V. *Physical Review Letters* **1973**, *31*, 32-35.
77. Wang, C. H.; Xia, J. L. *Journal of Chemical Physics* **1990**, *92*, 2603-2613.
78. Tonge, M. P.; Stubbs, J. M.; Sundberg, D. C.; Gilbert, R. G. *Polymer* **2000**, *41*, 3659-3670.
79. Hamersky, M. W.; Tirrell, M.; Lodge, T. P. *Langmuir* **1998**, *14*, 6974-6979.
80. Cavicchi, K. A.; Lodge, T. P. *Macromolecules* **2004**, *37*, 6004-6012.
81. Axelrod, D.; Koppel, D. E.; Schlessinger, J.; Elson, E.; Webb, W. W. *Biophys. J.* **1976**, *16*, 1055-1069.
82. Zhang, F.; Schmidt, W. G.; Hou, Y.; Williams, A. F.; Jacobson, K. *Proc. Natl. Acad. Sci. U. S. A.* **1992**, *89*, 5231-5235.
83. Bulinski, J. C.; Odde, D. J.; Howell, B. J.; Salmon, T. D.; Waterman-Storer, C. M. *J. Cell Sci.* **2001**, *114*, 3885-3897.
84. Johnson, M. E.; Berk, D. A.; Blankshtein, D.; Golan, D. E.; Jain, R. K.; Langer, R. S. *Biophys. J.* **1996**, *71*, 2656-2668.

85. Smith, B. A. *Macromolecules* **1982**, *15*, 469-472.
86. Cicerone, M. T.; Blackburn, F. R.; Ediger, M. D. *Macromolecules* **1995**, *28*, 8224-8232.
87. Pinte, J.; Joly, C.; Ple, K.; Dole, P.; Feigenbaum, A. *J. Agric. Food Chem.* **2008**, *56*, 10003-10011.
88. Inoue, T.; Nemoto, N.; Kojima, T.; Kurata, M. *Polym. J.* **1988**, *20*, 869-874.
89. Hiemenz, P.; Lodge, T. P. *Polymer Chemistry*; 2nd ed.; CRC Press: Boca Raton, FL, 2007.
90. Forrest, J. A.; Dalnoki-Veress, K. *Advances in Colloid and Interface Science* **2001**, *94*, 167-195.
91. de Gennes, P. G. *Eur. Phys. J. E* **2000**, *2*, 201-203.
92. Ellison, C. J.; Torkelson, J. M. *Nat. Mater.* **2003**, *2*, 695-700.
93. Roth, C. B.; McNerny, K. L.; Jager, W. F.; Torkelson, J. M. *Macromolecules* **2007**, *40*, 2568-2574.
94. Russell, T. P.; Kumar, S. K. *Nature* **1997**, *386*, 771-772.
95. Ellison, C. J.; Kim, S. D.; Hall, D. B.; Torkelson, J. M. *Eur. Phys. J. E* **2002**, *8*, 155-166.
96. Priestley, R. D.; Mundra, M. K.; Barnett, N. J.; Broadbelt, L. J.; Torkelson, J. M. *Aust. J. Chem.* **2007**, *60*, 765-771.
97. Fukao, K.; Uno, S.; Miyamoto, Y.; Hoshino, A.; Miyaji, H. *Phys. Rev. E* **2001**, *64*, 11.
98. Hartmann, L.; Gorbatschow, W.; Hauwede, J.; Kremer, F. *Eur. Phys. J. E* **2002**, *8*, 145-154.
99. Beaucage, G.; Composto, R.; Stein, R. S. *J. Polym. Sci., Part B: Polym. Phys.* **1993**, *31*, 319-26.
100. Keddie, J. L.; Jones, R. A. L.; Cory, R. A. *Faraday Discuss.* **1994**, *98*, 219-230.

101. Grohens, Y.; Hamon, L.; Reiter, G.; Soldera, A.; Holl, Y. *Eur. Phys. J. E* **2002**, *8*, 217-224.
102. Kim, S.; Mundra, M. K.; Roth, C. B.; Torkelson, J. M. *Macromolecules*, *43*, 5158-5161.
103. Dalnoki-Veress, K.; Forrest, J. A.; Murray, C.; Gigault, C.; Dutcher, J. R. *Phys Rev E Stat Nonlin Soft Matter Phys* **2001**, *63*, 031801.
104. Roth, C. B.; Dutcher, J. R. *Eur. Phys. J. E* **2003**, *12*, S103-S107.
105. Granick, S.; Bae, S. C. *Journal of Polymer Science Part B: Polymer Physics* **2006**, *44*, 3434-3435.

Chapter 2: Diffusion in Poly(isobutyl methacrylate) (PiBMA) Thin Films Parallel to Interfaces[†]

2.1 INTRODUCTION

The previous chapter contained a detailed discussion of the background of nanoconfined diffusion in polymer thin films. This chapter describes the characterization of the self-diffusion of nanoconfined poly(isobutyl methacrylate) (PiBMA) parallel to a planar silicon oxide substrate. PiBMA was specifically chosen for this study because we determined that the glass transition temperature (T_g) of this material is independent of film thickness on these substrates by spectroscopic ellipsometry. Conventionally, the bulk self-diffusion coefficient of any polymer is directly related to the proximity of the diffusion temperature to T_g .¹ By selecting a polymer with a film thickness independent T_g , such as PiBMA, any measured trend in the self-diffusion coefficient can be considered independently from changes in the self-diffusion coefficient due to T_g nanoconfinement effects. Additionally, the FRAPP procedure used here employs a periodic photobleached array of lines through which diffusion can be directly observed using a CCD camera mounted on an epifluorescence microscope. The combination of fluorescence imaging and photobleaching over a periodic array improves the FRAPP method such that it is self-referencing (e.g., diffusion measurements are not sensitive to unintended photobleaching during recovery) and enables additional statistical analysis of experimental data.

[†] This chapter reproduced in part with permission from “Nanoconfined Self-Diffusion of Poly(isobutyl methacrylate) in Films with a Thickness Independent Glass Transition” Katzenstein, J. M.; Janes, D. W.; Hocker, H. E.; Chandler, J. K.; Ellison, C. J. *Macromolecules* **2011**, *45*, 1544-1552. Copyright 2011 American Chemical Society.

2.2 T_g IN PiBMA FILMS

The T_g of thin polymer films can be measured by ellipsometry because the coefficient of thermal expansion (CTE) is different between the glassy and rubbery states of the polymer. Since the CTE for each polymer state is constant, the data well above and below the T_g in a plot of film thickness against temperature can be fit with straight lines by linear regression. The intersection of these lines corresponds to the T_g of the film. Figure 2.1 shows a representative ellipsometric scan for a film of PiBMA with a thickness of 50 nm at 25 °C.

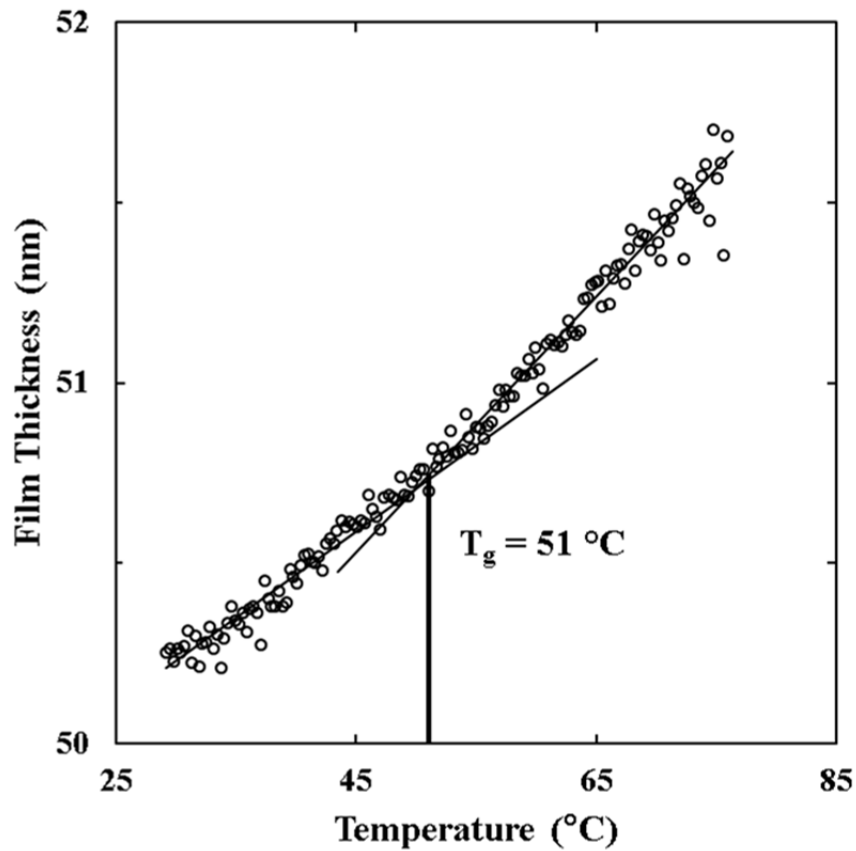


Figure 2.1: Representative ellipsometric scan for a 50 nm thick film of PiBMA. Every sixth data point collected is shown here for clarity. The linear regressions above and below the T_g uses a span of data more than 15 °C wide.

The T_g of PiBMA and fluorescently labeled PiBMA-NBD (PiBMA-7-nitro-2,1,3-benzoxadiazole), was measured for films ranging from 15 to 160 nm and from 18 to 125 nm, respectively, as shown in Figure 2.2. PiBMA-NBD was synthesized, as explained in the experimental section of this chapter, with the fluorophore as part of the polymerization initiator molecule and therefore is covalently bound to the polymer backbone. T_g measurements were performed by ellipsometry on silicon wafers with a native oxide layer as a substrate. However, the T_g results are expected to be similar on a quartz substrate, like those used for FRAPP experiments, due to a similar surface hydroxyl density ($\sim 5\text{--}7$ hydroxyls/nm²).^{2,3} In every case, the T_g measured for the thin film was identical to the bulk T_g as measured by DSC (51 °C) within the experimental error, ± 1 °C.⁴ The film thickness independence of T_g for PiBMA corresponds with what has previously been reported in the literature for a different molecular weight of PiBMA.⁵ Since identical T_g values are found, within error, for both labeled and unlabeled PiBMA, this is indicative that the attached fluorophore, which will be used to track diffusion, does not have significant interaction with the silicon oxide substrate. If there were a strong interaction between the NBD fluorophore and the hydroxyl groups on the silicon oxide surface, labeled polymers might be expected to show a film thickness dependent T_g due to changes in mobility at the polymer/substrate interface.

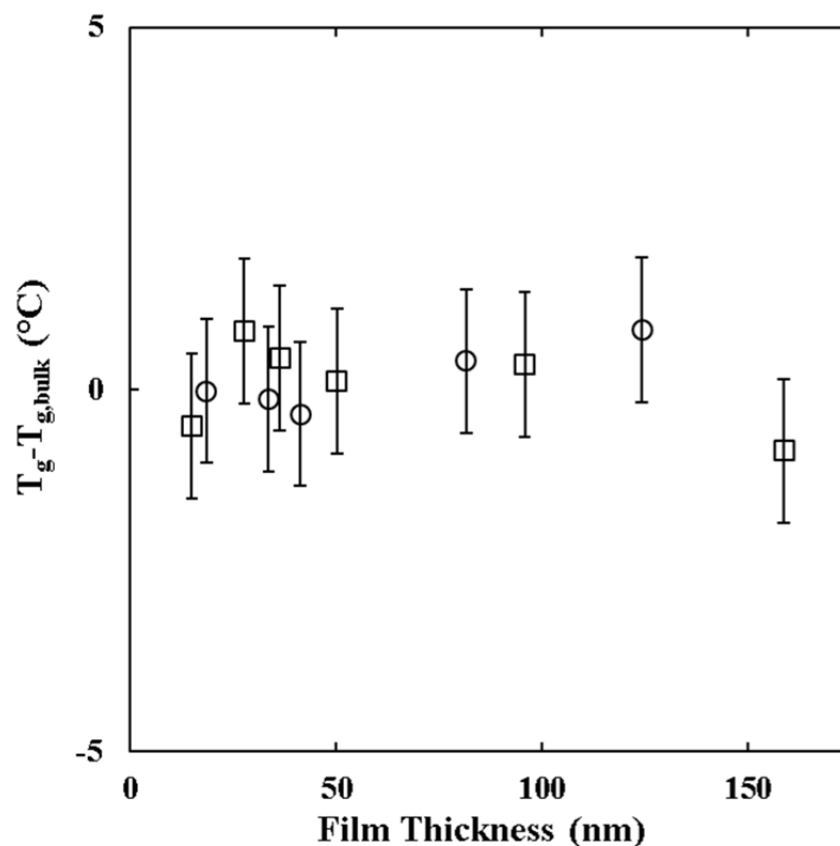


Figure 2.2: T_g data for PiBMA (□) and PiBMA-NBD (○) as a function of film thickness taken at 25 °C. The error bars indicate the error in ellipsometric measurements of T_g (± 1 °C).⁴ The bulk T_g for these materials is 51 °C, as measured by DSC and ellipsometry.

2.3 SELF-QUENCHING EFFECTS

An additional consideration necessary whenever fluorophores are used as probes for studying polymer physics is fluorescence self-quenching effects. Self-quenching is due to short range interactions between two fluorophores and can lead to the observation of reduced fluorescence intensity. This could, in turn, adversely affect the results of the diffusion measurement dramatically. In the case of spatially varying photobleaching experiments, such as those described in this chapter, it can appear as if molecules are diffusing opposite to their expected behavior. This is because as the fluorophores

disperse, the local concentration decreases, decreasing self-quenching effects and increasing the local fluorescence intensity.

While this phenomenon is well reported in fluorescence and biological sciences literature,⁶⁻⁹ it is not commonly discussed in the polymer physics field. One potential reason for this oversight is that the majority of studies of polymer physics using fluorophore based techniques use photon counting devices¹⁰⁻¹² which report the absolute intensity from a region of interest and cannot take into account spatial variations. However, it is important to keep the fluorophore loading below the self-quenching threshold in order to accurately characterize diffusion. This is counter to the inclination seen in many studies to simply increase the fluorophore loading in thinner films to increase the signal-to-noise ratio.

The self-quenching threshold is unique for each fluorophore/polymer system and can be characterized by systematically varying the total fluorophore loading in a polymer film by blending fluorescently labeled polymer with unlabeled polymer before spin coating. In the case of the PiBMA/NBD system used in this study, the 100% fluorescently labeled polymer was 21.7 kg/mol containing 1.8 wt% NBD covalently attached and the unlabeled polymer was 24.4 kg/mol. Solutions were spin cast into films and the fluorescence intensity was measured and normalized by both the film thickness and the amount of fluorophore in the film to give what can be considered an ‘intensity per fluorophore’. Figure 2.3 shows that below a fluorophore loading of 0.18 wt% the fluorescence intensity per fluorophore is unchanged with fluorophore content, but above this threshold the intensity per fluorophore decreases rapidly, indicative of self-quenching. Therefore, for all experiments in this chapter the total fluorophore loading is ≤ 0.18 wt%.

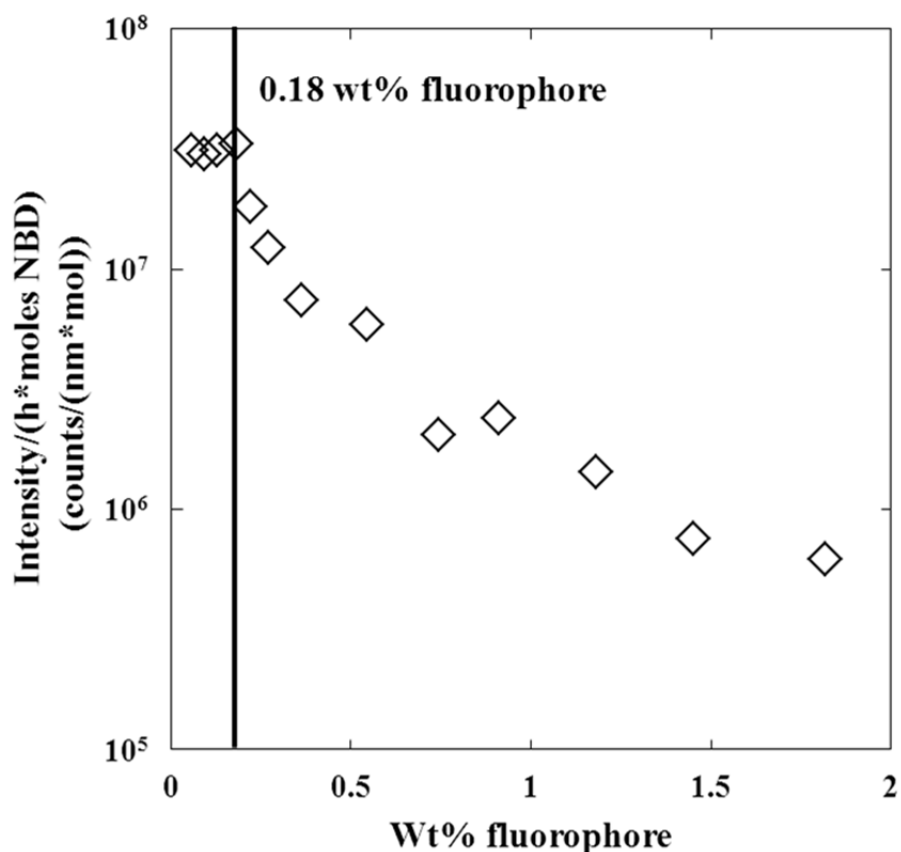


Figure 2.3: Fluorescence intensity per fluorophore at $\lambda_{\text{ex}} = 461 \text{ nm}$ and $\lambda_{\text{em}} = 520 \text{ nm}$ plotted against the amount of fluorophore in PiBMA-NBD films. The vertical line indicates the maximum amount of fluorophore that can be loaded into a PiBMA thin film without observing self-quenching effects. The amount of fluorophore was controlled by blending NBD labeled PiBMA with unlabeled PiBMA.

2.4 FLUORESCENCE RECOVERY AFTER PATTERNED PHOTBLEACHING (FRAPP)

FRAPP was originally developed by Axelrod in 1976 for the study of two-dimensional lateral mobility in regions of a cell¹³ and provides a useful platform for study of diffusion parallel to interfaces in polymer thin films. Details of this experiment, including theory and mathematics, will be presented later in this chapter. A cartoon of a generic FRAPP experiment is shown in Figure 2.4. Briefly, a fluorophore is incorporated into the system of interest and irreversibly chemically changed by high intensity light

(photobleached), then the recovery of intensity into the photobleached region is monitored as a function of time with lower intensity light. This recovery can be directly related to the diffusion coefficient of the fluorophore in the case of doped dyes, or the polymer chain in the case of covalently labeled polymers.

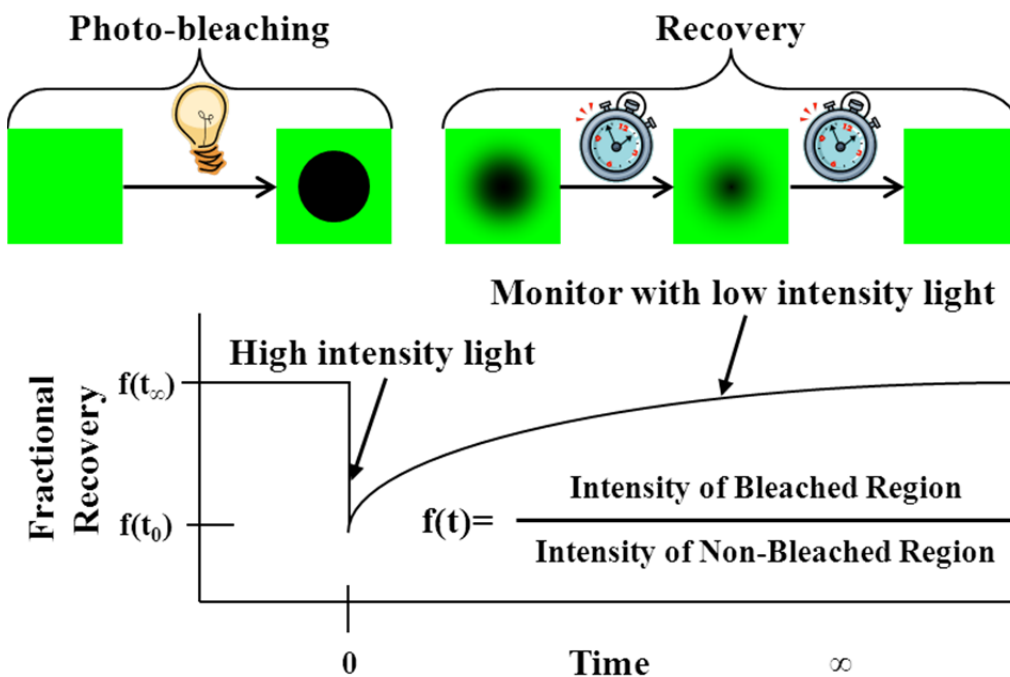


Figure 2.4: Cartoon of a generic FRAPP experiment.

FRAPP was chosen as the method for measuring diffusion coefficients parallel to interfaces in polymers for several reasons. One key consideration is that it is a very sensitive method, with reported diffusion coefficients as low as $10^{-15.5} \text{ cm}^2/\text{sec}$,¹⁴ which should be sufficient for any system of interest in this study. This is not a theoretical limit to this technique but a practical one over which diffusion can be observed within reasonable laboratory timeframes. Another advantage of this technique is that the photobleaching step of FRAPP experiments bypasses the fabrication challenges which

limit the use of isotopic approaches for study of diffusion parallel to interfaces. FRAPP has been previously applied to synthetic polymers to investigate both nanoconfined polymer diffusion parallel to interfaces^{10,12} and bulk diffusion of small molecule probes in a polymer matrix.¹⁵⁻¹⁷

2.5 SINGLE-SPOT DIFFUSION

The first FRAPP diffusion experiments carried out as part of this thesis were performed by photobleaching a single region of the film with a laser in a confocal microscope (see Experimental section for details). These measurements were used to validate FRAPP by measuring the diffusion coefficient in PiBMA and poly(methyl methacrylate) (PMMA) thick films and comparing these values to those found in the literature or calculated from theory.

Diffusion in polymer thin films is governed by the one-dimensional transient diffusion equation (eq. 2.1) in which C is the concentration (for which fluorescence intensity is an analog in this case), t is time, x is position, and D is the diffusion coefficient.

$$\frac{\partial C}{\partial t} = D \frac{\partial^2 C}{\partial x^2} \quad (2.1)$$

Eq. 2.2 is the solution to eq. 2.1 integrated to represent the total amount of species that has diffused into the bleached region up to time t . Eq. 2.2 was used to calculate the diffusion coefficient by least squares fitting using fractional recovery data as defined in Figure 2.4.¹⁸

$$\frac{M_t}{M_\infty} = \frac{f(t)-f(0)}{f(\infty)-f(0)} = 1 - \frac{8}{\pi^2} \sum_{n=0}^{\infty} \frac{1}{(2n+1)^2} \exp\left(\frac{-D(2n+1)^2\pi^2 t^2}{l^2}\right) \quad (2.2)$$

In eq. 2.2 M_t is the amount of fluorophore recovered at time t while M_∞ is the infinite time (complete) recovery. This can be calculated as the difference between the fluorescent intensity at time t , $f(t)$, and the initial fluorescence intensity, $f(0)$, divided by

the difference between the infinite time fluorescence intensity, $f(\infty)$, and the initial fluorescence intensity. In eq. 2.2 D (the diffusion coefficient) is the only fitting parameter as l is the length over which diffusion is measured which can be measured directly. A demonstration of the fluorescence micrographs collected during this study and the model fitting used to calculate the diffusion coefficient is shown in Figure 2.5. The solution assumes fixed boundary conditions, which are achieved by measuring intensity over a sufficiently long area such that there is no depletion of intensity at the boundaries of the region of interest, the white rectangle in Figure 2.5a. The convenience of this equation comes from using fractional recovery, which incorporates an internal reference (the exterior intensity) in every image taken to correct for potential photobleaching during imaging.

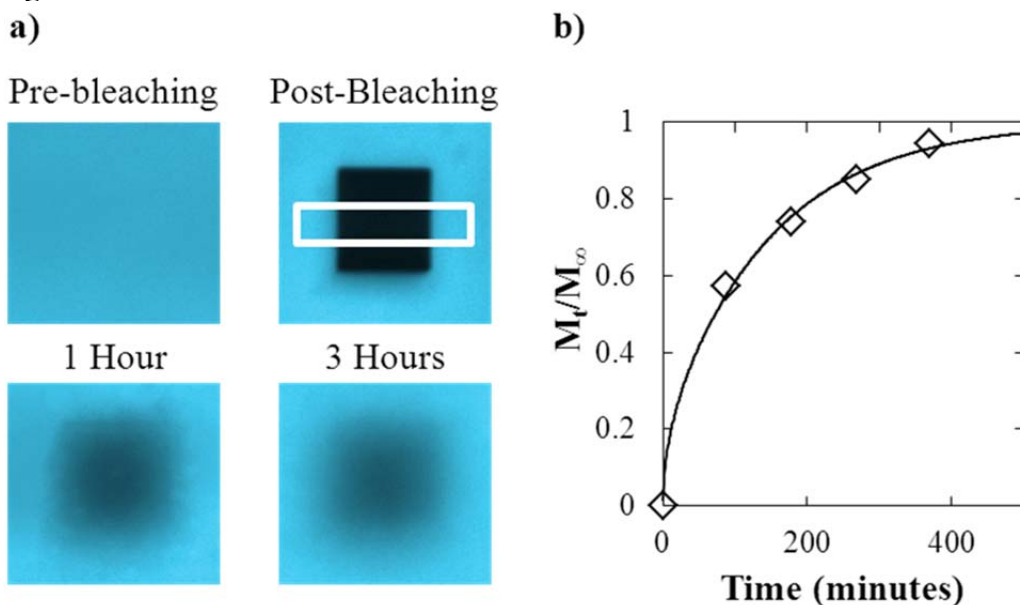


Figure 2.5: a) Fluorescence micrographs from a typical single-spot FRAPP experiment in a 150 nm thick film of PiBMA-NBD at 140 °C. The white rectangle indicates the region over which diffusion was measured and the photobleached spot is 30 μm x 33 μm . b) Plot of recovery M_t/M_∞ against time for the experiment. Solid line is fit to eq. 2.2 where D is the only fitted parameter.

Since the molecular weights of the polymers used in these initial studies are well below the critical molecular weight for entanglement for their respective polymers, PiBMA, ~28 kg/mol, and PMMA, ~20 kg/mol,¹⁹ bulk diffusion is expected to follow the Rouse model for unentangled polymer diffusion, eq. 2.3.^{20,21}

$$D = \frac{\rho RT \langle R^2 \rangle}{36M\eta_0} \quad (2.3)$$

In eq 2.3, ρ is the mass density, R is the ideal gas constant, T is the absolute temperature of the experiment, $\langle R^2 \rangle$ is the unperturbed mean-square end-to-end distance, M is the molecular weight, and η_0 is the zero shear viscosity.

The results for these single-spot FRAPP experiments are shown in Table 2.1. It is clear that FRAPP is a good technique for measuring diffusion in polymer films because the thick film diffusion coefficients obtained in this method match well with their expected values in bulk. Additionally, these preliminary studies demonstrate that FRAPP is sensitive over several orders of magnitude of the diffusion coefficient, in this study 10^{-10} cm²/sec to 10^{-14} cm²/sec. However, these single photobleached spot experiments have very low experimental throughput and the experimental error must be calculated from repeated experiments.

	Molecular Weight (kg/mol)	Film Thickness (nm)	Temp. (°C)	Measured Diffusion Coefficient (cm ² /sec)	Calculated Diffusion Coefficient (cm ² /sec)
PiBMA	10.4	140	140	$(1.2 \pm 0.5) \times 10^{-10}$	2.6×10^{-10} (1)
PMMA	10.5	300-325	160	$(9.9 \pm 1.3) \times 10^{-14}$	6.9×10^{-14} (2)

Table 2.1: Table of diffusion results from single-spot FRAPP experiments, error is from repeated measurements. (1) Value estimated from the Rouse model (eq. 2.3).²⁰ (2) Extrapolated from data using scaling theory for 12 kg/mol material.²²

2.6 DIFFUSION IN PHOTOBLEACHED ARRAYS

As previously stated, one of the significant issues with the single-spot method used initially is the slow experimental throughput. In order to determine the experimental error repeated experiments must be performed. Since each experiment takes about one day, this is a very slow process. The seemingly simple solution to photobleach multiple spots into the same film presents one of two problems. First, if the spots are photobleached too close together, this could violate the ‘infinite reservoir’ boundary condition imposed for eq. 2.2 and therefore the diffusion coefficient would be very difficult to determine. Second, if the spots are photobleached too far apart the magnification of the images would need to be reduced in order to capture them all and this decreases the apparent diffusion distance (number of pixels) that the polymer diffuses over the course of the experiment. A solution to these problems is to use photobleached arrays in which every period of the photobleached pattern is really an individual experiment. Therefore, the D and experimental uncertainty can be calculated from a single experiment over several periods of the array.

A detailed description of the procedure used for these studies can be found in the experimental section of this chapter; it is shown schematically in Figure 2.6. Briefly, photobleaching is performed using a photomask with a periodic array of lines and spaces (in this case 12.5 μm chrome lines on a 25 μm pitch pattern). Then, the relaxation of the pattern of high intensity and low intensity regions is monitored throughout the experiment in a subsequent recovery step where diffusion occurs.

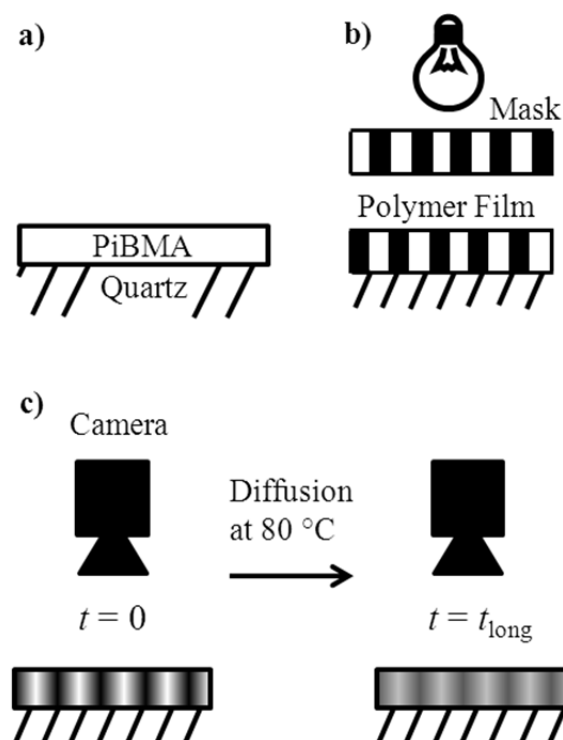


Figure 2.6: Schematic of the periodic array FRAPP experiment. a) Spin coating and annealing of a polymer film with a uniform fluorophore distribution. b) Photobleaching with a high intensity broadband light source through a mask to initially create a periodic array of fluorescent and non-fluorescent regions. c) Redistribution of fluorophores from the initial condition ($t=0$) to long times ($t=t_{\text{long}}$) as diffusion occurs over time causes a relaxation in the pattern monitored by an epifluorescence microscope. Light areas indicate regions of high fluorescent intensity and dark regions indicate regions of low fluorescent intensity.

Figure 2.7 shows fluorescence micrographs from a characteristic FRAPP experiment for a 127 nm thick film. Micrographs were collected at 1 h intervals throughout the course of the experiment. ImageJ²³ was used to plot normalized fluorescence intensity as a function of position for the image collected at each time point. A detailed guide to the calculation of the diffusion coefficient can be found in Appendix A. The intensity profile at each time is well represented by a sinusoid with a characteristic amplitude (A) and wavelength (λ) as indicated in Figure 2.7. This figure contains an image collected (a) before photobleaching, in which fluorophore labeled polymers are uniformly distributed throughout the film, (b) after patterned photobleaching and annealing for 1 h at 80 °C, where the periodic array of lines and spaces is clearly visible, and (c) after substantial diffusion has taken place where relaxation of the array is observed as fluorophore labeled polymers are redistributed from fluorophore-labeled polymer rich to fluorophore-labeled polymer deficient regions of the film. The intensity trace of the micrograph of the prebleached film is normalized to have an average intensity of one but is shown here only for comparison and does not enter into calculation of the diffusion coefficient. Each micrograph collected during the diffusion experiment is normalized based on its own maximum intensity and then vertically shifted so each time point has the same average value as the initial condition. The region of interest over which diffusion is calculated ($75 \mu\text{m} \times 96.75 \mu\text{m}$) in a 127 nm film contains $\sim 7 \times 10^{10}$ individual chains of PiBMA, which means the diffusion observed in these experiments correlates to an ensemble average diffusion coefficient.

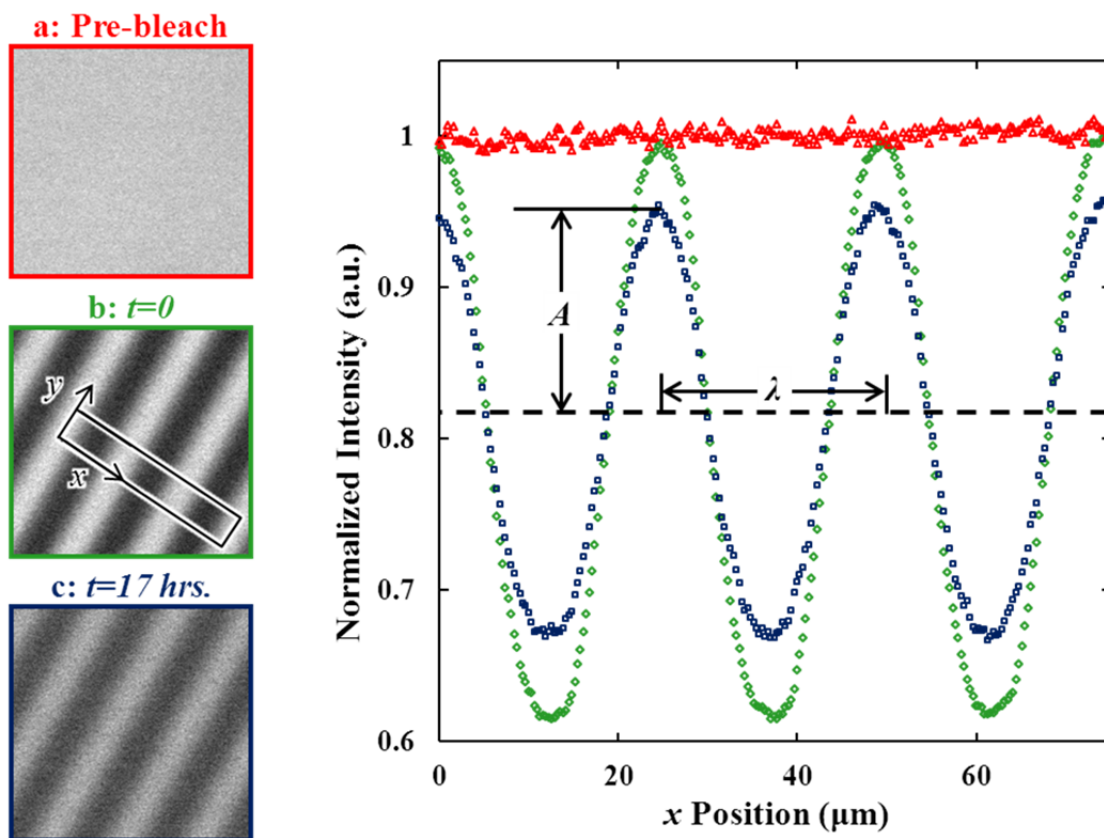


Figure 2.7: Fluorescence micrographs a) before photobleaching (\triangle) b) at the start of the diffusion experiment after patterned photobleaching and annealing (\diamond) and c) after significant recovery (\square) of a 127 nm film of PiBMA-NBD. Plot shows the normalized intensity as function of position (x) from a 300 pixel wide (in y) line integral perpendicular to the bleached pattern over several periods. ' A ' indicates the amplitude of the sinusoid and ' λ ' indicates the wavelength.

For a polymer melt well above its T_g , Fick's second law governs one-dimensional transient polymer self-diffusion using normalized fluorescence intensity (I) to represent the concentration of unbleached fluorophores, as measured by fluorescence intensity. The initial sinusoidal shape of the intensity profiles in Figure 2.7b sets the initial condition and periodic boundary conditions. Equation 2.4 shows that the solution for $I(x,t)$ is given by

$$I(x, t) = A_0 \cos\left(\frac{2\pi x}{\lambda}\right) e^{\frac{-4\pi^2 D}{\lambda^2} t} \quad (2.4)$$

where A_0 is the amplitude of the sinusoid used for the initial condition, λ is the wavelength of the sinusoid, t is the diffusion time, x is the position, and D is the diffusion coefficient. Finally, setting $I(0, t) = A(t)$ and rearranging eq 2.4 into a linear form with t yields eq 2.5

$$\ln\left(\frac{A(t)}{A_0}\right) = \frac{-4\pi^2 D}{\lambda^2} t \quad (2.5)$$

where $A(t)$ is the amplitude of the sinusoid at time t which decays as diffusion proceeds. The slope of the line $\ln(A(t)/A_0)$ against t is proportional to D , which can be calculated from the slope, M . Each collected intensity profile is fit with a simple sinusoid using a least-squares fitting procedure in order to calculate the amplitude, $A(t)$, and wavelength, λ , of the intensity profile for each time point.

The uncertainty in the diffusion coefficient, σ_D , is based on a propagation of error analysis of eq 2.5. The uncertainty in the wavelength, σ_λ , and the uncertainty in the slope M of $\ln(A(t)/A_0)$ against t , σ_M , both need to be considered. The uncertainty of the wavelength is the standard deviation of the wavelengths determined from the fit of each intensity profile and has a value of approximately one third the width of a single pixel (322.5 nm) on the camera used for imaging in all runs. The uncertainty of the slope is based on the 95% confidence limits of the linear regression. The final expression used to calculate the experimental uncertainty in the diffusion coefficient is shown in eq 2.6.

$$\sigma_D = \sqrt{\left(\frac{-\lambda M}{2\pi^2} \sigma_\lambda\right)^2 + \left(\frac{-\lambda^2}{4\pi^2} \sigma_M\right)^2} \quad (2.6)$$

Figure 2.8 demonstrates how the analysis technique used in this study is applied for a 127 nm film, the same film from the micrographs in Figure 2.7 were collected from. It is clear from this figure that $\ln(A(t)/A_0)$ plotted against time forms a straight line and that the wavelength, within the resolution of the camera, is a constant. The analysis

method for these experiments gives a diffusion coefficient of $(1.02 \pm 0.07) \times 10^{-12} \text{ cm}^2/\text{s}$. The diffusion coefficient was calculated using eq 2, and the uncertainty was calculated using eq 2.6.

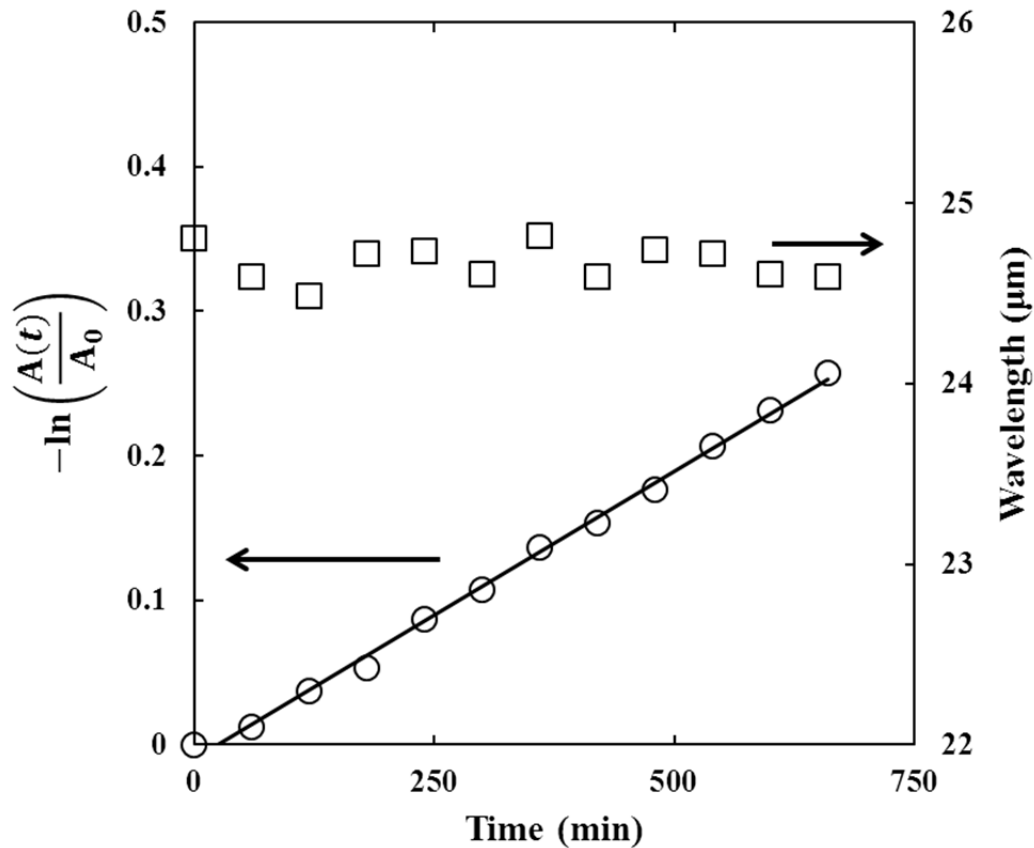


Figure 2.8: Results of a typical FRAPP experiment for a 127 nm film. The left axis shows the negative natural log of the amplitude normalized by the amplitude of the initial condition (A_0) (\circ), and the right axis contains the wavelength (\square) of the best fit sinusoid against time. The solid line through the amplitude data indicates best fit line that is then used with eq 2 to calculate the diffusion coefficient. The error in the amplitude is smaller than the symbols and is less than 4% for each data point.

The molecular weights of the polymers used in this study ($\sim 8.7 \text{ kg/mol}$) are well below the entanglement molecular weight for PiBMA, $\sim 28 \text{ kDa}$,¹⁹ as previously stated.

Therefore, bulk diffusion is expected to follow the Rouse model for unentangled polymer diffusion.^{20,21} Using eq. 2.3, $\rho = 1.071 \text{ g/cm}^3$ at $80 \text{ }^\circ\text{C}$,¹⁹ R is the ideal gas constant, $T = 353.15 \text{ K}$, $\langle R^2 \rangle = 8.52 \text{ nm}^2$,²⁴ M is the molecular weight, and $\eta_0 = 820 \text{ Pa}\cdot\text{s}$ is the zero shear viscosity (by a cone and plate fixture on a TA Instruments AR-2000ex rheometer under steady shear). Using eq. 2.3, the diffusion coefficient in this system is $1.05 \times 10^{-12} \text{ cm}^2/\text{sec}$ at $80 \text{ }^\circ\text{C}$. The diffusion coefficient for the 127 nm film represented in Figures 2.7 and 2.8 was $(1.02 \pm 0.07) \times 10^{-12} \text{ cm}^2/\text{s}$, which is identical, within uncertainty, to the calculated value. Because the diffusion coefficient calculated for the thicker films corresponds well with measured values from these experiments, FRAPP clearly allows for characterization of the diffusion of polymers in thin films, and the analysis method chosen consistently yields accurate results. Additionally, this technique also allows for characterization of the uncertainty in an individual measurement as described above, which previously had only been possible by repeated measurements on similar films.

Figure 2.9 displays the diffusion coefficient as a function of film thickness for PiBMA down to 30 nm . The results in this figure demonstrate that within two standard deviations, a 95% confidence interval, none of the data points are significantly different statistically from the other data points regardless of film thickness. For the PiBMA-NBD measurements, experimental uncertainty in the diffusion coefficient, as calculated by eq 2.6, was less than 9% of the diffusion coefficient for all film thicknesses measured. Additionally, this technique exhibits good reproducibility; for a set of three separately prepared $61 \pm 5 \text{ nm}$ films, the diffusion coefficients measured were, 1.10×10^{-12} , 1.22×10^{-12} , and $1.28 \times 10^{-12} \text{ cm}^2/\text{s}$. Diffusion parallel to confining interfaces was also measured on PiBMA-NBD-PiBMA, a polymer synthesized with a di-functional fluorophore containing initiator and therefore fluorophores in the middle of the polymer backbone. By UV/vis absorption measurements these polymers were shown to contain

two fluorophores per chain, likely due to coupling events that can be common the polymerization conditions. In this case also, no deviation in the diffusion coefficient from the Rouse model prediction was observed in films as thin as 34.9 nm. Because the diffusion coefficient is invariant with the number of fluorophores per polymer chain or their position along the polymer backbone, this indicates that the presence of fluorophores in the polymer does not impact the diffusion of the polymer chains.

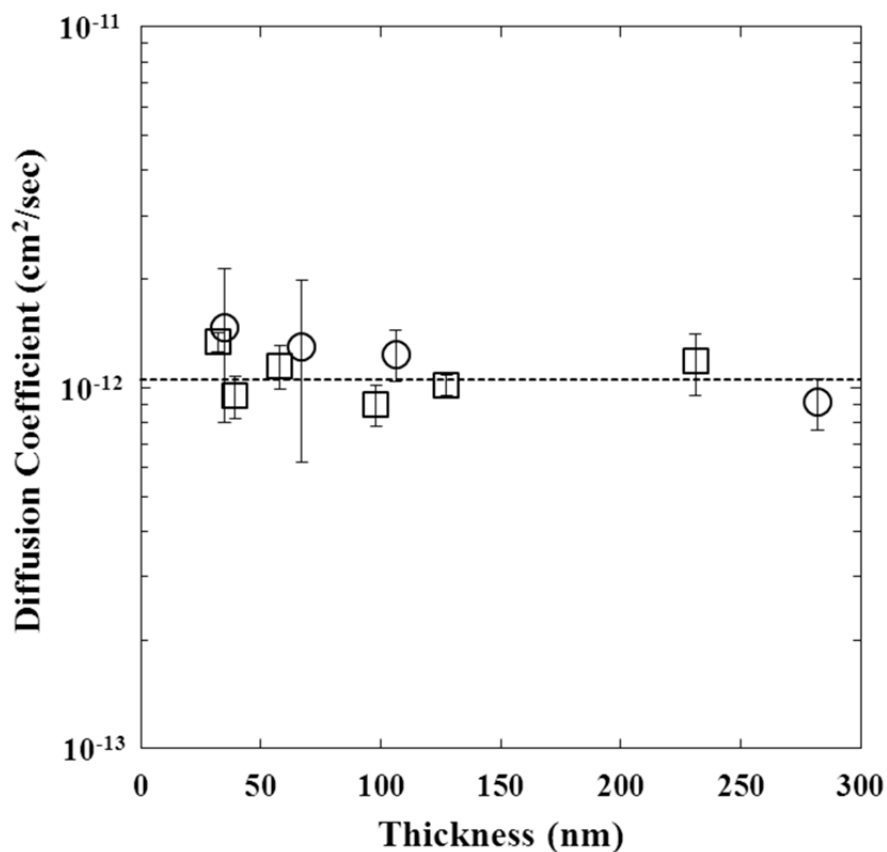


Figure 2.9: Diffusion coefficient at 80 °C of PiBMA-NBD (□) and PiBMA-NBD-PiBMA (○) as a function of film thickness recorded at 25 °C. The dashed line indicates the bulk diffusion coefficient estimated using the Rouse model for this molecular weight and temperature ($1.05 \times 10^{-12} \text{ cm}^2/\text{sec}$). Error bars indicate the uncertainty as calculated from eq 2.6.

This demonstrates a procedure to measure self-diffusion coefficients of polymers parallel to their confining interfaces in thin films based on FRAPP. The relaxation of a photobleached array of lines was directly observed and imaged via an epifluorescence microscope where the rate of relaxation is directly related to the self-diffusion coefficient of PiBMA. One of the primary features of this FRAPP method is the ability to directly image the polymer film during the experiment. Many biological experiments using FRAPP use a confocal microscope with a scanning photomultiplier tube or an epifluorescence microscope with a camera to image and analyze diffusion of a target species by bleaching a single-spot.^{25,26} By comparison, previous polymer studies employing FRAPP utilize a photon counting technique and measure the absolute fluorescence intensity from the region of interest.^{10,12,16} By imaging with a camera and then analyzing the fluorescence intensity profile, rather than tracking absolute intensity, the results do not rely on making certain assumptions about the experiment, such as no photobleaching during imaging, because the maximum intensity of each image is referenced internally. Additionally, the ability to reliably characterize the diffusion coefficient and experimental uncertainty from a single experiment substantially reduces the need for repeated trials of each film thickness studied, leading to an increase in experimental throughput. The FRAPP procedure used in this work provides a flexible platform for the study of diffusion in thin polymer films. This approach is not specific to this polymer, substrate, or even this fluorophore, so this basic setup can be tailored to examine a wide array of parameters that will be the subject of future work.

2.7 DISCUSSION OF DIFFUSION RESULTS

The PiBMA diffusion results in this study show that the diffusion coefficient of PiBMA is invariant with film thickness down to 30 nm ($\sim 14R_g$). In contrast, a previous

study on polystyrene indicated that D decreased for polystyrene films thinner than $\sim 50R_g$.¹⁰ In addition, the T_g of PiBMA was measured to be independent of film thickness down to 15 nm, about $7R_g$. This T_g result is identical to that of Priestley et al. for PiBMA with $M_n = 300$ kg/mol.⁵ In that study, additional measurements on a 14 nm thick fluorophore containing surface or substrate layer determined T_g selectively at each interface and showed that the T_g decreased by 6 °C for the 14 nm nearest the air interface and increased by 5 °C for the 14 nm closest to the substrate. This suggests the magnitude of the hydrogen-bonding interactions between the PiBMA repeat unit and the hydroxyls on the substrate are such that the increase in polymer T_g they promote balances exactly the reduction in T_g near the air interface of the film, resulting in no net change of average T_g with film thickness, as measured by ellipsometry. While the experimentally observed average T_g of PiBMA on silicon oxide substrates by ellipsometry is invariant with film thickness, the results of Priestley et al. indicate clearly that a distribution of T_g values exist within the thin film.

Examining the T_g of PiBMA in thin films is important to studies of diffusion parallel to interfaces because, at least in bulk, diffusion is related to the proximity of the diffusion temperature to the glass transition temperature ($T - T_g$). The effect of changing $T - T_g$ on D can be estimated by the Rouse model (eq 2.3) using a value for η_0 where T_g is adjusted by a WLF relationship¹ and the density is adjusted based on thermal expansion,¹⁹ all other parameters constant. By this protocol, an increase in T_g leads to a decrease in the diffusion coefficient, and a decrease in T_g produces an increase in the diffusion coefficient.

Using the layered T_g data of Priestley et al.⁵ and the protocol described above, diffusion coefficients near the air and substrate interfaces can be predicted. This estimation results in a PiBMA diffusion coefficient at 80 °C of 2.1×10^{-12} cm²/s in the

layer of the film closest to the air and a diffusion coefficient of $5.2 \times 10^{-13} \text{ cm}^2/\text{s}$ in the layer of the film closest to the substrate. Respectively, these values represent an increase by 100% and a decrease of 50% from the bulk value, well outside the experimental uncertainty of the bulk value we have measured for all film thicknesses. If the layers were significant contributors, it might be expected that there would be at least two populations of diffusing chains, one fast and one slow. More likely, however, there would be a continuous range of different diffusion coefficients, not just two populations. It is worth noting that simulations suggest that there may be different diffusion coefficients near different interfaces.^{27,28} This would significantly complicate the use of Fick's law with a single diffusion coefficient and would be reflected by model predictions that fit data poorly. At this time, all our data fit the Fickian diffusion model with a single diffusion coefficient quite well. More experiments will be needed to resolve these issues.

This connection has been considered in a follow-up commentary²⁹ to a previous study¹⁰ where a factor of 2 reduction in D parallel to the substrate was observed for a 50 nm thick polystyrene film¹⁰ on a silicon oxide substrate. The associated commentary hypothesized that the thickness dependence of D could be explained by an increase in film T_g of 7 °C, using a similar analysis to that outlined in the previous paragraph.²⁹ However, it has most commonly been shown that T_g decreases with decreasing film thickness for polystyrene films supported on silicon or silicon oxide substrates,³⁰ which appears inconsistent with this argument. Using the preceding analysis and the fact that T_g typically decreases with decreasing film thickness, one would expect an increasing D with decreasing film thickness for polystyrene at any given diffusion temperature.

Finally, neutron scattering measurements indicate the chain conformations in the plane of the film (normal to the confining dimension) retain their bulk unperturbed Gaussian conformations in polystyrene films as thin as $0.5R_{g,\text{bulk}}$.^{31,32} This chain

conformation result suggests that D in the plane of the film should be unchanged for polystyrene films as thin as $0.5R_{g,bulk}$. Given the current understanding of nanoconfinement effects on polystyrene, it is difficult to reconcile the results for polystyrene indicating decreasing D with decreasing film thickness under conditions where with the chain conformation is consistent with bulk, and more research is needed to develop a complete picture. Nonetheless, measurements of PiBMA chain conformations in nanoconfined films have not been performed, and therefore it is not possible to comment on how they may be affected at film thicknesses where D was measured in the present study.

2.8 CONCLUSIONS

FRAPP is a useful technique for measuring diffusion of polymers parallel to confining interfaces in thin films over several decades of diffusion coefficient. Using a periodic pattern of lines and spaces for photobleaching increases experiment throughput and reduces variability. Since the Rouse model predicts that the diffusion coefficient is not simply related to the temperature but the distance from the T_g of a polymer, PiBMA provides an ideal platform for initial studies as it demonstrates a film thickness independent T_g on SiO₂ substrates. In PiBMA, no change in the diffusion coefficient was observed down to 30 nm, even though there is expected to be a change in the T_g near each interface. FRAPP, as developed here, provides a flexible platform for future studies of a variety of parameters that could have an influence on nanoconfined diffusion of polymers.

2.9 EXPERIMENTAL

2.9.1 Materials

Chemicals used in this study were purchased from Fisher Scientific or Sigma-Aldrich, and all chemicals were used as received unless otherwise noted. Anisole and isobutyl methacrylate were purified by stirring with basic alumina and calcium hydride for 2 hrs and then filtered to remove solids. Tris(2-dimethylaminoethyl)-amine, Me₆TREN, was synthesized according to a published procedure.³³ Molecular weight and polydispersity data were measured using a Viscotek GPCMax VE 2001 gel permeation chromatography (GPC) solvent/sample module with a Viscotek Model 270 dual detector viscometer/light scattering detector and Viscotek VE 3580 refractive index detector with 2 I-Series mixed bed low MW columns. Fluorophore attachment was verified by an in-line Jasco FP-2020 Plus Intelligent Fluorescence Detector ($\lambda_{\text{excitation}} = 465 \text{ nm}$, $\lambda_{\text{emission}} = 520 \text{ nm}$, 18 nm bandpass). Molecular weights reported are relative to a conventional calibration curve created using PiBMA standards synthesized in house and absolutely characterized by Viscotek Triple Detect software combining light scattering, refractive index detection, and viscometry. Nuclear magnetic resonance (NMR) spectra were recorded on a Varian 400 MHz DirectDrive NMR with SMS sample changer. The glass transition temperature (T_g) of the bulk polymer samples was measured by differential scanning calorimetry (DSC) using a Mettler-Toledo DSC-1 with a 10 °C/min heating rate upon second heating.

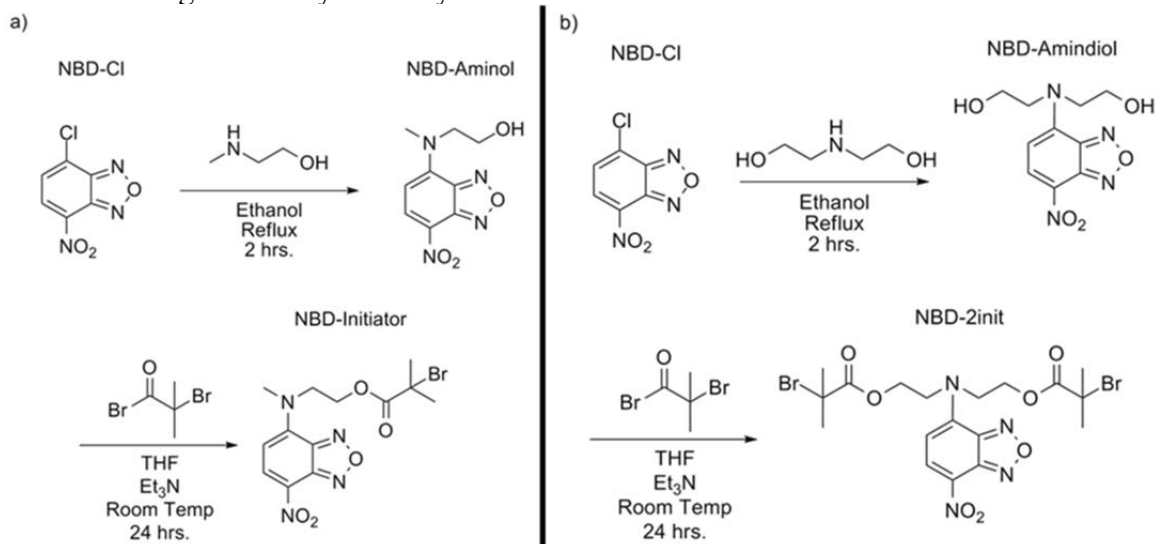
2.9.1.1 Initiator Synthesis

There are a variety of methods that can be used to synthesize polymers with fluorophores covalently bound to the backbone; one method is presented here and another in Chapter 3. A detailed discussion of these and some alternative approaches can be

found in Appendix B. Monodisperse PiBMA was synthesized using an initiator containing a covalently bound nitrobenzofurazan (NBD) fluorophore. The polymerization technique used was activators regenerated by electron transfer atom transfer radical polymerization (ARGET ATRP).³⁴⁻³⁶ ARGET ATRP is a controlled radical polymerization technique providing a relatively simple platform for synthesis of end-functionalized polymers³⁷ with good control over molecular weight and PDI along with flexible monomer and initiator choice. The most significant advantage of ARGET ATRP over conventional ATRP is that the added reducing agent decreases oxygen sensitivity and the amount of copper catalyst necessary for the polymerization.

Using established literature procedures,^{36,38,39} an ATRP initiator bearing a NBD fluorophore was synthesized and PiBMA-NBD was polymerized using this initiator. The monofunctional initiator was synthesized in two steps (Scheme 2.1a). First, 4-chloro-7-nitro-2,1,3-benzoxadiazole (NBD-Cl) was refluxed with a 3 fold molar excess of 2-(methylamino)ethanol in ethanol for 2 h, cooled, filtered, and washed with cold ethanol. The resulting orange solid was recrystallized from ethanol, and the solid filtrate was collected in 85% yield. The product, 2-[methyl-(7-nitro-2,1,3-benzoxadiazol-4-yl)amino]ethanol (NBD-Aminol), was dried and then dissolved in dry tetrahydrofuran and reacted with a 3 fold molar excess of dry 2-bromoisobutyryl bromide in the presence of dry triethylamine overnight at room temperature. After removing excess solvent, the product was dissolved in dichloromethane and washed with deionized water (seven times) and concentrated aqueous sodium bicarbonate (three times). Finally, the product was dried over magnesium sulfate, then the product is dried in a vacuum oven at 80 °C to remove solvent and excess 2-bromoisobutyryl bromide to give 2-(methyl(7-nitro-2,1,3-benzoxadiazol-4-yl)amino)ethyl 2-bromo-2-methylpropanoate (NBD-Initiator) with 67% yield for this step (overall yield 57%). The procedure to synthesize the di-functional

initiator 2,2'-(7-nitro-2,1,3-benzoxadiazol-4-ylazanediyl)bis(ethane-2,1-diyl)bis(2-bromo-2-methylpropanoate) (NBD-2init) (Scheme 2.1b), used to make polymers with the NBD fluorophore in the middle of the chain, is identical to the above procedure, except diethanolamine is used in place of 2-(methylamino)-ethanol to yield 2,2'-(7-nitro-2,1,3-benzoxadiazol-4-ylazanediyl)-diethanol (NBD-Amindiol) as an intermediate. For this case, 6 fold molar excess of triethylamine and 2-bromoisobutyryl bromide was used in the second step (Scheme 2.1b). All of the synthesized compounds were characterized by NMR in order to verify purity; within the limits of detection there were no remaining unreacted reagents in any of the synthesized initiators.

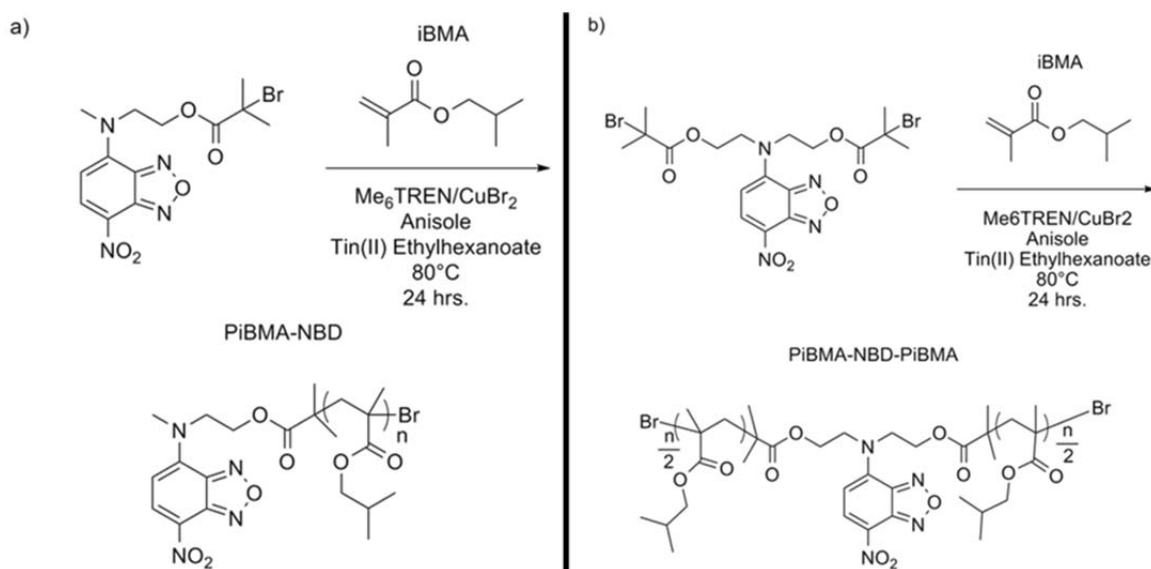


Scheme 2.1: a) Synthesis of mono-functional NBD bearing one ATRP initiator site for chain-end labeled polymers. b) Synthesis of di-functional NBD bearing two ATRP initiator sites for mid-chain labeled polymers.

2.9.1.2 Polymerization

To synthesize the polymers (Scheme 2.2), the NBD containing initiator was dissolved in anisole with isobutyl methacrylate. Copper(II) bromide (400 ppm copper to monomer) was used as a catalyst, and a ligand (Me₆TREN) at 10:1 molar ratio ligand to

copper was incorporated to aid in copper solubility. After the reactor was sealed and sparged with dry argon for 15 min, the reducing agent, tin(II) 2-ethylhexanoate, was injected, and the reaction was allowed to proceed for 24 h at 80 °C. The resulting polymer (PiBMA-NBD or PiBMA-NBD-PiBMA) was diluted with THF and run through basic alumina to remove the copper and ligand and then dried at 100 °C under vacuum to remove residual solvents. Fluorescently labeled polymers were then repeatedly dissolved in tetrahydrofuran and precipitated in ethylene glycol seven times to remove any unreacted initiator; the absence of a small molecule fluorescence peak in GPC was used to verify removal of all unattached fluorophores. Covalent attachment of the fluorophore was verified by comparing fluorescence and refractive index detectors on GPC to show coelution of the polymer and fluorophore. For PiBMA-NBD, 100% of the polymer chains, within error, are covalently bound to a single fluorophore by UV/vis absorption measurements (Hewlett-Packard 8452A diode array spectrophotometer). The fluorescently labeled PiBMA-NBD polymer was 5.8 wt % fluorophore with $M_n = 8.7$ kg/mol and PDI = 1.1. PiBMA-NBD-PiBMA was also synthesized ($M_n = 8.3$ kg/mol, PDI = 1.2), and by UV/vis absorption measurements these polymers were shown to contain two fluorophores per chain, likely due to coupling events that can be common to ARGET ATRP under some polymerization conditions. To synthesize PiBMA without a NBD fluorophore, the polymerization procedure was identical, except the initiator was ethyl 2-bromoisobutyrate ($M_n = 8.6$ kg/mol, PDI = 1.1). DSC measurements on both PiBMA-NBD and PiBMA confirm that the fluorophore has no measurable impact on the midpoint Tg (51 °C) of the bulk polymer for equivalent molecular weight polymers, also consistent with other bulk PiBMA samples of similar molecular weight.²⁴



Scheme 2.2: Synthesis of a) chain-end labeled PiBMA-NBD and b) mid-chain labeled PiBMA-NBD-PiBMA by ARGET ATRP.

2.9.2 Methods

2.9.2.1 Film Preparation

Films in this study were spin-coated (Specialty Coating Systems Spincoat G3-8) onto quartz (for FRAPP experiments) or silicon substrates with native oxide layers (for ellipsometry experiments) from solutions of either toluene or n-butanol. Quartz substrates were prepared by soaking in a piranha solution of 3:1 concentrated sulfuric acid to hydrogen peroxide and then rinsed with deionized water at least three times. Solution concentrations ranged from 0.5 to 6 wt % polymer in n-butanol, and spin speeds varied from 800 to 3000 rpm to control the film thickness.^{40,41} The polymer in the spin-coating solution for FRAPP experiments was comprised of fluorescently labeled polymer and a molecular weight matched unlabeled polymer to mitigate fluorescence self-quenching effects (fluorophore content < 0.18 wt%, see Figure 2.3). After spincoating, films were annealed under vacuum at room temperature overnight. Average thicknesses for FRAPP samples on quartz were measured using a Veeco Dektak 6M stylus profiler by recording

ten measurements near the center of the film with a tip radius of 12.5 μm and a stylus force of 7 mg. Films prepared on silicon substrates were characterized by ellipsometry using a J.A. Woollam M-2000D spectroscopic ellipsometer.

2.9.2.2 Thin Film T_g Determination

The T_g of thin films was characterized using an established spectroscopic ellipsometry procedure.^{42,43} The film is heated to 150 $^{\circ}\text{C}$, which is well above the bulk T_g (51 $^{\circ}\text{C}$) and the boiling point of the spin-coating solvent (118 $^{\circ}\text{C}$ for n-butanol, the highest boiling solvent used), and annealed for 15 min. Next, the film is cooled at 2 $^{\circ}\text{C}/\text{min}$ with an Instec mK 1000 temperature controller with a HCS 402 hot stage connected to a liquid nitrogen pump. The film thickness was plotted against sample temperature to identify T_g based on a layered model in which the only fitted parameters were the optical constants and thickness of the polymer film (WVase software, J.A. Woollam Co.).

2.9.2.3 FRAPP

For the preliminary single-spot experiments, the photobleached regions were created using an argon ion laser on a Leica SP2 AOBS Confocal Microscope using the 458, 476, and 488 nm laser lines. Imaging was performed on an Olympus IX 71 epifluorescence microscope using a wide blue filter set. Samples were heated on a Linkham TMS91 hot stage to a calibrated temperature.

For the patterned FRAPP experiments, photobleaching was performed using a Ronchi ruling (Edmund Optics) (chrome lines deposited on a quartz substrate with 12.5 μm lines on a 25 μm pitch) as a mask for creating a periodic array of bleached and unbleached regions. The sample was photobleached using an Optical Building Blocks ScopeLite 200 (a broadband intense light source) after cooling the sample to 4 $^{\circ}\text{C}$ in

order to prevent the chrome lines from forming indentations in the polymer film. Film bleaching is expected to be uniform through the film because the absorbance is 0.01 absorbance units per 100 nm of film thickness at a wavelength of 465 nm, as measured by UV/vis spectroscopy. This indicates that even for the thickest films used in this study (~280 nm), the bleaching light is attenuated a negligible amount (~5%) as it passes through the film; therefore, the photobleaching reaction takes place equally throughout the depth of the film. The film was then heated to 80 °C using a Linkham TMS91 hot stage and allowed to equilibrate for 1 h before starting to monitor the fluorescence recovery. Imaging was performed with a Hamamatsu Orca R2 camera with μ Manager software for camera control⁴⁴ on an Olympus BX 51 epifluorescence microscope coupled to a Photon Technologies QuantaMaster 40 fluorimeter. The excitation wavelength used was 465 nm with a 4 nm bandpass and an emission filter selected to collect all wavelengths greater than 520 nm. The depth of focus of the microscope is 2.9 μ m at 20X magnification, which is an order of magnitude larger than the thickest films used in this study; therefore, fluorescence from the entire depth of the film is captured in each image. Images were taken at intervals of 1 h with an automatic shutter employed to limit photobleaching during the course of the experiment. The typical exposure time for each data point is 4 seconds. See Figure 2.6 for a schematic of the experimental procedure. An experiment on a film that had not been photobleached confirmed that, with the amount of cumulative exposure from a typical FRAPP experiment (~30 s total exposure at 80 °C), <5% photobleaching is caused by imaging (Figure 2.10).

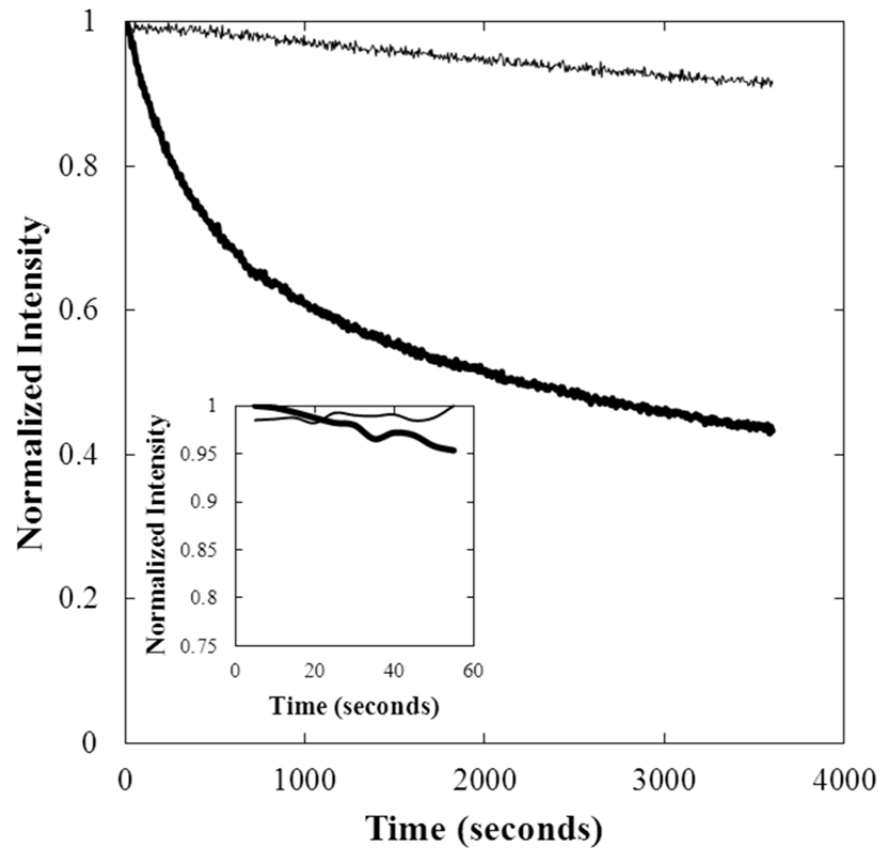


Figure 2.10: Photobleaching of PiBMA-NBD at room temperature (thin line) and 80 °C (thick line) at $\lambda_{\text{ex}} = 465$ and $\lambda_{\text{em}} = 520$. Inset shows first minute of photobleaching which is typical total amount of exposure time during a diffusion experiment showing <5% photobleaching occurs at 80 °C.

2.10 REFERENCES

1. Rubinstein, M.; Colby, R. H. *Polymer Physics*; Oxford University Press: Oxford, 2003.
2. Frankenburg, W. G. *Advances in catalysis and related subjects*; Academic Press: New York, New York, 1966.
3. McCafferty, E.; Wightman, J. P. *Surf. Interface Anal.* **1998**, *26*, 549-564.
4. Kim, S.; Hewlett, S. A.; Roth, C. B.; Torkelson, J. M. *Eur. Phys. J. E* **2009**, *30*, 83-92.
5. Priestley, R.; Mundra, M. K.; Barnett, N. J.; Broadbelt, L. J.; Torkelson, J. M. *Aust. J. Chem.* **2007**, *60*, 765-771.
6. Arbeloa, F. L.; Ojeda, P. R.; Arbeloa, I. L. *J. Lumines.* **1989**, *44*, 105-112.
7. Hamann, S.; Kiilgaard, J.; Litman, T.; Alvarez-Leefmans, F.; Winther, B.; Zeuthen, T. *Journal of Fluorescence* **2002**, *12*, 139-145.
8. Lakowicz, J. R.; Malicka, J.; D'Auria, S.; Gryczynski, I. *Anal. Biochem.* **2003**, *320*, 13-20.
9. Zhang, J. A.; Fu, Y.; Lakowicz, J. R. *J. Phys. Chem. C* **2007**, *111*, 1955-1961.
10. Frank, B.; Gast, A. P.; Russell, T. P.; Brown, H. R.; Hawker, C. *Macromolecules* **1996**, *29*, 6531-6534.
11. Smith, B. A. *Macromolecules* **1982**, *15*, 469-472.
12. Wong, J. S. S.; Hong, L.; Bae, S. C.; Granick, S. *Journal of Polymer Science Part B: Polymer Physics* **2010**, *48*, 2582-2588.
13. Axelrod, D.; Koppel, D. E.; Schlessinger, J.; Elson, E.; Webb, W. W. *Biophys. J.* **1976**, *16*, 1055-1069.
14. Cicerone, M. T.; Blackburn, F. R.; Ediger, M. D. *Macromolecules* **1995**, *28*, 8224-8232.
15. Smith, B. A.; Mumby, S. J.; Samulski, E. T.; Yu, L. P. *Macromolecules* **1986**, *19*, 470-472.

16. Tseng, K. C.; Turro, N. J.; Durning, C. J. *Polymer* **2000**, *41*, 4751-4755.
17. Van Keuren, E.; Schrof, W. *Macromolecules* **2003**, *36*, 5002-5007.
18. Crank, J. *Mathematics of Diffusion*; 2nd ed.; Oxford University Press: New York, 1975.
19. Bicerano, J. *Prediction of Polymer Properties*; 3rd ed.; Marcel Dekker, Inc.: New York, 2002.
20. Doi, M.; Edwards, S. F. *The Theory of Polymer Dynamics*; Clarendon Press: Oxford, 1986.
21. Rouse, P. E., Jr. *Journal of Chemical Physics* **1953**, *21*, 1272-80.
22. Milhaupt, J. M.; Lodge, T. P.; Smith, S. D.; Hamersky, M. W. *Macromolecules* **2001**, *34*, 5561-5570.
23. Abramoff, M. D., Magelhaes, P.J., Ram, S.J. *Biophotonics International* **2004**, *11*, 36-42.
24. *Polymer Handbook*; Barandrup, J.; Immergut, E. H.; Grulke, E. A., Eds.; Wiley and Sons: Hoboken, New Jersey, 1999.
25. Johnson, M. E.; Berk, D. A.; Blankschtein, D.; Golan, D. E.; Jain, R. K.; Langer, R. S. *Biophys. J.* **1996**, *71*, 2656-2668.
26. Zhang, F.; Schmidt, W. G.; Hou, Y.; Williams, A. F.; Jacobson, K. *Proc. Natl. Acad. Sci. U. S. A.* **1992**, *89*, 5231-5235.
27. Desai, T.; Keblinski, P.; Kumar, S. K. *Journal of Chemical Physics* **2005**, *122*, 8.
28. Torres, J. A.; Nealey, P. F.; de Pablo, J. J. *Phys. Rev. Lett.* **2000**, *85*, 3221-3224.
29. Russell, T. P.; Kumar, S. K. *Nature* **1997**, *386*, 771-772.
30. Forrest, J. A.; Dalnoki-Veress, K. *Adv. Colloid Interface Sci.* **2001**, *94*, 167-196.
31. Jones, R. L.; Kumar, S. K.; Ho, D. L.; Briber, R. M.; Russell, T. P. *Nature* **1999**, *400*, 146-149.

32. Jones, R. L.; Kumar, S. K.; Ho, D. L.; Briber, R. M.; Russell, T. P. *Macromolecules* **2001**, *34*, 559-567.
33. Fu, G. D.; Xu, L. Q.; Yao, F.; Zhang, K.; Wang, X. F.; Zhu, M. F.; Nie, S. Z. *ACS Appl. Mater. Interfaces* **2009**, *1*, 239-243.
34. Jakubowski, W.; Min, K.; Matyjaszewski, K. *Macromolecules* **2006**, *39*, 39-45.
35. Matyjaszewski, K.; Jakubowski, W.; Min, K.; Tang, W.; Huang, J. Y.; Braunecker, W. A.; Tsarevsky, N. V. *Proc. Natl. Acad. Sci. U. S. A.* **2006**, *103*, 15309-15314.
36. Pintauer, T.; Matyjaszewski, K. *Chem. Soc. Rev.* **2008**, *37*, 1087-1097.
37. Jakubowski, W.; Kirci-Denizli, B.; Gil, R. R.; Matyjaszewski, K. *Macromol. Chem. Phys.* **2008**, *209*, 32-39.
38. Bardajee, G. R.; Li, A. Y.; Haley, J. C.; Winnik, M. A. *Dyes Pigment.* **2008**, *79*, 24-32.
39. Kalinina, O.; Kumacheva, E. *Macromolecules* **1999**, *32*, 4122-4129.
40. Hall, D. B.; Underhill, P.; Torkelson, J. M. *Polym. Eng. Sci.* **1998**, *38*, 2039-2045.
41. Spangler, L. L.; Torkelson, J. M.; Royal, J. S. *Polym. Eng. Sci.* **1990**, *30*, 644-653.
42. Beaucage, G.; Composto, R.; Stein, R. S. *J. Polym. Sci. Pt. B-Polym. Phys.* **1993**, *31*, 319-326.
43. Keddie, J. L.; Jones, R. A. L.; Cory, R. A. *Faraday Discuss.* **1994**, *98*, 219-230.
44. Edelstein, A.; Amodaj, N.; Hoover, K.; Vale, R.; Stuurman, N. *Computer Control of Microscopes Using μ Manager*; John Wiley & Sons, Inc., 2001.

Chapter 3: Self-Diffusion of Poly(isobutyl methacrylate) in Multi-layer thin films

3.1 MOTIVATION

In the previous chapter fluorescence recovery after patterned photobleaching (FRAPP) was presented as a useful technique for the study of diffusion of polymers parallel to confining interfaces in thin films. Using this technique poly(isobutyl methacrylate) (PiBMA) on silicon oxide substrates was found to have a film thickness independent diffusion coefficient at T_g+29 °C. Furthermore, PiBMA exhibits a glass transition temperature (T_g) independent of film thickness on these substrates. The reason that PiBMA has a film thickness independent T_g is a balance of the hydrogen bonding with hydroxyls on the substrate and the enhanced mobility at the free surface.¹ By masking the hydrogen bonding at the substrate with another polymer film, PiBMA could exhibit a film thickness dependent T_g . With this in mind, there have been some recent studies that have suggested interesting directions for further study of diffusion in PiBMA thin films. One such study by Evans and coworkers using x-ray photon correlation spectroscopy demonstrated that effect of nanoconfinement on the modulus of a polymer may be decreased at temperatures much higher than T_g (T_g+40 °C).² Additionally, a study has suggested that, even in the case of polymers with film thickness dependent T_g s, the segmental dynamics associated with T_g may be film thickness invariant.³ Multi-layer films can be used to examine the diffusion of PiBMA at various T_D-T_g where T_D is the temperature at which the diffusion coefficient is measured and the effect of T_D-T_g on diffusion in thin films in which there is film thickness dependence to T_g is observed. The results in this chapter are preliminary and additional experiments will be necessary prior to publication of these results.

3.2 MULTI-LAYER FILMS

In order to mask the hydroxyls on a quartz or silicon wafer substrate by using a secondary polymer under-layer, there are several criteria that must be met by the polymer. First, it should be glassy at temperatures examined in diffusion experiments. This limits dewetting of the under-layer polymer film and retains a high substrate modulus as varying substrate modulus could add an additional variable to the diffusion experiments. Further, it needs to be non-fluorescent as any extra fluorescence could confound the results of the FRAPP experiment. Finally, it should be immiscible with PiBMA to limit inter-diffusion of the polymer layers. A desirable, but not required, condition is that there is a solvent for PiBMA that does not dissolve this confining under-layer as this will allow for sequential spin coating of the polymer layers rather than constructing the multi-layer via film floating techniques.

A polymer that meets all of these criteria is poly(cyclohexylethylene) (PCHE) (structure shown in Figure 3.1a) the hydrogenated form of polystyrene synthesized via palladium catalyzed hydrogenation reactions at high pressure.⁴ PCHE has a midpoint T_g of ~ 140 °C, is non-fluorescent, and is not soluble in n-butanol which is used for spin coating PiBMA. A schematic of the multi-layer films used in this chapter is shown in Figure 3.1b.

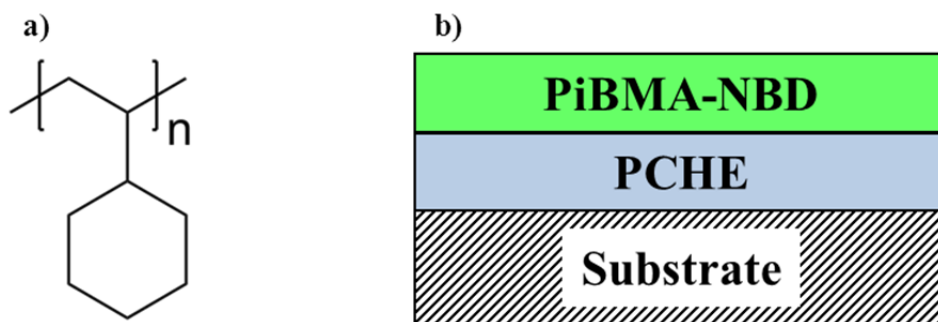


Figure 3.1: a) Structure of PCHE b) Schematic of multi-layer film

3.3 PRELIMINARY RESULTS

Preliminary results indicate that the hypothesis of masking the hydroxyls on the substrate with a polymer film does indeed lead to a moderate decrease in the T_g of the PiBMA film. At 20 nm the T_g decreases by about 2 °C from the thick film value. This represents a significant change in the diffusion coefficient as it is very sensitive to temperature as will be discussed later.

3.3.1 High Temperature Diffusion Results

The diffusion coefficient as a function of film thickness for PiBMA multi-layer films was measured from 150 nm to 18 nm at 78 °C ($T_g + 20$ °C) (Figure 3.2). In thick films the measurements are in reasonably good agreement with the prediction of the Rouse model (within 10 %). This indicates that the PCHE under-layer has no effect on the bulk diffusion coefficient and it does not interfere with the FRAPP experiment. At film thicknesses of about 35 nm the diffusion coefficient appears to increase monotonically with decreasing film thickness.

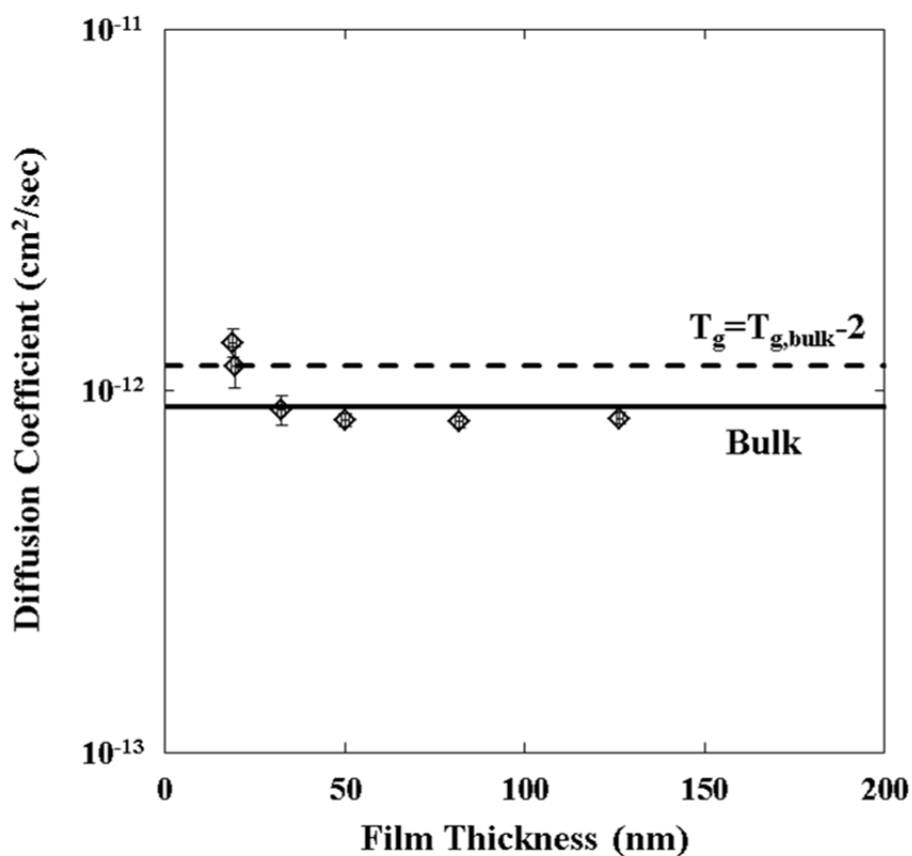


Figure 3.2: Diffusion coefficient as a function of film thickness for PiBMA multi-layer films at 78 °C. Solid line indicates bulk diffusion coefficient calculated from the Rouse model. Dashed line indicates the diffusion coefficient if the sample is 2 °C further from T_g . Error bars represent a 95% confidence interval.

3.3.2 Low Temperature Diffusion Measurements

Figure 3.3 contains preliminary data for diffusion at 66 °C ($T_g + 8$ °C). In these data there seems to be an upward trend with decreasing film thickness, which is consistent with higher temperature results. However, the diffusion coefficient in thick films does not correspond very well with the calculation based on the Rouse model. A difference of about 50 % is observed in ~150 nm thick films. This is potentially because the zero-shear viscosity measurements (a major component of the Rouse model

calculations) needed to be extrapolated ~ 35 °C below the range where measurements were actually made (100-160 °C). In the rheological measurements as the T_g of the polymer is approached the viscosity increases very rapidly the experimental error increases significantly in steady shear experiments. In order to improve the accuracy of the predicted diffusion coefficient the rheology measurements should be repeated at lower temperatures using an oscillatory experiment. For this reason the preliminary data is presented here, but no commentary on its implications will be included in the rest of this chapter.

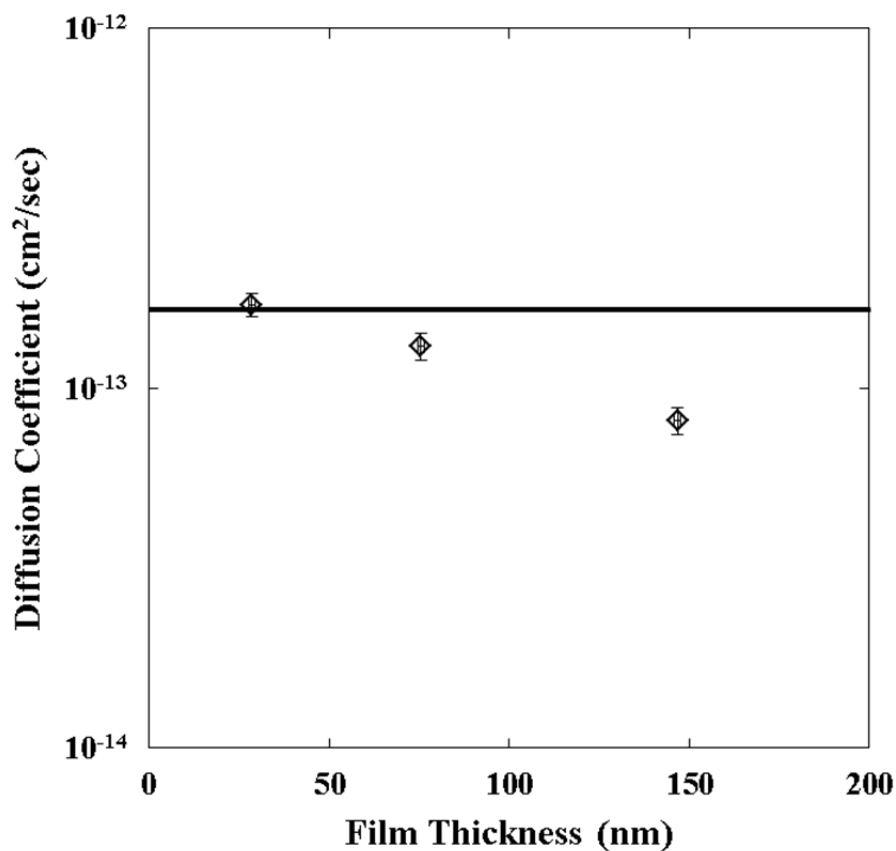


Figure 3.3: Diffusion coefficient as a function of film thickness for PiBMA multi-layer films at 66 °C. Solid line indicates the bulk diffusion coefficient calculated from the Rouse model. Error bars represent a 95% confidence interval.

3.4 DISCUSSION OF DIFFUSION RESULTS

The diffusion coefficient of polymers is very sensitive to the temperature at which the experiment is carried out, as previously stated. Figure 3.4 shows the diffusion coefficient of PiBMA predicted from the Rouse model as a function of temperature. A WLF fit to the zero-shear viscosity data was employed to predict η_0 , the zero shear viscosity, in the Rouse model (eq. 3.1).

$$D = \frac{\rho RT \langle R^2 \rangle}{36M\eta_0} \quad (3.1)$$

In eq 3.1, ρ is the mass density, R is the ideal gas constant, T is the absolute temperature of the experiment, $\langle R^2 \rangle$ is the unperturbed mean-square end-to-end distance, and M is the molecular weight. Density also changes with temperature, however over a 50 °C range it changes less than 3% and has a minimal impact on the diffusion coefficient. It is clear that even the 2 °C change in the distance from T_g (from T_g+20 °C to T_g+22 °C) measured at 20 nm represents as 31% change in the diffusion coefficient, well outside the typical experimental uncertainty of ~10% in FRAPP measurements of the diffusion coefficient described in this chapter.

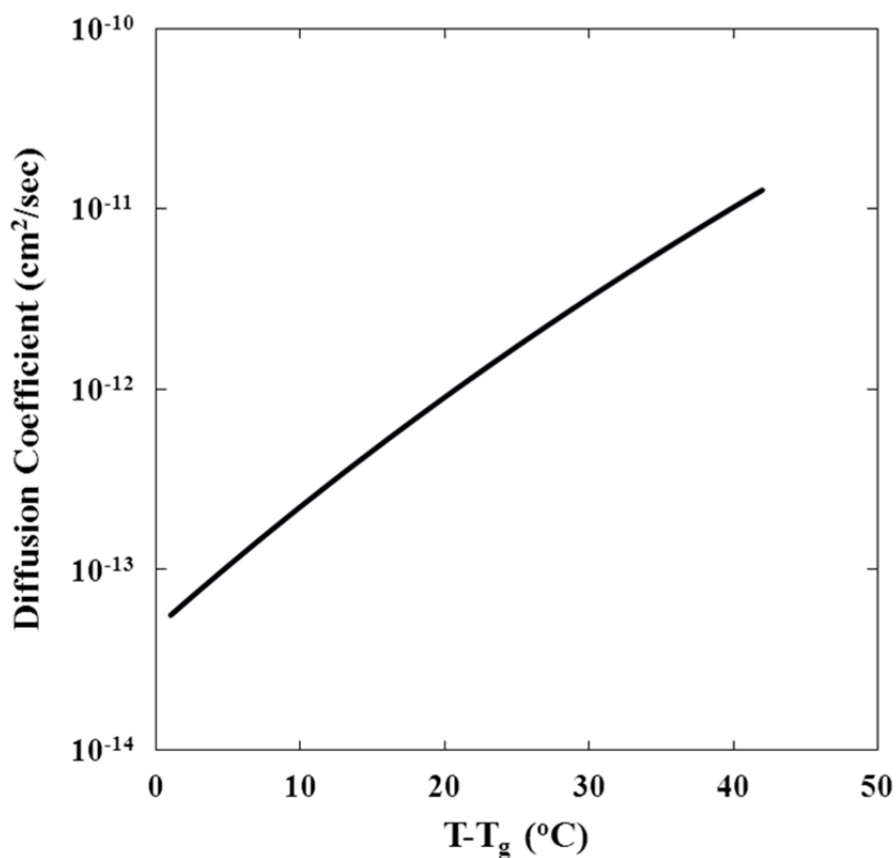


Figure 3.4: Diffusion coefficient of PiBMA as a function of T-T_g

Notably, the diffusion coefficient for a 19 nm thick film deviates from the bulk value exactly as predicted from the T_g depression at that film thickness (see dotted line in Figure 3.2). This indicates that changes in polymer diffusion in thin films might be accounted for systematically by correcting for T_g changes via the WLF equation. This is exactly the hypothesis that was put forth in a commentary⁵ attempting to explain the results of a previous study⁶ as discussed in Chapter 2.7.

In this study the ‘thermal’ T_g is measured and seems to quantitatively account for changes in diffusion coefficient with film thickness. The thermal’ T_g, is what is measured when some property of the polymer undergoes a change in its temperature dependence, like the coefficient of thermal expansion as measured by ellipsometry.⁷ This is different

from the ‘dynamic’ T_g which is based on some direct measure of segmental dynamics like those observed with dielectric spectroscopy. While these two types of T_g appear to be related, they may not necessarily behave in the same manner. In order to examine the difference between these two phenomena, one recent study looked at both the ‘thermal’ and ‘dynamic’ T_g s and found that only the ‘thermal’ T_g shows any change with nanoconfinement.³

Clearly, a significant amount of experiments remain to complete this study. First of all, a more complete set of data for the T_g of the bilayer films as a function of film thickness is needed. It would be helpful for the sake of ellipsometric model fitting to be able to use dynamic values for the optical constants of the PCHE layer as a function of temperature rather than simply the room temperature values. While it should not impact the location of the transition, it would help the fitting of the PiBMA layer which at the moment is rather noisy making the calculation of the T_g less accurate. Secondly, the issue of the viscosity measurement at lower temperatures needs to be resolved in order to be able to more accurately characterize the bulk diffusion coefficient at these temperatures. Additionally, in this study it would be interesting to look at the activation energy for diffusion over a wide range of temperatures and see if there is a deviation from WLF behavior near T_g . This could allow for comparison to the work by Evans and coworkers regarding the effects of nanoconfinement being most relevant nearest to T_g .²

3.5 EXPERIMENTAL

3.5.1 Materials

Chemicals used in this study were purchased from Fisher Scientific or Sigma-Aldrich. All purifications and polymerizations were performed under vacuum or in an argon atmosphere using standard Schlenk techniques.⁸ Custom glassware for anionic

polymerizations was purchased from ChemGlass or made at the University of Texas at Austin in the Chemistry glass shop. Molecular weight and polydispersity data were measured using a Viscotek GPCMax VE 2001 gel permeation chromatography (GPC) solvent/sample module with a Viscotek Model 270 dual detector viscometer/light scattering detector and Viscotek VE 3580 refractive index detector with 2 I-Series mixed bed low MW columns using tetrahydrofuran (THF) as an eluent at 1 mL/min. Molecular weights are calculated using a triple detector method. Fluorophore attachment was verified by an in-line Jasco FP-2020 Plus Intelligent Fluorescence Detector ($\lambda_{\text{excitation}} = 465 \text{ nm}$, $\lambda_{\text{emission}} = 520 \text{ nm}$, 18 nm bandpass). Nuclear magnetic resonance (NMR) spectra were recorded on a Varian 400 MHz DirectDrive NMR with SMS sample changer. The midpoint glass transition temperature (T_g) of the bulk polymer samples was measured by differential scanning calorimetry (DSC) using a Mettler-Toledo DSC-1 with a 10 °C/min heating rate upon second heating.

3.5.1.1 Purification of iBMA Monomer

The iBMA monomer was added to a 500 mL Schlenk flask and freeze-pump-thawed to remove dissolved oxygen. It was then trap-to-trap distilled to a second flame dried 500 mL Schlenk flask containing 1 g calcium hydride for every 10 g monomer and stirred for 1 hour. The monomer was trap-to-trap distilled into a second 500 mL Schlenk flask and taken inside the glove box where it was titrated while stirring with trioctylaluminum until a yellow color persisted. Finally, the monomer was distilled into a burette, freeze-pump-thawed three times and attached to the anionic polymerization reactor.

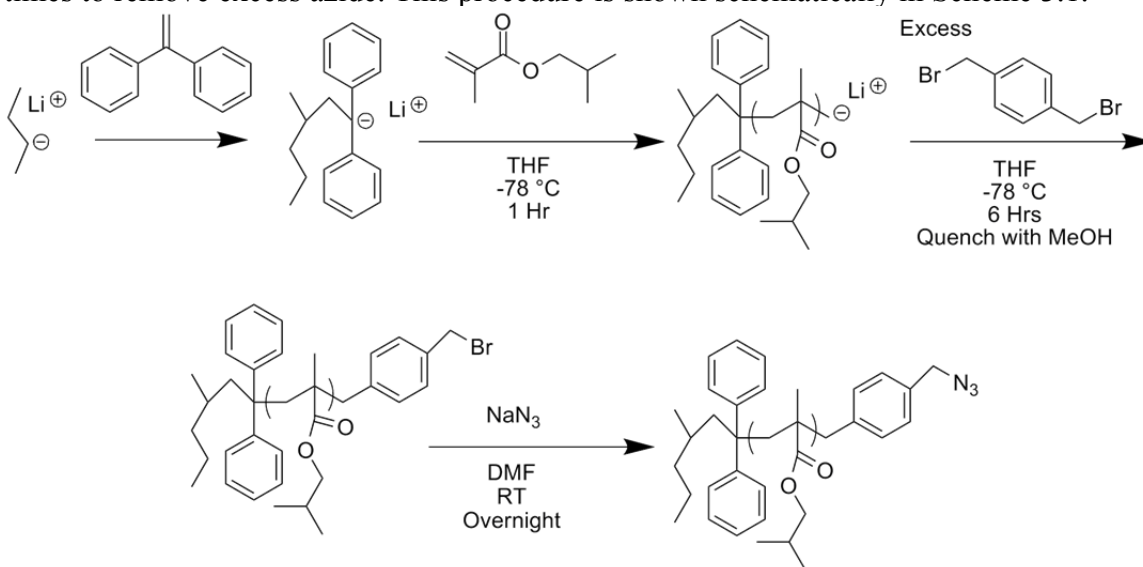
3.5.1.2 Purification of Tetrahydrofuran

Roughly 1 mL of n-butyllithium (2.5 M in hexanes) solution per 20 mL solvent was added to a 1 L Schlenk flask in the glove box. The solvent was removed from the n-butyl lithium solution *in vacuo* and then tetrahydrofuran (THF) was dispensed into this flask from a Pure Solv MD-2 solvent system containing two activated alumina columns to remove trace water and stirred for 1 hour. The THF was then trap-to-trap distilled into a second 1 L Schlenk flask and freeze-pump-thawed to remove any possible dissolved oxygen. Another 500 mL Schlenk flask was taken into the glove box where α,α' -dibromo-p-xylene (DBX, 97% purity) was added to the flask and a portion (~5-10%) of the THF was trap-to-trap distilled into this flask. The flask containing the majority of the THF was then attached to the anionic polymerization reactor.

3.5.1.3 Polymerization

All ratios for polymerization are reported relative to moles of sec-butyllithium initiator and the procedure is based on a similar method found in the literature.⁹ An anionic reactor with six molar excess dry lithium chloride salt and a stir bar was fitted with a manifold, airlock, THF flask, thermocouple well, and plug. It was flame dried five times with special attention paid to drying the very hydrophilic lithium chloride salt. The THF was added and cooled with a dry ice/isopropanol bath to -70 °C and sec-butyllithium (1.4 M in cyclohexane) was added via gas tight syringe. It is very important that the temperature be maintained at this level throughout the reaction or else deprotonation of the THF solvent can occur terminating the polymerization. After stirring for 15 minutes, 1.2 molar excess of purified diphenylethylene (twice distilled over n-butyllithium) was added via gas tight syringe turning the reactor bright red and stirred for one hour. At this point a few drops of the monomer were added via the airlock until the reaction mixture turns clear and stirred for 15 minutes, then the remainder of the

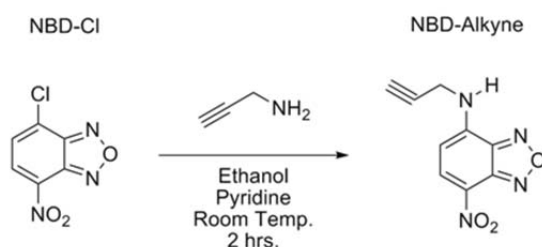
monomer was added while keeping an eye on the temperature to maintain it below -70 °C. After the monomer was completely added, the burette was removed from the airlock and the flask containing the dissolved DBX was added to the airlock (~ 10 molar excess). When the polymerization had proceeded for one hour, the DBX was introduced through the airlock and stirred for two hours upon which time methanol sparged with argon (~ 5 mL) was injected then 30 minutes later the reactor was vented. The polymer was precipitated three times out of a 50/50 vol% methanol/deionized water solution to remove unreacted DBX. The resulting polymer had a $M_n = 7,700$ g/mol and a PDI = 1.06. Only a portion of the resulting polymer was used for labeling. The azide-terminated PiBMA was prepared by dissolving the polymer in N,N-dimethylformamide (DMF) with a three molar excess of sodium azide and stirring at room temperature overnight. Caution, no metals, not even a metal spatula, should be used in the handling of azides and no halide containing solvents should be used. A separate clearly labeled waste container should be used for all azide containing liquids. The polymer was then precipitated in water three times to remove excess azide. This procedure is shown schematically in Scheme 3.1.



Scheme 3.1: Anionic polymerization of azide terminated PiBMA

3.5.1.4 Fluorophore Attachment

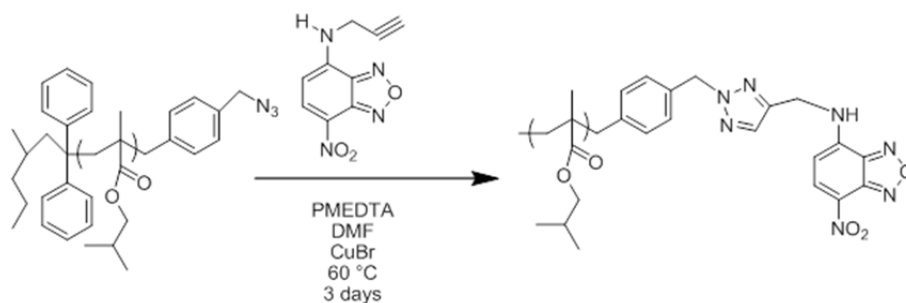
A nitrobenzofurazan (NBD) fluorophore was covalently attached to the PiBMA using established literature procedures for Cu^I-catalyzed azide/alkyne cycloaddition “click chemistry”.¹⁰⁻¹² The alkyne functionalized fluorophore was prepared by dissolving 4-chloro-7-nitro-2,1,3-benzoxadiazole (NBD-Cl) in ethanol in the presence of pyridine and adding propargylamine (3-amino-1-propyne) drop-wise and stirring for two hours at room temperature (Scheme 3.2).¹¹ The solvent was removed under vacuum and the resulting solid was give 7-nitro-N-(prop-2-ynyl)-2,1,3-benzoxadiazol-4-amine (NBD-Aminyne) in 54% yield, purity was verified by NMR.



Scheme 3.2: Synthesis of alkyne-bearing NBD fluorophore

To attach the NBD-Aminyne to the polymer, each were dissolved in DMF at ~5 wt% (dried with calcium hydride and alumina) and a copper solubilizing ligand (N,N,N',N'',N'''-Pentamethyldiethylenetriamine, PMEDTA, 1:1 ratio of copper to ligand) was added to the polymer solution, the ratio of fluorophore to polymer was 3:1. Cu(I)Br (1.5:1 ratio of copper to azide groups) was added to a third flask inside a glove box and sealed, then the two other solutions were added to this flask by cannula and the reaction was allowed to proceed for two days at 40 °C. The resulting polymer (PiBMA-NBD, Scheme 3.3) was precipitated in a 50/50 vol% acetonitrile and deionized water solution seven times to remove excess fluorophore as verified by absence of a small molecule

fluorescence peak in GPC. By UV/Vis, 10% of the polymer chains contain a covalently attached fluorophore by comparison with NBD-Aminyne in the same solvent, however this is still over the self-quenching threshold at 0.28 wt% NBD. In experience, click reactions involving methacrylate polymers have significantly lower degrees of attachment than styrenic polymers.



Scheme 3.3: Attachment of NBD-Aminyne to PiBMA-Az via click reaction

3.5.2 Methods

3.5.2.1 Film Preparation

Bi-layer films in this study were spin-coated (Specialty Coating Systems Spincoat G3-8) onto quartz (for FRAPP experiments) or silicon substrates with native oxide layers (for ellipsometry experiments). PCHE was spin coated from solutions in toluene and then annealed at 150 °C in air for 20 minutes when no further reduction in film thickness was observed by ellipsometry. PiBMA was spin coated from solutions in n-butanol and then annealed at 120 °C until no decrease in film thickness was observed by ellipsometry. Solution concentrations ranged from 0.5 to 6 wt % polymer in n-butanol, and spin speeds varied from 800 to 3000 rpm to control the film thickness.^{13,14} Silicon substrates were prepared by soaking in a piranha solution of 3:1 concentrated sulfuric acid to hydrogen peroxide and then rinsed with deionized water at least three times. A caution about

piranha solution, it should be stored separately with the cap vented to allow for evolved hydrogen gas to escape. The reaction of the two reagents that comprise piranha solution is very exothermic, so it should only be used in containers that can handle temperatures of up to 240 °C and all materials should be handled with acid resistant gloves. Quartz substrates were cleaned by soaking in a solution of 10:10:80 wt% potassium hydroxide: deionized water: ethanol solution and then rinsed with deionized water and tetrahydrofuran at least three times. The polymer in the spin-coating solution for FRAPP experiments was comprised of fluorescently labeled polymer and a molecular weight matched unlabeled polymer to mitigate fluorescence self-quenching effects (fluorophore content < 0.18 wt%, see Section 2.3). Films prepared on silicon substrates were characterized by ellipsometry using a J.A. Woollam M-2000D spectroscopic ellipsometer.

3.5.2.2 Determination of Thin Film T_g

The T_g of thin films was characterized using an established spectroscopic ellipsometry procedure.^{15,16} The film is heated to 120 °C, which is well above the bulk T_g (58 °C) and the boiling point of the spin-coating solvent (118 °C for n-butanol, the highest boiling solvent used), and annealed for 10 min. Next, the film is cooled at 2 °C/min with an Instec mK 1000 temperature controller with a HCS 402 hot stage connected to a liquid nitrogen pump. The film thickness was plotted against sample temperature to identify T_g based on a layered model in which the only fitted parameters were the optical constants and thickness of the PiBMA film (WVase software, J.A. Woollam Co.).

3.5.2.3 FRAPP

For the patterned FRAPP experiments, photobleaching was performed using a Ronchi ruling (Edmund Optics) (chrome lines deposited on a quartz substrate with 12.5 μm lines on a 25 μm pitch) as a mask for creating a periodic array of bleached and unbleached regions. The sample was photobleached using an Optical Building Blocks ScopeLite 200 (a broadband intense light source). Film bleaching is expected to be uniform through the film because the absorbance is 0.01 absorbance units per 100 nm of film thickness at a wavelength of 465 nm, as measured by UV/vis spectroscopy. This indicates that even for the thickest films used in this study (~ 280 nm), the bleaching light is attenuated a negligible amount ($\sim 5\%$) as it passes through the film; therefore, the photobleaching reaction takes place equally throughout the depth of the film. The film was then heated to the desired temperature using a Linkham TMS91 hot stage and allowed to equilibrate for 1 h before starting to monitor the fluorescence recovery. Imaging was performed with a Hamamatsu Orca R2 camera with μ Manager software for camera control¹⁷ on an Olympus BX 51 epifluorescence microscope coupled to a Photon Technologies QuantaMaster 40 fluorimeter. The excitation wavelength used was 445 nm with an 8 nm bandpass and an emission filter selected for all wavelengths greater than 520 nm. The depth of focus of the microscope is 2.9 μm , which is an order of magnitude larger than the thickest films used in this study; therefore, fluorescence from the whole depth of the film is captured in each image. Images were taken at intervals of 1 h with a typical exposure time of 4 seconds and an automatic shutter employed to limit photobleaching during the course of the experiment. A detailed discussion of the experimental procedure and data analysis can be found, as previously mentioned, in Appendix A.

3.6 REFERENCES

1. Priestley, R.; Mundra, M. K.; Barnett, N. J.; Broadbelt, L. J.; Torkelson, J. M. *Aust. J. Chem.* **2007**, *60*, 765-771.
2. Evans, C. M.; Narayanan, S.; Jiang, Z.; Torkelson, J. M. *Physical Review Letters* **2012**, *109*, 038302.
3. Boucher, V. M.; Cangialosi, D.; Yin, H.; Schonhals, A.; Alegria, A.; Colmenero, J. *Soft Matter* **2012**, *8*, 5119-5122.
4. Gehlsen, M. D.; Bates, F. S. *Macromolecules* **1993**, *26*, 4122-4127.
5. Russell, T. P.; Kumar, S. K. *Nature* **1997**, *386*, 771-772.
6. Frank, B.; Gast, A. P.; Russell, T. P.; Brown, H. R.; Hawker, C. *Macromolecules* **1996**, *29*, 6531-6534.
7. Donth, E. *The Glass Transition: Relaxation Dynamics in Liquids and Disordered Materials*; Springer: Heidelberg, Germany, 2001.
8. Ndoni, S.; Papadakis, C. M.; Bates, F. S.; Almdal, K. *Review of Scientific Instruments* **1995**, *66*, 1090-1095.
9. Ho, C.-C.; Dai, C.-A.; Su, W.-F. *Journal of Applied Polymer Science* **2009**, *111*, 1571-1580.
10. Binder, W. H.; Sachsenhofer, R. *Macromolecular Rapid Communications* **2007**, *28*, 15-54.
11. McGill, N. W.; Williams, S. J. *J. Org. Chem.* **2009**, *74*, 9388-9398.
12. Rostovtsev, V. V.; Green, L. G.; Fokin, V. V.; Sharpless, K. B. *Angewandte Chemie International Edition* **2002**, *41*, 2596-2599.
13. Hall, D. B.; Underhill, P.; Torkelson, J. M. *Polym. Eng. Sci.* **1998**, *38*, 2039-2045.
14. Spangler, L. L.; Torkelson, J. M.; Royal, J. S. *Polym. Eng. Sci.* **1990**, *30*, 644-653.
15. Beaucage, G.; Composto, R.; Stein, R. S. *J. Polym. Sci. Pt. B-Polym. Phys.* **1993**, *31*, 319-326.
16. Keddie, J. L.; Jones, R. A. L.; Cory, R. A. *Faraday Discuss.* **1994**, *98*, 219-230.

17. Edelstein, A.; Amodaj, N.; Hoover, K.; Vale, R.; Stuurman, N. *Computer Control of Microscopes Using μ Manager*; John Wiley & Sons, Inc., 2001.

MARANGONI EFFECT DRIVEN TOPOGRAPHIC PATTERNING IN THIN POLYMER FILMS

Chapter 4: Directing Convection to Pattern Thin Polymer Films *

4.1 INTRODUCTION

Significant research efforts in the last several decades have been invested in the development of methods to fabricate micro- and nano-scale features in polymer films because of their importance in a variety of applications.^{1,2} The most obvious example of this is photolithography,³ a critical processing step in the \$300 billion microelectronics industry.⁴ In order to fabricate semi-conductors rapid fabrication of very high resolution and very low defect patterns is required. Most manufacturers invest a significant portion of their resources, both in physical footprint and capital, to these ends. However, there is significant need for other micron and submicron patterning methodologies for applications not related to microelectronics. This is especially true in a laboratory setting or in an industrial setting where there isn't access to clean-room infrastructure, which can be very costly. One example alternative is soft lithography, which uses elastomeric stamps with topographic structures to print and/or mold complementary patterns.^{5,6} This can be of specific use in processing biological materials⁷⁻⁹ in ways that could not be easily achieved via photolithography.

Another alternative method for creating micro- or nano-scale topographic patterns in polymer thin films is by directing instabilities generated at interfaces and their resultant convective flow. At first glance, it would seem that convection is typically experienced in everyday life as a stochastic phenomenon that would render it difficult to

* This chapter reproduced in part from "Directing Convection to Pattern Thin Polymer Films" Janes, D. W.; Katzenstein, J. M.; Shanmuganathan, K.; Ellison, C. J. *Journal of Polymer Science Part B: Polymer Physics* **2013**, *51*, 535-545 with permission from John Wiley and Sons, copyright 2013.

direct and reproducibly form patterns. However, over the last 15 years or so a variety of studies have shown that it can be done.¹⁰

In this chapter several techniques to direct convective flow will be discussed. These include “coffee ring patterning” (arguably the most well-known technique),¹¹ lithographically induced self-assembly (LISA),¹² and electrohydrodynamic patterning (EHP)¹³ in polymer thin films. This chapter will focus on the methodology and patterns formed, however detailed reviews of the physics of fluid flow in thin films are available elsewhere.^{14,15}

4.2 PATTERNING USING EVAPORATIVE SELF-ORGANIZATION

Upon evaporation of the solvent of a dilute suspension of non-volatile particles, such as coffee particles in water, a ring-like pattern forms because the edge of the drying droplet gets ‘pinned’ to the substrate. Evaporation from the edge gets replenished from solvent that was in the middle to maintain the fixed contact line. The outward flow driven by evaporation drags suspended particles to the edge of the drop leaving dense ring-like structures. This phenomenological understanding of the commonly observed “coffee ring” stains¹⁶ has inspired research into a variety of methods for controlled deposition of polymers, biomolecules, microspheres, nanoparticles, etc.^{17,18} These techniques provide a relatively simple route to creating complex ordered structures on the micron and submicron length scales. Recent reviews^{11,19} describe how this process can be tuned using particle size and shape,²⁰ thermal Marangoni flows,²¹ composition-driven Marangoni flows,²² patterned substrates,²³ and other techniques. In this section are a few examples of this technique specifically focused on polymers in confined geometries or demixing of homopolymer blends.

As described, convective motion inside of an evaporating liquid drop containing non-volatile particles results in periodic deposition of those particles. By controlling the dynamics of the drying process, the resulting pattern can be manipulated.¹¹ In one study, a solution of polystyrene (PS) in chloroform was placed between sliding glass plates with fixed relative velocities to produce different controlled patterns (see Figure 4.1).²⁴ A diverse set of patterns were formed, including dots, stripes, and ladders simply by changing polymer concentration.

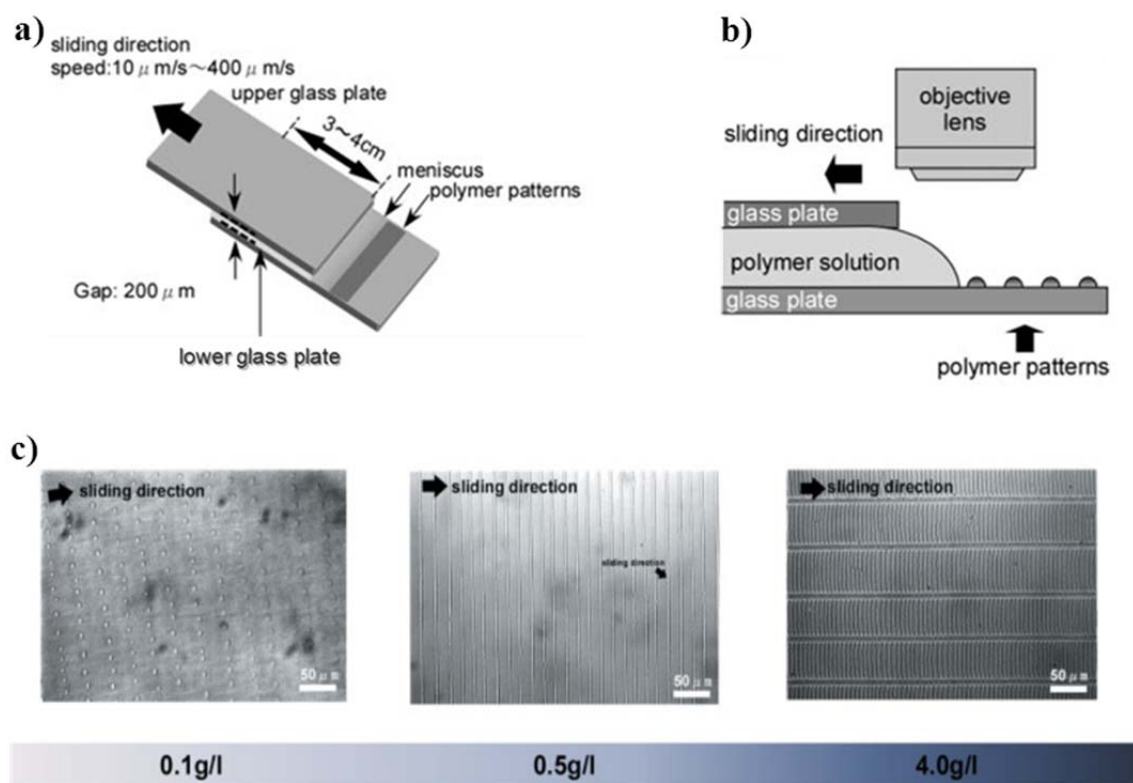


Figure 4.1: a) Top view and b) side view schematic illustrations of the parallel-plate geometry in which the upper plate slides over the lower stationary plate at a fixed speed with a polymer solution confined between the plates. c) Optical micrographs of patterns produced from different PS in chloroform solution concentrations at a constant sliding speed of $50 \mu\text{m/s}$. Reproduced from ref. ²⁴ with permission from John Wiley and Sons, © 2005.

Complementing evaporative self-organization with lithography increases the possibilities for patterning in colloidal thin films. For example, Harris et al.²⁵ used a mask with hexagonally packed circular openings above a droplet containing silica microspheres and PS nanoparticles. In this way, evaporation proceeded more rapidly in the open regions than the protected regions. This patterning of evaporation rates, and the resulting convective flow, was used to direct particle deposition on the substrate.

In addition to simple evaporation, phase separation of immiscible polymers and its sensitive dependence on confining interfaces can also be exploited to create patterns in thin films.²⁶⁻²⁹ If two immiscible polymers are co-cast from a common solvent, the evaporation can destabilize the solution and phase separation occurs. As evaporation proceeds and the films vitrify the morphology of the resulting film is dependent on the original casting conditions. In one study, Cui and Han²⁷ cast PS and poly(2-vinyl pyridine) (PVP) from a solution of ethylbenzene, a good solvent for both, and then dried the film in a chamber with controlled airflow. Under some conditions, an ordered honeycomb pattern of microwells were formed. An example atomic force microscopy (AFM) image is shown in Figure 4.2a that has hexagonally-packed, 2.5 μm diameter wells that are 480 nm deep. To explain this feature formation, the authors estimated that large temperature gradients across the depth of the film ($\Delta T = 26$ °C) due to evaporative cooling causes the critical dimensionless number for Bénard-Marangoni instabilities³⁰ to exceed its critical threshold value. Schematically, this process is shown in Figure 4.2b.

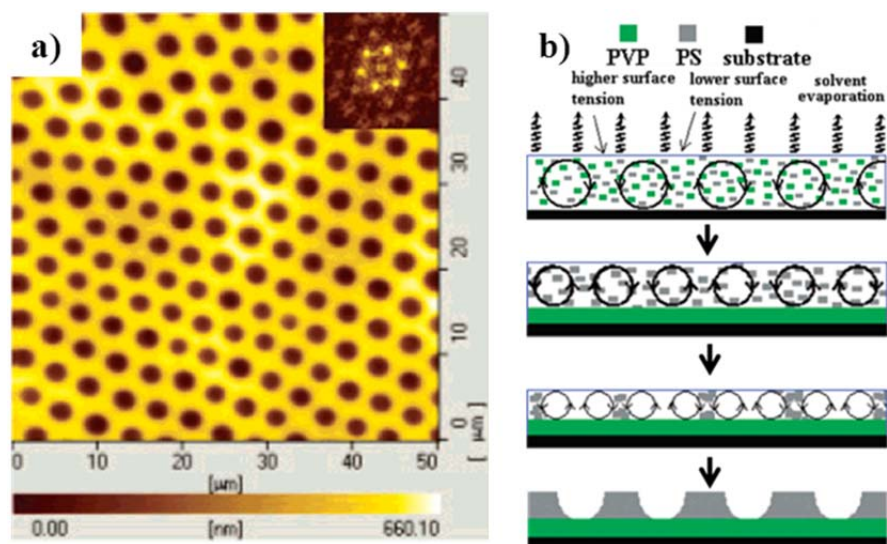


Figure 4.2: a) AFM topographical image of the honeycomb patterns resulting from co-casting PS ($M_w = 220$ kDa) and PVP ($M_w = 11$ kDa) from ethylbenzene solution (4 wt.% polymer, 4:1 weight ratio of PS to PVP) onto a mica substrate with an applied $1 \text{ L}\cdot\text{min}^{-1}$ airflow. The inset is a fast-Fourier transform of the AFM image. b) Schematic of the drying process the authors proposed to explain the phenomenological results. Adapted with permission from “Honeycomb pattern formation via polystyrene/poly(2-vinylpyridine) phase separation” Cui, L.; Han, Y. C. *Langmuir* **2005**, 21, 11085-11091. Copyright 2005, American Chemical Society.

4.3 PATTERNING BY TEMPERATURE-INDUCED INSTABILITIES

Another approach to create topographic features in polymer thin films was first demonstrated by Chou and coworkers.^{12,31-34} In these experiments, instabilities were generated in supported polymer films in the melt state by holding another plate (a mask) near its surface. They named this process lithographically induced self-assembly (LISA) that is shown schematically in Figure 4.3a.¹² In the first studies of this approach the polymer film thickness and the distance between it and the mask were both less than one micron. Upon heating the film to a liquid state, above its glass transition temperature (T_g) instabilities generated at the surface of the polymer film cause the polymer to flow

upwards towards the mask. After long enough time, an array of hexagonally-packed pillars formed from the substrate to the mask above. A representative AFM height image of these pillars, taken after mask removal, is shown in Figure 4.3b.

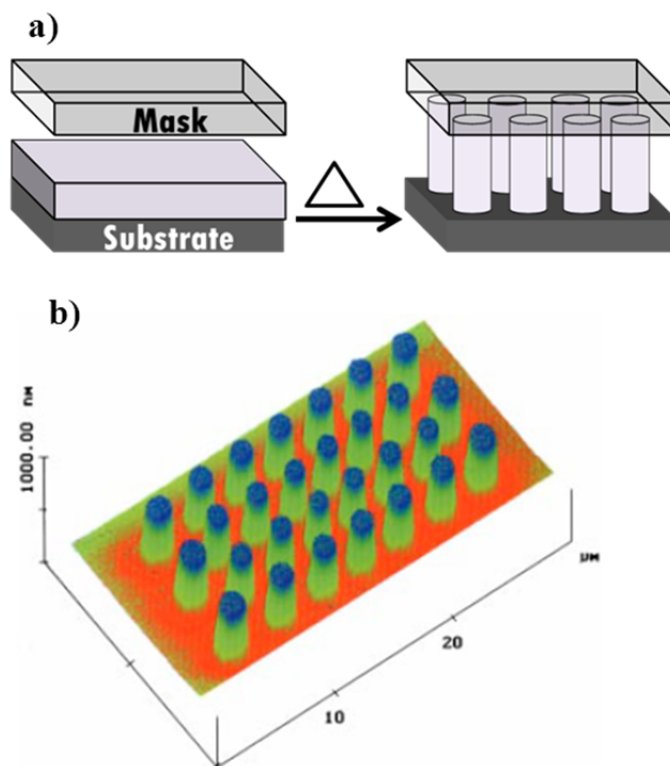


Figure 4.3: a) A schematic representation of lithographically induced self-assembly (LISA) as demonstrated by Chou and Zhuang.¹² A 95 nm thick supported film of poly(methyl methacrylate) (PMMA, $M_w = 2$ kDa) is brought in close contact with a mask. After heating the film to 130 °C, the polymer flows into pillars that span the mask/substrate gap, which are subsequently preserved by cooling below T_g . b) shows an example AFM image of pillars which formed against a mask with a protruding rectangle. The pillars are 440 nm tall and 2 μm in diameter. Reprinted with permission from “Lithographically induced self-assembly of periodic polymer micropillar arrays” Chou, S. Y.; Zhuang, L. *J. Vac. Sci. Technol. B* **1999**, 17, 3197-3202. Copyright 1999, American Vacuum Society.

Additionally, the use of a relief pattern on the LISA mask can help to direct the placement and registration of the pillars. In this way pillars were formed with a maximum

height-to-diameter aspect ratio of 0.5, with a 1.6 μm diameter. One notable feature of this process is that the surface area of the resulting topographic structure is higher than the initial film. This suggests that the forces involved in creating topography are strong enough to overcome the surface tension of the film. In other experiments, the surface energy of the mask was tuned in order to cause the polymer to coat the entire bottom of the mask protrusions, rather than forming cylindrical pillars. The resulting topography in this case is a positive replica of the entire mask pattern.³¹

Other research groups have also performed experiments similar to LISA,³⁵⁻³⁹ however the underlying physical mechanism for these phenomena are still an open question. The origin of pillar formation was not originally attributed to thermal convection (buoyancy-driven, Rayleigh-Bénard instabilities⁴⁰) or thermo-capillary convection (surface tension-driven, Bénard-Marangoni instabilities³⁰) due to lack of *intentionally* applied thermal gradients. Furthermore, the dimensionless values commonly used to characterize these effects were below critical thresholds typically associated with instability formation.¹² However, a study of convection in photocrosslinkable poly(dimethylsiloxane) in 100-300 μm thick films with intentionally applied temperature gradients was performed by Kumacheva and coworkers and in these experiments the critical thresholds for instabilities are exceeded.^{41,42}

Chou and Zhuang originally hypothesized that local fluctuations in charge density on the surfaces of the mask and film were in close enough proximity to influence each other.¹² If this is the case, then electrostatic forces drive the polymer from the film to the mask in areas of complementary image charge. Later theoretical studies from Pease and Russel demonstrated that a charge density of only $\sim 1 \text{ mC/m}^2$ is sufficient for this to be the mechanism of pillar formation.⁴³

Steiner and coworkers also performed experiments similar to LISA in which the mask was slightly cooler than the liquid polymer film.^{38,39,44} In addition to pillars, as previously demonstrated, other structures including stripes or spirals were also generated with a featureless mask. Through these studies, they were able to develop an expression to relate the spacing of the structures to experimental parameters and material properties, such as the acoustic quality factor of the substrate.^{38,45} Physically, they postulated that coherent reflections of thermal radiation exert pressure at the polymer/air interface. Other more recent work from Troian and coworkers re-evaluated this theory and developed an alternative hypothesis based on thermo-capillary convection overcoming surface tension. These results agreed well with both previously collected⁴⁶ and new³⁵ experimental data.

4.4 ELECTROHYDRODYNAMIC PATTERNING

Electric fields can also be used to destabilize liquid polymer thin films in order to form topographic structures. This process, first demonstrated by Schäffer et al.,¹³ is called electrohydrodynamic patterning (EHP). However, this was not the first time that electrostatic fields had been applied to polymer thin films. Previous research had shown that electric fields could be used to orient block copolymer domains⁴⁷⁻⁵⁰ and phase separated polymer blend structures^{51,52} in thin films. Furthermore, electrostatic charges, though not generated via externally applied fields, had been postulated as the cause of topographic feature formation in LISA.¹²

Schematically, EHP is very similar to LISA (see Figure 4.4a) but an electric field is applied between the mask and the film substrate. Like LISA, when the polymer film is heated to a liquid state, the polymer flows towards the mask and the features can be locked in by quenching the polymer below its T_g . As in the case of the controlled surface energy experiments in LISA, the flow is directed towards protrusions on the mask

creating positive replicas of the relief structures. An example of this is the AFM image shown in Figure 4.4b.

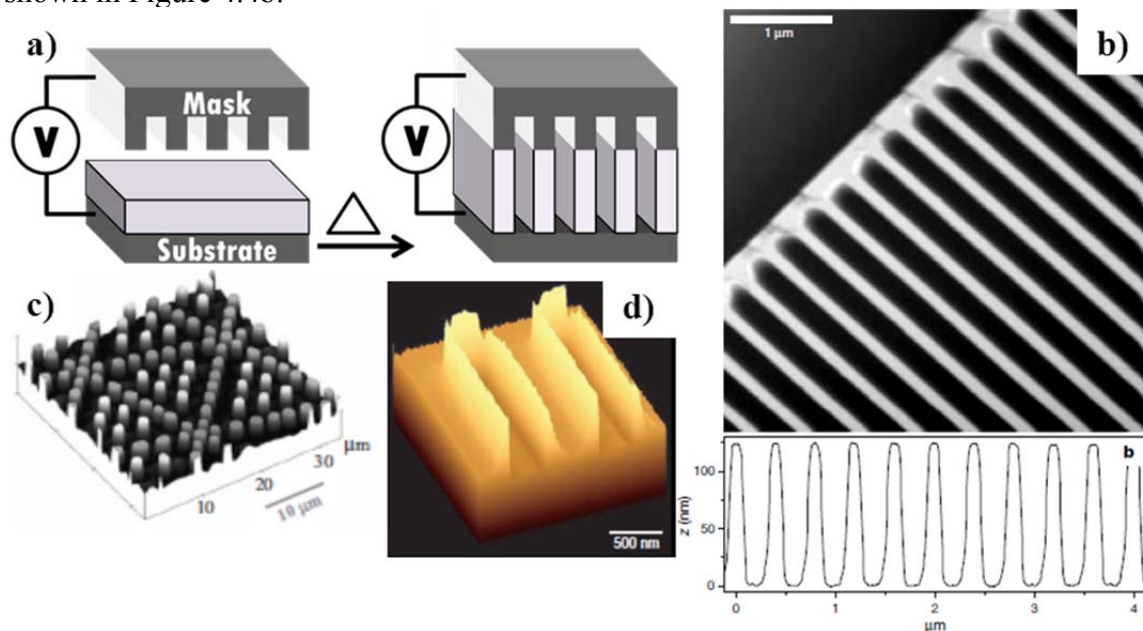


Figure 4.4: a) A schematic representation of electrohydrodynamic patterning (EHP) as demonstrated by Schäffer et al.¹³. A 45 nm thick film of brominated PS is placed 80 nm from a mask patterned by lines that had a width of 200 nm and a height of 170 nm. A voltage of 42 V was applied. After heating the film to 170 °C for 14h, the polymer flows toward the mask protrusions, which are subsequently preserved by cooling below T_g . b) An example top down AFM image and height profile of the 140 nm wide lines that resulted. Reprinted by permission from Macmillan Publishers Ltd: *Nature* (ref. ¹³), copyright 2000. c) An example AFM image of an EHP pattern formed by employing a mask with a protruding triangular grid that directed the pillar size and placement. Reproduced from ref. ⁵³ with permission from John Wiley and Sons © 2006. d) An example SEM micrograph of PMMA structures that resulted after EHP patterning of a PS/PMMA bilayer film and selective rinsing of PS. Reprinted by permission from Macmillan Publishers Ltd: *Nature Materials* (ref. ⁵⁴), copyright 2002.

Using EHP Schäffer et al.¹³ were able to form features 140 nm wide and 125 nm tall, or an aspect ratio of 0.83. Since high aspect ratio features are desirable for many patterning applications, this spurred many other studies leveraging this technique,⁵⁵⁻⁵⁸

summarized in a review article by Wu and Russel.⁵⁹ For example, Wu et al.⁵³ used masks with regular topographic structures to create hierarchical arrays of pillars and lines (see Figure 4.4c). Additionally, using EHP in conjunction with polymer bilayers can form more complex or smaller structures than those formed using a single polymer film.⁶⁰⁻⁶³ Additionally, Morariu et al. fabricated lines 100 nm wide and 160 nm tall (Figure 4.4d) by selectively dissolving away one of the polymers after topography had been formed by EHP.⁵⁴ In this study the mask had 1 μm wide lines, so the bilayer technique led to an order of magnitude increase in patterning resolution. EHP has also been used with polymers, such as block copolymers⁵⁸ and crystalline polymers⁵⁵ to direct their intrinsic nano-scale structures. Finally, EHP is not fundamentally limited to polymers, Dickey et al. used photopolymerizable liquids so that the room-temperature pillar formation process occurred in < 1 s, the fastest reported.^{64,65}

EHP has been described theoretically in several studies^{62,63,66-70} and while the details of these models vary, the force acting against the surface tension of the film is always electrostatic attraction from the imposed electric field. Qualitatively, EHP and LISA create very similar structures and if the original theory of Chou and Zhuang¹² is correct as to the cause of LISA, the two methodologies are identical except that EHP employs a stronger driving force.^{43,59} Most EHP experiments to date have used direct current to generate electric fields, but some recent theoretical studies have also looked at the possibility of using alternating current or complementing direct current with alternating current.^{71,72}

Creation of well-ordered arrays of small (submicron) pillars using a featureless mask via EHP is one of the challenges remaining for this technique. One of the issues is that while higher electric field strengths should decrease features size,¹³ Lau and Russel showed that this is limited by the dielectric breakdown of the material.⁷³ They point out

in this study that careful selection of the materials can improve the results. For example, by filling the gap between the mask and polymer with an ionic liquid, which does not break down dielectrically like air, they were able to create submicron pillars. However, these pillars were poorly ordered and had substantial diameter variation. This is similar to the study by Deshpande and Chou,³² where the gap between the polymer film and the mask was filled with oil and LISA was performed. In this study, they believed the wetting characteristics of the polymer on the mask was the cause of the pillar irregularity.

4.5 CONCLUSIONS

Convective flow is often an easy yet powerful way to create topographic features in polymer films. Previous techniques developed for this purpose leverage evaporation or gradients in temperature or electric field. In the next chapter a new technique will be described that uses convection caused by compositionally induced gradients in surface energy towards a similar end. Due to the phenomenological complexity, transport models can be useful for material selection in order to obtain the desired feature size, spacing, and registration with directing templates.

These patterning techniques could potentially be used in a variety of applications such as structural color,⁷⁴ superhydrophobic surfaces,⁷⁵ microfluidics,³² biological microarrays,⁷⁶ and photonic waveguides.⁷⁷ There are still many unexplored aspects of these and other alternative patterning processes that could be used for, or allow, an application yet unidentified. One good example of how this has happened in the past is development of soft lithography. Advances in this technique enabled lab-on-a-chip technologies through rapid prototyping and fabrication of microfluidic devices for processing of biological materials.^{7,8}

4.6 REFERENCES

1. Nie, Z.; Kumacheva, E. *Nature Materials* **2008**, *7*, 277-290.
2. del Campo, A.; Arzt, E. *Generating Micro- and Nanopatterns on Polymeric Materials*; 2 ed.; Wiley-VCH: Weinheim, 2011.
3. Bruning, J. H. *Proc. SPIE* **2007**, *6520*, 652004.
4. Thompson, S. E.; Parthasarathy, S. *Mater. Today* **2006**, *9*, 20-25.
5. Rogers, J. A.; Nuzzo, R. G. *Mater. Today* **2005**, *8*, 50-56.
6. Xia, Y.; Whitesides, G. M. *Annu. Rev. Mater. Sci.* **1998**, *28*, 153-184.
7. Kim, P.; Kwon, K. W.; Park, M. C.; Lee, S. H.; Kim, S. M.; Suh, K. Y. *BioChip J.* **2008**, *2*, 1-11.
8. Whitesides, G. M.; Ostuni, E.; Takayama, S.; Jiang, X.; Ingber, D. E. *Annu. Rev. Biomed. Eng.* **2001**, *3*, 335-373.
9. Bernard, A.; Renault, J. P.; Michel, B.; Bosshard, H. R.; Delamarche, E. *Adv. Mater.* **2000**, *12*, 1067-1070.
10. Steiner, U. In *Nanoscale Assembly Chemical Techniques*; Huck, W. T. S., Ed.; Springer Science+Business Media, Inc.: New York, 2005, p 1-24.
11. Han, W.; Lin, Z. Q. *Angew. Chem.-Int. Edit.* **2012**, *51*, 1534-1546.
12. Chou, S. Y.; Zhuang, L. *J. Vac. Sci. Technol. B* **1999**, *17*, 3197-3202.
13. Schäffer, E.; Thurn-Albrecht, T.; Russell, T. P.; Steiner, U. *Nature* **2000**, *403*, 874-877.
14. Oron, A.; Davis, S. H.; Bankoff, S. G. *Rev. Mod. Phys.* **1997**, *69*, 931-980.
15. Craster, R. V.; Matar, O. K. *Rev. Mod. Phys.* **2009**, *81*, 1131-1198.
16. Deegan, R. D.; Bakajin, O.; Dupont, T. F.; Huber, G.; Nagel, S. R.; Witten, T. A. *Nature* **1997**, *389*, 827-829.
17. Choi, S.; Stassi, S.; Pisano, A. P.; Zohdi, T. I. *Langmuir* **2010**, *26*, 11690-11698.

18. Zeng, H. B.; Kristiansen, K.; Wang, P.; Bergli, J.; Israelachvili, J. *Langmuir* **2011**, *27*, 7163-7167.
19. Larson, R. G. *Angew. Chem.-Int. Edit.* **2012**, *51*, 2546-2548.
20. Yunker, P. J.; Still, T.; Lohr, M. A.; Yodh, A. G. *Nature* **2011**, *476*, 308-311.
21. Hu, H.; Larson, R. G. *J. Phys. Chem. B* **2006**, *110*, 7090-7094.
22. Truskett, V.; Stebe, K. J. *Langmuir* **2003**, *19*, 8271-8279.
23. Vakarelski, I. U.; Chan, D. Y. C.; Nonoguchi, T.; Shinto, H.; Higashitani, K. *Phys. Rev. Lett.* **2009**, *102*.
24. Yabu, H.; Shimomura, M. *Adv. Funct. Mater.* **2005**, *15*, 575-581.
25. Harris, D. J.; Hu, H.; Conrad, J. C.; Lewis, J. A. *Phys. Rev. Lett.* **2007**, *98*.
26. Xue, L. J.; Zhang, J. L.; Han, Y. C. *Prog. Poly. Sci.* **2012**, *37*, 564-594.
27. Cui, L.; Han, Y. C. *Langmuir* **2005**, *21*, 11085-11091.
28. Cui, L.; Li, B. Y.; Han, Y. C. *Langmuir* **2007**, *23*, 3349-3354.
29. Mitov, Z.; Kumacheva, E. *Phys. Rev. Lett.* **1998**, *81*, 3427-3430.
30. Bénard, H. *Rev. Gén. Sciences Pure Appl.* **1900**, *11*, 1261 - 1271.
31. Chou, S. Y.; Zhuang, L.; Guo, L. *Appl. Phys. Lett.* **1999**, *75*, 1004-1006.
32. Deshpande, P.; Chou, S. Y. *J. Vac. Sci. Technol. B* **2001**, *19*, 2741-2744.
33. Chen, L.; Zhuang, L.; Deshpande, P.; Chou, S. *Langmuir* **2005**, *21*, 818-821.
34. Deshpande, P.; Sun, X.; Chou, S. Y. *Appl. Phys. Lett.* **2001**, *79*, 1688-1690.
35. McLeod, E.; Liu, Y.; Troian, S. M. *Phys. Rev. Lett.* **2011**, *106*, 175501.
36. Peng, J.; Wang, H.; Li, B.; Han, Y. *Polymer* **2004**, *45*, 8013-8017.
37. Masclaux, C.; Gourgon, C.; Perret, C.; Labau, S. *Microelectron. Eng.* **2011**, *88*, 2048-2051.

38. Schäffer, E.; Harkema, S.; Roerdink, M.; Blossey, R.; Steiner, U. *Macromolecules* **2003**, *36*, 1645-1655.
39. Schäffer, E.; Harkema, S.; Roerdink, M.; Blossey, R.; Steiner, U. *Adv. Mater.* **2003**, *15*, 514-517.
40. Rayleigh, R. *Phil. Mag. Ser. 6* **1916**, *32*, 529-546.
41. Li, M.; Xu, S.; Kumacheva, E. *Macromolecules* **2000**, *33*, 4972-4978.
42. Xu, S.; Li, M.; Mitov, Z.; Kumacheva, E. *Progr. Org. Coatings* **2003**, *48*, 227-235.
43. Pease, L. F.; Russel, I. W. B. *The Journal of Chemical Physics* **2006**, *125*, 184716.
44. Nedelcu, M.; Morariu, M. D.; Harkema, S.; Voicu, N. E.; Steiner, U. *Soft Matter* **2005**, *1*, 62-65.
45. Schäffer, E.; Harkema, S.; Blossey, R.; Steiner, U. *Europhys. Lett.* **2002**, *60*, 255.
46. Dietzel, M.; Troian, S. M. *J. Appl. Phys.* **2010**, *108*, 074308.
47. Amundson, K.; Helfand, E.; Davis, D. D.; Quan, X.; Patel, S. S.; Smith, S. D. *Macromolecules* **1991**, *24*, 6546-6548.
48. Amundson, K.; Helfand, E.; Quan, X.; Smith, S. D. *Macromolecules* **1993**, *26*, 2698-2703.
49. Amundson, K.; Helfand, E.; Quan, X. N.; Hudson, S. D.; Smith, S. D. *Macromolecules* **1994**, *27*, 6559-6570.
50. Morkved, T. L.; Lu, M.; Urbas, A. M.; Ehrichs, E. E.; Jaeger, H. M.; Mansky, P.; Russell, T. P. *Science* **1996**, *273*, 931-933.
51. Venugopal, G.; Krause, S.; Wnek, G. E. *J. Polym. Sci., Part C: Polym. Lett.* **1989**, *27*, 497-501.
52. Venugopal, G.; Krause, S.; Wnek, G. E. *Chem. Mater.* **1992**, *4*, 1334-1343.
53. Wu, N.; Pease, L. F.; Russel, W. B. *Adv. Funct. Mater.* **2006**, *16*, 1992-1999.

54. Morariu, M. D.; Voicu, N. E.; Schaffer, E.; Lin, Z.; Russell, T. P.; Steiner, U. *Nature Materials* **2003**, *2*, 48-52.
55. Goldberg-Oppenheimer, P.; Kohn, P.; Langford, R. M.; Steiner, U. *Small* **2012**, *8*, 2595-2601.
56. Goldberg-Oppenheimer, P.; Steiner, U. *Small* **2010**, *6*, 1248-1254.
57. Voicu, N. E.; Harkema, S.; Steiner, U. *Adv. Funct. Mater.* **2006**, *16*, 926-934.
58. Voicu, N. E.; Ludwigs, S.; Steiner, U. *Adv. Mater.* **2008**, *20*, 3022-3027.
59. Wu, N.; Russel, W. B. *Nano Today* **2009**, *4*, 180-192.
60. Leach, K. A.; Gupta, S.; Dickey, M. D.; Willson, C. G.; Russell, T. P. *Chaos* **2005**, *15*, 047506.
61. Reddy, P. D. S.; Bandyopadhyay, D.; Sharma, A. *J. Phys. Chem. C* **2012**, *116*, 22847-22858.
62. Roberts, S. A.; Kumar, S. *Phys. Fluids* **2010**, *22*, 122102.
63. Amarandei, G.; Beltrame, P.; Clancy, I.; O'Dwyer, C.; Arshak, A.; Steiner, U.; Corcoran, D.; Thiele, U. *Soft Matter* **2012**, *8*, 6333-6349.
64. Dickey, M. D.; Collister, E.; Raines, A.; Tsiartas, P.; Holcombe, T.; Sreenivasan, S. V.; Bonnecaze, R. T.; Willson, C. G. *Chem. Mater.* **2006**, *18*, 2043-2049.
65. Dickey, M.; Raines, A.; Collister, E.; Bonnecaze, R.; Sreenivasan, S. V.; Willson, C. G. *J. Mater. Sci.* **2008**, *43*, 117-122.
66. Wu, N.; Pease, L. F.; Russel, W. B. *Langmuir* **2005**, *21*, 12290-12302.
67. Pease, L. F.; Russel, W. B. *J. Non-Newtonian Fluid Mech.* **2002**, *102*, 233-250.
68. Verma, R.; Sharma, A.; Kargupta, K.; Bhaumik, J. *Langmuir* **2005**, *21*, 3710-3721.
69. Gambhire, P.; Thaokar, R. M. *Phys. Rev. E* **2012**, *86*, 036301.
70. Deshpande, P.; Pease, L. F., III; Chen, L.; Chou, S. Y.; Russel, W. B. *Phys. Rev. E* **2004**, *70*, 041601.

71. Roberts, S. A.; Kumar, S. *J. Fluid Mech.* **2009**, *631*, 255-279.
72. Gambhire, P.; Thaokar, R. M. *Phys. Fluids* **2010**, *22*, 064103.
73. Lau, C. Y.; Russel, W. B. *Macromolecules* **2011**, *44*, 7746-7751.
74. Zhao, Y.; Xie, Z.; Gu, H.; Zhu, C.; Gu, Z. *Chem. Soc. Rev.* **2012**, *41*, 3297-3317.
75. Meuler, A. J.; McKinley, G. H.; Cohen, R. E. *ACS Nano* **2010**, *4*, 7048-7052.
76. Zawko, S. A.; Schmidt, C. E. *Lab on a Chip* **2010**, *10*, 379-383.
77. Grego, S.; Huffman, A.; Lueck, M.; Stoner, B. R.; Lannon, J. *Microelectron. Eng.* **2010**, *87*, 1846-1851.

Chapter 5: Patterning by Photochemically Directing the Marangoni Effect *

5.1 INTRODUCTION - THE MARANGONI EFFECT

Small variations in temperature or composition at a fluid interface, often spontaneously generated, can cause local changes in surface energy and promote dramatic movement of fluids. This phenomenon, referred to as the Marangoni Effect,^{1,2} is familiar to most people in the “tears” or “legs” that form in a glass of wine. It is in this medium that this effect was first observed in 1855 by James Thomson (brother of Lord Kelvin).³ This effect is named after the Italian physicist Carlo Marangoni who studied the effect at the University of Pravia and published his dissertation in 1865 called “Sull'espansione delle gocce liquid” which roughly translates to “Expansion of liquid drops”.⁴ The effect more generally describes many phenomena, from thickening of a tear film lipid layer in the human eye⁵ to ‘fingering instabilities’ in spreading thin films.⁶

5.1.1 Patterning via the Marangoni Effect

This chapter details a new procedure in which surface energy patterns are programmed into amorphous, solid polymer films by triggering a photochemical reaction in exposed areas using ultraviolet (UV) light and a photomask. Upon heating the polymer above its glass to liquid transition temperature (T_g), the patterned surface energy directs Marangoni flow of the liquid polymer film to produce a diversity of prescribed topographic structures. These structures are potentially suitable for a variety of applications, such as the facile creation of soft lithography stamps⁷ like those used for

* This chapter reproduced in part from:

“Patterning by Photochemically Directing the Marangoni Effect” Katzenstein, J. M.; Janes, D. W.; Cushen, J. D.; Hira, N. B.; McGuffin, D. L.; Prisco, N. A.; Ellison, C. J. *ACS Macro Letters* **2012**, *1*, 1150-1154.

Copyright 2012, American Chemical Society

“Directing Convection to Pattern Thin Polymer Films” Janes, D. W.; Katzenstein, J. M.; Shanmuganathan, K.; Ellison, C. J. *Journal of Polymer Science Part B: Polymer Physics* **2013**, *51*, 535-545 with permission from John Wiley and Sons, copyright 2013.

transistor arrays,⁸ microfluidic devices,⁹ printing of microparticles,¹⁰ fabrication of templates for guidance of neurite growth,¹¹ or engineered anti-fouling surfaces.^{12,13} Given that as little as 10 seconds of light exposure time is sufficient to induce feature formation, this approach could be compatible with high speed roll-to-roll processes for patterning large areas. This is not the first example where the Marangoni Effect has been used in order to create controlled patterns. Previously, this effect has also been exploited to manipulate the motion and position of fluids,^{14,15} to influence the surface roughness of spin coated films,¹⁶ to align nano-particles,¹⁷ or to create colloidal crystal films (Figure 5.1).¹⁸

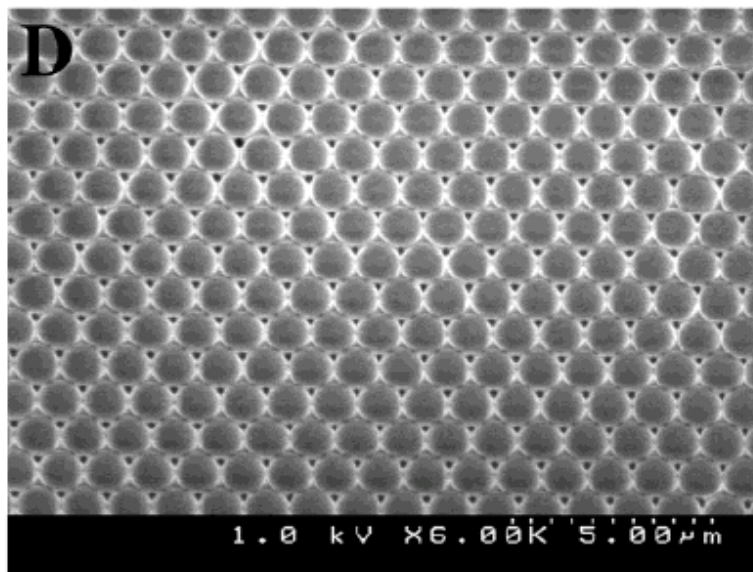


Figure 5.1: SEM image of a top view of the silica colloidal (1 μm diameter) crystal films demonstrating the high degree of long-range ordering created via isothermal evaporation-induced self-assembly. This technique utilizes thermal Marangoni convective currents to deposit the colloidal particles. Reprinted with permission from “Colloidal crystal films: Advances in universality and perfection” Wong, S.; Kitaev, V.; Ozin, G. A. *J. Am. Chem. Soc.* **2003**, *125*, 15589-15598. Copyright 2003, American Chemical Society.

The formation of surface topography on a polymer film by Marangoni-driven flow consists of two basic steps (Figure 5.2). First, a polymer film well below T_g , here 2900 g/mol polystyrene (PS), is exposed to light, in this case a 200 W metal-halide lamp with broadband output from ~200-600 nm, through a photomask for a short period of time to induce a photochemical reaction in the exposed polymer throughout the depth of the film supported on a silicon wafer or glass slide. Next, the film is heated for 10 minutes to well above the polymer's T_g (~ 61 °C for this PS) to reduce its viscosity and facilitate flow. During this time, the surface energy pattern imposed by the photochemical reaction induces flow of material from unexposed regions with relatively low surface energy to exposed regions with relatively high surface energy. The result is a prescribed surface topography formed by the Marangoni Effect that was directed by patterning the photochemical reaction in the solid state during light exposure through the photomask.

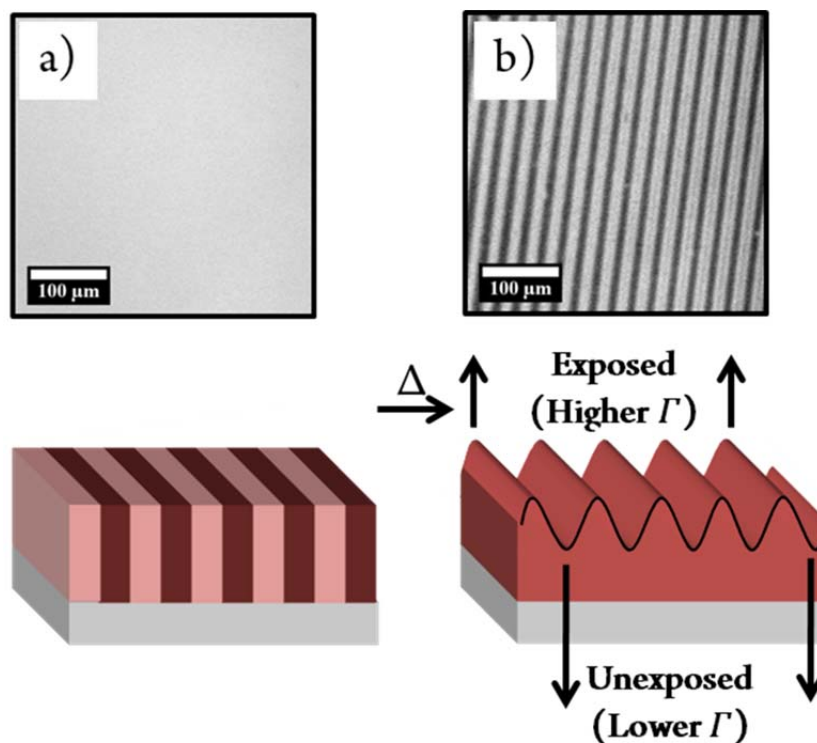
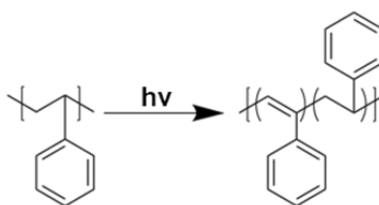


Figure 5.2: Schematic illustration of the steps involved in feature formation in a PS thin film. a) A brightfield micrograph of a glassy polymer film (~150 nm thick) after exposure to light through a photomask which induces a photochemical reaction in exposed regions and an associated patterned surface energy. For the PS films employed here, there is higher surface energy in the exposed regions. No topography can be detected by atomic force microscopy after this stage. b) After heating the same film to 110 °C, where the polymer becomes a liquid, the patterned surface energy drives formation of topographic features via the Marangoni Effect.

5.2 POLYSTYRENE (PS) PHOTOCHEMISTRY

5.2.1 Fluorimetry

The exposure of PS to low to moderate doses UV light is known to cause dehydrogenation of the carbon-carbon bonds in the backbone of the polymer chain resulting in double bond formation (Scheme 5.1).¹⁹⁻²³



Scheme 5.1: Dehydrogenation of PS by exposure to UV light.

These double bonds create ‘stilbene-like’ chemical structures from a portion of the repeat units which have significantly red-shifted fluorescence spectra relative to neat PS. Accordingly, solution fluorimetry was used to qualitatively confirm the creation of ‘stilbene-like’ structures as evidenced by significant fluorescence signal at wavelengths where PS precursors do not fluoresce (Figure 5.3).²¹ PS in tetrahydrofuran (THF) solution samples were prepared for this study for exposed and unexposed films because solid-state PS fluorescence emission is dominated by excited state phenyl ring dimers which fluoresce in the same region as these ‘stilbene-like’ structures.²⁴

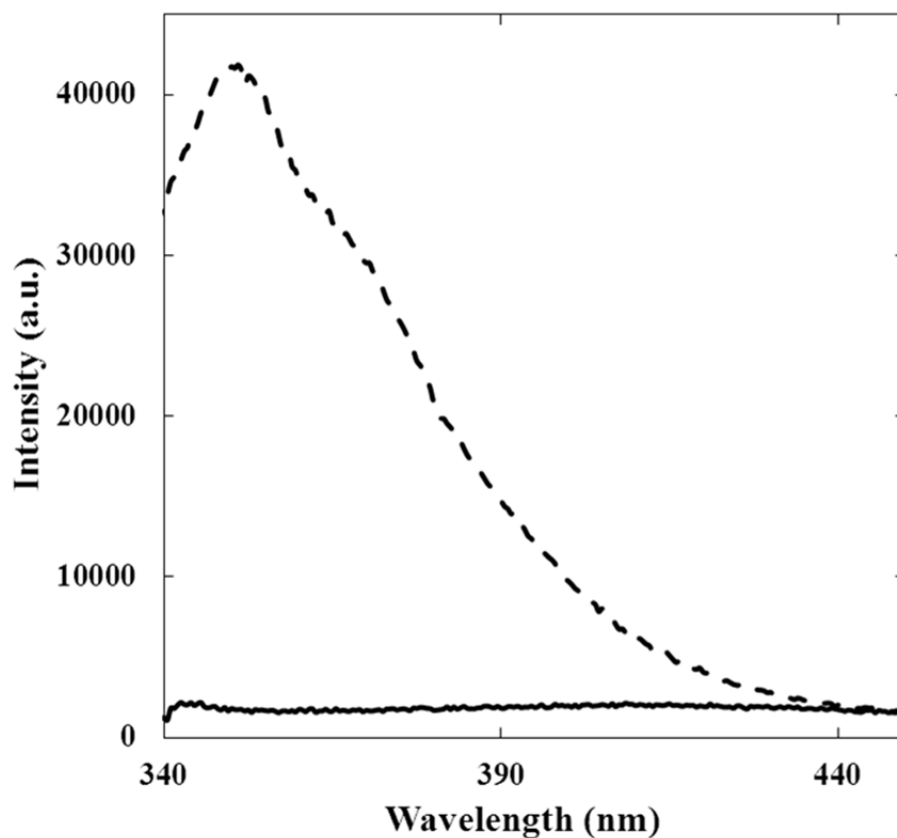


Figure 5.3: Fluorescence spectra of PS precursor (solid line) and PS exposed to UV light for two minutes (dashed line), both in THF solutions at 0.05 mg/mL. For both samples $\lambda_{\text{ex}} = 310$ nm.

5.2.2 Quantification of Backbone Conversion

Previous research shows that a common pathway for photo-conversion of PS is dehydrogenation of the polymer backbone to form C=C double bonds along the polymer chain. Figure 5.4a contains the complete Fourier transform infrared spectroscopy (FTIR) spectra collected for PS as a function of UV exposure dose and Figure 5.4b shows an expanded region of interest. The peak at 1601 cm^{-1} in these FTIR spectra is associated with carbon-carbon double bond stretching and has been correlated in this manner by others for characterizing the degradation of polyolefin materials.¹⁹ This region also corresponds to the carbon-carbon stretch in conjugated alkenes,²⁵ like those that would

result from dehydrogenation of the PS backbone. Since conjugated carbon-carbon double bonds in phenyl rings are also present in this peak, it is not straightforward to use this peak for quantitative analysis. Additionally, a second peak appears at 1689 cm^{-1} due to ‘alkenyl’ C=C stretching²⁵ is also not convenient for quantification due to lack of information about the completely converted state.

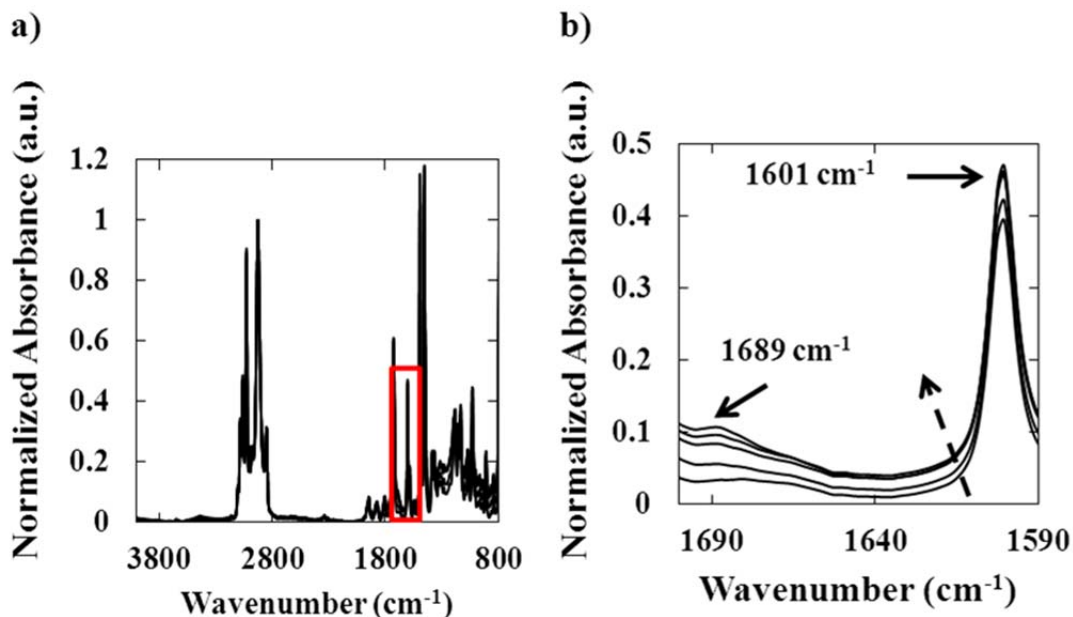


Figure 5.4: a) Full and b) selected region of interest [indicated by rectangle in a)] FTIR spectra for PS as a function of exposure dose. All spectra are normalized to tallest peak in the phenyl ring region (2926 cm^{-1}). The dashed arrow indicates the direction of increasing exposure dose.

Dehydrogenation of the PS backbone can be quantitatively determined as a function of the exposure dose by tracking the peak from $2800 - 2964\text{ cm}^{-1}$ corresponding to methylene C-H bond stretching which decreases as alkanes are converted to alkenes in the backbone. By comparing this to the peak corresponding to the carbonyl in the initiator used for polymerization (1720 cm^{-1}), which is unaffected by UV exposure, the dehydrogenation of the PS backbone can be quantified. Figure 5.5 shows the percent

conversion of the carbon-carbon bonds in the PS backbone to its dehydrogenated form as a function of exposure dose.

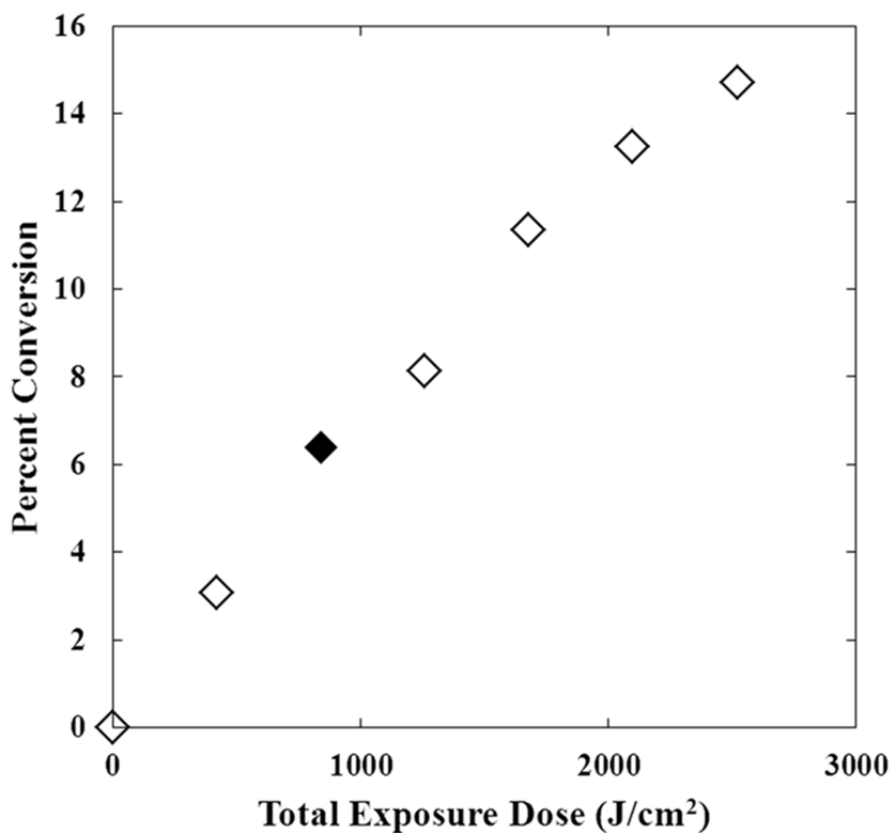


Figure 5.5: Percent conversion of PS backbone to carbon-carbon double bonds as a function of exposure dose by infrared spectroscopy. The filled data point represents the typical dose and conversion used in this study.

From this analysis, the exposure dose used in this study (840 J/cm^2 , the total dose from all wavelengths of the broadband source) converts 6.4% of backbone bonds to alkenes. The photoconversion increases monotonically with exposure dose. Additionally, the PS films used in this study ($\sim 150 \text{ nm}$ thick) absorb $<15\%$ of the incident light at the peak absorbance wavelength (260 nm) and $<10\%$ of the total broadband incident light.

This indicates that the photochemical changes to the polymer should be relatively uniform throughout the depth of the film.

5.2.3 Contact Angle Measurements

The change in surface chemistry is qualitatively detectable by measuring a test liquid contact angle on the PS film surface. Figure 5.6 shows a reduction in water contact angle with exposure dose from $90.6 \pm 0.5^\circ$ before exposure to $88.8 \pm 0.8^\circ$ after exposure dose of 2500 J/cm^2 , corresponding to a 14% conversion of the backbone as shown in Figure 5.5. This change is indicative of a change in the chemical structure of the polymer at the surface. Two additional test liquids were evaluated [glycerol and 300 g/mol poly(ethylene glycol)] and all showed a decrease in contact angle following exposure of the PS film to UV light (also Figure 5.6). It is important to note that determination of the surface energy directly is very challenging for polymers due to their tendency to absorb or dissolve in many small molecule test liquids. A simple extrapolation to ~14% conversion between PS and an analog with a dehydrogenated backbone, poly(phenyl acetylene), indicates that the change in test liquid contact angle in Figure 5.6 corresponds to a change in surface energy of less than one dyne/cm. The Maragoni analysis described in this chapter shows that the minimum critical surface energy differences necessary to induce Marangoni driven flow are roughly 0.01 dyne/cm.

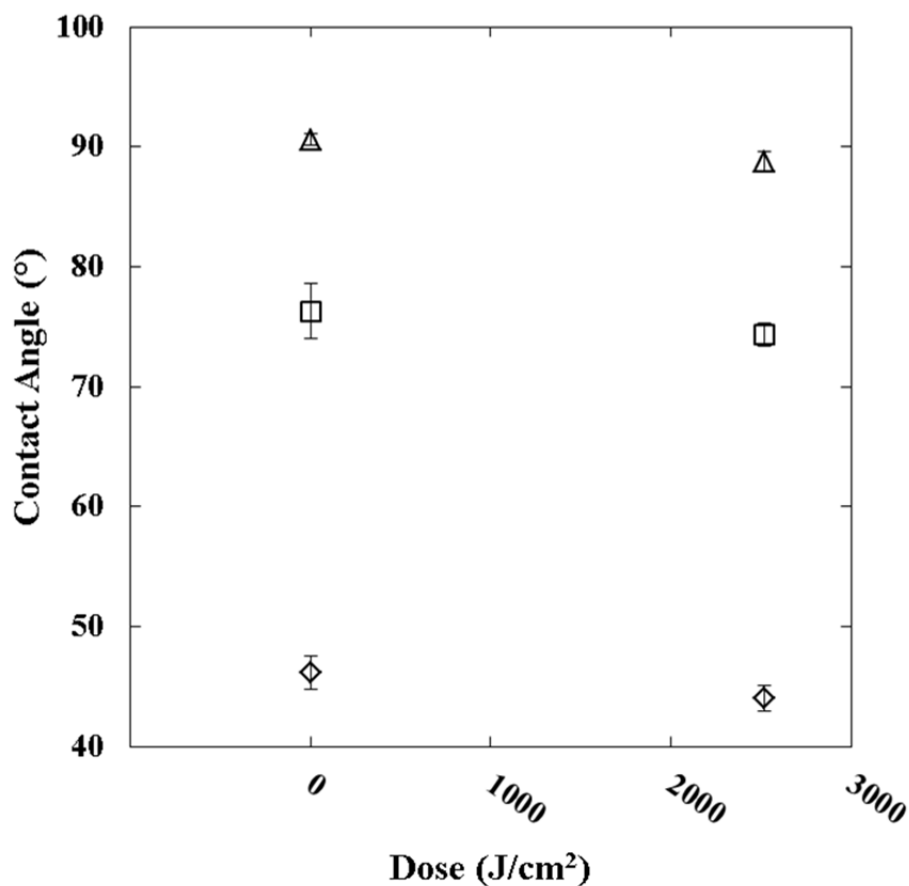


Figure 5.6: Contact angle of PS as a function of exposure dose for water (Δ), glycerol (\square), and poly(ethylene glycol) (\diamond). Error bars indicate standard deviation from ten measurements. Changes are all statistically significant ($p < 0.01$).

5.3 TOPOGRAPHIC PATTERN VARIETY

To further explore the capabilities of forming line and space patterns with this method, photomasks with periods of 100 μm (Figure 5.7a), 25 μm (Figure 5.7b), and 10 μm (Figure 5.7c) were examined. The periodicity of features formed matches that of the photomask, while the topography exhibits curvature not present in the mask itself. Additionally, these features appear over an area as large as the output of the light source, which in principle is scalable to high throughput processing methods.

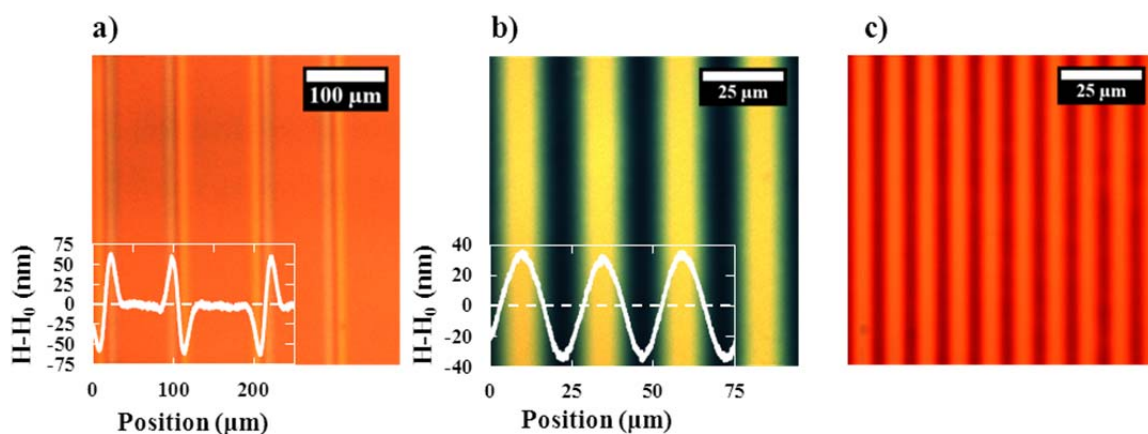


Figure 5.7: Various line pattern periods created in ~ 150 nm thick PS films with overlaid profilometry traces showing topography formed by using photomasks with different line spacing of a) $100\ \mu\text{m}$ chrome lines with a $200\ \mu\text{m}$ pitch b) $12.5\ \mu\text{m}$ chrome lines on a $25\ \mu\text{m}$ pitch and c) $5\ \mu\text{m}$ chrome lines on a $10\ \mu\text{m}$ pitch. For part c), the profilometer stylus is too large for accurate characterization of the topography. Panel a) highlights that Marangoni-driven patterning is sensitive to the local gradient in surface energy, which occurs only near interfaces of exposed and unexposed regions which are a smaller portion of the overall image in a) than b) or c).

Formation of surface topography through directing the Marangoni Effect is not limited to lines and spaces; it can be applied to any arbitrary design as long as a UV transparent photomask is available. In this way, it is possible to transfer more complex patterns such as triangles (Figure 5.8a) or ‘longhorns’ (Figure 5.8b). Additionally, multiple exposures with either the same (Figure 5.8c-d) or different (Figure 5.8e-f) line and space masks can be used to create more complex patterns.

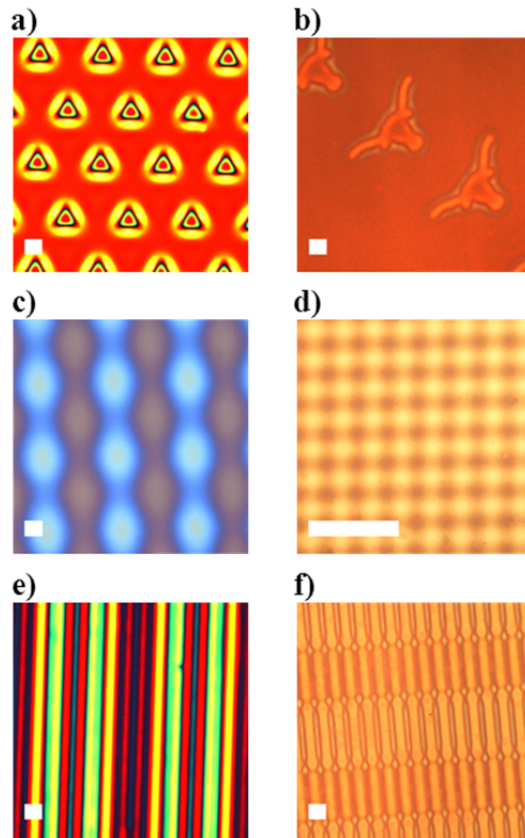


Figure 5.8: Various patterns formed by photochemically directed Marangoni flow. Patterns shown in a) triangular pillars with triangular area exposed to light, that rise up above the film, and b) ‘longhorn’ patterns which sink into the film, both are 1:1 replications of patterns on the photomask. Patterned c) large (formed by the $12.5\ \mu\text{m}$ chrome lines on a $25\ \mu\text{m}$ pitch photomask) and d) small (formed by the $5\ \mu\text{m}$ lines on a $10\ \mu\text{m}$ pitch photomask) mounds are formed by exposure through the same line-and-space mask twice with the mask turned 90° between exposures. Pattern e) lines-in-lines is the result of two exposures of different line-and-space periods parallel to each other and f) ‘dogbones’ by the same method with the second mask turned 90° between exposures. For e) and f) one exposure utilized a $12.5\ \mu\text{m}$ chrome lines on a $25\ \mu\text{m}$ pitch photomask while the second exposure used a $5\ \mu\text{m}$ lines on a $10\ \mu\text{m}$ pitch photomask. Colors are interference patterns caused by changes in film height. All films are 100-300 nm thick before patterning and have scale bars of $30\ \mu\text{m}$.

5.3.1 Controlled Directionality of Feature Formation

Two different types of masks were used to create topographic features using this technique with opposite directionality. In one case the desired feature (number 16 and outlining box) was protected from light and the surrounding region was exposed, causing the features to sink into the film (Figure 5.9a). For the second case, only the desired features (triangles) were exposed to light and the topographic features rise out of the film (Figure 5.9b). These images and their corresponding profilometer traces clearly indicate that by controlling which regions of a film are exposed to light, the directionality (depressions in to the film surface or rising out of the film surface) of the resulting topography can be controlled.

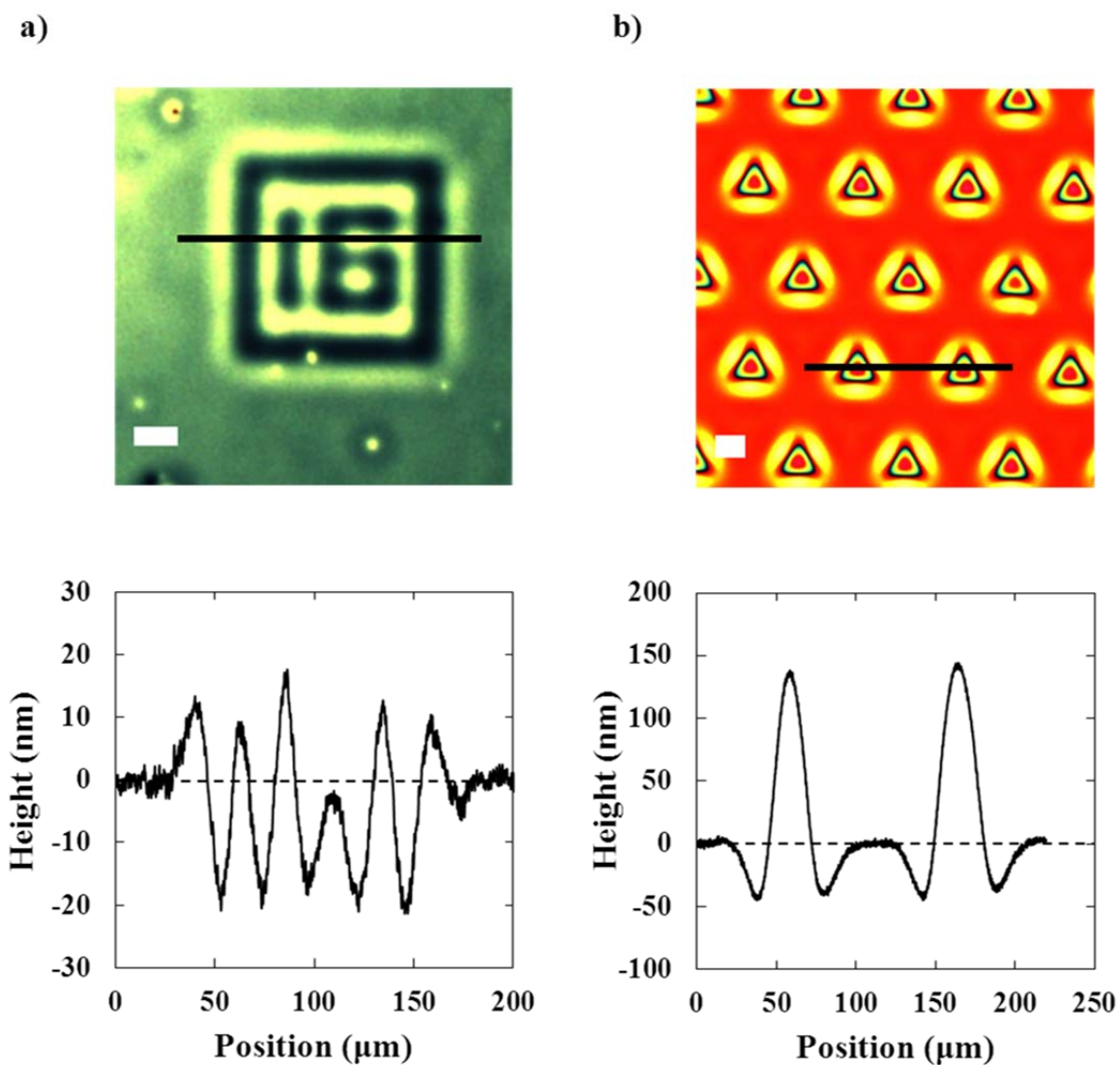


Figure 5.9: Brightfield micrographs (top) and corresponding profilometry traces (bottom) of topographic features a) that sink into the film and b) that rise out of the film. Dark lines on micrographs indicate region where profilometry trace was collected

5.4 REPEATABILITY OF TOPOGRAPHY FORMATION

Generally, relatively short time ($\sim 1-10$ min) and/or low-temperature ($\sim T_g + 50$ °C) post-UV exposure annealing conditions are typically used to generate Marangoni-driven formation of topographic features. However, longer times and/or higher temperature

annealing conditions can be used to cause these structures to dissipate completely, resulting in recovery of a featureless film. Optical micrographs of two successive cycles are provided in Figure 5.10 to illustrate this concept. The current hypothesis is that over long time or high-temperature annealing conditions, the polymer chains within exposed and unexposed regions interdiffuse. Since the surface energy gradient that drives Marangoni flow diminishes from such interdiffusion, capillary forces favoring a featureless film surface eventually dominate and the height variations dissipate. The peak to valley feature heights measured after a constant post-exposure heating time for the two cycles were 45 nm and 41 nm, respectively. The exact reason for the decrease in feature height from the first cycle to the next is not yet clear, but it could be due to smaller imposed surface energy gradients with successive photoexposure events.

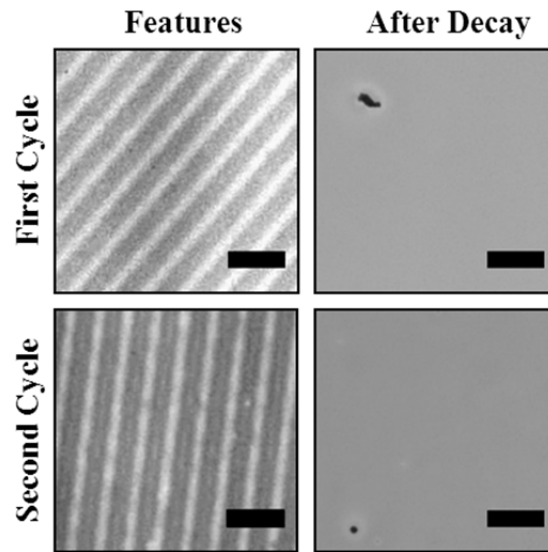


Figure 5.10: Repeated topographic feature formation using the photochemically directed Marangoni process in a single PS film with an initial film thickness of ~ 140 nm. The left column contains optical micrographs of topographic features formed after exposure through a photomask with $12.5 \mu\text{m}$ chrome lines on a $25 \mu\text{m}$ pitch and annealing at 120°C for 60 minutes. The right column contains optical micrographs of the same film after 60 minutes of annealing at 145°C , where features have completely dissipated. Scale bars are $50 \mu\text{m}$.

5.5 TOPOGRAPHIC PATTERN TRANSFER AND OVERLAYERS

Low-molecular weight PS was initially used in these experiments because its low viscosity enables relatively fast Marangoni flow in the melt state and its photochemistry is well-understood. However, it may not be the most practical material for real applications due to poor mechanical properties and depressed T_g (~ 61 °C). To expand the utility of this low-molecular weight PS, a variety of mechanisms exist for transferring the pattern from the film in which they were originally formed to more robust materials. For example, Fig. 5.11 demonstrates transfer of topographic patterns into Sylgard 184, a thermosetting silicone elastomer often used as a soft lithography mask.²⁶⁻²⁸

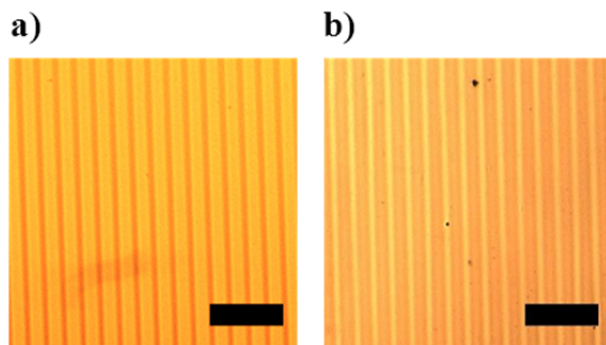


Figure 5.11: Optical micrographs of a) PS film ‘master’ with topography formed by photochemically directing Marangoni-driven flow and b) pattern transferred into Sylgard® 184 after curing at room temperature for 24 hours and subsequent heating to 100 °C for 2 hours to complete crosslinking. Scale bars are 100 μm .

Many film materials and device manufacturing processes implement topographic structures in multilayer films composed of different materials. Fig. 5.12 shows that an overlayer of another material, such as poly(methyl methacrylate) (PMMA), gold or poly(ethylene glycol) (PEG), can be placed between the mask and PS film without suppressing the patterned photochemical reaction during photoexposure or Marangoni-driven pattern formation. In this demonstration, gold was sputter deposited onto PS, PEG

was simply dispensed directly on PS and the PMMA film was floated onto PS, all prior to the photoexposure step. No topographic features developed when the same procedure was performed on a single PMMA film, likely because no surface energy pattern is generated in PMMA under these photoexposure conditions. We believe pattern formation in a multilayer film could be universal for many adjoining materials provided the additional layers are not too rigid and do not substantially absorb/reflect the UV light responsible for photochemical patterning.

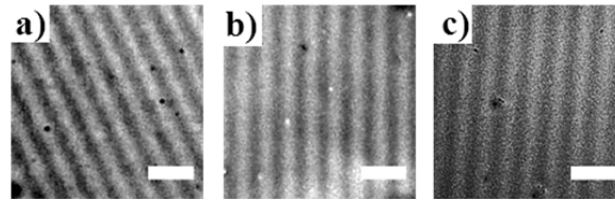


Figure 5.12: Optical micrographs of Marangoni driven topography formation in 150 nm thick PS films with various overlayers placed on top before photoexposure and thermal annealing. Topography was generated with a) 95 nm PMMA overlayer, a glassy polymer, b) 52 nm sputter deposited gold overlayer, a metal, and c) 300 g/mol PEG overlayer, a liquid polymer (washed off with water before imaging). Scale bars are 50 μm . Similar topography can also be formed by first photoexposing the PS film and then depositing the overlayer prior to heating the film to develop topography.

5.6 MARANGONI NUMBER CALCULATIONS

Feature formation in PS films results from Marangoni instabilities caused here by a pre-patterned surface energy gradient. The critical Marangoni number (Ma_c) for the formation of surface instabilities is reported by others as 80.^{29,30} The general form of the Marangoni number is shown in eq. 5.1³¹

$$Ma = -\frac{\Gamma' H^2 \nabla C_{PS}}{\mu D} \quad (5.1)$$

where Ma is the Marangoni number, Γ' is the surface energy change with composition, ∇C_{PS} is the gradient in the concentration of PS with position, H is the characteristic

length of the surface energy gradient, in this case the half pitch of the photomask, μ is the viscosity and D is the diffusion coefficient.

In our estimation, we assumed surface energy changes linearly with polymer composition (i.e., between endpoints of neat PS and its fully dehydrogenated form) and that the concentration changes linearly with position which means that ∇C_{PS} reduces to $\Delta C_{PS}/H$. Using these simplifications, eq. 5.1 can be written as shown in eq. 5.2, the form that will be used for future calculations.

$$Ma = -\frac{\Gamma' H^2 \frac{\Delta C_{PS}}{H}}{\mu D} = -\frac{\Gamma' H \Delta C_{PS}}{\mu D} \quad (5.2)$$

From this point each of the terms can be calculated independently and if $Ma = Ma_c = 80$ then $\Delta C_{PS} = \Delta C_{PS}^*$ where ΔC_{PS}^* is the minimum level of PS dehydrogenation for features to develop.

The Rouse model²⁹ for unentangled polymer diffusion can be used to estimate the diffusion coefficient for PS at 110 °C using eq. 5.3

$$D = \frac{\rho R T \langle R^2 \rangle}{36 M \mu} \quad (5.3)$$

where ρ is the density, R is the ideal gas constant, T is the absolute temperature, M is the molecular weight of the polymer and $\langle R^2 \rangle$ is the unperturbed mean-square end-to-end distance of the polymer.³² For this polymer $\langle R^2 \rangle = (9.12 \times 10^{-10} \text{ mol} \cdot \text{m}^2 / \text{kg}) \cdot M$,³³ $\rho = 988 \text{ kg/m}^3$ at 110 °C,³⁴ $T = 383.15 \text{ K}$, $R = 8.3114 \text{ kg} \cdot \text{m}^2 / \text{s}^2 / \text{mol} / \text{K}$.

It is interesting to note that the Rouse model predicts that the Marangoni number for polymer melts is independent of M in unentangled polymers (i.e., D scales as $1/\mu$). Interestingly, for entangled polymers, more common in many commercial applications, the Marangoni number theoretically decreases with increasing molecular weight, $Ma \sim M^{-1.1}$ (i.e., $\mu D \sim M^{1.1}$).³⁰ Therefore, higher extents of dehydrogenation are required to

compensate for the M dependence of the Marangoni number for Marangoni-driven flow to occur in entangled polymers.

In order to approximate Γ' , a group contribution method for calculating surface energy at 298 K is sufficient.^{33,34} First, the cohesive energy density (e_{coh}) for PS and fully dehydrogenated PS, which is identical to poly(phenyl acetylene) (PPA) is needed, $e_{coh,PS} = 406.4 \text{ J/cm}^3$ and $e_{coh,PPA} = 510.8 \text{ J/cm}^3$. Note that the molar volume of PPA was also calculated via a group contribution method, but the molar volume of PS was calculated based on the known mass density. Next, the empirical correlation $\Gamma = 0.75e_{coh}^{2/3}$ can be used to calculate the surface energy for each species³⁴ yielding $\Gamma_{PS} = 41.1 \text{ dyne/cm}$, $\Gamma_{PPA} = 47.9 \text{ dyne/cm}$. From these results, $\Gamma' = -7.12 \times 10^{-7} \text{ kg} \cdot \text{m}^3 / \text{mol} \cdot \text{s}^2$ by dividing the difference in surface energy by the concentration of bulk PS (9486 mol/m^3) which would need to be 100% dehydrogenated for realizing the largest change in surface energy.

Combining all of these parameters and using $H = 5 \text{ }\mu\text{m}$, the half-pitch of the smallest line space pattern, eq. 5.4 can finally be used to calculate ΔC_{PS}^* .

$$80 = - \frac{\left(-7.12 \times 10^{-7} \frac{\text{kg} \cdot \text{m}^3}{\text{mol} \cdot \text{s}^2}\right) (5.0 \times 10^{-6} \text{ m}) \Delta C_{PS}^*}{7.97 \times 10^{-14} \frac{\text{kg} \cdot \text{m}}{\text{s}}} \quad (5.4)$$

$$\Delta C_{PS}^* = 1.79 \frac{\text{mol}}{\text{m}^3} \quad (5.5)$$

This value of ΔC_{PS}^* corresponds to a conversion of 0.02% of the bonds in PS converting to PPA.

A more conservative estimate would assume the molar volumes of PS and PPA are equal. Recalculating using this approximation gives the result $\Gamma_{PPA} = 41.9 \text{ dyne/cm}$, $\Gamma' = -7.48 \times 10^{-8} \text{ kg} \cdot \text{m}^3 / \text{mol} \cdot \text{s}^2$. Using this figure $\Delta C_{PS}^* = 17.1 \text{ mol/m}^3$ or 0.18% of bonds being dehydrogenated. Even using this more conservative approach, the experimentally

measured conversion of PS units to their dehydrogenated form was at least an order of magnitude above this critical threshold for all samples.

5.7 KINETICS OF MARANGONI DRIVEN TOPOGRAPHY FORMATION

In this system, the topographic features undergo two stage behavior as a function of the thermal development time above the T_g of the polymer such as that shown in Figure 5.13. In the first stage, the surface energy gradient imposed by the photochemical partial dehydrogenation of the polymer backbone leads to growth in feature height. After significant thermal heating, however, the feature height begins to decrease. This dissipation is believed to be related to the interdiffusion of the exposed and unexposed regions of the polymer which reduces the surface energy gradient and therefore the Marangoni Effect driving force for topography. This balance of forces provided the framework for the experiments and a future collaboration to develop numerical simulations in order to more completely characterize this patterning technique has begun. There appear to be three main process parameters for controlling the size of topographic features formed: photoexposure dose (and therefore backbone conversion), initial film thickness, and temperature (which influences both viscosity and the diffusion coefficient of the polymer). All of these experiments were performed using a 12.5 μm chrome line on a 25 μm pitch photomask and the height reported is the maximum height (peak to valley) of the sinusoidal topographic profile. It is important to note that features below approximately 5 nm in peak to valley height were not measurable by profilometry.

5.7.1 Exposure Dose

The first process parameter investigated was photoexposure dose (Figure 5.13), which corresponds to the degree of conversion of the polymer backbone and thus the strength of the surface energy gradient leading to Marangoni-driven flow. Figure 5.5

shows the conversion of the PS backbone as function of exposure dose. Unsurprisingly, with increased photoexposure dose the number of carbon-carbon double bonds in the backbone monotonically increases which leads to larger feature formation.

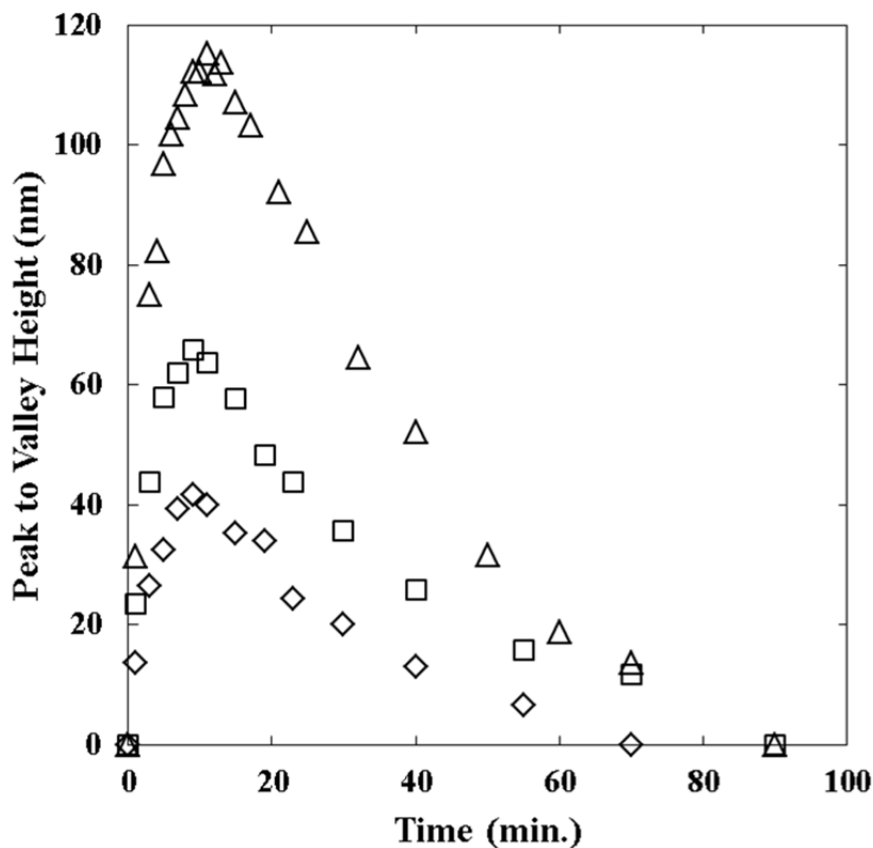


Figure 5.13: Peak to valley height as a function of heating time at 136 °C with exposure doses of 840 J/cm² (Δ), 420 J/cm² (□), and 210 J/cm² (◇) on films with an initial thickness of 130 nm.

5.7.2 Initial Film Thickness

An additional parameter that impacts the development of topography is the initial thickness of the PS film, see Figure 5.14. The effects of this parameter are arguably the least intuitive to understand. It appears that in thinner films, while the absolute magnitude of the features is smaller than those in thicker films they are actually larger relative to the initial film thickness (see inset of Figure 5.14). Furthermore, the thinner the film the more

slowly the features reach their peak amplitude. Both of these results can conceptually be explained by the visco-capillary force which increases with decreasing film thickness. This leads to the larger features relative to the initial thickness and, since a larger percentage of the material in the film needs to move, the slower time to maximum feature height.

With the thinnest films, dewetting becomes a significant issue in the measurement of feature height as the experiment proceeds. Additionally, thin films begin to exhibit non-sinusoidal feature profile mostly likely also due to the films dewetting from the substrate. Data on this film is included as a demonstration of these effects and the decay rate does not correspond to the other film thicknesses for this reason.

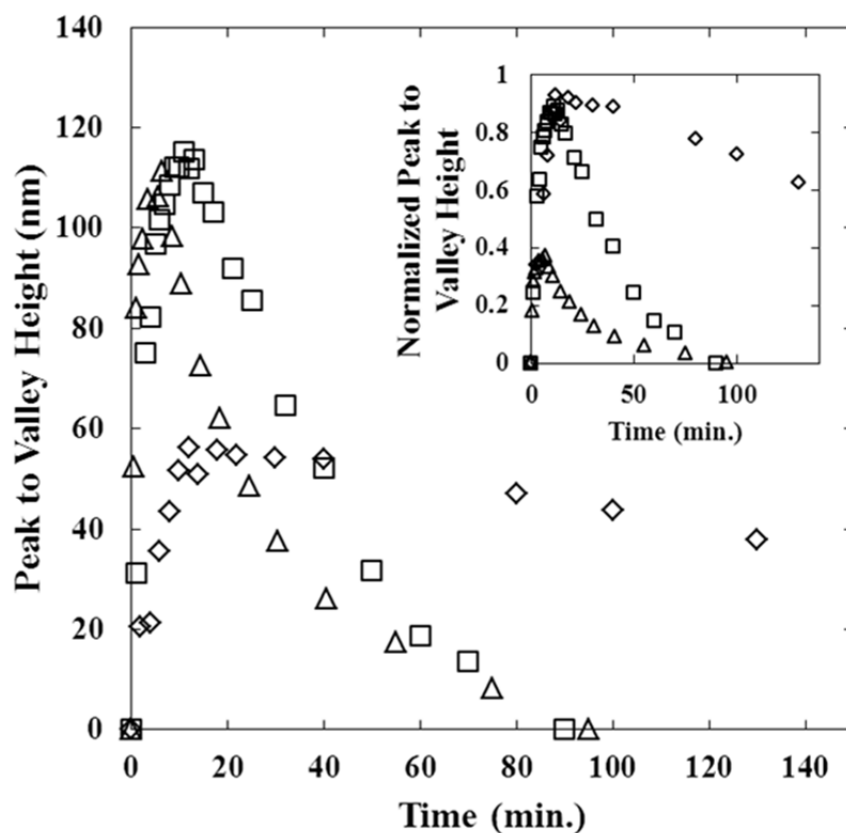


Figure 5.14: Peak to valley height as a function of heating time at 136 °C with exposure doses of 840 J/cm² at film thicknesses of 300 nm (Δ), 130 nm (\square), and 60 nm (\diamond). Inset shows peak to valley heights normalized by the initial thickness of the film.

5.7.3 Temperature

The final parameter examined is the thermal annealing temperature, see Figure 5.15 for data. This parameter impacts the viscosity, which is related to the capillary driving force, and inter-diffusion rate through the diffusion coefficient. Fairly obviously, higher temperatures lead to faster feature growth and decay. What is slightly less obvious is that the maximum feature size increases with temperature as well. This seems to be a function of how the magnitude of the competing forces, Marangoni driven flow and diffusion, vary with temperature. Since the viscosity of PS at any given temperature

decreases with decreasing molecular weight which leads to the topography developing more quickly in a low viscosity film. The critical Marangoni number criterion only determines whether or not surface instabilities *will* occur, but does not address the kinetics of feature formation. Therefore, to develop the pattern in the shortest time with the highest possible Marangoni number, a low M polymer is preferable such as the 2900 g/mol PS, with a T_g of 61 °C, that was used in this study. The inset of Figure 5.15 demonstrates that for the data collected at 140 °C the decay portion of the kinetic data, agrees well with the characteristic timescale for diffusion at each temperature. The characteristic timescale is estimated as $H^2/4D$ where H is the half-pitch of the photomask (12.5 μm) and D is the diffusion coefficient of PS at that temperature. At 140 °C the characteristic diffusion time is 30 minutes, at 130 °C it is 75 minutes, and at 120 °C it is 260 minutes.

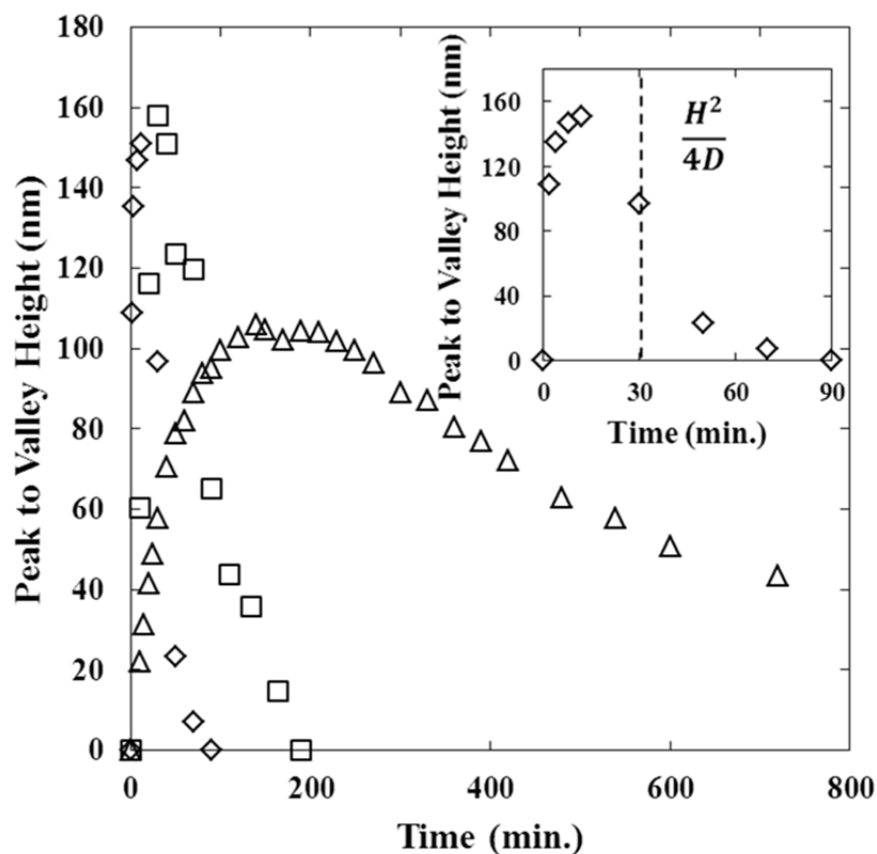


Figure 5.15: Peak to valley height as a function of heating time at 120 °C (Δ), 130 °C (\square), and 140 °C (\diamond) with exposure doses of 840 J/cm² at film thicknesses of 145 nm. Inset is 140 °C data with a vertical dashed line at the characteristic diffusion time for PS at this temperature.

5.8 CONTROL EXPERIMENTS

5.8.1 Light Filtering and Fluorescently Labeled PS

To confirm that the cause of feature formation was related to the polystyrene UV photochemistry, fluorophore containing PS was used. A 385 nm long pass filter was placed between the photomask and the light source in order to absorb all of incident UV light that is absorbed by PS while still passing light absorbed by the fluorophore. This long pass filter attenuates the total incident light by 19%, but the total dose is well above the amount necessary for writing the surface energy pattern in absence of the optical

filter. Bright field imaging shows there was no change in the surface of the film after exposure (Figure 5.16a), but fluorescence imaging shows that wavelengths greater than 385 nm still penetrated the film and photobleached the fluorophore (Figure 5.16b). Finally, upon heating this film for one hour at 110 °C and examining it every 10 minutes by optical microscopy, no features were observed at any time (Figure 5.16c). This demonstrates that exposure to UV light which PS absorbs is necessary to induce a patterned surface energy which can then later be developed into surface topography.

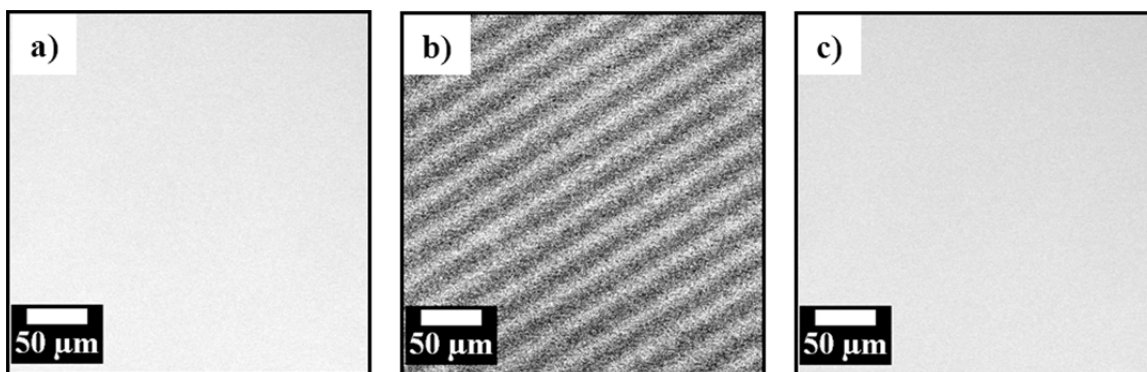


Figure 5.16: Micrographs showing the effect of blocking all wavelengths absorbed by a PS film with a 385 nm long pass filter during light exposure. a) Bright field micrograph immediately after exposure. b) Fluorescence micrograph showing photobleaching of NBD-labeled PS after exposure with the long pass filter in place; light areas indicate high fluorophore concentrations in regions protected by the photo mask. c) Bright field micrograph of the same region after 1 hour at 110 °C showing no topography

5.8.2 X-ray Photoelectron Spectroscopy (XPS)

A possible explanation for the increase in local surface energy and the appearance of new fluorescence centers could be oxidation of the surface of the PS film during photoexposure. Because the initiator fragment in PS synthesized by ATRP (used in most of this study) contains oxygen, XPS was performed on an anionically synthesized sample of polystyrene with similar molecular weight, also verified to undergo Marangoni driven

patterning. XPS was performed to determine if oxygen containing species were present at the surface of the film. Figure 5.17 contains the survey scans for both exposed and unexposed films of polystyrene. The spectra are identical and this indicates that there was no change in the chemical composition of the surface of the film during exposure, which is consistent with dehydrogenation of the polymer backbone as the predominant chemistry that occurs during photoexposure. Additional experiments where photoexposure was performed under an argon atmosphere and topography still formed (Figure 5.19) when no oxidation was possible.

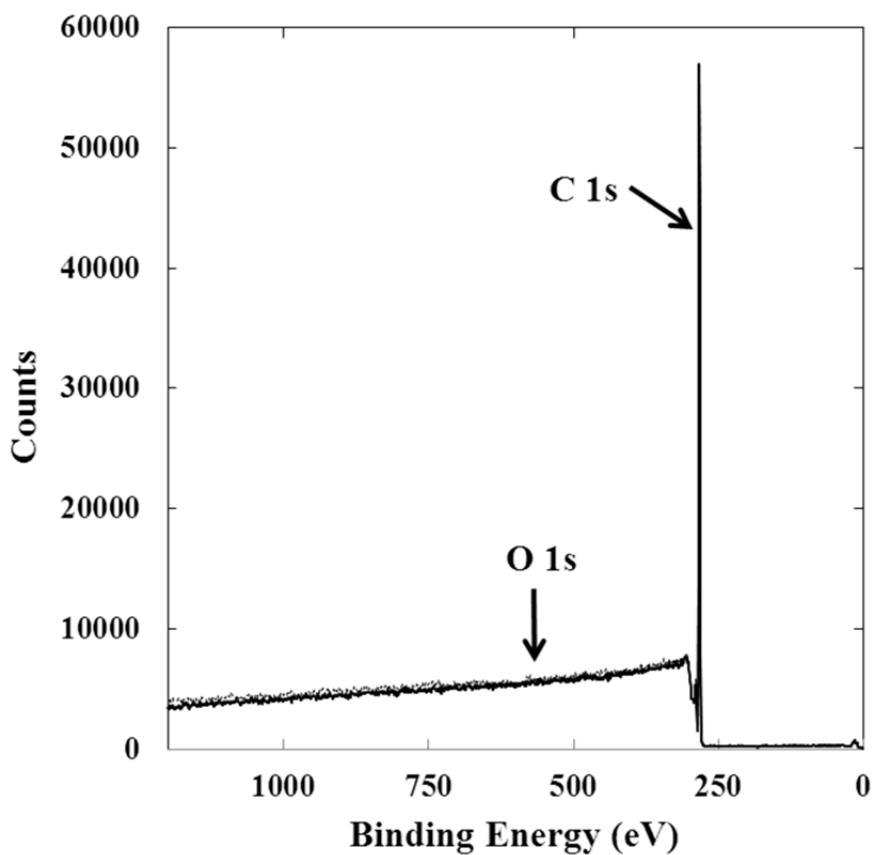


Figure 5.17: XPS spectra of unexposed (dashed line) and exposed (solid line) PS films. No peak is observed at 531 eV which is characteristic of the presence of oxygen.

5.8.3 Gel Permeation Chromatography (GPC)

To confirm that the polymer chains did not undergo crosslinking or other polymer-polymer chain coupling reactions during exposure, the neat polymer and light exposed polymer were both characterized by GPC by flood exposing two films approximately 1 μm thick with twice the dose used for the majority of the experiments in this study (1680 J/cm^2). Under these conditions, the films absorbed 90-100% of the incident light near 260 nm throughout the depth of the film. These two films produced roughly 13 mg of polymer which was dissolved at standard concentrations in 1mL of THF for analysis. The refractive index chromatograms before and after exposure agrees within error (Figure 5.18). It is worth noting that no high molecular weight material was detected in light scattering signal either, where signal intensity is proportional to molecular weight.

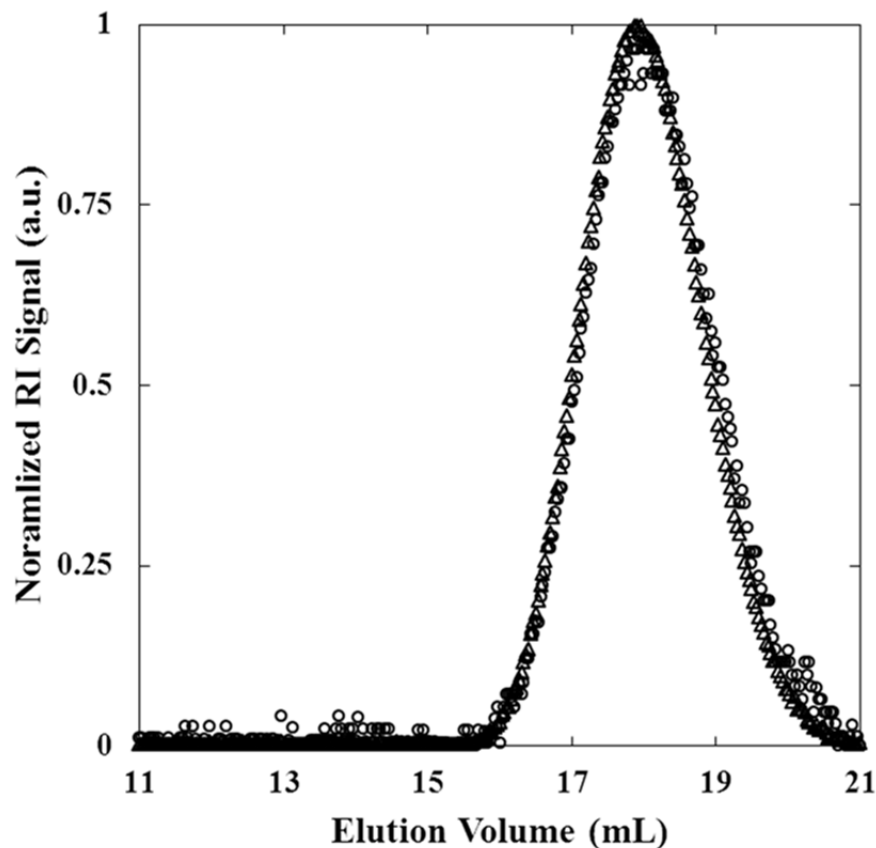


Figure 5.18: Plot of refractive index vs. time collected by GPC for neat PS (Δ) and PS exposed to the light source (\circ).

5.8.4 Infrared Camera

One potential hypothesis for topographic feature formation was local heating in the exposed regions causing a change in surface energy due to chain end rearrangement. It is known that surface energy decreases with increasing molecular weight and this is due to enrichment of the chain ends at the surface of the film.^{35,36} However, during spin coating the film is rapidly vitrified which means that the chain ends do not have a chance to go to their equilibrium location. A FLIR camera was used in order to measure the temperature of the film and of the mask during photoexposure (Figure 5.19) and only after significant exposure, does the mask slightly rise above the of the polymer (~ 61 °C),

which means that this is not a probable cause of topographic feature formation. Note that these experiments were performed without a collimating lens on the light source which would lead to higher local temperature rise due to the narrower beam spot than the collimated light typically used. Furthermore, films pre-annealed well above T_g to allow chain end equilibration to be reached before photoexposure well below the T_g still developed topography after patterned exposure and heating.

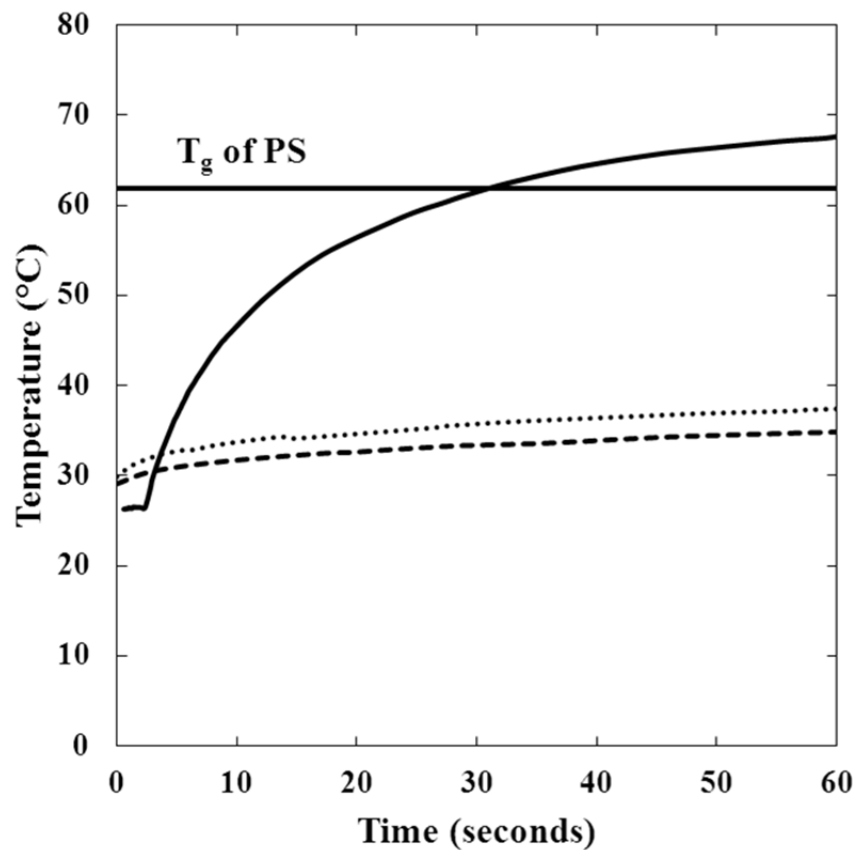


Figure 5.19: Temperature of clean quartz (dotted line), PS film (dashed line) and chrome on quartz photomask (solid line) during photoexposure as a function of time. Horizontal line indicates the T_g of the PS used for these experiments

5.8.5 Mask Sink-In

Finally, in order to verify that topography was not caused by the indentation of the photomask in the PS film, several experiments were performed. First, using arbitrarily shaped photomasks (such as pyramids as shown in Figure 5.7) and performing profilometry demonstrated that exposed areas *rose* out of the film and therefore did not propagate into the film promoted from mask indentations. Second, an experiment was performed where films were maintained at $-100\text{ }^{\circ}\text{C}$ during UV light exposure only. High-purity argon was passed over the films during this step to limit water condensation on the film surface. At this temperature the polymer film is $\sim 160\text{ }^{\circ}\text{C}$ below its glass transition temperature, rendering indentations arising from mask sink-in unlikely given the PS is deep in the glassy state. Under these exposure conditions features still formed upon heating without the mask being present (Figure 5.20). Finally, AFM was performed on films after room temperature UV exposure but before heating and no topographical features were detected. These pieces of evidence clearly eliminate mask sink-in as playing any role in this patterning approach.

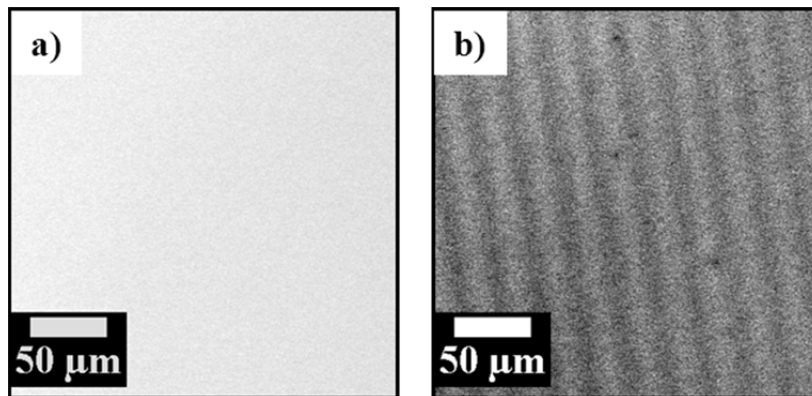


Figure 5.20: Bright field micrographs of a PS film a) immediately after UV exposure for 45 seconds at $-100\text{ }^{\circ}\text{C}$ and following b) 1 hour of heating at $110\text{ }^{\circ}\text{C}$ to develop the topography.

5.9 CONCLUSIONS

This study demonstrates a new approach to creating three-dimensional topography through the photochemical generation of surface energy patterns in PS films. Dehydrogenation of the PS backbone alkane bonds by UV light results in an increase in the surface energy only in the exposed regions. Upon heating the polymer to a liquid, the Marangoni Effect causes these preprogrammed high surface energy exposed regions to rise, revealing the topography without the presence of the mask or a wet- or dry-etch development process. This process is not fundamentally limited to PS, experiments performed using poly(para-trimethylsilylstyrene) were equally amenable. In general, this approach could be applied to any light absorbing polymer that undergoes a photochemical change along with related formation of surface energy gradients. The short exposure and annealing times coupled with the diversity of prescribed patterns that can be created make this approach potentially useful for high-throughput processing for a wide variety of applications.

5.10 EXPERIMENTAL

5.10.1 Materials

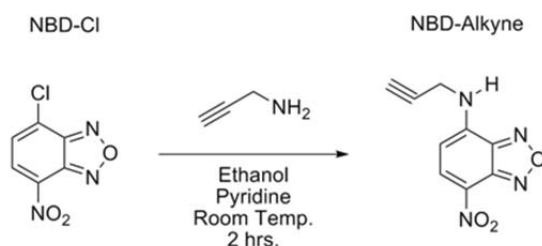
Chemicals used in this study were purchased from Fisher Scientific or Sigma Aldrich and used as received unless otherwise noted. Anisole and styrene were purified by stirring with basic alumina and calcium hydride for two hours and then filtered to remove solids. Tris(2-dimethylamino-ethyl)amine, Me₆TREN, was synthesized according to a published procedure.³⁷ Molecular weight and polydispersity data were measured using a Viscotek GPCMax VE 2001 Gel Permeation Chromatography (GPC) Solvent/Sample module with a Viscotek Model 270 Dual Detector Viscometer/Light Scattering detector, Viscotek VE 3580 Refractive Index Detector with 2 I-Series Mixed

Bed Low MW Columns using tetrahydrofuran (THF) as an eluent at 1 mL/min. Polymers were absolutely characterized by Viscotek Triple Detect software combining light scattering, refractive index detection and viscometry. Nuclear Magnetic Resonance (NMR) spectra were recorded on a Varian 400 MHz DirectDrive NMR with SMS sample changer. The midpoint glass transition temperature (T_g) of the bulk polymer samples were measured by differential scanning calorimetry (DSC) using a Mettler-Toledo DSC-1 with a 10 °C/min heating rate upon second heating. UV/Vis measurements were performed on a Thermo Scientific Evolution 220 UV-Visible Spectrophotometer.

The polymerization technique used to synthesize materials for this study was activators regenerated by electron transfer atom transfer radical polymerization (ARGET ATRP).³⁷⁻³⁹ Polystyrene (PS) ($M_n = 2900$, PDI = 1.2) was synthesized by dissolving an initiator (ethyl 2-bromoisobutyrate, 10:1 initiator to reducing agent) and styrene in anisole at 50 wt% solvent. Copper(II) bromide at 350 ppm copper to monomer was used as a catalyst and a ligand (Me_6TREN , 10:1 ligand to copper) was incorporated to aid in copper solubility. After the reactor was sealed and sparged with dry argon for 15 minutes, the reducing agent, tin(II) 2-ethylhexanoate, was injected and the reaction was allowed to proceed for 24 hours at 90°C. The resulting polymer was diluted with THF and run through basic alumina to remove the copper and ligand, dried under vacuum above the T_g (61 °C midpoint by DSC) of the polymer to remove residual solvents and then freeze dried from benzene.

For fluorescence microscopy experiments, a nitrobenzofurazan (NBD) fluorophore was covalently attached to the PS using established literature procedures for Cu^I -catalyzed azide/alkyne cycloaddition “click chemistry”.⁴⁰⁻⁴² The alkyne functionalized fluorophore was prepared by dissolving 4-chloro-7-nitro-2,1,3-benzoxadiazole (NBD-Cl) in ethanol in the presence of pyridine and adding

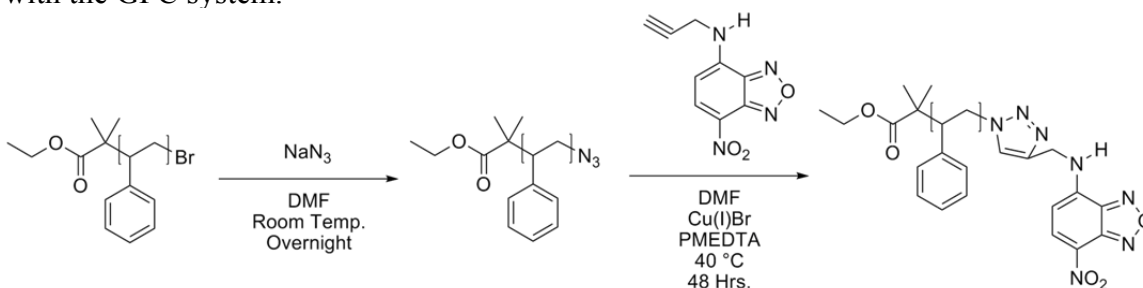
propargylamine (3-amino-1-propyne) drop-wise and stirring for two hours at room temperature (Scheme 5.2). The solvent was removed under vacuum and the resulting solid was purified by column chromatography (30% Ethyl acetate/petroleum spirits) to give 7-nitro-N-(prop-2-ynyl)-2,1,3-benzoxadiazol-4-amine (NBD-Aminyne) in 54% yield, purity was verified by NMR.



Scheme 5.2: Synthesis of alkyne-bearing NBD fluorophore

The azide-terminated PS (Scheme 5.3) was prepared by dissolving the polymer in N,N-dimethylformamide (DMF) with a three molar excess of sodium azide and stirring at room temperature overnight. The polymer was then precipitated in water three times to remove excess azide. As a reminder, no metals, not even a metal spatula, should be used in the handling of azides and no halide containing solvents should be used. A separate clearly labeled waste container should be used for all azide containing liquids. To attach the NBD-Aminyne to the polymer, each were dissolved in DMF at ~5 wt% (dried with calcium hydride and alumina) and a copper solubilizing ligand (N,N,N',N'',N''-Pentamethyldiethylenetriamine, PMEDTA, 1:1 ligand to copper) was added to the polymer solution, the ratio of fluorophore to polymer was 3:1. Cu(I)Br (1.5:1 copper to azide groups) was added to a third flask inside a glove box and sealed, then the two other solutions were added to this flask by cannula and the reaction was allowed to proceed for two days at 40 °C. The resulting polymer (PS-NBD) was precipitated in methanol seven

times to remove excess fluorophore as verified by absence of a small molecule fluorescence peak in GPC. By UV/Vis, 70% of the polymer chains contain a covalently attached fluorophore by comparison with NBD-Aminyne in the same solvent. Fluorophore attachment to the PS was verified by a Jasco FP-2020 Plus Intelligent Fluorescence Detector ($\lambda_{\text{excitation}} = 465 \text{ nm}$, $\lambda_{\text{emission}} = 520 \text{ nm}$, 18 nm bandpass) in line with the GPC system.



Scheme 5.3: ‘Click’ reaction of NBD fluorophore with PS polymer

5.10.2 Methods

5.10.2.1 Sample Preparation

Films in this study were spin coated (Specialty Coating Systems Spincoat G3-8) onto glass, quartz or silicon substrates with native oxide layers from solutions of either toluene or cyclopentanone. Glass and quartz substrates were prepared by soaking in a solution of ethanol, deionized water and potassium hydroxide (80/10/10 wt%) and then rinsed with deionized water and tetrahydrofuran at least three times. New silicon substrates with native oxide were prepared by repeated rinsing with isopropyl alcohol and acetone. Solution concentration was 4 wt% polymer and spin speeds varied from 800 – 1500 RPM to control the film thickness.^{43,44} The films were stabilized against dewetting by adding 1 wt% 50,000 g/mol PS (PDI = 1.06; Pressure Chemical). After spin coating, films were placed in a vacuum chamber at room temperature overnight. Average thicknesses for samples on glass were measured using a Veeco Dektak 6M Stylus Profiler

by recording ten measurements near the center of the film with a stylus force of 7 mg and a tip radius of 12.5 μm . Films prepared on silicon substrates were characterized by ellipsometry using a J.A. Woollam M-2000D Spectroscopic Ellipsometer.

5.10.2.2 Topographic Feature Formation

In order to create the surface energy pattern in the film, the spin coated films were placed on a non-reflecting surface and exposed to light from an Optical Building Blocks ScopeLite 200 (a broadband light source, intensity of 14 W/cm^2 at 4 mm from the liquid light guide outlet) through a mask for one minute for samples on glass (total dose = 840 J/cm^2) or ten seconds for samples on silicon (total dose = 140 J/cm^2 ; only features in Figures 4a and 4e were exposed on silicon) at a distance of 4 mm unless otherwise specified. Reduced exposure was appropriate for samples on silicon substrates due to the substrate reflectivity and substrate light absorption. Light intensity was measured using a Radiometer Fieldmax TO (Coherent) capable of a wavelength range 250 nm to 11,000 nm. A collimating lens was used for photoexposures shown in Figures 5.7-5.11 and for kinetic studies shown in Figures 5.12-5.14, however the exposure doses used were kept constant. The collimating lens was able to spread the light over the entire area of the films used and gave more even illumination; this led to more even topography over a larger area.

Line masks were Ronchi rulings (Edmond Optics), other mask patterns were from chrome on quartz photomasks (Photronics, Inc.). After light exposure, the film was heated to 110 $^{\circ}\text{C}$ for ten minutes on an Instec mK 1000 temperature controller with a HCS 402 hot stage and the resulting pattern was imaged using an optical microscope. The topography was characterized using the same stylus profiler used to determine film thickness. Color bright field imaging was performed on an Olympus BX 60 microscope

with a Spot Insight QE camera. Fluorescence imaging was performed with a Hamamatsu Orca R2 CCD camera with μ Manager software for camera control⁴⁵ on an Olympus BX 51 epifluorescence microscope. For imaging of NBD labeled polymers the excitation wavelength used was 465 nm with a 4 nm bandpass while the emission filter selected for all wavelengths greater than 520 nm.

5.10.2.3 Other Experimental Techniques

Fourier transform infrared (FTIR) spectra were recorded on a Thermo Nicolet 6700 FTIR with liquid nitrogen cooled MCT-B detector. Films were solution cast from carbon tetrachloride on a pressed potassium bromide disk. Fluorescence spectroscopy was performed on polymer solutions in THF on a double-beam Photon Technologies QuantaMaster 40 with a photomultiplier tube detection system with 4 nm excitation slits and 2 nm emission slits. Contact angles were measured with a Ramé-Hart, inc. NRL C.A. goniometer (Model #100-00). Atomic force microscopy (AFM) was performed using an Agilent 5500 AFM in tapping mode. All AFM images were obtained using antimony-doped silicon tapping mode AFM tips from Veeco with a resonant frequency of 300 kHz and a force constant of 20-80 N/m. X-ray photoelectron spectrometry (XPS) spectra were recorded using a commercial X-ray photoelectron spectrometer (Kratos Axis Ultra), utilizing a monochromatic Al-K α X-ray source ($h\nu = 1486.5$ eV), hybrid optics (employing a magnetic and electrostatic lens simultaneously) and a multi-channel plate and delay line detector coupled to a hemispherical analyzer. The photoelectron take-off angle was normal to the surface of the sample and 45° with respect to the X-ray beam. The pressure in the analysis chamber was typically 4×10^{-9} Torr during data acquisition. Casa XPS analysis software was used to determine the stoichiometry of the samples from

corrected peak areas and employing Kratos sensitivity factors for each element of interest.

5.11 REFERENCES

1. Larson, R. G. *Angewandte Chemie International Edition* **2012**, *51*, 2546-2548.
2. Scriven, L. E.; Sternling, C. V. *Nature* **1960**, *187*, 186-188.
3. Thomson, J. *On certain curious motions observable at the surfaces of wine and other alcoholic liquors*, 1855.
4. Marangoni, C. *Sull'espansione delle gocce liquide*, 1865.
5. Bron, A. J.; Tiffany, J. M.; Gouveia, S. M.; Yokoi, N.; Voon, L. W. *Exp. Eye Res.* **2004**, *78*, 347-360.
6. Cazabat, A. M.; Heslot, F.; Troian, S. M.; Carles, P. *Nature* **1990**, *346*, 824-826.
7. Xia, Y. N.; Whitesides, G. M. *Annu. Rev. Mater. Sci.* **1998**, *28*, 153-184.
8. Briseno, A. L.; Mannsfeld, S. C. B.; Ling, M. M.; Liu, S.; Tseng, R. J.; Reese, C.; Roberts, M. E.; Yang, Y.; Wudl, F.; Bao, Z. *Nature* **2006**, *444*, 913-917.
9. Wu, H. K.; Odom, T. W.; Chiu, D. T.; Whitesides, G. M. *J. Am. Chem. Soc.* **2003**, *125*, 554-559.
10. Rolland, J. P.; Maynor, B. W.; Euliss, L. E.; Exner, A. E.; Denison, G. M.; DeSimone, J. M. *J. Am. Chem. Soc.* **2005**, *127*, 10096-10100.
11. Rajnicek, A. M.; Britland, S.; McCaig, C. D. *J. Cell Sci.* **1997**, *110*, 2905-2913.
12. Carman, M. L.; Estes, T. G.; Feinberg, A. W.; Schumacher, J. F.; Wilkerson, W.; Wilson, L. H.; Callow, M. E.; Callow, J. A.; Brennan, A. B. *Biofouling* **2006**, *22*, 11-21.
13. Schumacher, J. F.; Carman, M. L.; Estes, T. G.; Feinberg, A. W.; Wilson, L. H.; Callow, M. E.; Callow, J. A.; Finlay, J. A.; Brennan, A. B. *Biofouling* **2007**, *23*, 55-62.
14. Gallardo, B. S.; Gupta, V. K.; Eagerton, F. D.; Jong, L. I.; Craig, V. S.; Shah, R. R.; Abbott, N. L. *Science* **1999**, *283*, 57-60.
15. Grunze, M. *Science* **1999**, *283*, 41-42.
16. Strawhecker, K. E.; Kumar, S. K.; Douglas, J. F.; Karim, A. *Macromolecules* **2001**, *34*, 4669-4672.

17. Cai, Y.; Newby, B. M. Z. *J. Am. Chem. Soc.* **2008**, *130*, 6076-6077.
18. Wong, S.; Kitaev, V.; Ozin, G. A. *J. Am. Chem. Soc.* **2003**, *125*, 15589-15598.
19. Millan, M. D.; Locklin, J.; Fulghum, T.; Baba, A.; Advincula, R. C. *Polymer* **2005**, *46*, 5556-5568.
20. Nagai, N.; Matsunobe, T.; Imai, T. *Polym. Degrad. Stabil.* **2005**, *88*, 224-233.
21. Nurmukhametov, R.; Volkova, L.; Kabanov, S. *Journal of Applied Spectroscopy* **2006**, *73*, 55-60.
22. Simons, J. K.; Chen, J. M.; Taylor, J. W.; Rosenberg, R. A. *Macromolecules* **1993**, *26*, 3262-3266.
23. Zhang, D.; Dougal, S. M.; Yeganeh, M. S. *Langmuir* **2000**, *16*, 4528-4532.
24. Mundra, M. K.; Ellison, C. J.; Behling, R. E.; Torkelson, J. M. *Polymer* **2006**, *47*, 7747-7759.
25. Coates, J. In *Encyclopedia of Analytical Chemistry*; Meyers, R. A., Ed.; John Wiley & Sons Ltd.: Chichester, 2000, p 10815-10837.
26. Peng, J.; Wang, H.; Li, B.; Han, Y. *Polymer* **2004**, *45*, 8013-8017.
27. Rogers, J. A.; Nuzzo, R. G. *Materials Today* **2005**, *8*, 50-56.
28. Xia, Y.; Whitesides, G. M. *Annual Review of Materials Science* **1998**, *28*, 153-184.
29. Reichenbach, J.; Linde, H. J. *Colloid Interface Sci.* **1981**, *84*, 433-443.
30. Weh, L. *Mater. Sci. Eng. C-Biomimetic Supramol. Syst.* **1999**, *8-9*, 463-467.
31. Wu, K. H.; Lu, S. Y.; Chen, H. L. *Langmuir* **2006**, *22*, 8029-8035.
32. Doi, M.; Edwards, S. F. *The Theory of Polymer Dynamics*; Clarendon Press: Oxford, 1986.
33. *Polymer Handbook*; Brandrup, J.; Immergut, E. H.; Grulke, E. A., Eds.; Wiley and Sons: Hoboken, New Jersey, 1999.

34. Bicerano, J. *Prediction of Polymer Properties*; 3rd ed.; Marcel Dekker, Inc.: New York, 2002.
35. Elman, J. F.; Johs, B. D.; Long, T. E.; Koberstein, J. T. *Macromolecules* **1994**, *27*, 5341-5349.
36. Jalbert, C.; Koberstein, J. T.; Yilgor, I.; Gallagher, P.; Krukoni, V. *Macromolecules* **1993**, *26*, 3069-3074.
37. Fu, G. D.; Xu, L. Q.; Yao, F.; Zhang, K.; Wang, X. F.; Zhu, M. F.; Nie, S. Z. *ACS Appl. Mater. Interfaces* **2009**, *1*, 239-243.
38. Jakubowski, W.; Kirci-Denizli, B.; Gil, R. R.; Matyjaszewski, K. *Macromol. Chem. Phys.* **2008**, *209*, 32-39.
39. Pintauer, T.; Matyjaszewski, K. *Chem. Soc. Rev.* **2008**, *37*, 1087-1097.
40. Binder, W. H.; Sachsenhofer, R. *Macromolecular Rapid Communications* **2007**, *28*, 15-54.
41. McGill, N. W.; Williams, S. J. *J. Org. Chem.* **2009**, *74*, 9388-9398.
42. Rostovtsev, V. V.; Green, L. G.; Fokin, V. V.; Sharpless, K. B. *Angewandte Chemie International Edition* **2002**, *41*, 2596-2599.
43. Hall, D. B.; Underhill, P.; Torkelson, J. M. *Polym. Eng. Sci.* **1998**, *38*, 2039-2045.
44. Spangler, L. L.; Torkelson, J. M.; Royal, J. S. *Polym. Eng. Sci.* **1990**, *30*, 644-653.
45. Edelstein, A.; Amodaj, N.; Hoover, K.; Vale, R.; Stuurman, N. *Computer Control of Microscopes Using μ Manager*; John Wiley & Sons, Inc., 2001.

Chapter 6: Cross-linkable Topographic Features Created via Orthogonal Photochemistry and the Marangoni Effect

6.1 INTRODUCTION

The topographic features formed by Marangoni flow as described in the previous chapter are not dimensionally stable at high temperature. While there can be advantages to the ‘cyclability’ of the process, that is the features can be erased from a film and new ones written (see Section 5.4), many industrially relevant processes require high temperatures or solvents for deposition of over-layers in the construction of multi-layer films which would render this approach unsuitable for use. A route to overcome this obstacle, utilizes ‘orthogonal photochemistry’ to preserve the topographic features after they are formed. In this approach, two different benzophenone based sensitizers are doped into the polymer film and activated sequentially. The first compound is used to induce topographic feature formation via the Marangoni Effect while the second is used to cross-link the film and stabilize the topographic features during prolonged heating or exposure to solvents.

6.2 ORTHOGONAL PHOTOCHEMISTRY

Orthogonal chemistry generally means that two species or protecting groups are activated independently of one another. In this case the method of selection of one species or another is through the selection of the wavelength of light tailored to the absorbance of individual species. A schematic of the process used is shown in Figure 6.1a. First, the film is exposed through a photomask and a bandpass filter at a wavelength that activates a species that photochemically grafts to create regions of relatively high and low surface energy. Next, upon heating the polymer through its glass transition temperature (T_g) to reduce its viscosity, the Marangoni effect causes the polymer to flow

from unexposed (low surface energy) to exposed (high surface energy) region. This creates three-dimensional topography reflective of the photomask pattern. If no further steps are taken, upon additional heating the topography dissipates due to inter-diffusion of the exposed and unexposed regions leading to recovery of a flat film. However, if the film is exposed again at a through a bandpass filter at a wavelength that is absorbed by a light activated cross-linker, the features become thermally stable and do not dissipate with additional heating.

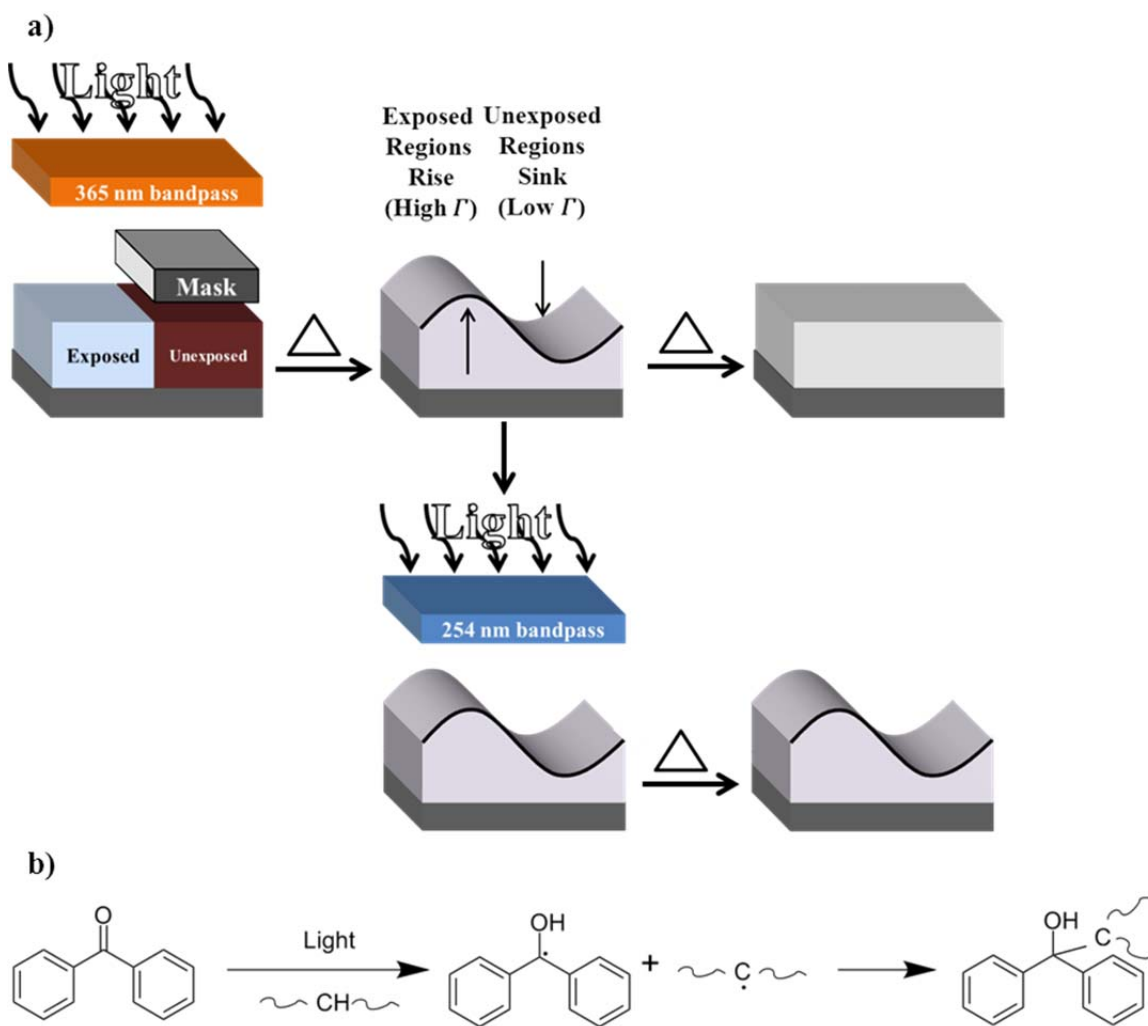


Figure 6.1: Schematic of orthogonal photochemistry used for a) topographic feature formation via the Marangoni effect and subsequent cross-linking in the second exposure. b) Generic attachment of benzophenone to a carbon atom via hydrogen abstraction.

6.2.1 Host Polymer

Poly(isobutyl methacrylate) (PiBMA) was selected as the host polymer in which to form topography in these experiments for a few reasons. First, and perhaps most importantly, it is nearly completely transparent at all of the relevant wavelengths so it will not interfere with the photochemistry of the light activated compounds. Second, it

has a T_g that is only moderately above room temperature (55 °C for the bulk polymer) which allows feature development to occur relatively rapidly at temperatures that do not degrade the polymer.

6.2.2 Photoactive Compounds

A major challenge is selection of two light absorbing compounds that both act on PiBMA, but have different activating wavelengths. Benzophenones were selected as the photoactive species for both steps of this project because of their ambient stability and well-understood photochemistry.¹ Extensive literature has demonstrated that benzophenone is a non-specific hydrogen abstractor that forms radical intermediates. A common result following hydrogen abstraction is coupling between the benzophenone and the hydrogen abstraction site. This process is depicted in Figure 6.1b.² Furthermore, PiBMA containing 5.5 mol% copolymerized benzophenone pendant groups has been shown to photo cross-link in a previous study.² The photosensitizer used to induce topographic feature formation via the Marangoni effect is a commercially available benzophenone derivative, Michler's Ketone (MK, Figure 6.2a). The compound used to cross-link the film after feature formation is a di-functional benzophenone derivative ethane-1,2-diyl bis(3-benzoylbenzoate) or bis-benzophenone (BB, Figure 6.2b). The synthesis of this compound³ can be found in the experimental section at the end of this chapter. Figure 6.2c shows the percent transmission by UV/Vis of each of these compounds doped into PiBMA and the absorbance of PiBMA itself along with the wavelengths that were used to activate the individual species. At 365 nm MK is strongly absorbing and the BB absorbs less than 3% of incident light, even in these thicker films.

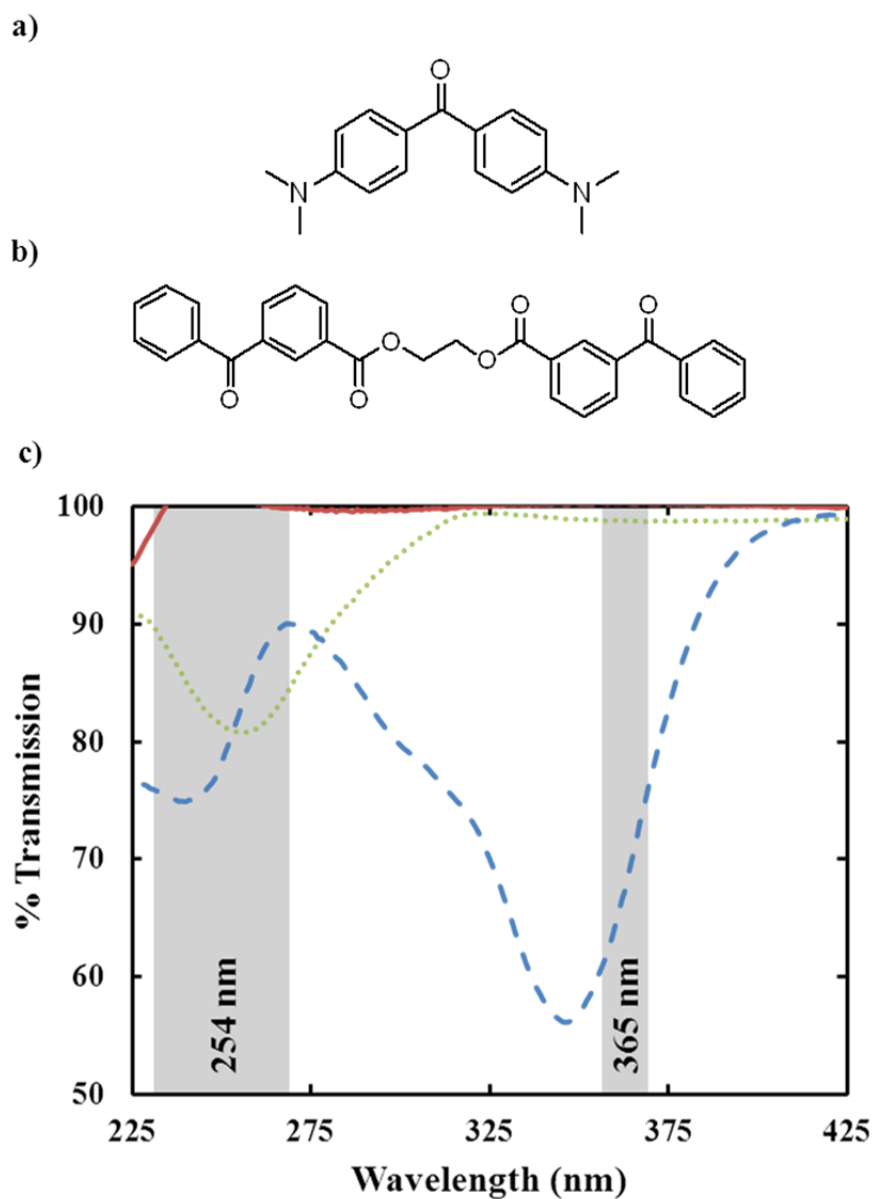


Figure 6.2: a) Structure of Michler's ketone (MK). b) Structure of bis-benzophenone (BB). c) UV/Vis absorption spectra of PiBMA (solid line), PiBMA with 10 wt% MK (dashed line), and PiBMA with 10 wt% BB (dotted line). Films were all approximately 400 nm thick on quartz. Shaded regions indicate bandpass filters used to activate MK (365 nm, 10 nm FWHM) and the BB (254 nm, 40 nm FWHM).

Through the use of bandpass filters during photoexposure, the MK can be selectively activated independent of BB, allowing topography to develop without cross-linking. It is important to note that it is not important if the MK also absorbs light when the BB is being activated because at this point the topography is already in place so further activation of the MK does not impact the final topographic state of the film.

6.3 FEATURE FORMATION AND CROSS-LINKING

Figure 6.3a demonstrates that topography can be formed in a film of PiBMA containing only 2 wt% MK by exposure to 6 J/cm^2 through the 365 nm bandpass filter on top of a photomask followed by heating for 60 minutes at $125 \text{ }^\circ\text{C}$. All photoexposure doses are measured through the bandpass filter used for the exposure step. The peak to valley height of these features is 75 nm. If heated further at $170 \text{ }^\circ\text{C}$, the features dissipate as shown in Figure 6.3b. The addition of 10 wt% BB to the thin film and identical procedures to develop topography with a 230 nm peak to valley height (Figure 6.3c) is not sufficient to stabilize topography under the same conditions as above (Figure 6.3d). This image is representative of the pattern deterioration over the entire sample. The reason that the features are larger in the film containing both BB and MK is that at the same temperature the heating step in which topography develops is further from the T_g of the film due to plasticization. This will be discussed in more detail later in the chapter. However, if after feature formation (Figure 6.3e) the exact same film is subsequently exposed to 8 J/cm^2 through the 254 nm bandpass filter and subjected to the same heating conditions the change in the topography is persists (Figure 6.3f). There is a change in the topographic feature peak to valley height to 270 nm after cross-linking, this may be due to stress induced by cross-linking process being relieved upon heating. The changes that occur happen within a few minutes of heating and then do not change further with

continued heating. Additionally, features have been observed to form with similar light intensity with light exposure times of 5 seconds followed by 5 minutes of heating (Figure 6.4), which indicates that the potential throughput of this technique is relatively high. Furthermore, experiments in which the photomask has isolated topographic features demonstrates clearly that the exposed regions of the film 'rise' upon heating the polymer above its T_g .

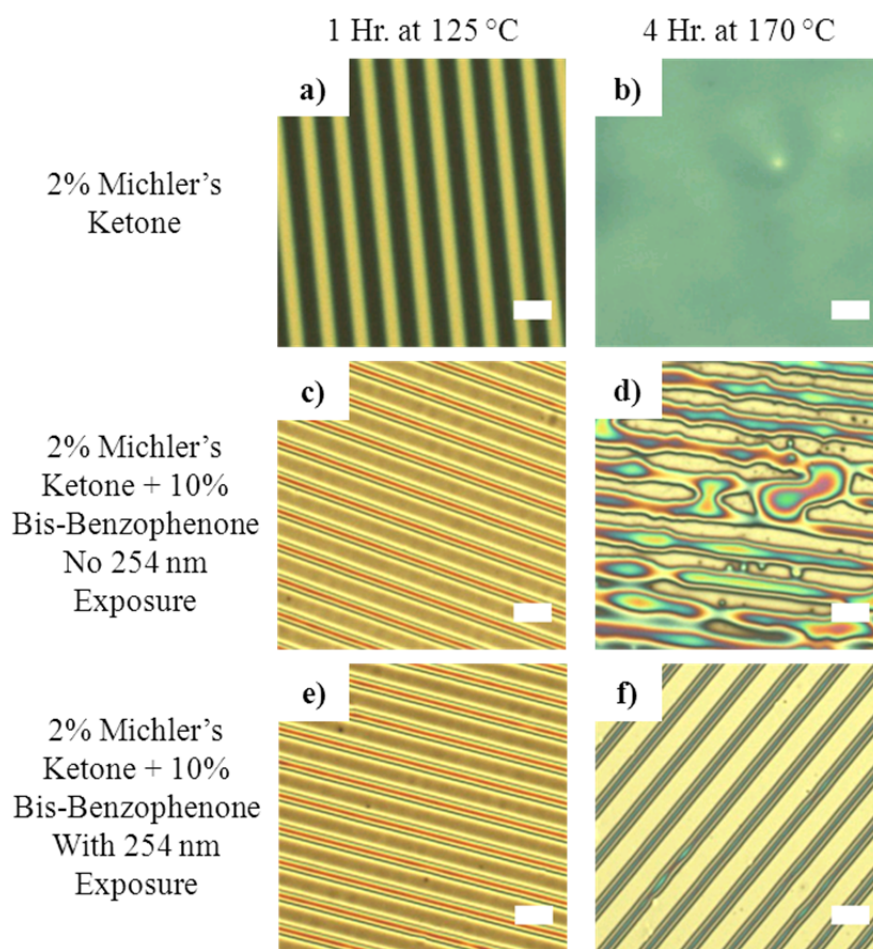


Figure 6.3: Films with only 2% MK a) immediately after features formed by heating and b) after the features decay with continued heating. Films containing 2% MK and 10% BB c) immediately after features formed by heating and d) after the features decay after continued heating without exposure at 254 nm. Films containing 2% MK and 10% BB e) immediately after features formed by heating and f) after exposure at 254 nm to cross-link and continued heating showing topographic feature stabilization. Scale bars are 30 μm . Colors are formed from interference due to changes in film thickness. All films are roughly 100 nm thick before patterning.

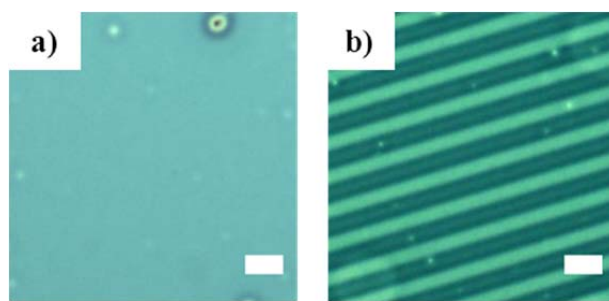


Figure 6.4: Film of PiBMA with 2% MK and 10 wt% BB a) after 5 seconds of photoexposure and b) topographic features formed after 5 minutes of subsequent heating at 125 °C. Topography is roughly 15 nm in peak to valley height at this point. Scale bars are 30 μm .

This was not the first example of benzophenones being used as a way to activate topography formation; another recent study used a benzophenone derivative as a method of shifting the wavelength of light used to create surface relief structures in polystyrene exposed in the liquid state from ~ 254 nm to 365 nm.⁴ However in their previous work⁵ they hypothesized that their surface relief structures formed due to differences in “diffusibilities” with significant molecular weight changes upon exposure rather than Marangoni driven flow. As will be discussed later in this chapter, no changes in molecular weight were observed during this process.

6.4 QUANTIFICATION OF PHOTO-CONVERSION

6.4.1 Michler’s Ketone

In its photoexcited state, a benzophenone can abstract hydrogen non-specifically from neighboring C-H bonds, leading to the formation of a hydroxyl group in place of the original carbonyl as previously discussed. 4,4’ substituted benzophenone derivatives, like MK, are expected to exhibit similar behavior. Fourier transform infrared spectroscopy (FTIR) of films spin cast on double-side polished silicon wafers was used to track the conversion of both MK and BB. For MK, 2 wt% was doped into a PiBMA film (see

Figure 6.5 for representative FTIR spectra). The carbonyl in the center of the molecule exhibits an absorption peak at 1601 cm^{-1} according to an online database⁶ which decreases as a function of exposure dose. Potential changes in film thickness can be accounted for by normalizing to the peak corresponding to the carbonyl in the methacrylate group and initiator fragment ($1701\text{-}1770\text{ cm}^{-1}$). While there is some broadening to this peak due to chemical changes in the system, the total number of ester carbonyls in this peak, and therefore the peak area, should remain constant. The conversion calculated in this manner is shown in Figure 6.6. This experiment was performed with a light intensity of 65.8 mW/cm^2 through the 365 nm bandpass filter which results in significant conversion of the MK very rapidly, $\sim 40\%$ within the first minute. Furthermore, since features were observed with exposures of 5 seconds as previously discussed (Figure 6.4) this indicates that very little conversion of the MK ($\sim 5\%$) is necessary for topography formation.

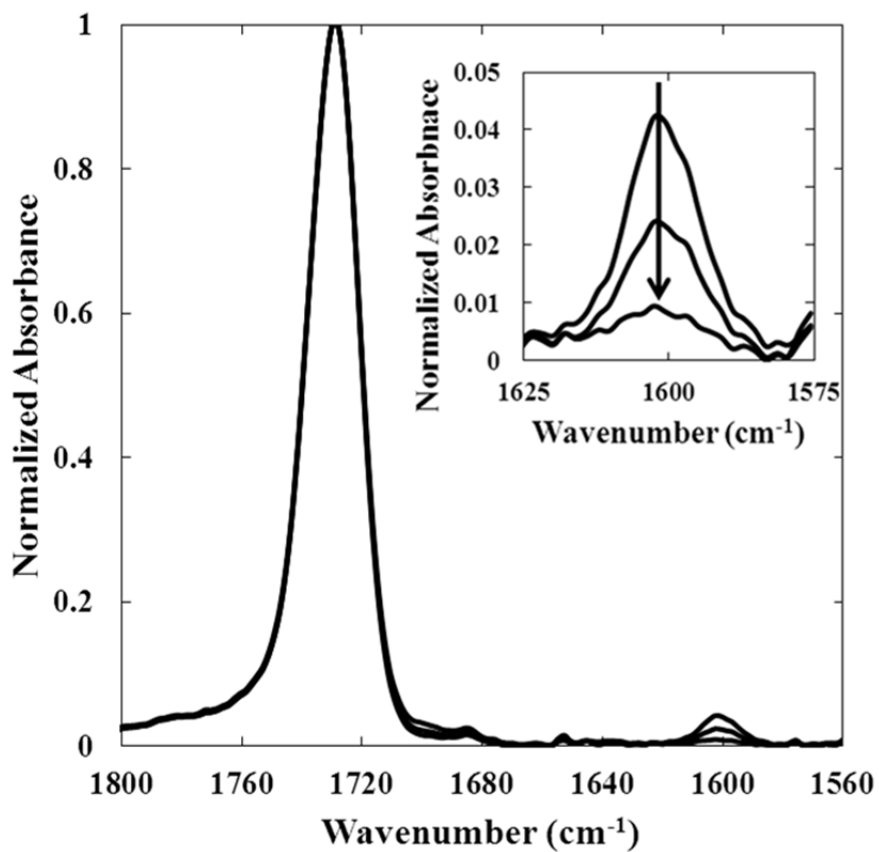


Figure 6.5: Representative IR spectra, inset shows MK carbonyl peak with an arrow indicating the direction of increasing photoexposure. In the direction of the arrow the photoexposure doses for each spectrum are 0 J/cm², 4 J/cm², and 125 J/cm². Data are normalized to the tallest carbonyl peak.

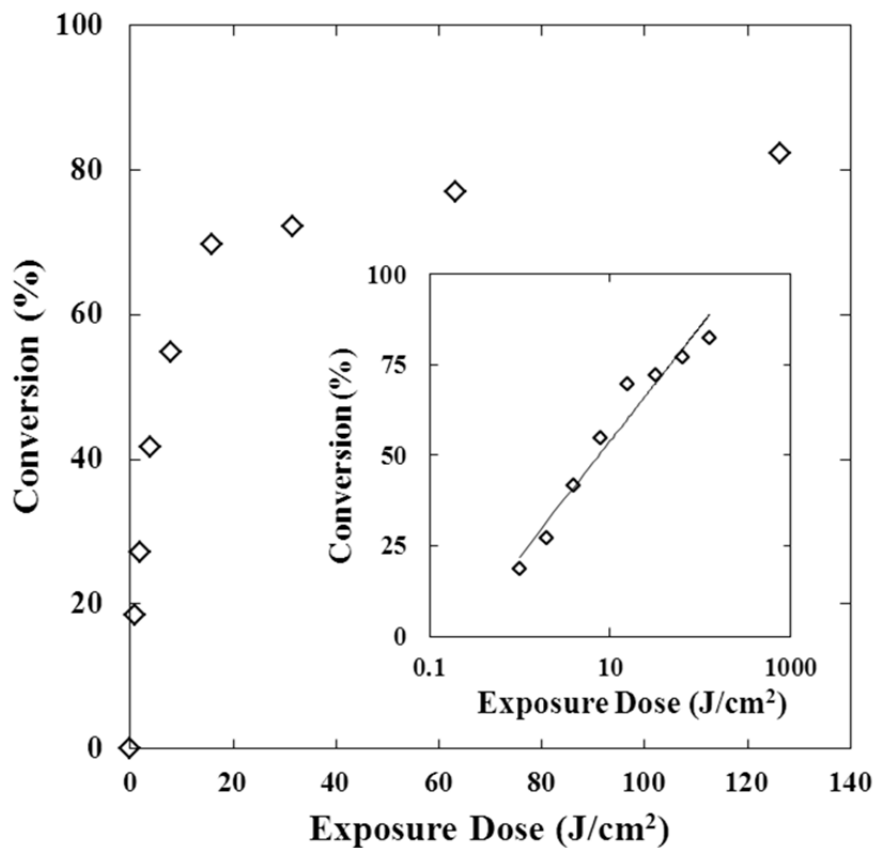


Figure 6.6: Conversion of MK by FTIR. Inset is on a logarithmic scale with best fit line to guide the eye.

Generically, hydroxyl containing materials have higher surface energies than the corresponding ketone analogs, for example poly(vinyl alcohol) has a significantly higher (by ~ 9 dyne/cm) surface energy than poly(vinyl acetate).⁷ Local increases in surface energy can lead to Marangoni driven flow upon heating the polymer through its T_g . While not a direct measure of surface energy, contact angles of various test liquids were measured by goniometry on PiBMA with 2 wt% MK. No statistically significant change in contact angle with exposure time was observed using 300 g/mol poly(ethylene glycol) as a test liquid (Figure 6.7) even after 30 J/cm² of exposure through the 365 nm bandpass filter. However, the change necessary to induce Marangoni driven flow is less than 0.1

dyne/cm, well within the uncertainty of the contact angle measurements. It is important to note that if the surface energy did not change in some fashion, topography would not form upon heating. Water, while the most common test liquid, proved to be an unsuitable for these measurements as it rapidly absorbs into the PiBMA film. As previously mentioned, exposed regions of the film rise during heating after photoexposure using a mask with isolated topographic features. This is an indication of surface energy rising in these regions as the Marangoni effect causes the polymer to flow from regions of relatively low surface energy to relatively high surface energy.

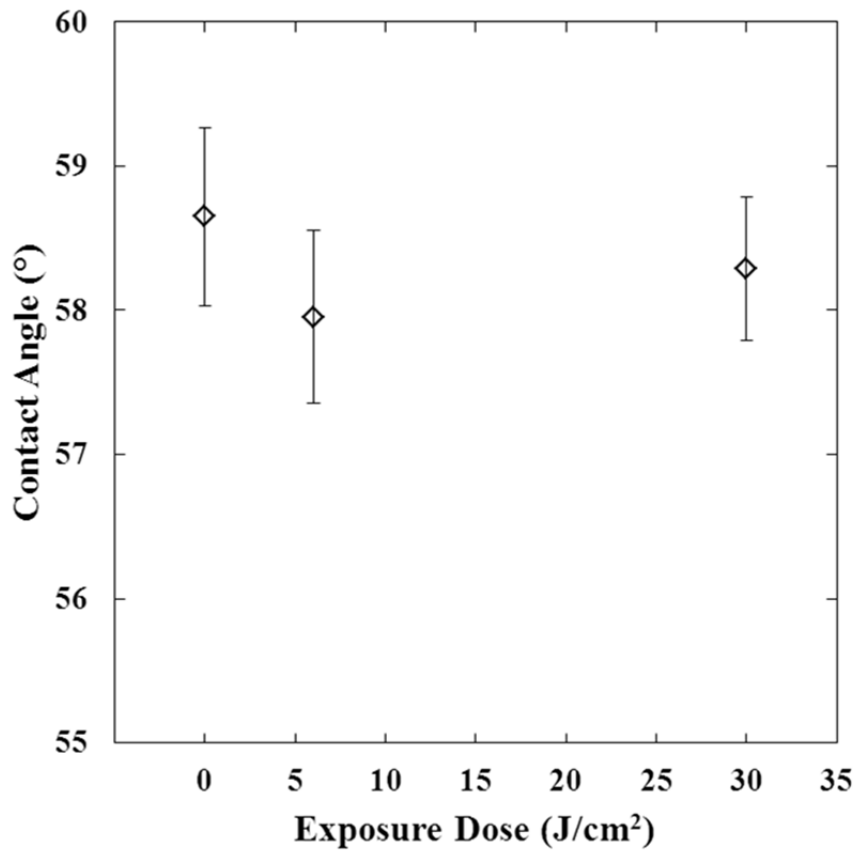


Figure 6.7: Contact angle of poly(ethylene glycol) on PiBMA films with 2 wt% MK as a function of exposure dose. Error bars represent standard deviations from 10 measurements.

Gel permeation chromatography (GPC) confirms that there is a covalent attachment of the MK to the PiBMA backbone during photoexposure using the 365 nm bandpass filter. Figure 6.8a shows fluorescence traces from fluorimeter that is in line with the GPC system set to detect MK ($\lambda_{\text{excitation}} = 386 \text{ nm}$, $\lambda_{\text{emission}} = 457 \text{ nm}$). Before photoexposure only one fluorescence peak exists, corresponding to the ‘small molecule dump’ elution volume at the end of the GPC run. However, after photoexposure there are two peaks, one corresponding to the ‘small molecule dump’ and the other that corresponds with the refractive index detector peak which is sensitive to polymer concentration. Furthermore, no differences between the exposed and unexposed films are present in the elution curves given by the refractive index detector, indicating that there is no chain-chain coupling or molecular weight shifts during the photoexposure that activates the MK (Figure 6.8b).

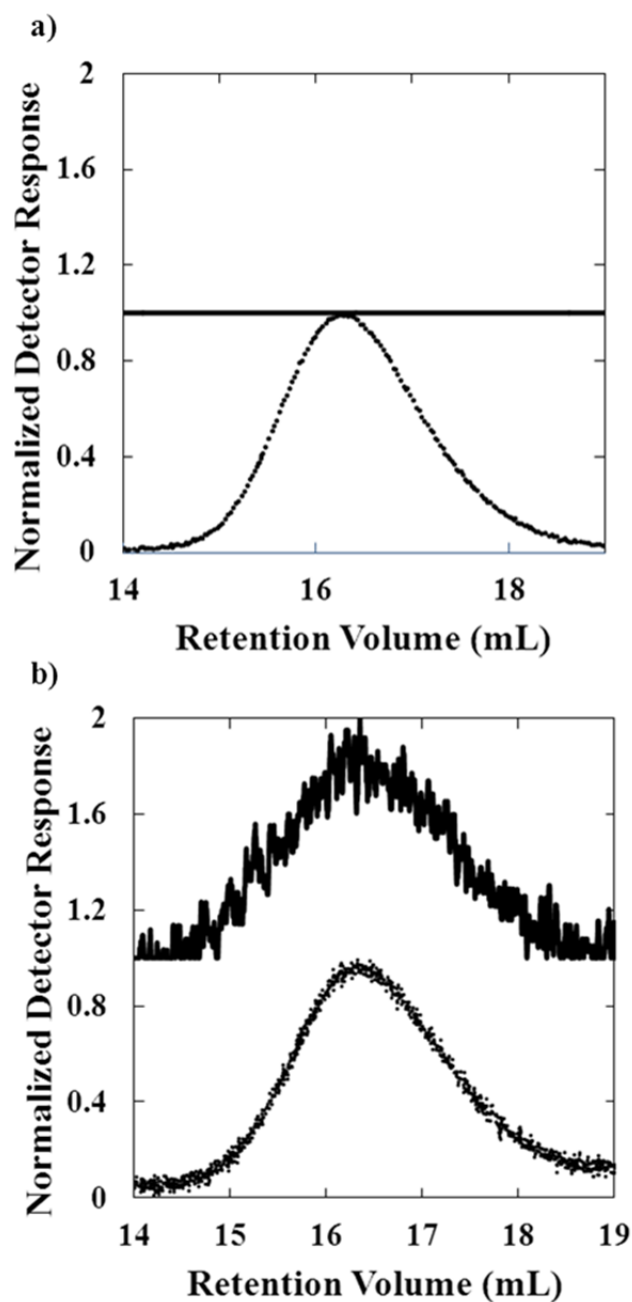


Figure 6.8: Gel permeation chromatography of PiBMA + 2 wt% MK. a) Before photoexposure showing a peak in the refractive index detector (broken line) no fluorescence peak (solid line). b) After photoexposure showing coincident refractive index and fluorescence peaks indicating covalent attachment of MK to the polymer. The fluorescence signal has been vertically shifted for clarity.

6.4.2 Bis-Benzophenone

To characterize the photochemical conversion of BB 10 wt% was doped into a film of PiBMA. Conversion is characterized using the area under carbonyl peak of the BB that appears at 1666 cm^{-1} normalized to the ester carbonyl peak ($1701\text{-}1770\text{ cm}^{-1}$) (see Figure 6.9 for representative FTIR Spectra) and increases monotonically with exposure dose (Figure 6.10).

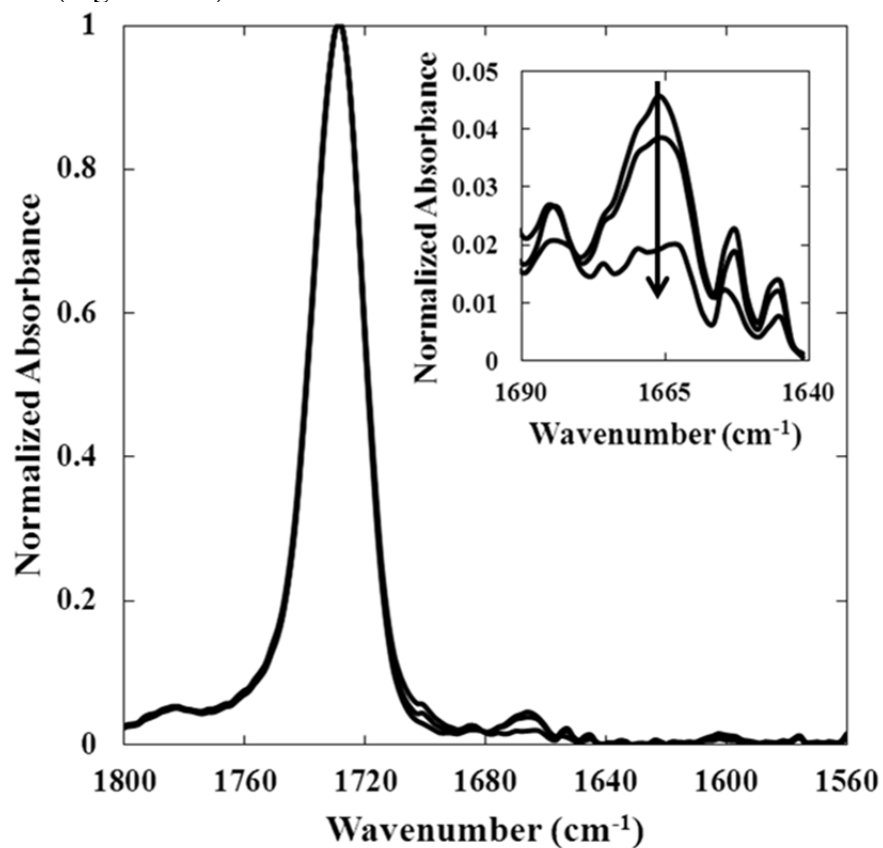


Figure 6.9: Representative IR spectra, inset shows the BB carbonyl peak with an arrow indicating the direction of increasing photoexposure. In the direction of the arrow the photoexposure doses for each spectrum are 0 J/cm^2 , 0.5 J/cm^2 , and 4 J/cm^2 . Data are normalized to the tallest carbonyl peak.

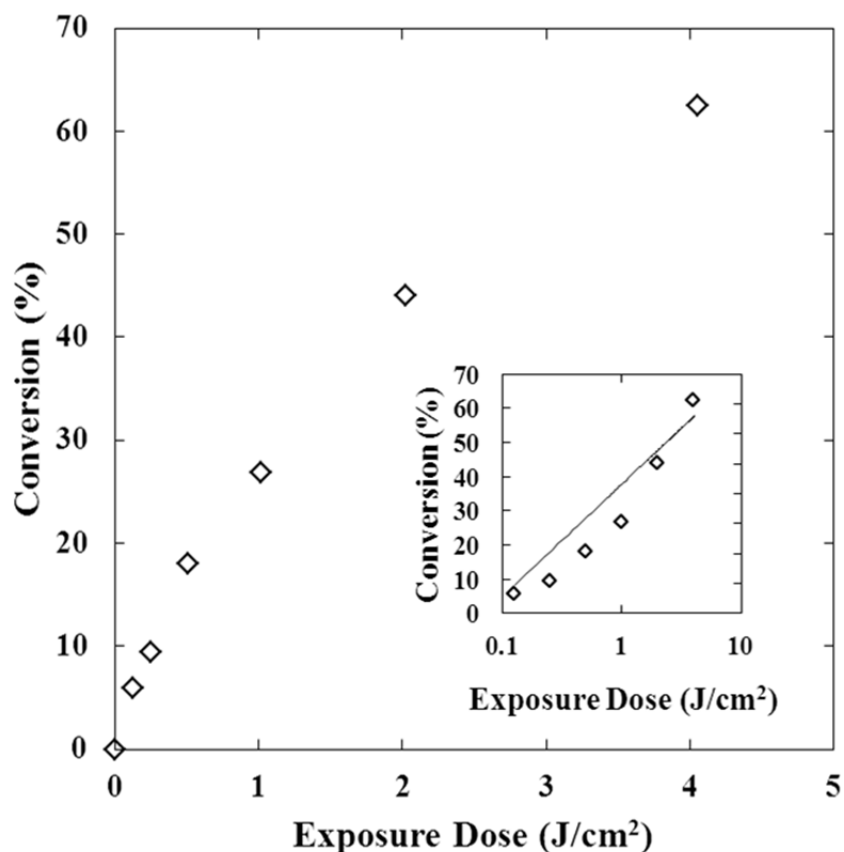


Figure 6.10: Conversion of BB by FTIR. Inset is on a logarithmic scale with best fit line to guide the eye.

Cross-linking of the polymer films is necessary in order to stabilize the topography from thermal dissipation. In order to characterize the degree of cross-linking, both the loading of BB and photoexposure dose through the 254 nm bandpass filter were varied. After light exposure, the film thickness was measured and then films were soaked in tetrahydrofuran (THF), which is a good solvent for the polymer and BB, dried at 80 °C for ten minutes, and the film thickness was reanalyzed. Table 6.1 shows the soluble percent of the polymer, as characterized by a reduction in film thickness, as a function of both cross-linker loading and exposure dose. As is expected, increasing exposure dose and amount of cross-linker both decrease the soluble fraction of the polymer films. These

experiments were designed to guide the loading and dose necessary to stabilize the topography and impart heat insensitivity as achieved in Figure 6.3. As shown previously (Figure 6.4) the 10 wt% BB and 8 J/cm² photoexposure was sufficient to prevent topographic feature decay over extended periods of time at high temperatures even though 74% of the film dissolves upon soaking in THF. It is possible that additional photoexposure may allow for a decreased loading of BB or a reduction in the topographic feature size change after cross-linking.

Cross-linker content	Exposure Dose			
	0.5 J/cm ²	2 J/cm ²	8 J/cm ²	16 J/cm ²
5 wt% BB	100%	100%	100%	94%
10 wt% BB	100%	100%	74%	51%
15 wt% BB	100%	100%	29%	25%

Table 6.1: Percent of polymer film dissolved as a function of both wt% BB (balance is PiBMA) and exposure dose through the 254 nm bandpass filter. Solubility is defined as percentage reduction in film thickness after the film is soaked in THF and dried as characterized by spectroscopy ellipsometry.

6.5 PiBMA PLASTICIZATION

One of the significant issues with using small molecule dopants in polymer films is plasticization of the film, which causes a reduction in the T_g of the film. Since the bulk T_g of the PiBMA used in this study is relatively close to room temperature (55 °C midpoint), addition of >10% small molecule additives could reduce the T_g significantly to the point that during exposure the modest heating caused by the light source could cause the polymer to undergo a phase change to a liquid state. Table 6.2 contains the T_g of the compositions used in this study. It is for this reason that all exposures were performed with active cooling to 15 °C so that samples remained glassy during photoexposure.

PiBMA (wt%)	MK (wt%)	BB (wt%)	T _g Midpoint (°C)
100	0	0	55
98	2	0	48
90	0	10	34
88	2	10	27

Table 6.2: T_g of various compositions used in this study showing plasticization effect of small molecules on PiBMA.

6.6 CONCLUSION

In this chapter a method of stabilizing topography created from Marangoni driven flow against thermal dissipation was achieved via orthogonal photochemistry of benzophenones. To form topography, a commercially available benzophenone (MK) covalently attaches to the polymer chain during photoexposure through a 365 nm bandpass filter while the polymer is in the solid state. Upon heating to a liquid state, topography forms via the Marangoni effect due to gradients in surface energy imparted by local attachment of MK to the polymer chain with no observed shift in molecular weight. In order to stabilize this topography a di-functional benzophenone (BB) derivative forms cross-links between polymer chains upon photoexposure through a 254 nm bandpass filter. The topography appears to be stable indefinitely, even at temperatures that otherwise have been shown cause degradation of the topographic pattern. Future work to reduce the amount of small molecules added to the polymer film necessary for both topography formation and cross-linking is necessary for the increased utility of this process.

6.7 EXPERIMENTAL

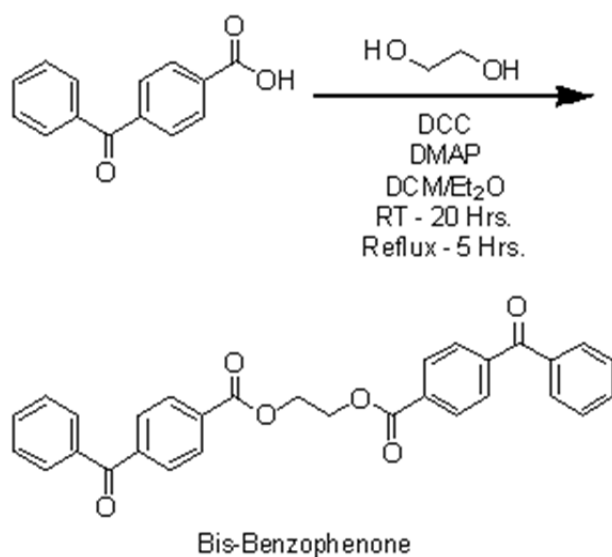
6.7.1 Materials and Material Characterization

Chemicals used in this study were purchased from Fisher Scientific or Sigma Aldrich and used as received unless otherwise noted. Anisole and isobutyl methacrylate were purified by stirring with basic alumina and calcium hydride (roughly 1g/100mL liquid each) for two hours and then filtered to remove solids. Tris(2-dimethylamino-ethyl)amine, Me₆TREN, was synthesized according to a published procedure.⁸ Molecular weight and polydispersity data were measured using a Viscotek GPCMax VE 2001 Gel Permeation Chromatography (GPC) Solvent/Sample module with a Viscotek Model 270 Dual Detector Viscometer/Light Scattering detector, Viscotek VE 3580 Refractive Index Detector with 2 I-Series Mixed Bed Low MW Columns using tetrahydrofuran (THF) as an eluent at 1 mL/min. Polymers were characterized absolutely by Viscotek Triple Detect software combining light scattering, refractive index detection and viscometry. Experiments to detect the attachment of photoactive compounds were performed with a Jasco FP-2020 Plus Intelligent Fluorescence Detector (18 nm bandpass) in line with the GPC system. Nuclear Magnetic Resonance (NMR) spectra were recorded on a Varian 400 MHz DirectDrive NMR with SMS sample changer. The midpoint glass transition temperature (T_g) of the bulk and doped polymers were measured by differential scanning calorimetry (DSC) using a Mettler-Toledo DSC-1 with a 10 °C/min heating rate upon second heating. UV/Vis measurements were performed on a Thermo Scientific Evolution 220 UV-Visible Spectrophotometer.

The polymerization technique used to synthesize materials for this study was activators regenerated by electron transfer atom transfer radical polymerization (ARGET ATRP).⁸⁻¹⁰ Poly(isobutyl methacrylate) (PiBMA) ($M_n = 10.6$ kg/mol, PDI = 1.16) was synthesized by dissolving an initiator (ethyl 2-bromoisobutyrate) and styrene in anisole

(70 wt% solvent). Copper(II) bromide (400 ppm copper to monomer) was used as a catalyst and a ligand (Me₆TREN, 10:1 ligand to copper) was incorporated to aid in copper solubility. After the reactor was sealed and sparged with dry argon for 15 minutes, the reducing agent, tin(II) 2-ethylhexanoate (10:1 initiator to reducing agent), was injected and the reaction was allowed to proceed for 24 hours at 90°C. The resulting polymer was diluted with THF and run through basic alumina to remove the copper and ligand, dried under vacuum above the T_g (55 °C midpoint by DSC) of the polymer to remove residual solvents and then freeze dried from benzene.

Bis-benzophenone (ethane-1,2-diyl bis(3-benzoylbenzoate), BB) was synthesized according to a published procedure, see Scheme 6.1.³ To explain in more detail, 3-benzoyl-benzoic acid (6.7 g) was dissolved in a three neck flask fitted with a reflux condenser in 250 mL methylene chloride and 50 mL diethyl ether along with 4-pyrrolidinopyridine (0.4 g) and dicyclohexylcarbodiimide (6.1 g) and the reaction was sparged with dry argon for 30 mins. Ethylene glycol (0.93 g) was separately dissolved in about 20 mL of methylene chloride and sparged with dry argon for 10 minutes and then cannulated into the reaction vessel. The reaction was allowed to proceed at room temperature overnight and then refluxed for five hours. The reaction mixture was then filtered and washed with fresh methylene chloride. The solution was then liquid/liquid extracted with deionized water (3 x 100mL), 5% acetic acid (3 x 100 mL), deionized water (2 x 100 mL) and concentrated sodium chloride solution (1 x 100 mL). The organic layer was then dried with magnesium sulfate and the solvent removed by rotary evaporator and the solids were recrystallized out of ethanol and collected as a white powder (yield 2.56 g, 36%, ~70% purity).



Scheme 6.1: Synthesis of bis-benzophenone, adapted from Ref. ³

6.7.2 Methods

6.7.2.1 Film preparation

Films in this study were spin coated (Specialty Coating Systems Spincoat G3-8) onto silicon substrates with native oxide layers from solutions of amyl acetate, which was a good solvent for all components. Substrates were prepared by soaking in a solution of ethanol, deionized water and potassium hydroxide (80/10/10 wt%) and then rinsed with deionized water and tetrahydrofuran at least three times. Spin coating solution concentrations were 4-8 wt% polymer in amyl acetate and spin speeds varied from 800 – 1500 RPM to control the film thickness.^{11,12} After spin coating, films were annealed on a hot plate at 150 °C for 20 minutes, at this point film thicknesses did not decrease with additional heating. Film thicknesses were characterized by ellipsometry using a J.A. Woollam M-2000D Spectroscopic Ellipsometer.

6.7.2.2 Topography Formation, Characterization, and Other Equipment

In order to create the surface energy pattern in the film, the spin coated films were exposed to light from an Optical Building Blocks ScopeLite 200, a broadband light source. For activation of MK, samples were exposed through a 365 nm (10 nm FWHM) bandpass filter (Edmond Optics). Masks were Ronchi rulings which are evenly spaced chrome lines on a quartz mask (Edmond Optics). During exposure, films were cooled to 15 °C with an Instec mK 1000 temperature controller with a HCS 402 hot stage connected to a liquid nitrogen pump to prevent the photo-masks from sinking into the film (see Table 6.2 for T_g of various compositions). Activation of the BB for cross-linking was performed using the same light source and a 254 nm (40 nm FWHM) bandpass filter (Edmond Optics). A critical point on the use of these bandpass filters is that the arrow on the side must be pointed toward the light source; ('shiny' side up) if not, the films heat up much more rapidly and it is impossible to get accurate intensity measurements as the filters emit IR radiation due to heating. Light intensity was measured using a Radiometer Fieldmax TO (Coherent) capable of a wavelength range 250 nm to 11,000 nm. The topography was characterized using a Veeco Dektak 6M Stylus Profiler by recording peak to valley height with a stylus force of 7 mg and a tip radius of 12.5 μm . Bright field microscopy was performed on an Olympus BX 60 microscope with a Spot Insight QE camera. Fourier transform infrared (FTIR) spectra to characterize conversion of photo-active molecules were recorded on a Thermo Nicolet 6700 FTIR with liquid nitrogen cooled MCT-B detector.

6.8 REFERENCES

1. Jeyaprakash, J. D.; Samuel, S.; Ruhe, J. *Langmuir* **2004**, *20*, 10080-10085.
2. Christensen, S. K.; Chiappelli, M. C.; Hayward, R. C. *Macromolecules* **2012**, *45*, 5237-5246.
3. Carroll, G. T.; Sojka, M. E.; Lei, X. G.; Turro, N. J.; Koberstein, J. T. *Langmuir* **2006**, *22*, 7748-7754.
4. Ubukata, T.; Yamamoto, S.; Moriya, Y.; Fujii, S.; Yokoyama, Y. *J. Photopolym Sci. Technol.* **2012**, *25*, 675-678.
5. Ubukata, T.; Moriya, Y.; Yokoyama, Y. *Polym. J.* **2012**, *44*, 966-972.
6. National Institute of Advanced Industrial Science and Technology. Spectral Database for Organic Compounds. <http://sdb.srioddb.aist.go.jp/sdb/> (Accessed January 31, 2013).
7. Lee, L.-H. *Journal of Applied Polymer Science* **1968**, *12*, 719-730.
8. Fu, G. D.; Xu, L. Q.; Yao, F.; Zhang, K.; Wang, X. F.; Zhu, M. F.; Nie, S. Z. *ACS Appl. Mater. Interfaces* **2009**, *1*, 239-243.
9. Jakubowski, W.; Kirci-Denizli, B.; Gil, R. R.; Matyjaszewski, K. *Macromol. Chem. Phys.* **2008**, *209*, 32-39.
10. Pintauer, T.; Matyjaszewski, K. *Chem. Soc. Rev.* **2008**, *37*, 1087-1097.
11. Hall, D. B.; Underhill, P.; Torkelson, J. M. *Polym. Eng. Sci.* **1998**, *38*, 2039-2045.
12. Spangler, L. L.; Torkelson, J. M.; Royal, J. S. *Polym. Eng. Sci.* **1990**, *30*, 644-653.

Chapter 7: Future Work

7.1 INTRODUCTION

While significant progress has been made in both the study and manipulation of the mobility in polymer thin films using light there are still a variety of interesting directions this research could take. In this chapter some of these possibilities are explored along with some relevant background references and discussion of some possible challenges.

7.2 NANOCONFINED DIFFUSION

With the framework for FRAPP as a tool to study the effect of nanoconfinement on diffusion in polymer thin films there are still several areas of interest for future research.

7.2.1 Symmetric Interfaces

While the work presented in this chapter begins to look at the effect of varying the confining interfaces, many places where polymer thin films are used the film is confined between two solid interfaces. One example of the relevance of this study might be examining how a polymer surfactant flows in nano-sized cracks in rocks that may contain oil. Even though no signal problems have been observed in films down to 19 nm thick, one possible advantage of this study might be that use of several thin films on top of one another. This could increase the signal to noise by being able to perform FRAPP on multiple very thin films at the same time and allow study of even thinner films. Furthermore, by tuning the interfaces the relationship between T_g and film thickness could be changed as well. For example, just as PCHE under-layers leads to a reduction in T_g with decreasing film thickness for PiBMA over-layers, a confining layer of an immiscible poly(methacrylic acid) could lead to additional attraction to PiBMA on both

interfaces and increase the T_g with decreasing film thickness. This could allow for a more comprehensive study of the relationship between nanoconfinement effects on T_g and those on diffusion.

There are a few challenges to this type of study though. The first major challenge is fabrication of the multi-layer film. While sequential spin coating could be used in the bi-layer of PCHE and PiBMA, no solvent was identified that could dissolve PCHE but *not* PiBMA to spin coat on a top layer. An alternative approach is to use film floating techniques to float a PCHE film on water and pick it up with a bi-layer of PCHE and PiBMA that have already been fabricated.

7.2.2 Nanocomposites

Polymer nanocomposites have become ubiquitous in a variety of commercial applications. For example, polymer/silicate nanocomposites were first introduced by Toyota in 1985 as a way to improve the mechanical properties of car parts and were found in passenger cars by 1989.¹ Exfoliation of nanofiller particles is key to property enhancement and part of the exfoliation processes requires diffusion of polymers along and between the filler particles.² For this reason, the study of diffusion in nanocomposites is an attractive direction for future study using FRAPP. Nanocomposites allow for access to a significantly wider range of surface area to volume ratio systems, and therefore higher degrees of nanoconfinement, than possible in thin films. Significant studies have already been conducted on a variety of aspects of nanocomposites including polymer conformation (both theoretically³ and experimentally⁴) as well gradients in T_g as a function of distance from the nanoparticle surface.⁵ One study used elastic recoil detection (an isotopic technique, see Chapter 1.4.2.1 for similar techniques) to study self-diffusion of polystyrene in the presence of surface modified silica nanoparticles.⁶ In these

instances, they found that changes in diffusion coefficient could be attributed to ‘bottlenecking’ of molecules as they diffusion between adjacent particles.

A good model system to begin study of diffusion in nanocomposites is PiBMA containing dispersed colloidal silica nanoparticles. These nanoparticles are readily available in solution and have shown to be easily dispersed in various acrylate and methacrylate polymers.^{7,8} Previous research has also demonstrated a change from the bulk T_g in several polymers as a function of nanoparticle loading using these types of particles⁸ which indicates that there are nanoconfinement effects induced by these particles as well. The objective would to determine if diffusion is described by basic space filling models of spherical inclusions with changes in diffusion temperature or volume fraction of particles.⁹

7.2.3 Molecular Weight Effects

Another topic of interest is the crossover between the Rouse ($D \sim M^{-1}$) and reptation ($D \sim M^{-2.3}$) regimes which has been the topic of several previous studies in bulk polymers.¹⁰⁻¹³ In bulk, entanglements give rise to the high viscosity of long chain polymers as well as their mechanical properties.¹⁴ Furthermore, entanglements impact many thin film properties, such as dewetting.¹⁵ Therefore, it is important to understand at what molecular weight a thin polymer film begins to entangle. In nano-confined freestanding (no substrate) films, one study observed a reduction in entanglement density.¹⁶ There is also evidence that the presence of an interface can change the way that diffusion scales with molecular weight. As described in Chapter 1, near a free interface diffusion was found to scale as $M^{-2.5}$,¹⁷ and near a supporting interface as $M^{-1.5}$ for polystyrene on silicon substrates¹⁸ rather than $M^{-2.3}$ as in bulk.

It is possible to use FRAPP to determine whether there is a shift in the critical molecular weight for entanglement and the scaling for diffusion with molecular weight with decreasing film thicknesses. The most obvious difficulty of this study is that it is very dependent on synthesis. Whereas with the other studies described a single fluorescently labeled polymer can be synthesized in a large batch, in this study a polymerization would need to be carried out for each molecular weight of interest. This could be a very time intensive process given the need for a high degree of accuracy in molecular weight and very low PDI requirements of these studies. However, once synthesized the various molecular weight polymers could be used in combination with any sort of confining interfaces, as described previously, to examine a wide range parameters and how they impact diffusion in thin films.

7.3 MARANGONI DRIVEN TOPOGRAPHIC PATTERNING

Marangoni-driven topographic pattern formation is a new technique that has significant potential for a variety of applications as detailed in this and the previous two chapters. However, to realize some of these applications, significant additional effort is required.

7.3.1 Simulations and Theory

While significant progress has been made toward understanding the parameters that impact the Marangoni patterning technique on a phenomenological basis, simulation studies could improve understanding of its physical underpinnings. The literature contains a few previous simulation studies on similar patterning methods.^{19,20} Even though there were a few key differences between these studies and our work, namely their photochemical reactions were reversible and their fluid was assumed to be Newtonian. However, these previous studies might form the basis for a framework to

simulate Marangoni polymer patterning outlined in this thesis. Simulations could help to better understand the effect of a variety of process parameters, such as the effect of surface energy, film thickness, and temperature. A first-principles understanding of the Marangoni patterning process could allow for quantitative optimization and prediction of feature formation by varying factors such as material selection and exposure dose to exhibit precise control over topographic feature sizes and location.

7.3.2 Sub-Micron Patterning

The ability to pattern features on a sub-micron length scale would make this approach significantly more attractive for some applications. To date, the smallest features observed had a characteristic length scale on the order of a few microns in films 100-200 nm thick. At least an order of magnitude increase in patterning resolution is needed to achieve sub-micron features. One of the limiting factors so far is the resolution limit for proximity (shadow) printing (eq 6.1).²¹

$$b_{min} = \frac{3}{2} \sqrt{\lambda \left(s + \frac{z}{2} \right)} \quad (6.1)$$

Where b_{min} is the minimum feature size, s is the gap between the film surface and the mask, λ is the wavelength of light, and z is the film thickness. This shows that the results for this process are strongly dependent on the size of the gap between the polymer and the photomask. Since the films are glassy and on substrates that are not perfectly smooth, intimate contact over the whole area of the film is very challenging. For example, given typical parameters of 254 nm light, near the peak absorbance of polystyrene, and a 145 nm film thickness with an air gap of only 1.5 μm , the resolution patterning limit is $\sim 1 \mu\text{m}$. Clearly to create features with smaller characteristic dimensions an alternative method for creating surface energy gradients will be necessary. An important consequence of decreasing the topographic feature size in this process is

that the Marangoni number scales as the square of the characteristic dimension. A decrease in feature size by one order of magnitude would decrease the Marangoni number by two orders of magnitude. Using PS photochemistry as described in Chapter 5, it appears that the Marangoni number would still be above the critical threshold of 80, however only by an order of magnitude rather than the current three orders of magnitude. It may become important, if alternative chemistries are explored in conjunction with the goal of reducing feature size to ensure that the size, of the surface energy gradients imposed increase correspondingly.

7.3.2.1 Laser Induced Periodic Structures (LIPS)

In previous studies lasers, have been used to induce periodic structures on the surface of both metals²²⁻²⁴ and polymers.^{25,26} The literature in this field does not, in many cases, seem to offer a complete physical explanation of this phenomenon. However, experimentally the laser based technique used to induce the surface structures could possibly be harnessed to create surface energy gradients. Simply put, a polymer film on any substrate is exposed directly to linearly polarized light from an excimer source ($\lambda = 254$ nm or $\lambda = 193$ nm). A grating pattern develops on the film which is thought to be a consequence of the propagation of an evanescent wave along the film surface that produces a spatially varying dose. This grating pattern could be used to create the surface energy gradient that could then be developed into topography via the Marangoni effect through heating. Using this technique the periodicity of the topographic features is related to the wavelength of light used. For example, in one study exposure using 193 nm laser light led to 150 nm features and exposure with 248 nm light led to 190 nm features in polymer films.²⁵ The literature tends to use a single step technique due to local heating caused by the film absorption of laser light, and in the case of metals it is this local

heating and accompanying thermal expansion that causes the topography to be formed. However, the same exposure technique should be able to be adapted to write a surface energy gradient into the film without heating it through its T_g .

7.3.2.2 Direct Write

Another possibility for sub-micron patterning is to use a light source that can focus on a spot the size of the desired features. This is similar to the way electron beam lithography can be used to ‘write’ a pattern into traditional photoresists to create photo or nano-imprint lithography masks. One potential way to adapt this approach to Marangoni-driven patterning would be to use either confocal or two-photon microscopy. While, most commonly used for imaging, if a suitable photo-active compound can be found, the laser scanning head on either of these instruments could potentially focus on a sub-micron spot size and be rastered to write a surface energy pattern of an arbitrary shape into a solid polymer film for later topography development. In the case of two-photon microscopy the surface energy gradients could also be used to create three-dimensional gradients in surface energy potentially resulting in the formation of more complex topography. The biggest drawback to this approach is that it is very slow. Each feature would have to be exposed to light individually significantly reducing the throughput of this process.

7.3.3 Larger Surface Energy Gradients

A clear result of the Marangoni number calculations is that larger aspect ratio features result from larger surface energy gradients. This is due to both the rise in feature height, as well as the potential to shrink the pitch of the features while maintaining the Marangoni number above its critical threshold for feature formation. There are several photochemical reactions that lead to significant changes in chemical structure, and potentially associated with large changes in surface energy. One example is deprotection

of poly(p-t-butyloxycarbonyloxystyrene) with a photoacid generator²⁷ leading to a reduction in the advancing water contact angle by 14°,²⁸ as compared with ~2° for polystyrene (Chapter 5.2.3). However, there may be some other challenges that arise when chemical changes this drastic result from photoexposure. Thickness variations could be observed from the deprotection step itself because the photochemical products, CO₂ and isobutylene, are gasses. Furthermore, the exposed and unexposed regions may no longer be miscible. Currently, we believe that the unexposed region mixes with the exposed region on heating because of the Marangoni effect and in the absence of this potential to mix, the topography may be very different than that formed by the chemistries currently employed. However, since we have not yet test this in detail, we cannot anticipate full physical consequences of this situation. The use of multi-layer films in which one film contains a fluorophore will enable tracking of whether the layers still intermix during feature formation or merely slide on top of one another.

7.3.4 Alignment of Block Co-Polymers

Previous studies have shown that the application of directional shear stress to ordered block co-polymers has improved their large scale alignment.^{29,30} When topography is formed via the Marangoni effect there clearly is local shear stress caused by the deformation of the polymer surface. It is possible, that by placing an unaligned block co-polymer film on top of the photoactive polymer layer the strain imparted by the formation of topography may be sufficient to align the block co-polymer micro-domains. As shown in section 5.5, placing a polymer layer on top of the active layer does not seem to impede feature formation. The block co-polymer would either need to be transparent to the wavelength of light used to photochemically create the surface energy gradient or put on top after the surface energy pattern is made. With regards to the Marangoni driven

topography process it is simplest to think in terms of the strain caused by increased surface area of film after topographic features are formed. In the literature strain amplitudes of 50-100% were imparted to the film for several hours in order to achieve high degrees of alignment.³⁰ However, in the case where 150 nm features are created with a 10 μm pitch only 0.006% strain is imparted based on the very small aspect ratio of the topographic features and for a relatively short period of time, a significant barrier to overcome for this to be successful. The simplest way to increase the amount of strain applied would be to significantly increase the aspect ratio of the features, therefore this objective would have to be considered alongside the strategies for sub-micron patterning described above.

7.4 REFERENCES

1. Okada, A.; Usuki, A. *Macromolecular Materials and Engineering* **2006**, *291*, 1449-1476.
2. Vaia, R. A.; Giannelis, E. P. *MRS Bull.* **2001**, *26*, 394-401.
3. Termonia, Y. *J. Polym. Sci. Pt. B-Polym. Phys.* **2010**, *48*, 687-692.
4. Nakatani, A. I.; Chen, W.; Schmidt, R. G.; Gordon, G. V.; Han, C. C. *Polymer* **2001**, *42*, 3713-3722.
5. Papon, A.; Montes, H.; Hanafi, M.; Lequeux, F.; Guy, L.; Saalwachter, K. *Physical Review Letters* **2012**, *108*, 5.
6. Gam, S.; Meth, J. S.; Zane, S. G.; Chi, C. Z.; Wood, B. A.; Seitz, M. E.; Winey, K. I.; Clarke, N.; Composto, R. J. *Macromolecules* **2011**, *44*, 3494-3501.
7. Janes, D. W.; Moll, J. F.; Harton, S. E.; Durning, C. J. *Macromolecules* **2011**, *44*, 4920-4927.
8. Moll, J.; Kumar, S. K. *Macromolecules* **2011**, *45*, 1131-1135.
9. Sangani, A. S.; Yao, C. *J. Appl. Phys.* **1988**, *63*, 1334-1341.
10. Drzewinski, A.; van Leeuwen, J. M. J. *Phys. Rev. E* **2008**, *77*, 8.
11. Kubo, T.; Nose, T. *Polym. J.* **1992**, *24*, 1351-1361.
12. Richter, D.; Willner, L.; Zirkel, A.; Farago, B.; Fetters, L. J.; Huang, J. S. *Macromolecules* **1994**, *27*, 7437-7446.
13. Sun, Q.; Faller, R. *Macromolecules* **2006**, *39*, 812-820.
14. Wool, R. P. *Macromolecules* **1993**, *26*, 1564-1569.
15. Reiter, G. *Macromolecules* **1994**, *27*, 3046-3052.
16. Si, L.; Massa, M. V.; Dalnoki-Veress, K.; Brown, H. R.; Jones, R. A. L. *Phys Rev Lett* **2005**, *94*, 127801.

17. Pu, Y.; Rafailovich, M. H.; Sokolov, J.; Gersappe, D.; Peterson, T.; Wu, W. L.; Schwarz, S. A. *Phys. Rev. Lett.* **2001**, *87*, 4.
18. Zheng, X.; Rafailovich, M. H.; Sokolov, J.; Strzhemechny, Y.; Schwarz, S. A.; Sauer, B. B.; Rubinstein, M. *Phys. Rev. Lett.* **1997**, *79*, 241-244.
19. Golovin, A. A.; Volpert, V. A. *Physics of Fluids* **2007**, *19*, 122104.
20. Golovin, A. A.; Volpert, V. A. *Mathematical Modelling of Natural Phenomena* **2008**, *3*, 27-54.
21. Madou, M. J. *Fundamentals of Microfabrication: The Science of Miniaturization*; Second Edition ed.; CRC Press: Boca Raton, Florida, 2002.
22. Emmony, D. C.; Howson, R. P.; Willis, L. J. *Applied Physics Letters* **1973**, *23*, 598-600.
23. Siegrist, M.; Kaech, G.; Kneubuhl, F. K. *Applied physics* **1973**, *2*, 45-46.
24. Young, J. F.; Preston, J. S.; van Driel, H. M.; Sipe, J. E. *Physical Review B* **1983**, *27*, 1155-1172.
25. Bolle, M.; Lazare, S.; Leblanc, M.; Wilmes, A. *Applied Physics Letters* **1992**, *60*, 674-676.
26. Kim, D. Y.; Tripathy, S. K.; Li, L.; Kumar, J. *Applied Physics Letters* **1995**, *66*, 1166-1168.
27. Frechet, J. M. J.; Eichler, E.; Ito, H.; Willson, C. G. *Polymer* **1983**, *24*, 995-1000.
28. *Advanced Nanomaterials*; Geckeler, K. E.; Nishide, H., Eds.; Wiley-VCH: Weinheim, Germany, 2010.
29. Pujari, S.; Keaton, M. A.; Chaikin, P. M.; Register, R. A. *Soft Matter* **2012**, *8*, 5358-5363.
30. Gupta, V. K.; Krishnamoorti, R.; Chen, Z. R.; Kornfield, J. A.; Smith, S. D.; Satkowski, M. M.; Grothaus, J. T. *Macromolecules* **1996**, *29*, 875-884.

Appendices

APPENDIX A: DETERMINATION OF THE DIFFUSION COEFFICIENT IN A POLYMER THIN FILM BY FRAPP

A.1 Introduction

In this appendix a step by step procedure for determining the diffusion coefficient in a polymer thin film using the setup in CPE 3.430 along with ImageJ,¹ Micro-Manager,² PTI Felix, and Microsoft Excel. There are images and screenshots that are meant to be illustrative of the various components and steps involved. Significant opportunities may be present for optimization and automation of this procedure, specifically with regards to data analysis. However, this represents an effective method that works at this time.

A.2 Sample Preparation and Photobleaching

Films of fluorescently labeled polymer should be spin coated onto quartz. The best substrate used to date is a 1" by 1" by ¼" quartz plate from Chemglass (part number CGQ-0620-03). These substrates are thick enough to have good stability, but not so thick that it is difficult to heat them to the desired temperature. With regards to spin coating, n-butanol is a good solvent for smooth films of poly(isobutyl methacrylate) (PiBMA). The thickness of the films can be controlled by the solution concentration and the spin speed.^{3,4} It is important to keep the overall fluorophore concentration below the self-quenching threshold (see Section 2.3) in order to get accurate diffusion results. The self-quenching threshold changes based on the selection of polymer and fluorophore, but in the case of PiBMA with a nitrobenzofurazan (NBD) fluorophore it is 0.18 wt%. The fluorophore loading can be controlled by blending of fluorescently labeled and unlabeled polymer.

For photobleaching, a Ronchi ruling (Edmond Optics, Figure A.1) is a good photomask since it is an even array of lines and spaces. These masks should use quartz as a substrate for the chrome lines and not glass to improve photobleaching. A good example mask is stock #57-886 which has a pitch of 25 μm . If using the Scopelite (Optical Building Blocks) as a light source for photobleaching, exposure times are usually in the range of 1-3 minutes, but as intensity from the light source can fluctuate this can also vary some. Use of a collimating lens is recommended as this will make the fluorescence intensity profiles ‘flatter’ and easier to analyze. Other things that can impact photobleaching are the film thickness, the pitch of the photomask used, and the distance from the collimating lens to the sample.



Figure A.1: Ronchi ruling from Edmond Optics (<http://www.edmundoptics.com>)

A.3 Data Collection

The raw data for these experiments is a series of fluorescence micrographs taken over a period of time while the polymer film is heated to the desired diffusion temperature. This section will review the equipment and software necessary to collect these images.

A.3.1 Equipment Setup

The equipment used for these experiments is a QuantaMaster 40 (Photon Technologies) coupled to an Olympus BX 51 upright light microscope (Figure A.3).



Figure A.2: QuantaMaster 40 Fluorimeter

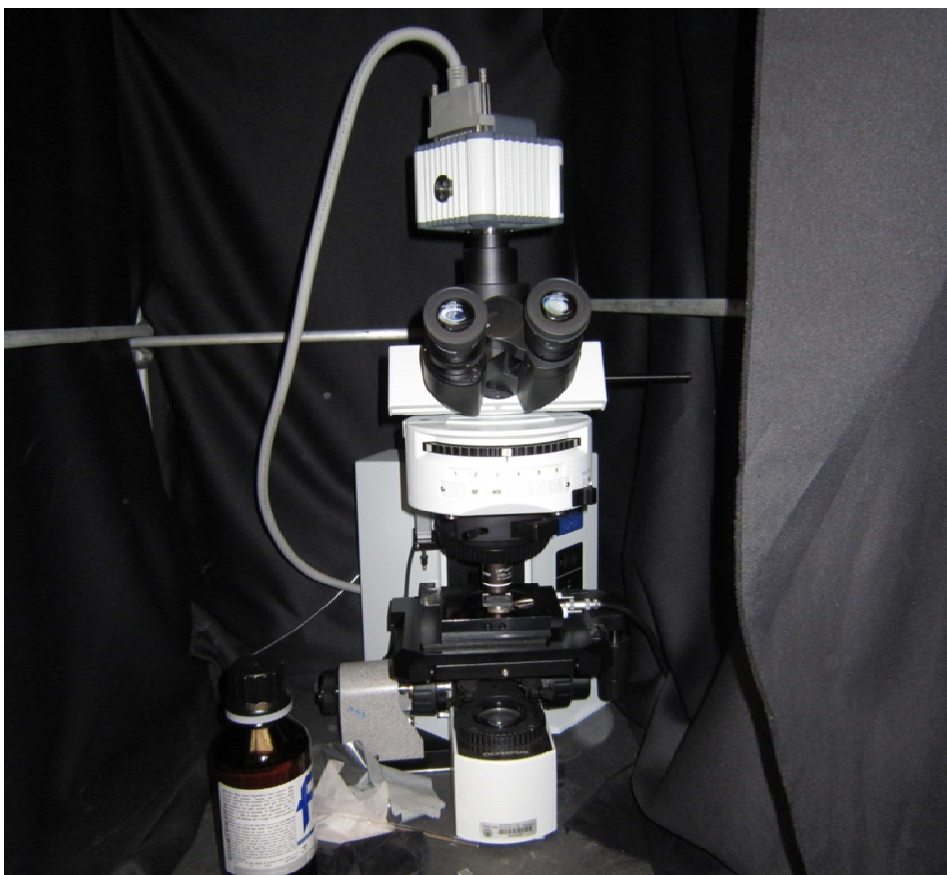


Figure A.3: Olympus BX51 Microscope

The first step is to ensure that the correct accessories are in place inside the fluorimeter. This equipment can be used for solid samples and cuvette fluorescence spectra in addition to serving as a light source for the microscope. The inside of the fluorimeter should look like Figure A.4. The lens that needs to be in place is indicated by a red arrow. There is a rectangle drawn on the bottom of the fluorimeter indicating proper positioning of this lens and care should be taken that nothing is between the lens and the front side of the fluorimeter as this would block the light path.

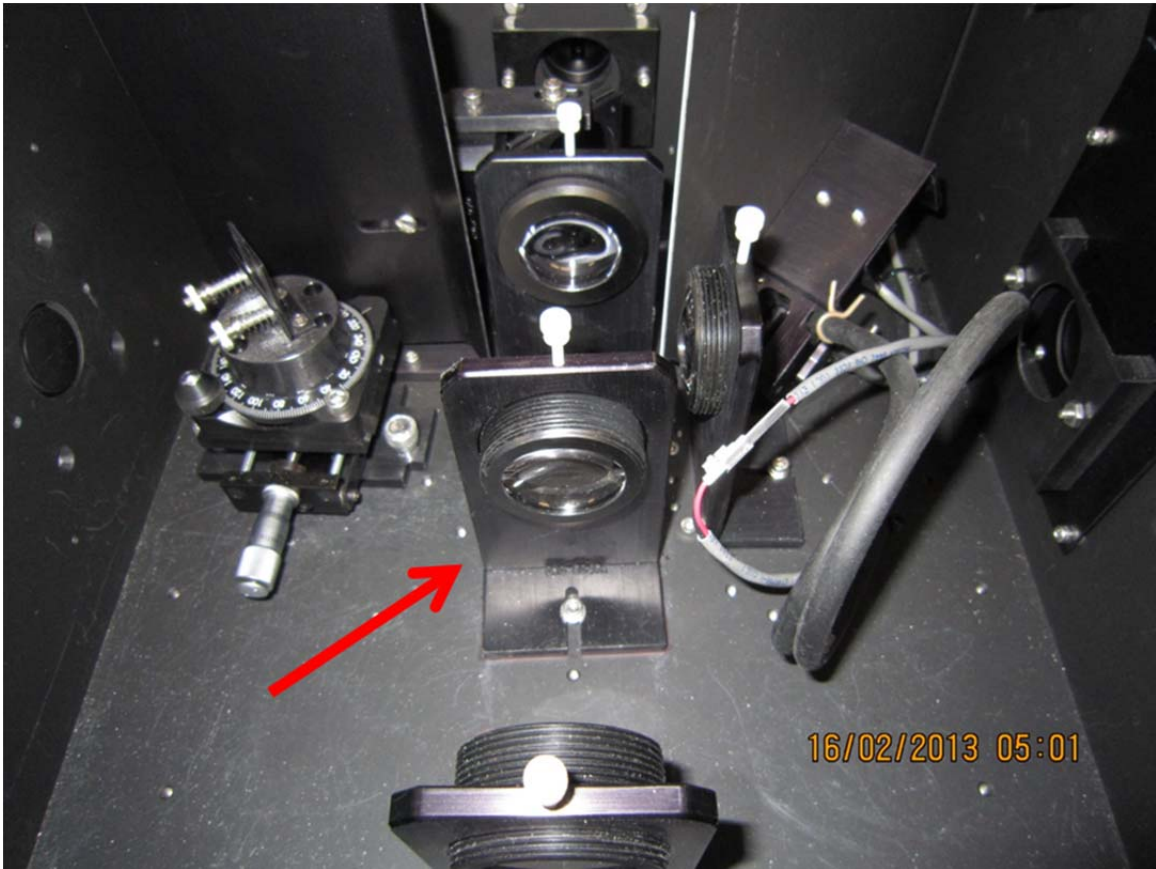


Figure A.4: Inside of the fluorimeter set up to serve as the microscope light source. The lens that must be installed is indicated with a red arrow.

After this, all of the equipment needs to be turned on. The light source (Figure A.5) should be turned on first because on ignition an electrical surge is possible that could damage other components. Next the fluorimeter controllers and camera need to be turned on. Figure A.6), all of the buttons are outlined in red in the figure. The button on the top most box (camera control) needs to be held until the indicator light turns green. Additionally, the shutter controller toggle switches (outlined in yellow) should be set to 'Manual' and 'Open'. No second shutter is installed, so this toggle switch does not control anything.

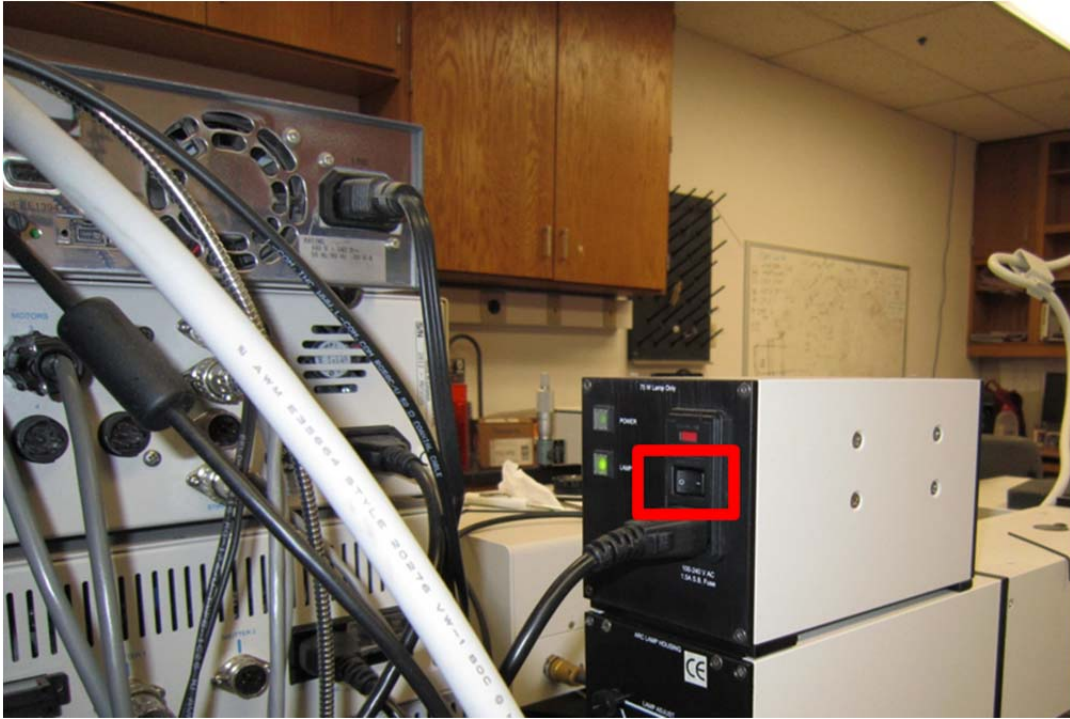


Figure A.5: Microscope light source power switch

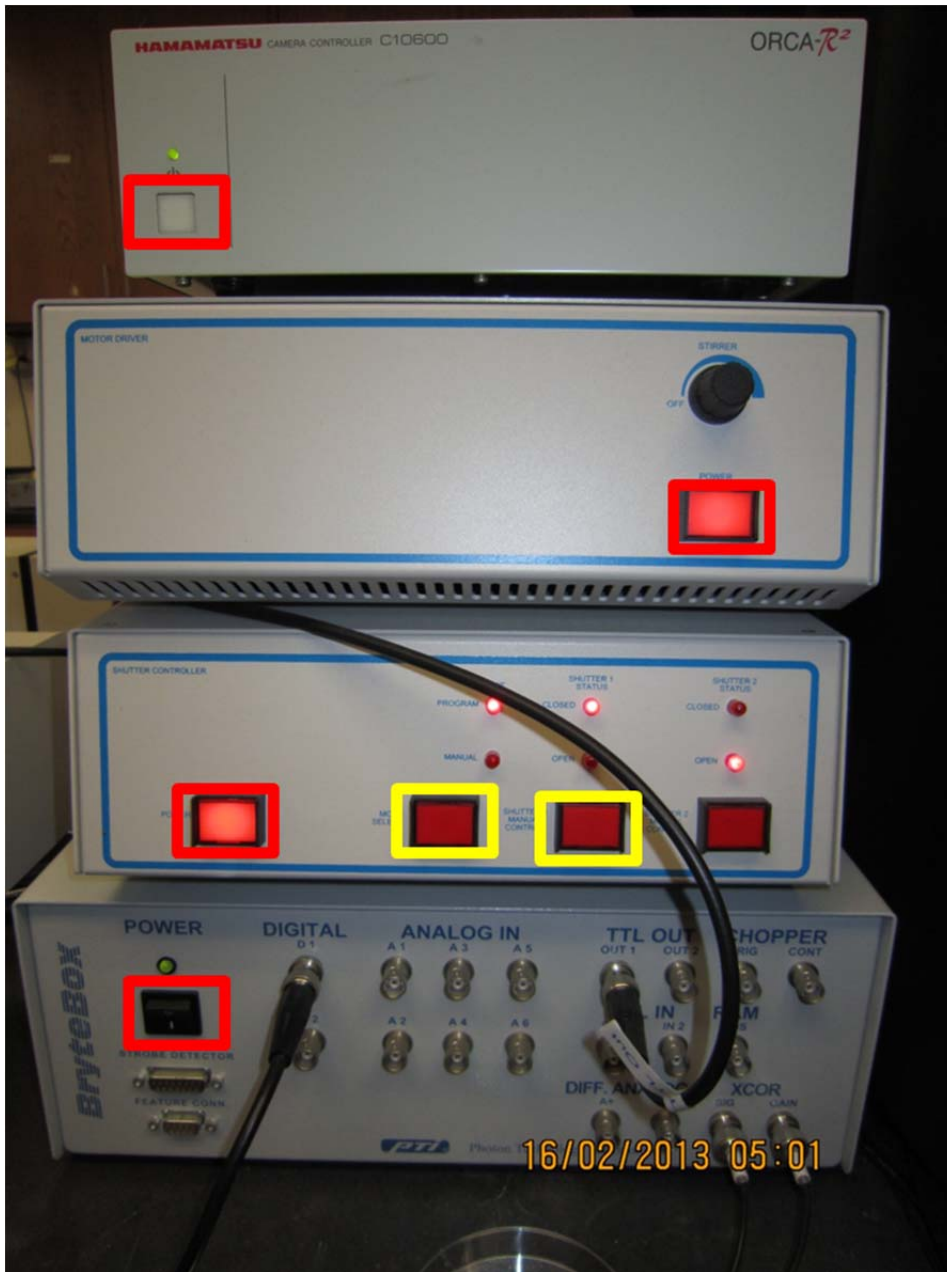


Figure A.6: Controller and camera power switches (outlined in red) and shutter control toggles (outlined in yellow).

Next the excitation slit width should be set on the micrometers (in red in Figure A.7). These both should be set to the same setting and the conversion is $1 \text{ mm} = 4 \text{ nm}$, for

example if the micrometers are set to 1.5 mm then the excitation slit width is 6 nm. For diffusion experiments 8 nm (2 mm setting) has worked well.



Figure A.7: Location of excitation slit micrometers

The final step before switching to computer control is positioning of the sample. The Linkham TMS91 hot stage should be placed on the stage under the objective with a small aluminum puck over the heating element and the quartz slide with the film on it should be placed on top of the puck (Figure A.8). A drop of silicon oil should be placed between both the puck and heating element as well as between the quartz plate and the puck as a heat conduction fluid and to improve the stability of the sample. Make sure to use silicon oil that has not been contaminated as many common contaminants are fluorescent.

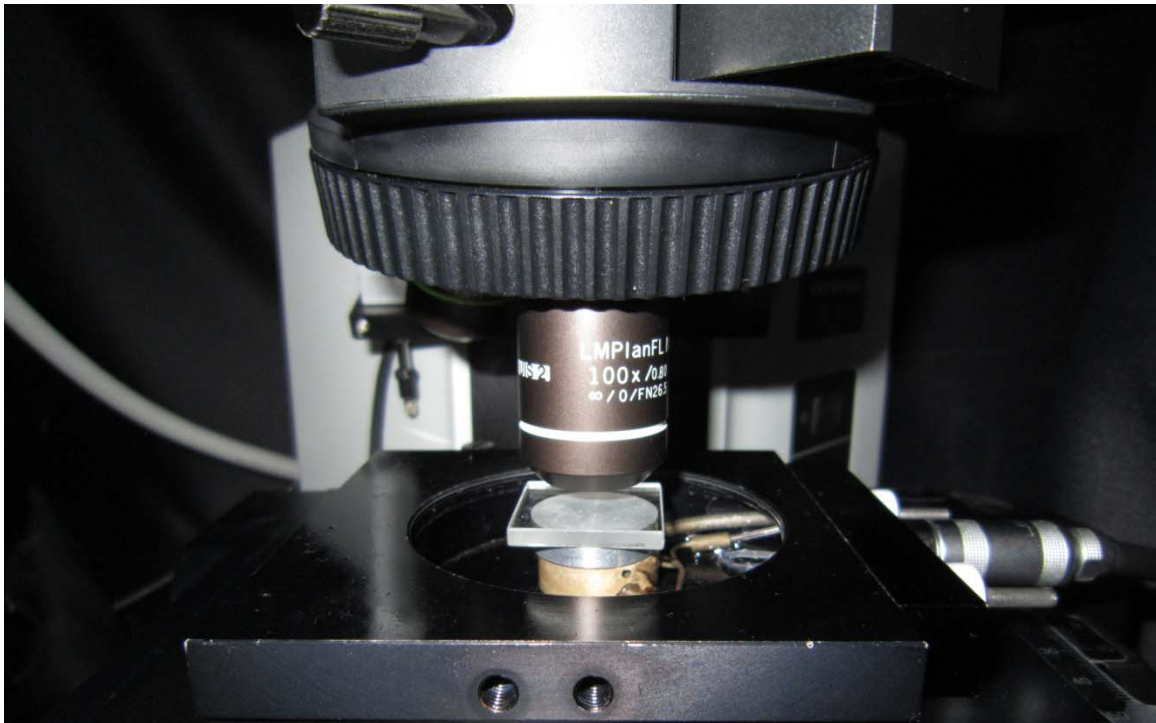


Figure A.8: Hot stage setup with sample in center

Switching over to software setup, two different programs need to be started, PTI Felix and Micro-Manager. PTI Felix controls the light source and shutter, while Micro-Manager is for camera control. Open PTI Felix through Windows Start Menu, on starting the program will prompt for a user name and password, the user name is 'Administrator' and the password is 'pti' (Figure A.9).



Figure A.9: PTI Felix login screen

Next go to Acquisition→Open Acquisition and double click on ‘Record and Image’. A control panel shown in Figure A.10 will appear on the screen, all windows except for this one can be minimized. There are only a few settings on this panel that will actually affect the experiment, the rest do not need to be adjusted. First, double check that in the drop down box labeled ‘Script:’ that ‘Timebased’ is selected. With the current long pass filter installed, the ‘Excitation’ should be set to 445 nm. The ‘Duration’ should be set to the amount of time for each exposure in seconds and the ‘Pause’ should be set to the amount of time between exposures in seconds. For example, if the desired exposure interval is one hour and each exposure is two seconds then ‘Pause’ should be 3598 seconds (3600 sec/hr – 2 sec/exposure), this counts from the end of one exposure to the start of the subsequent one. Finally ‘Repeats’ is the number of images to collect, given the current state of the system the maximum is a total of 18 hours for an experiment regardless of the interval time. After all these settings are correct, click on ‘Acquire (Prep)’ and wait for the fluorimeter to run through its start-up, clicking can be heard as the monochrometers set the correct wavelength.

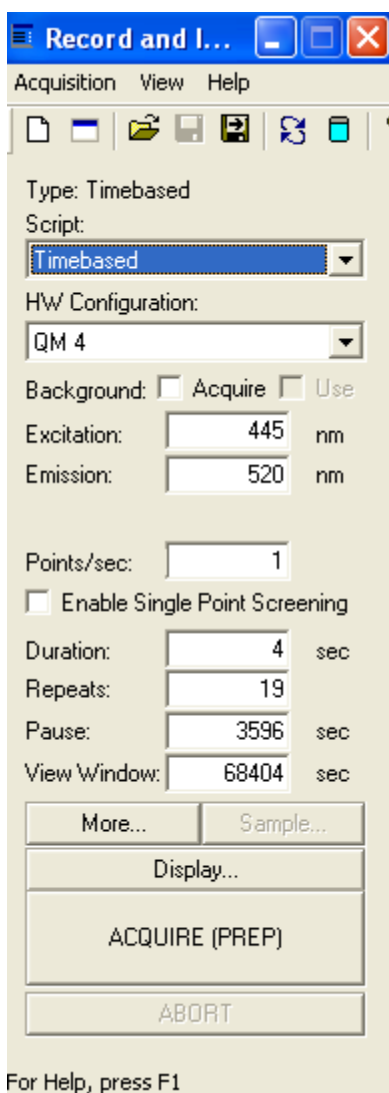


Figure A.10: Record and Image Control Panel

Next open 'Micro-Manager-1.3' from the Windows Start Menu and when it starts up load 'C:\Program Files\Micro-Manager-CO.cfg' (Figure A.11). This will bring up the main control panel for the camera (Figure A.12). Clicking 'Live' will bring up the current camera view and 'Exposure [ms]' sets the exposure time in milliseconds.



Figure A.11: Micro-Manager startup screen

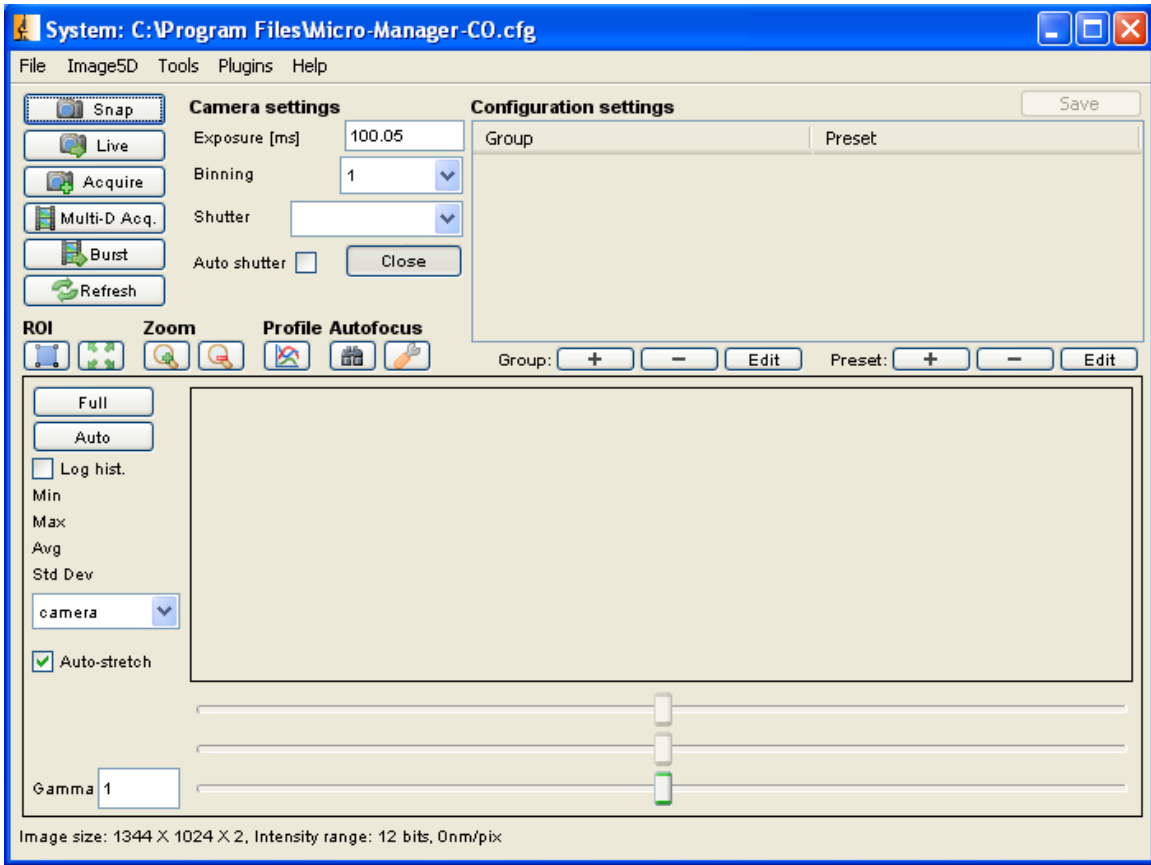


Figure A.12: Micro-Manager main control panel

There are two filters that are installed in the microscope (Figure A.13). Setting '2' is for bright-field imaging and '3' is for fluorescence imaging. Before continuing set the filter wheel to '2' and rotate the nosepiece to the 10X objective.



Figure A.13: Filter wheel with shutter switch in red box.

The next step before starting the diffusion experiment is to focus on the sample film. If the image appears too bright, try reducing the exposure time, 10 ms should be sufficient for bright-field imaging. If the image appears saturated, a uniform grey, reduce this setting to 6 ms. Using the course focus knob lower the stage all the way down and then slowly back up until the first focal plane, which should be your sample film. Use the fine adjust to get make sure it is completely in focus, use a piece of dust or some other defect as a way to find the film. The focus knobs are indicated by the arrow in Figure A.14. A good way to identify the film is that it is the first in focus plane that ‘moves’ when the stage is moved. Even though the diffusion experiment may not be performed using the 10X objective, it is always best to focus with this objective first. There are two reasons for this: first it spreads out the light limiting photobleaching, second it has the largest depth of focus and therefore it is easiest to do.

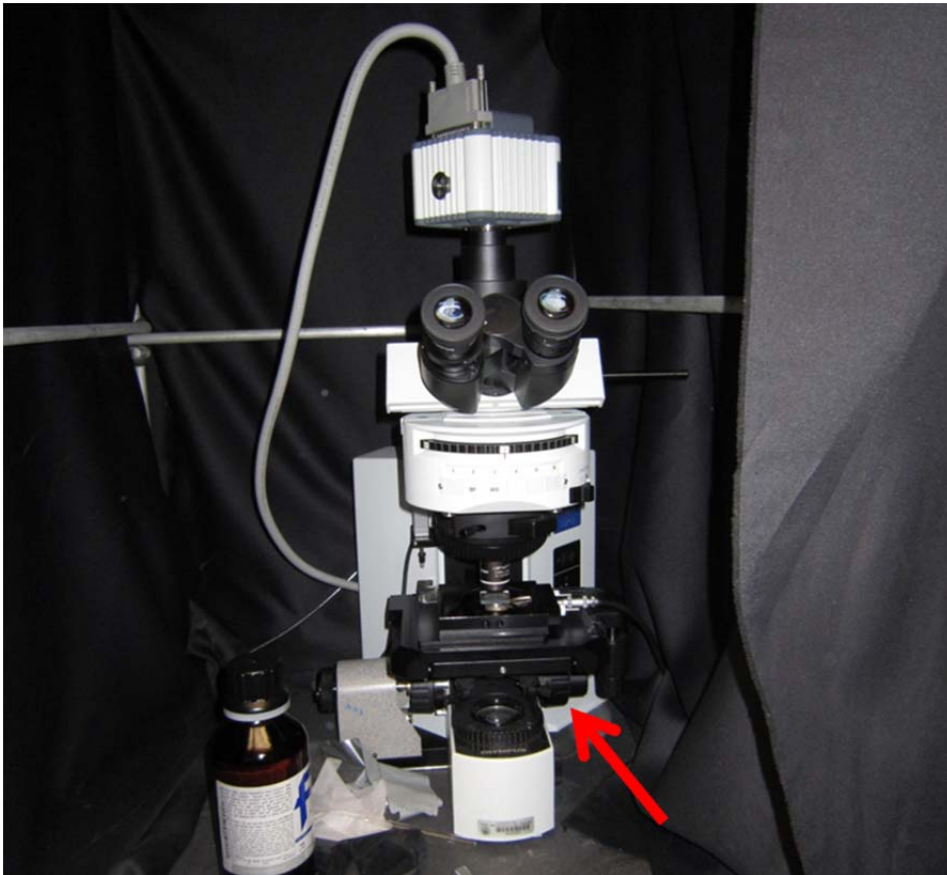



Figure A.14: Location of focus knobs

After the film is in focus, move some piece of dust or film imperfection to the center of the film, switch to the desired magnification for the diffusion experiment and refocus on the film. At this point switch the filter wheel to '3' and check the fluorescence image of the film. An exposure time of ~ 1500 ms is appropriate for fluorescence imaging of relatively thick films at room temperature, but it can be adjusted as needed. Click on 'Stop' to freeze the camera image. It is important to expose the film for as little time as possible to limit photobleaching so while active imaging is not taking place close the microscope shutter using the switch in the red box in Figure A.13 above.

To check the fluorescence intensity profile for evenness and shape use the line tool on the ImageJ toolbar (). Double clicking on the line tool button will bring up the option to change the line width, slide this to the maximum setting (300 pixels). Draw a line by clicking on the image and dragging roughly perpendicular to the photobleached pattern over several periods. Click on Analyze→Plot Profile or press Ctrl+K to see the intensity trace across this line. The profile should be flat, that is the tops and bottoms should be roughly in line and the shape should be sinusoidal. See Figure A.15 for an example of a good fluorescence intensity profile. If the intensity profile does not look acceptable look around multiple areas of the film or attempt to photobleach a new film.

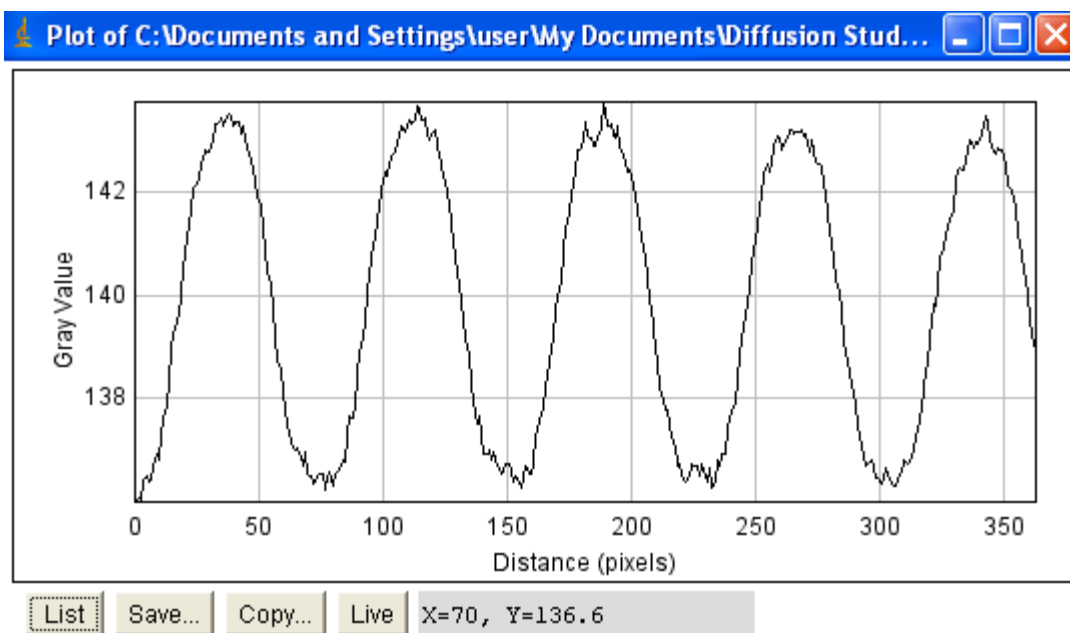


Figure A.15: Example of an acceptable fluorescence intensity profile before heating the thin film. Note the peaks and valleys roughly line up.

Now the film can be heated to the desired temperature. The control for the Linkham hot stage is to the right of the microscope outside of the dark box (Figure A.16).

In order to program a temperature press 'New' and the temperature program screen will come up. Enter the desired heating rate in °C/min and press enter, then the final temperature in °C and press enter (this is labeled 'Limit' on the screen), and finally the amount of time it should stay at that temperature in minutes and press enter twice. Press start and then the red light next to 'Load' should begin to flash after a few seconds and the temperature should begin to rise. After it reaches the desired temperature the 'Time' counter will begin to decrease. In order for it to stay at this temperature indefinitely press 'Hold'. However, for safety reasons it is advisable to just set the time to something much longer than the experiment, ~1300 minutes or so, so there will always be an automatic shutoff of the heater element at some point. The film should be allowed to equilibrate at temperature for at least 45 minutes before proceeding.



Figure A.16: Linkham hot stage control panel.

Now that the film is heated, exposure should be kept to a minimum as much as possible, photobleaching occurs much faster at elevated temperature. Switch the filter wheel to '2' and change the exposure time to 10 ms. Click live and then open the shutter. The film will have shifted some due to thermal expansion, refocus on the film in bright field as quickly as possible. In order to determine the appropriate exposure time for the diffusion experiment switch the filter to '3' and adjust the exposure time until an acceptable image is obtained. Close the shutter as much as possible between adjustments.

The final step to starting the diffusion experiment is setting up the automated imaging. First, using the toggle switch on the shutter control, switch from 'Manual' to

‘Program’ (left yellow rectangle in Figure A.6) then open the shutter on the microscope. No light should be visible as the program for the shutter should be triggered closed. At this point close all of the black flaps around the microscope to limit room light getting in and clip it shut with large binder clips around the frame.

Next go to ‘Tools’ on the μ Manager control screen and select ‘Device/Property Browser’ shown in Figure A.17. There are three settings that need to be adjusted here for automated imaging: 1) ‘Hamamatsu_DCAM-Exposure’ should equal the exposure time in milliseconds 2) ‘Hamamatsu_DCAM-Trigger’ should be set to ‘Edge’ and ‘Hamamatsu_DCAM-TriggerPolarity’ should be set to ‘Positive’. If this is different from the exposure time (‘Duration’) in the PTI Felix ‘Record and Image’ window click on ‘Abort’ in this window, enter the new exposure time into the ‘Duration’ box and click ‘Acquire (Prep)’ again (Figure A.10).

Note, after the experiment is over, if the camera is to be used again for any reason manually (for example, setting up another experiment) the ‘Hamamatsu_DCAM-Trigger’ setting needs to be set to ‘Software’ before proceeding, if not the software will not start the camera and the program will need to be restarted. Close this window when these settings are entered.

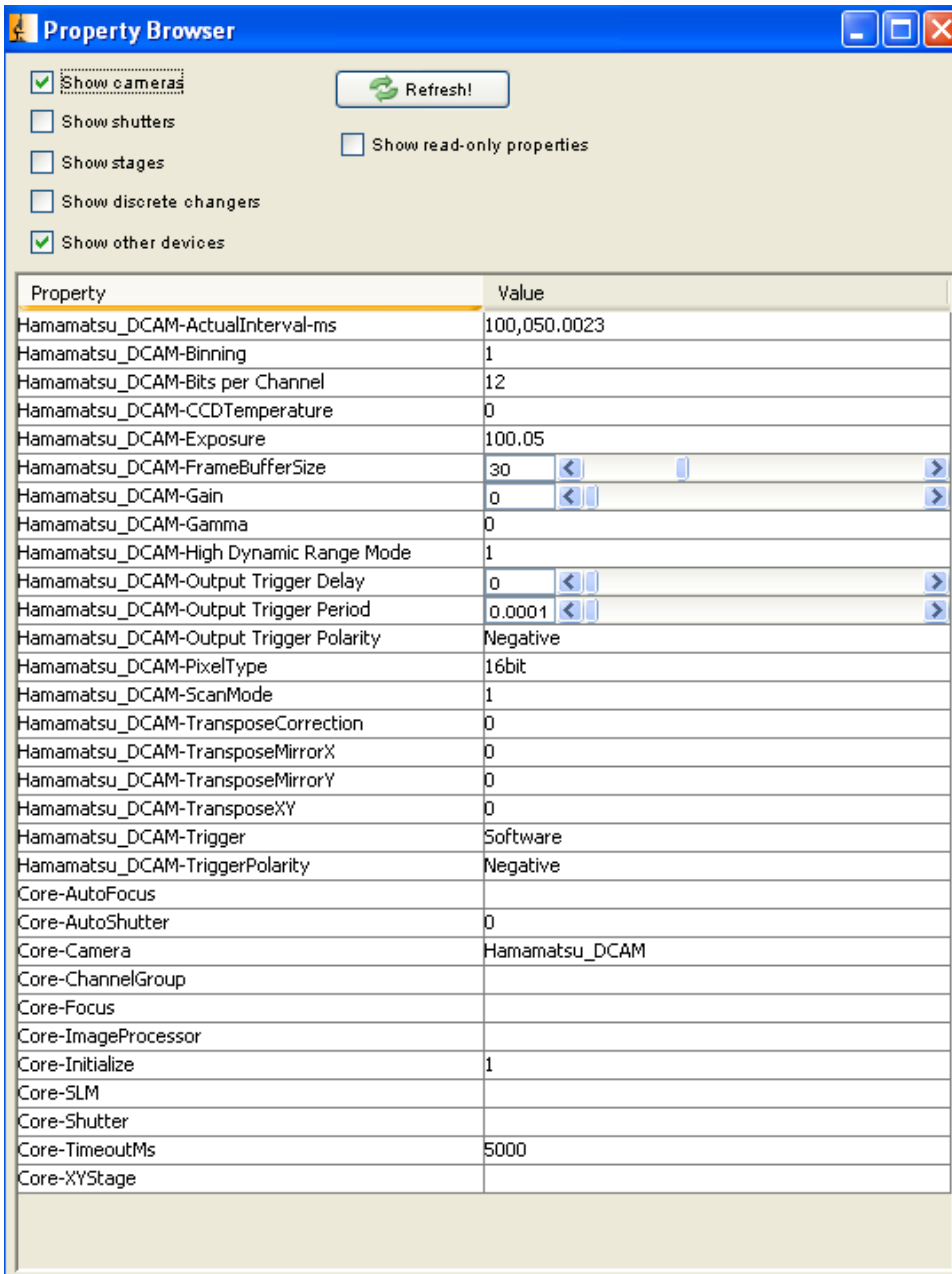



Figure A.17: Micro-Manager device/property browser

Click on ‘Multi-D Acq.’ on the left hand side of the control panel to bring up the window shown in Figure A.18. Here in the top left corner under ‘Time Points’ set the number of images to 210 (maximum with the current setup) and the time interval to 0. A

currently unresolved software glitch causes it to collect an image every ~4.3 minutes regardless of triggering, therefore the number of images collected must be this high in order to get through 18 hours of data collection. Note that due to this glitch, regardless of the time interval between successive images, the maximum amount of data collection time is the same. Near the bottom, click next to 'Directory Root' on the  button and select a save location for the stack. Note that this will create all of the image files in this folder so it is recommended to have a separate folder for each experiment. Finally enter the prefix for the files under 'Name Prefix'. To begin the experiment click 'Acquire' and then in the 'Record and Image' window from PTI Felix click 'Start'. At this point an audible click of the shutter opening should be heard followed by a click when it closes and the first image should appear. The experiment will now run for the desired time and collect images at the preset intervals.

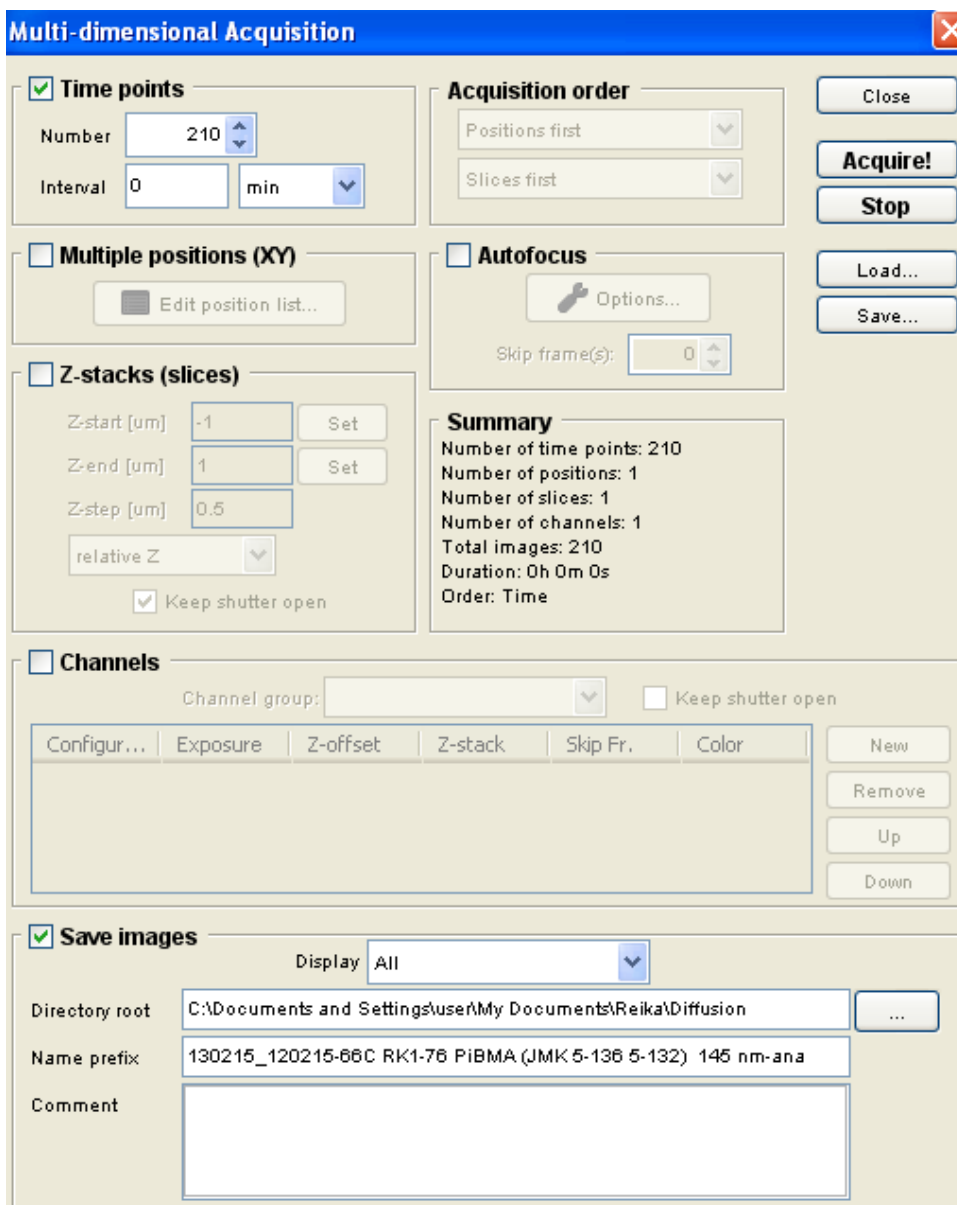


Figure A.18: Micro-Manager Multi-dimensional acquisition window

A.4 Data Analysis

After image collection is complete do not close the window that contains the images. There is a slider at the bottom that will allow you to scroll through from one to the next. Due to the previously mentioned software glitch, only some of the images will

be unique, in the case where the interval between data points is one hour, this is every 12 images. It is always possible to tell when there is a new distinct image because of subtle shifts in the image. The first step in the analysis is to collect the fluorescence intensity profiles from each of the images. It is important to collect these profiles as close to perfectly perpendicular to the pattern as possible or else the wavelength will be off in the calculations. In order to do this set the line width to one (the minimum) and draw a line on the image along the pattern, this is much easier to do accurately than exactly draw a line perpendicular. Press Ctrl+M and a measurement window will pop up that includes the angle of the line you have drawn. Repeat this until 7-10 measurements have been collected and average the angle, 90° from this will be the best estimate for perpendicular. For the measurements demonstrated in Figure A.19, the average angle is 91.3° so therefore the correct angle to measure at is as close to 1.3° as possible.

	Area	Mean	Min	Max	Angle	Length
1	511	203.838	142.867	250.584	91.572	510.192
2	771	213.878	162.519	266.974	91.488	770.260
3	661	207.376	159.600	275	90.694	660.048
4	745	208.831	152.887	255.726	90.924	744.097
5	739	213.961	159.902	272.537	91.397	738.219
6	663	204.805	121.498	260.598	91.730	662.302
7	679	214.107	162.469	278.637	91.014	678.106

Figure A.19: Angle sample measurements

Reset the line width to its maximum (300 pixels) and draw a line as close to perfectly perpendicular as possible, the ImageJ toolbar at the top will show the current angle of the line and this can be double checked by pressing Ctrl+M to measure the line used (see Figure A.20).

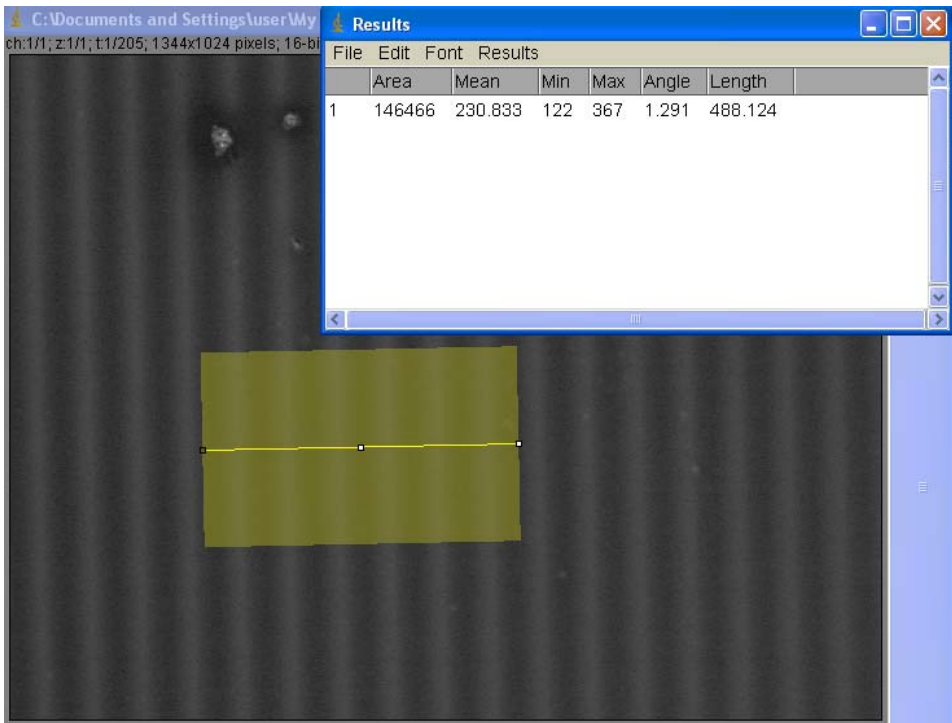


Figure A.20: Diffusion image with correctly drawn line, inset shows angle is $\sim 1.3^\circ$

Open a new Excel workbook and name each tab with the time points used (60 min, 120 min, etc.). Then go to each image in turn and press Ctrl+K then 'List' to show the numerical values and copy and paste these columns of the intensity profiles into the tab in Excel that corresponds to the correct time. Scroll from one image to the next using the bar at the bottom of the image and the analysis line will remain in exactly the same place. It is very important that this curve is sinusoidal (as demonstrated in Figure A.15 above) or else the curve fitting in the later steps will have significant error.

The next step is to identify one local maximum as the solution to the diffusion equation employs periodic boundary conditions with the end points set to maxima. Since there is so much noise in some of the data a three or five point moving average is useful for this step only. After a maximum is identified delete all data in the rows above that

point in the spreadsheet, at this point a graph of intensity vs. position should look like Figure A.21.

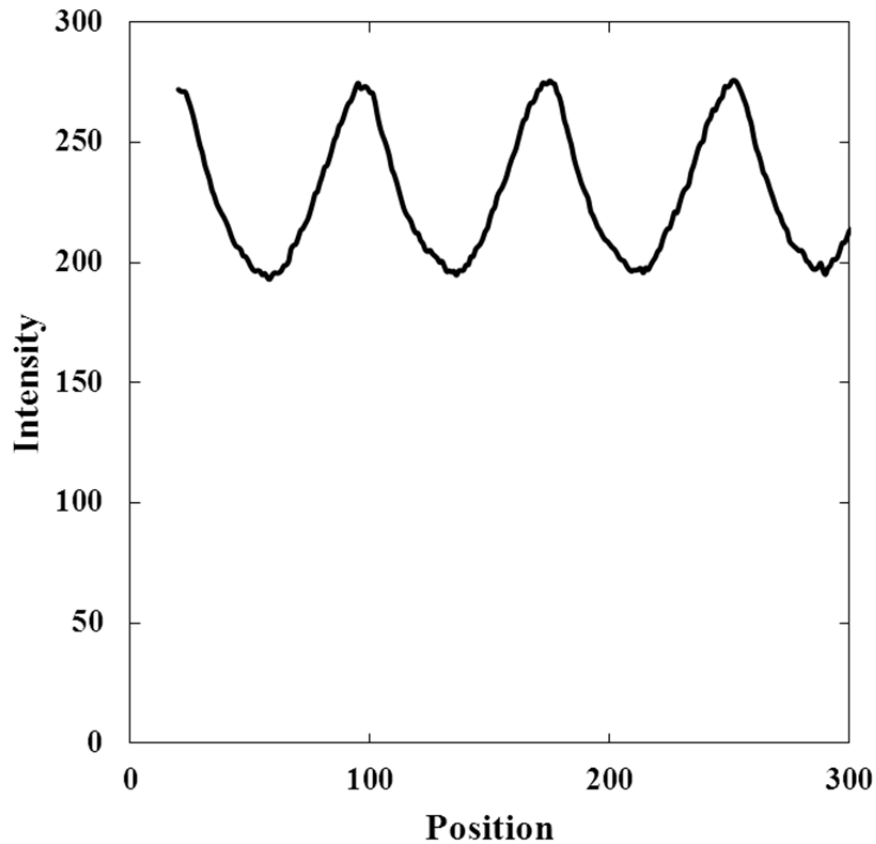


Figure A.21: Intensity vs. position plot for one time point

Insert a column between A and B, this is going to be the actual position rather than simply the pixel number. In new cell B1 insert '0' and then in B2 the formula should be '=B1+pixel_size'. With the current objectives and camera the pixel sizes are 10X = 0.645 $\mu\text{m}/\text{pixel}$, 20X = 0.3225 $\mu\text{m}/\text{pixel}$, 50X = 0.129 $\mu\text{m}/\text{pixel}$, 100X = 0.0645 $\mu\text{m}/\text{pixel}$. Next, in column D normalize the fluorescence intensity values with the formula '=C1/max(\$C\$1:\$C\$500)', if there are more than 500 rows in use, increase the maximum value. In column E insert the formula '=\$H\$1*cos(2*pi()*B1/\$H\$2)+\$H\$3', This will

generate the fitted sinusoid based on the X position. In H1 insert an initial guess for amplitude (A), in H2 an initial guess for the wavelength (λ) which should match the period of the photomask used, and in H3 an initial guess for the vertical shift (roughly the midpoint of the sinusoid). In F1 insert the formula ‘=(E1-D1)^2’ for the least squares fitting of the calculated sinusoid to the measured sinusoid. Finally in cell J1 insert the formula ‘=sum(f1:f500)’, again if there are more than 500 rows in use adjust the maximum. When completed the spreadsheet should look like Figure A.22.

	A	B	C	D	E	F	G	H	I	J
1	20	0	272.0254	0.986234	0.966167	0.000403		0.133093		0.117383
2	21	0.3225	271.3049	0.983621	0.965718	0.000321		24.65538		
3	22	0.645	271.1178	0.982943	0.964373	0.000345		0.833074		
4	23	0.9675	270.84	0.981936	0.962142	0.000392				
5	24	1.29	267.99	0.971603	0.95904	0.000158				
6	25	1.6125	265.0846	0.96107	0.955087	3.58E-05				
7	26	1.935	261.6191	0.948505	0.950311	3.26E-06				
8	27	2.2575	257.5226	0.933653	0.944743	0.000123				
9	28	2.58	252.9924	0.917229	0.938421	0.000449				
10	29	2.9025	248.6848	0.901612	0.931388	0.000887				
11	30	3.225	245.5507	0.890249	0.923692	0.001118				
12	31	3.5475	240.7551	0.872863	0.915383	0.001808				
13	32	3.87	237.58	0.861351	0.90652	0.00204				
14	33	4.1925	234.611	0.850587	0.89716	0.002169				
15	34	4.515	230.2351	0.834722	0.887367	0.002772				
16	35	4.8375	227.7772	0.825811	0.877208	0.002642				

Figure A.22: Completed Excel spreadsheet for one time point in a diffusion experiment.

In order to fit the calculated sinusoid and extract the A and λ values use the ‘Solver’ tool (in the ‘Data’) menu. Adjust cells H1:H3 in order to make cell J1 a minimum (see Figure A.23) and click ‘Solve’. It is helpful to plot the measured and calculated curves (Figure A.24 for an example) to see if it is a good fit. Repeat this procedure for all time points.

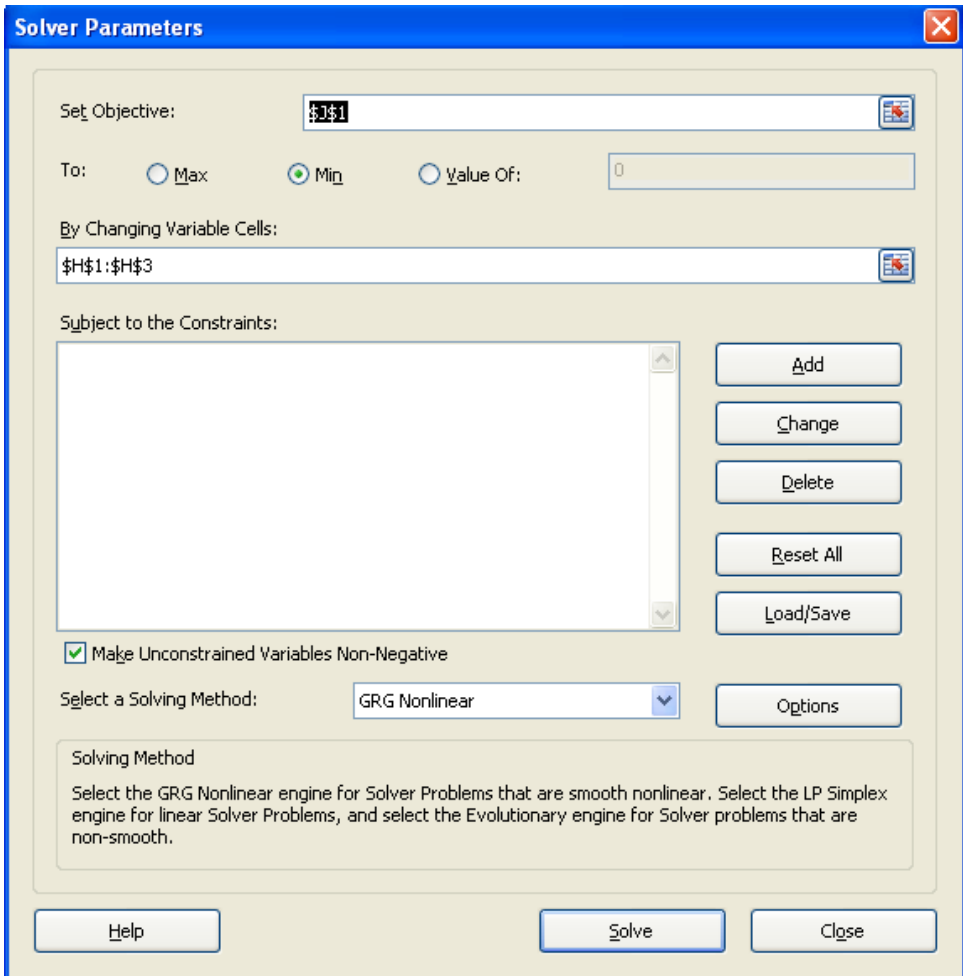


Figure A.23: Solver window setup for parameter calculation

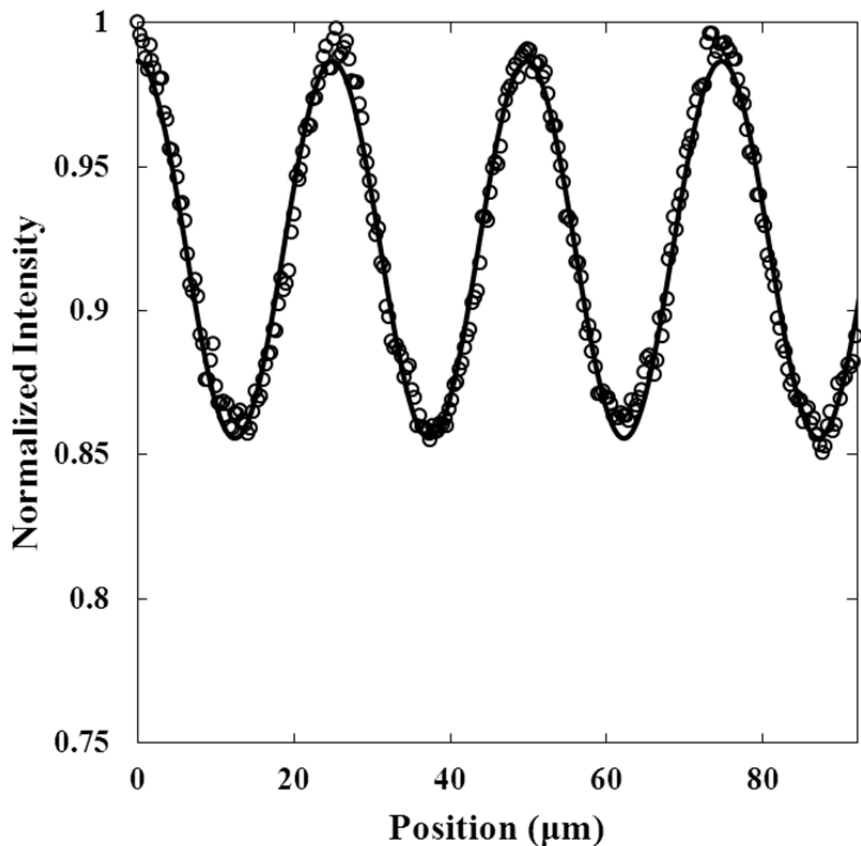


Figure A.24: Example curve fitting. Open symbols represent data points and the solid line is the best fit curve.

After the calculated sinusoids are all complete create a new tab for the combined data and calculation. Create a table of time, A and λ values collected from all the separate tabs. Insert columns to convert time to seconds, and the amplitude to $\ln(A/A_0)$ where A_0 is the A value for the initial condition. Plot $\ln(A/A_0)$ against time and fit a straight line to these data and use the ‘Add Trendline’ function to fit a straight line with the intercept through zero. This table should look like Figure A.25a, plot like Figure A.25b.

a)

	A	B	C	D	E	F
1	Time (min)	Time (sec)	Amp	AmpN	lnAmpN	λ (μm)
2	0	0	0.134969	1	0	24.58862
3	60	3600	0.133093	0.986101	-0.014	24.65538
4	120	7200	0.13016	0.964363	-0.03629	24.66802
5	180	10800	0.126781	0.939331	-0.06259	24.58192
6	240	14400	0.122729	0.909309	-0.09507	24.56539
7	300	18000	0.11965	0.886494	-0.12048	24.66224
8	360	21600	0.117967	0.874028	-0.13464	24.62877
9	420	25200	0.113137	0.838242	-0.17645	24.53156
10	480	28800	0.111053	0.822803	-0.19504	24.61051
11	540	32400	0.108619	0.804767	-0.2172	24.62012
12	600	36000	0.105808	0.783937	-0.24343	24.71301
13	660	39600	0.102653	0.760563	-0.2737	24.61578
14	720	43200	0.098508	0.729856	-0.31491	24.52215
15	780	46800	0.095578	0.708143	-0.34511	24.50179

b)

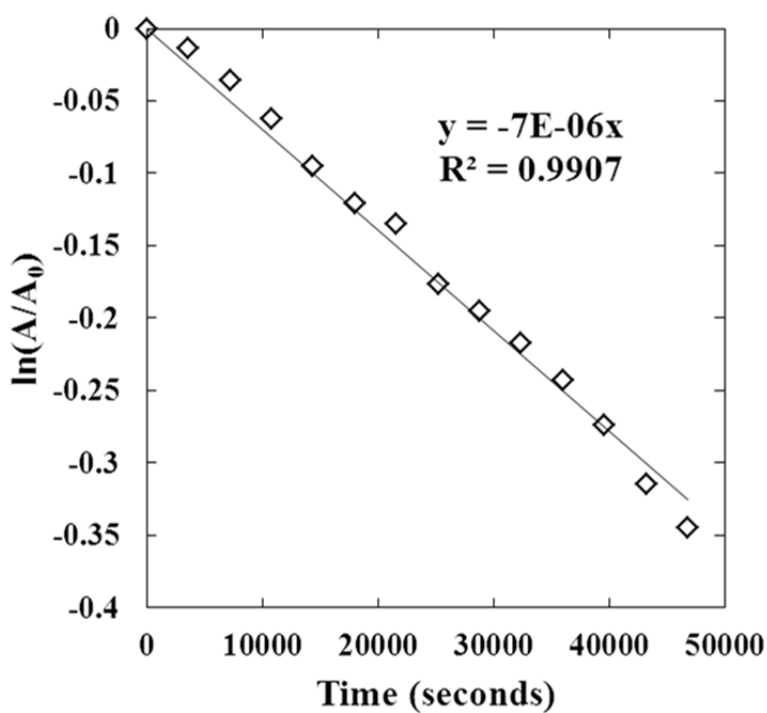


Figure A.25: a) Data table for diffusion experiment. b) Plot of data (open symbols) and best fit line (solid line), the slope is used to calculate the diffusion coefficient.

The diffusion coefficient and error can be calculated from these data. In the ‘Data’ menu select ‘Data Analysis’ and then ‘Regression’. For the ‘Input Y Range’ select the column of $\ln(A/A_0)$ and for ‘Input X Range’ select the time in seconds column. Select the check box for ‘Constant is Zero’ to set the y-intercept to zero and the ‘Confidence Level’ to 95%. Finally, select an output location, in this example it is just further over to the right on the worksheet. Figure A.26 shows what this window should look like when properly setup using the data from Figure A.25a.

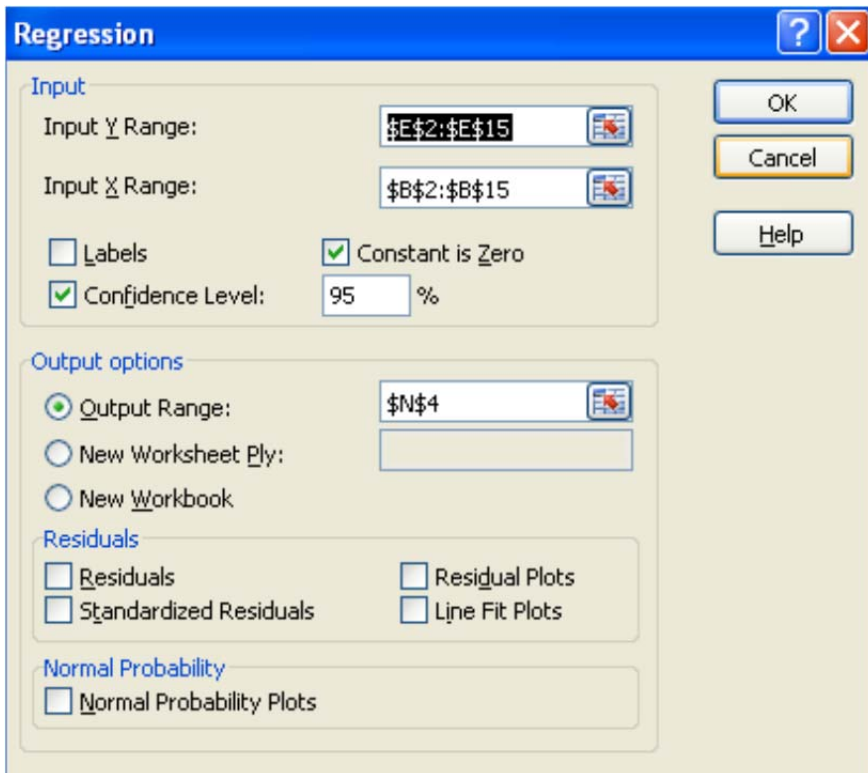


Figure A.26: Linear regression setup

The diffusion coefficient itself is going to be calculated from eq. A.1 in which D is the diffusion coefficient, λ is the average of the wavelengths from all time points (24.6 μm or 0.00246 cm in this example), and M is the slope of the best fit line which will

appear in the ‘Coefficients’ column and ‘X Variable 1’ row of the output of the linear regression (-6.9×10^{-6} in this example).

$$D = \frac{-M\lambda^2}{4\pi^2} \quad (\text{A.1})$$

In this example the diffusion coefficient is 1.07×10^{-12} cm²/sec. The final item to calculate is the experimental uncertainty (σ_D) which is calculated from eq. A.2 based on the standard deviation of the wavelength measurements (σ_λ) and the error in the slope calculation (σ_M).

$$\sigma_D = \sqrt{\left(\frac{-\lambda M}{2\pi^2} \sigma_\lambda\right)^2 + \left(\frac{-\lambda^2}{4\pi^2} \sigma_M\right)^2} \quad (\text{A.2})$$

In this example $\sigma_\lambda = 6.1 \times 10^{-6}$ cm, the standard deviation of column F in Figure A.25a, so the 95% confidence value is twice this, or 1.2×10^{-5} cm. The standard error in the slope is the average of the difference of the 95% confidence limits calculated from the linear regression. Take the difference of the value under ‘Lower 95%’ and the one other ‘Upper 95%’ that will appear in the results from the linear regression (Figure A.26) and divide by two to get $\sigma_M = 2.3 \times 10^{-7}$. The reason to divide by two is that the two numbers may not be equidistant from the value for M based on the scatter of the data, so this average gives a representative value to use in eq. A.2. From here the values can be inserted into eq. A.2 and final experimental result for the diffusion coefficient is $1.07 \pm 0.04 \times 10^{-12}$ cm²/sec.

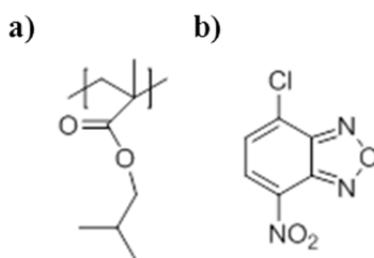
A.5 References

1. Abramoff, M. D., Magelhaes, P.J., Ram, S.J. *Biophotonics International* **2004**, *11*, 36-42.
2. Edelstein, A.; Amodaj, N.; Hoover, K.; Vale, R.; Stuurman, N. *Computer Control of Microscopes Using μ Manager*; John Wiley & Sons, Inc., 2001.
3. Hall, D. B.; Underhill, P.; Torkelson, J. M. *Polym. Eng. Sci.* **1998**, *38*, 2039-2045.
4. Spangler, L. L.; Torkelson, J. M.; Royal, J. S. *Polym. Eng. Sci.* **1990**, *30*, 644-653.

APPENDIX B: FLUORESCENTLY LABELED POLYMERS

B.1 Introduction

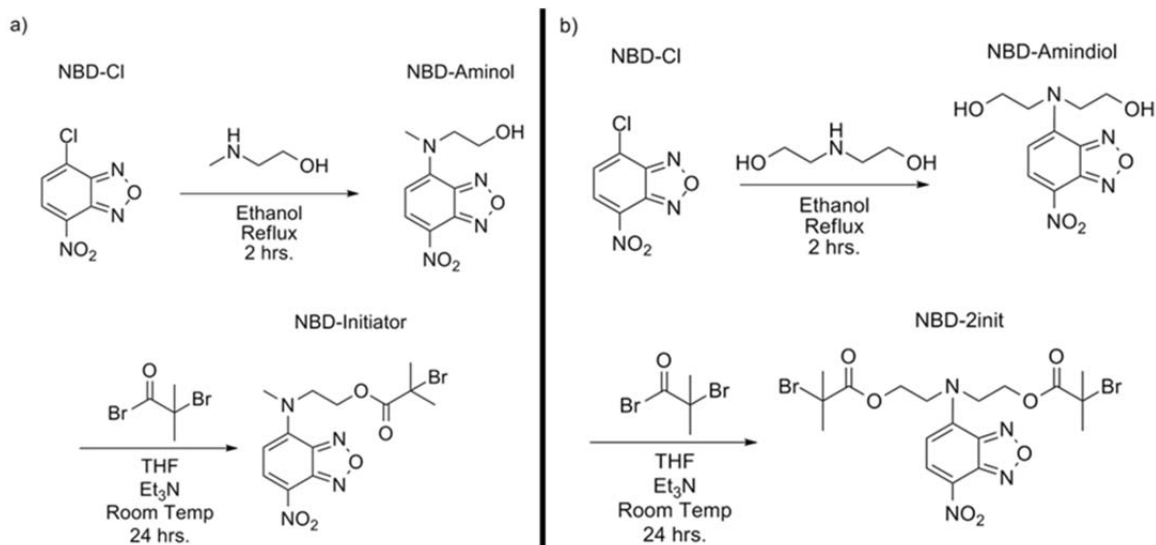
There are a wide variety of techniques that can be used to synthesize polymers with covalently attached fluorophores. Over the course of this work many of these approaches were attempted, with varying degrees of success. Focusing on poly(isobutyl methacrylate) (PiBMA) (see Scheme B.1a for the generic structure) as the polymer and nitrobenzofurazan (NBD) as the fluorophore, this appendix will review some of the strengths and weaknesses of the various approaches along with tips for the various reactions and purification. Broadly, there are two classes of approaches, those that incorporate NBD into the polymerization and those that attach NBD to some functional group in post-polymerization. NBD is available commercially as NBD-Cl (Scheme B.1b) from both Sigma Aldrich and Fisher Scientific and reacts readily with almost any primary or secondary amine which makes it a relatively flexible molecule to work with.



Scheme B.1: a) Structure of PiBMA b) Structure of NBD-Cl

B.2 NBD Incorporated Into Polymerization

The synthesis technique used for the materials in Chapter 2 involves atom transfer radical polymerization. An NBD containing mono-functional (Scheme B.2a) or di-functional (Scheme B.2b) ATRP initiator is synthesized. This procedure is adapted from Kalinina and Kumacheva.¹



Scheme B.2: a) Synthesis of mono-functional NBD bearing one ATRP initiator site for chain-end labeled polymers. b) Synthesis of di-functional NBD bearing two ATRP initiator sites for mid-chain labeled polymers

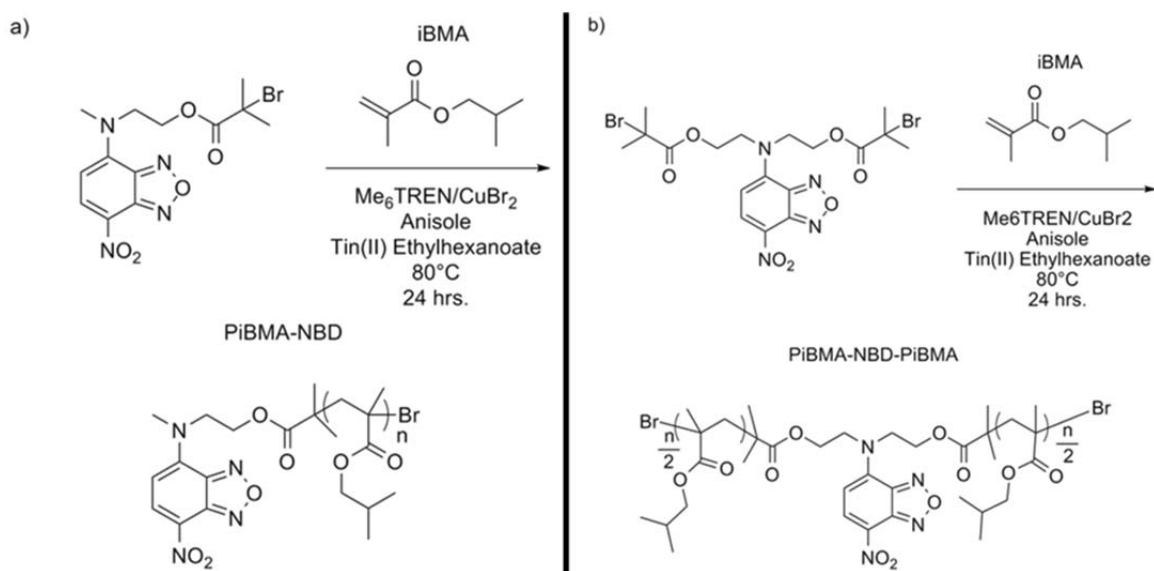
With regards to the NBD-amine synthesis, the reaction is insensitive to air or water, but the NBD-Cl should be allowed to completely dissolve in ethanol before addition of three molar excess 2-(methylamino)ethanol or diethanolamine before refluxing for two hours. After cooling in the freezer for several hours it should be washed with cold ethanol before recrystallization. Best results are obtained if after recrystallization it is left in the freezer overnight to completely precipitate. The solid product should also be washed with cold ethanol before drying.

The second step of the reaction, attachment of the initiator moiety, is adapted from Bardajee.² This reaction is water sensitive and therefore the liquid reagents (tetrahydrofuran, triethylamine and 2-bromoisobutyryl bromide) should be dried over calcium hydride and alumina before being either cannulated or injected via de-gassed syringe into a flask containing the NBD-amine that has been purged with argon for at

least 15-20 minutes. The flask should be cooled in an ice water bath before injection of the 2-bromoisobutyryl bromide, but it can be allowed to warm up during the reaction to room temperature. After overnight stirring, filter out the resulting solids (ammonium salts) and remove the solvent by rotovap. After drying, the solids should be re-dissolved in methylene chloride and liquid/liquid extracted in a separation funnel against deionized water (7 times) and concentrated sodium bicarbonate solution (3 times) before drying the organic layer over magnesium sulfate. Then the product can be dried, it is recommended to wrap the vial in aluminum foil and place in the vacuum oven at ~ 80 °C until the solids no longer have an odor; this can take about two days. This will remove the high boiling residual 2-bromoisobutyryl bromide. The key to successfully targeting molecular weights is to make sure the NMR of the product is clear of residual reagents from this reaction which can be difficult to remove.

These reagents are then used to start ARGET ATRP reactions to make either end-labeled (Scheme B.3a) or mid-chain labeled ATRP polymerizations. With regards to these polymerizations, the best result for the end-labeled polymer was run at 80 °C for 20 hours with 2.5 g of monomer. This was done via a three flask method. In one flask was a stock solution of some solvent (anisole) and the reducing agent (tin(II)-ethylhexanoate, 10:1 initiator to reducing agent is typically used). This stock solution should be designed such that 2 mL of the stock contains the proper amount of reducing agent and the total volume should be about 10 times this. The second flask contained the initiator in solvent. This solution had to be heated to ~ 100 °C in order to fully dissolve the initiator. The reaction flask contained the monomer, the rest of the solvent, Copper(II) Bromide (400 ppm copper to monomer) and Tris[2-(dimethylamino)ethyl]amine (Me_6TREN) to solubilize the copper at 10:1 Me_6TREN :Copper. Me_6TREN can be synthesized according to published procedures,³ or purchased commercially. All three flasks were sparged for

15 minutes and then the stock solutions were injected via degassed syringe into the reaction flask. In this reaction the ratio of monomer to initiator was 50:1. The molecular weight synthesized in this manner was very close to the ideal molecular weight calculated from the ratio of monomer to initiator. In order to purify this polymer, it should be precipitated out of a 50/50 mixture of acetonitrile and deionized water until by GPC the fluorimeter ($\lambda_{\text{excitation}} = 465 \text{ nm}$, $\lambda_{\text{emission}} = 520 \text{ nm}$) shows no small molecule peak from the unattached NBD.



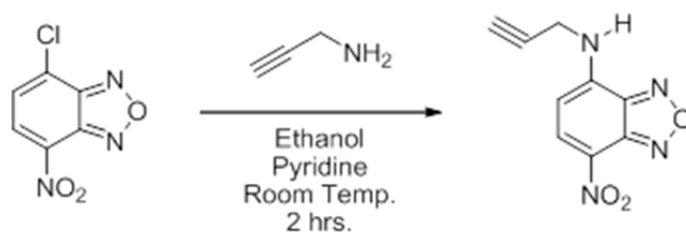
Scheme B.3: Synthesis of a) chain-end labeled PiBMA-NBD and b) mid-chain labeled PiBMA-NBD-PiBMA by ARGET ATRP.

B.3 Post-Polymerization Functionalization

B.3.1 Click Chemistry

One route to fluorescently labeled polymers is to use copper catalyzed azide-alkyne cycloaddition,⁴ also known as click chemistry, to attach NBD to a polymer that has been functionalized with the complementary functional group. One of the most significant advantages to this approach is that there is no need to synthesize a molecular

weight matched unlabeled version in order to dilute the fluorophore and avoid self-quenching. Since NBD is attached after polymer synthesis, some of the polymer can be kept aside unlabeled and is exactly the same molecular weight as the labeled polymer. NBD in these reactions will contain an alkyne group (NBD-Alkyne, see Scheme B.4), synthesized as adapted from the literature.⁵ There are several papers that reference synthesis of this compound, but this one has been successful so far.

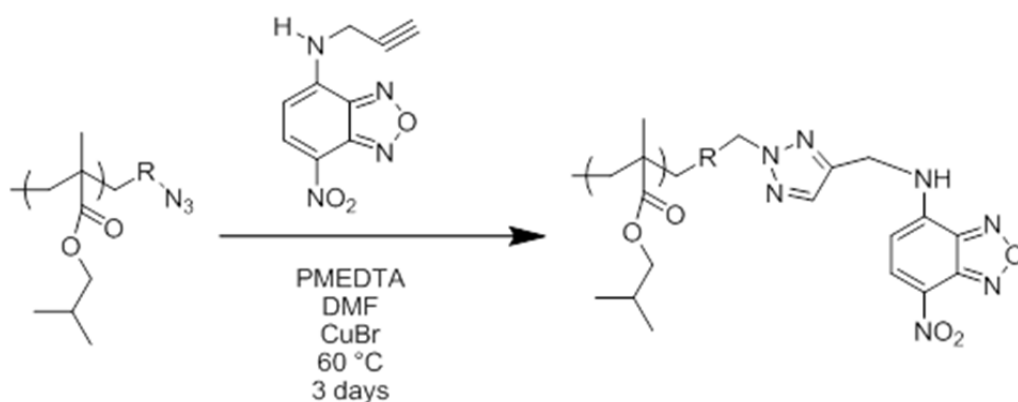


Scheme B.4: Synthesis of NBD-Alkyne

One point of note, however, is that the purification of this compound is very challenging, and the solvents recommended in this or other references do not lead to satisfactory purification by column chromatography, especially on large scales. It may be possible to recrystallize the product; however it is soluble in most solvents at room temperature. Additionally, when attempting to run NMR in chloroform there often are undissolved solids, which also contain the desired product. This fraction is soluble in *N,N'*-dimethylformamide (DMF) or dimethyl sulfoxide (for NMR). It may be simpler to proceed with the coupling reaction to the polymer and then remove the excess unreacted NBD-Cl via precipitation since this the major non-volatile impurity and it will not interfere with the click reaction. It is possible to characterize the ratio of NBD-Alkyne to NBD-Cl by NMR to allow more accurate setup of the click reaction. In chloroform the NBD-Alkyne has a doublet peak at 8.52 ppm and the unreacted NBD-Cl has two doublet

peaks that should have identical areas at 7.65 ppm and 8.45 ppm. If the NMR is run in DMSO, the product has a doublet peak at 8.55 ppm and the unreacted NBD-Cl has a doublet peak at 8.0 ppm.

The remainder of this section will focus on different ways to synthesize azide functionalized PiBMA, so here the click reaction itself will be discussed. This reaction (Scheme B.5) is very sensitive to oxygen because the Copper(I) Bromide (CuBr) will rapidly oxidize to copper oxide and the reaction will terminate. Therefore this reaction is set up in three flasks. In one flask the azide terminated polymer and copper solubilizing ligand N,N,N',N',N''-pentamethyldiethylenetriamine (PMEDA) are dissolved in DMF. In a second flask the NBD-Alkyne is dissolved in DMF. These flasks should be sparged with argon for ~15 minutes per 50 mL of solution. The third flask should be taken into a glove box where CuBr is stored along with a septum, a stir bar, and a zip tie. The reactants should be used in a molar ratio of 1:1.5:1.5:3 azide:PMEDA:CuBr:Alkyne. After weighing out the CuBr into the flask, seal it with the septum, the stir bar inside and zip tie before removing it from the glove box. Then the solutions in the other two flasks can be transferred by cannula into the flask with the CuBr. This reaction can be run at moderate temperatures (<60 °C) without concern, provided the reaction flask is not more than half full. Allowing the reaction to run for about three days (over a weekend) seems to give the highest label content results seen so far via this method.

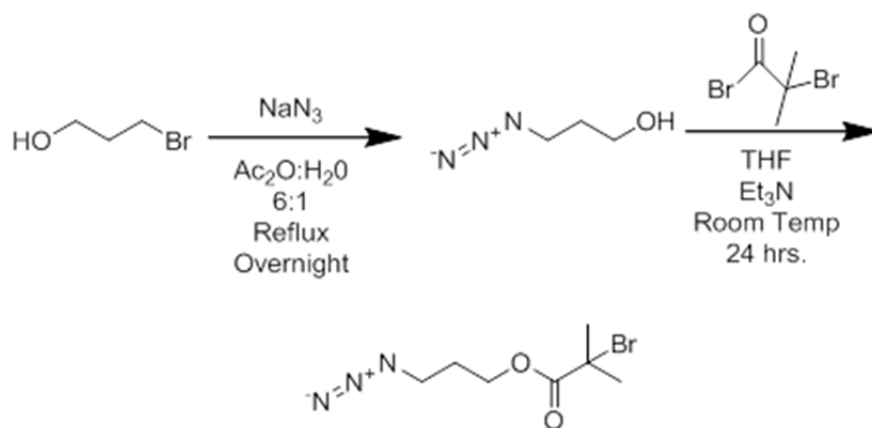


Scheme B.5: Click reaction of NBD-Alkyne with an azide containing polymer

B.3.2 ATRP

At first glance, it would appear that it would be very simple to use ATRP polymerizations and then attach NBD via a click reaction. This is because the bromine end of the growing polymer chain can be replaced with an azide group simply by stirring with sodium azide in DMF and then attaching the fluorophore directly. However, in reality this proves to be more complicated due to chain-chain coupling events that can mask end bromine groups. Several approaches were attempted to combat this including running reactions to lower conversion in order to limit these events. None were particularly successful, but may be for other types of polymers, like styrenics.

One approach that led to a high degree of labeling (~35% in initial trials) is synthesizing an azide containing ATRP initiator (Scheme B.6).⁶ This reference was only used in order to complete the first step of the reaction (synthesis of azido-propanol) and is followed exactly. The second step, attachment of the initiator moiety, was performed exactly as above to make NBD initiators (second step of Scheme B.2a). That being said, the PDI of the polymers made in the few trials using this technique was greater than the 1.2 needed to for diffusion experiments. Further optimization would probably be able to resolve these issues and make this a viable approach.

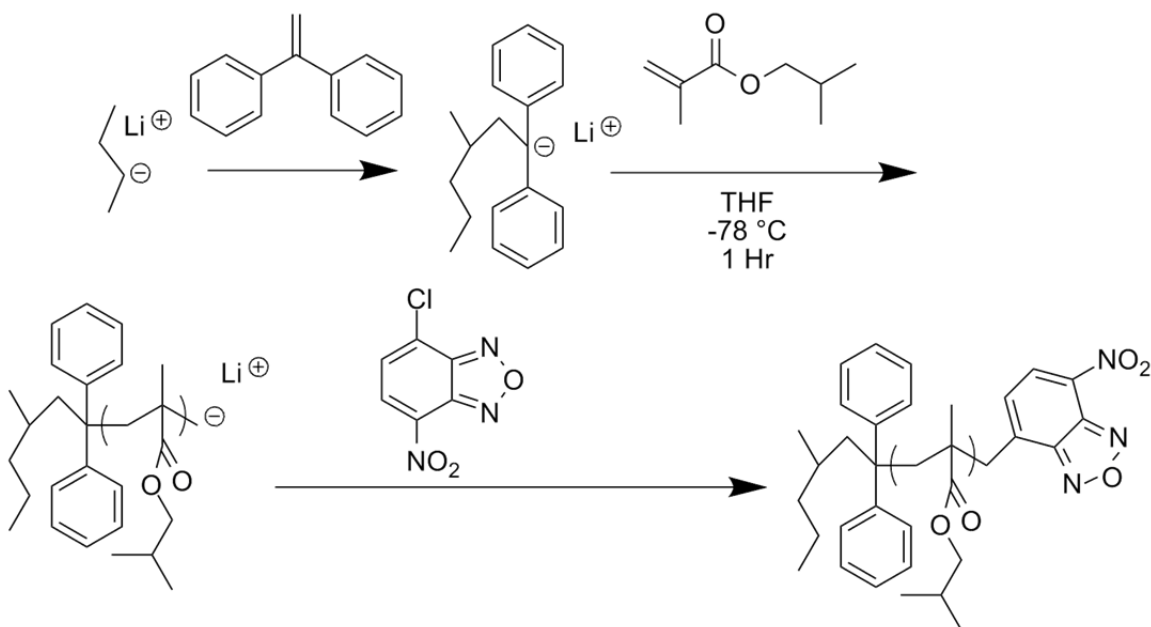


Scheme B.6: Synthesis of azide ATRP initiator

B.3.3 Anionic Polymerization

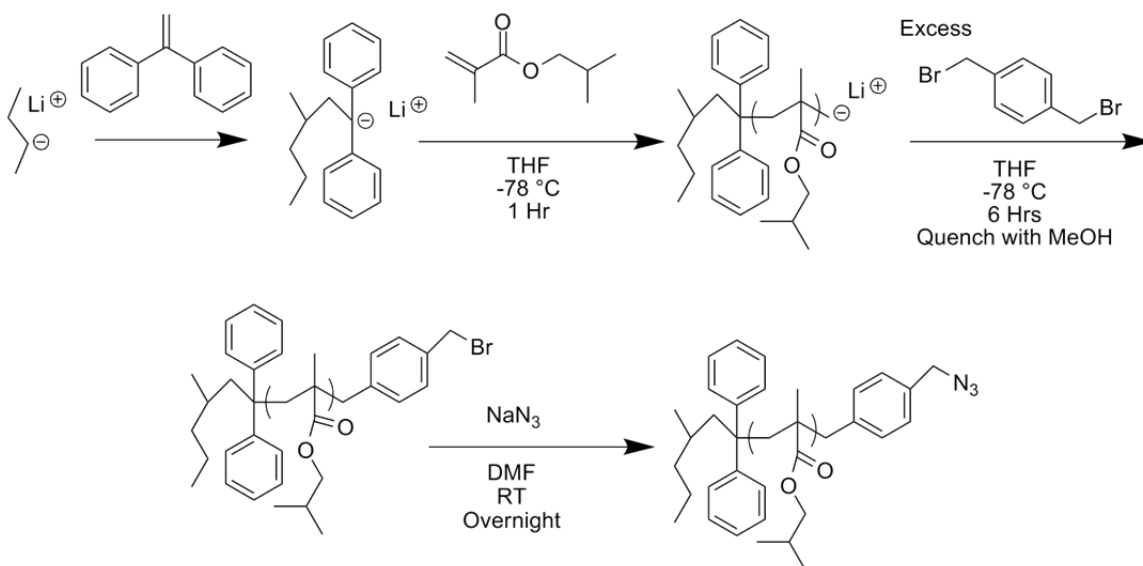
Anionic polymerizations are another route to synthesis of NBD labeled polymers. The biggest potential benefit to anionic polymerizations over ATRP is that anionic can be used for much larger polymer batches without significant scale up issues and with very high yields. Furthermore, there is no concern about the removal of copper or other impurities from the final product. The drawback, however, is the stringent purity requirements, use of pyrophoric reagents, time, and specialty glassware. That being said, the expertise does exist in this group to perform these reactions and it is a useful technique.

Two different routes to these polymers have been explored so far. The first route, the ‘simple’ route (Scheme B.7) is simply to take advantage of the anions’ ability to undergo nucleophilic substitution with the chlorine on NBD-Cl. This was tested on poly(methyl methacrylate) and led to moderate attachment levels.



Scheme B.7: 'Simple' anionic polymerization of PiBMA-NBD

The other approach is based on using a di-functional xylene, in this case α,α' -dibromo(p-xylene), (DBX), as a terminating agent (Scheme B.8).⁷ This approach uses the same substitution approach as the previous one, except that it is then followed by a click reaction to attach NBD. In the most successful polymerization using this approach lithium chloride was used in a 6 molar excess to the initiator and diphenylethylene was 1.2 molar excess. In order to add the DBX, a solvent flask was taken into the glove box where it was stored, and 5 molar excess to the initiator was added to the flask and sealed under argon. Then tetrahydrofuran can be dispensed directly into the flask from the solvent system or distilled from a separate flask. It will require a moderate amount of solvent to dissolve the DBX entirely, but the DBX needs to be added to the reactor as quickly as possible to avoid coupling reactions without warming up the solution too much. After the reaction is complete, azide can be added to the dried polymer by stirring 3 molar excess sodium azide with the polymer at room temperature overnight in DMF.



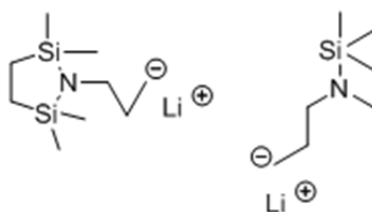
Scheme B.8: Halide end-capped anionic polymerization of PiBMA and azide attachment.

B.4 Other Potential Routes

There are several approaches that have not been previously attempted but could be if the need for a pathway not described above becomes necessary for any reason.

B.4.1 Protected Anionic Initiators

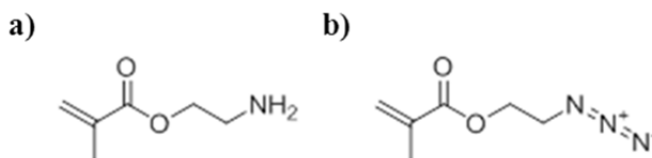
One interesting option is to build a functional group into the initiator of an anionic polymerization. Due to the sensitivity of these reactions, any functional halide, amine, or hydroxyl has to be protected during the polymerization. Some of these protected initiators used to be available from FMC Lithium but do not appear to be any longer. Description of the synthesis procedures for some of these compounds appear in a patent,⁸ and the structures appear in Scheme B.9. The idea behind this is that NBD-Cl rapidly reacts with amines and could simply be attached to the polymer after polymerization.



Scheme B.9: Protected amine containing anionic polymerization initiators

B.4.2 Functional Monomers

Another possibility for attachment of NBD is the incorporation of a functional monomer during polymerization. Care would have to be taken that the amount of incorporation was low enough (1-2 per chain) so that the polymer still behaved like PiBMA in diffusion experiments. As discussed in Chapter 2, the location of the fluorophore along the polymer backbone has no effect on its diffusion. Two options are immediately apparent for these monomers. First would be co-polymerization with an amine containing monomer such as 2-aminoethyl methacrylate (available from Polysciences, Scheme B.10a) and then using the amine group to attach to NBD. A second option would be the incorporation of an azide containing monomer, such as 2-azidoethyl methacrylate (Scheme B.10b)⁹ which could then be used in a click reaction with NBD-Alkyne.



Scheme B.10: Functional monomers: a) amine methacrylate b) azide methacrylate

B.5 References

1. Kalinina, O.; Kumacheva, E. *Macromolecules* **1999**, *32*, 4122-4129.
2. Bardajee, G. R.; Li, A. Y.; Haley, J. C.; Winnik, M. A. *Dyes Pigment.* **2008**, *79*, 24-32.
3. Fu, G. D.; Xu, L. Q.; Yao, F.; Zhang, K.; Wang, X. F.; Zhu, M. F.; Nie, S. Z. *ACS Appl. Mater. Interfaces* **2009**, *1*, 239-243.
4. Tornøe, C. W.; Christensen, C.; Meldal, M. *The Journal of Organic Chemistry* **2002**, *67*, 3057-3064.
5. McGill, N. W.; Williams, S. J. *J. Org. Chem.* **2009**, *74*, 9388-9398.
6. Mantovani, G.; Ladmiral, V.; Tao, L.; Haddleton, D. M. *Chemical Communications* **2005**, *0*, 2089-2091.
7. Ho, C.-C.; Dai, C.-A.; Su, W.-F. *Journal of Applied Polymer Science* **2009**, *111*, 1571-1580.
8. Schwindeman, J. A.; Granger, E. J.; Quirk, R. P.; Hall, R. W.; Letchford, R. J. *Protected amine initiators and polymers derived therefrom*, WO2000050479A1 2000.
9. Canalle, L. A.; van Berkel, S. S.; de Haan, L. T.; van Hest, J. C. M. *Advanced Functional Materials* **2009**, *19*, 3464-3470.

References

1. American Chemical Society National Historic Chemical Landmarks. Bakelite: The World's First Synthetic Plastic. .
<http://portal.acs.org/portal/PublicWebSite/education/whatischemistry/landmarks/bakelite/index.htm> (Accessed February 11, 2013).
2. History - DuPont Heritage Timeline: Nylon.
http://www2.dupont.com/Phoenix_Heritage/en_US/1939_c_detail.html (Accessed February 11, 2013).
3. How Stuff Works: How Nonstick Cookware Works.
<http://home.howstuffworks.com/nonstick-cookware.htm> (Accessed February 8, 2013).
4. Gaston Narada: What is a Lithium Battery? <http://www.gaston-lithium.com/> (Accessed February 8, 2013).
5. Vendra, V. K.; Wu, L.; Krishnan, S. *Nanomaterials for the Life Sciences Vol.5: Nanostructured Thin Films and Surfaces.*; WILEY-VCH Verlag GmbH & Co. KGaA: Weinheim, 2010.
6. Rubinstein, M.; Colby, R. H. *Polymer Physics*; Oxford University Press: Oxford, 2003.
7. Einstein, A. *Ann. Phys. (Weinheim, Ger.)* **1906**, *19*, 371-381.
8. Einstein, A. *Ann. Phys. (Weinheim, Ger.)* **1905**, *17*, 549-560.
9. Stokes, G. G. *Trans. Cambridge. Phil. Soci.* **1851**, *9*, 8-106.
10. Rouse, P. E., Jr. *Journal of Chemical Physics* **1953**, *21*, 1272-80.
11. Doi, M.; Edwards, S. F. *The Theory of Polymer Dynamics*; Clarendon Press: Oxford, 1986.
12. de Gennes, P. G. *Journal of Chemical Physics* **1971**, *55*, 572-579.
13. Jones, R. A. L.; Richards, R. W. *Polymers at Surfaces and Interfaces*; Cambridge University Press: Cambridge, 1999.
14. Lodge, T. P. *Physical Review Letters* **1999**, *83*, 3218-3221.

15. Byutner, O.; Smith, G. D. *J. Polym. Sci. Pt. B-Polym. Phys.* **2001**, *39*, 3067-3071.
16. Fleischer, G.; Appel, M. *Macromolecules* **1995**, *28*, 7281-7283.
17. Pearson, D. S.; Fetters, L. J.; Graessley, W. W.; Strate, G. V.; Vonmeerwall, E. *Macromolecules* **1994**, *27*, 711-719.
18. Bartels, C. R.; Crist, B.; Graessley, W. W. *Macromolecules* **1984**, *17*, 2702-2708.
19. Tao, H.; Lodge, T. P.; von Meerwall, E. D. *Macromolecules* **2000**, *33*, 1747-1758.
20. von Meerwall, E. D. *Advances in Polymer Science* **1984**, *54*, 1-29.
21. Appel, M.; Fleischer, G. *Macromolecules* **1993**, *26*, 5520-5525.
22. Kubo, T.; Nose, T. *Polym. J.* **1992**, *24*, 1351-1361.
23. Richter, D.; Willner, L.; Zirkel, A.; Farago, B.; Fetters, L. J.; Huang, J. S. *Macromolecules* **1994**, *27*, 7437-7446.
24. Drzewinski, A.; van Leeuwen, J. M. J. *Phys. Rev. E* **2008**, *77*, 8.
25. Sun, Q.; Faller, R. *Macromolecules* **2006**, *39*, 812-820.
26. Huang, Y.; Paul, D. R. *Macromolecules* **2006**, *39*, 1554-1559.
27. Pfromm, P. H.; Koros, W. J. *Polymer* **1995**, *36*, 2379-2387.
28. Priestley, R. D.; Ellison, C. J.; Broadbelt, L. J.; Torkelson, J. M. *Science* **2005**, *309*, 456-459.
29. Kawana, S.; Jones, R. A. L. *Eur. Phys. J. E* **2003**, *10*, 223-230.
30. Khare, R.; dePablo, J. J.; Yethiraj, A. *Macromolecules* **1996**, *29*, 7910-7918.
31. Luengo, G.; Schmitt, F. J.; Hill, R.; Israelachvili, J. *Macromolecules* **1997**, *30*, 2482-2494.
32. Yang, Z.; Fujii, Y.; Lee, F. K.; Lam, C.-H.; Tsui, O. K. C. *Science* **2010**, *328*, 1676-1679.

33. Stafford, C. M.; Vogt, B. D.; Harrison, C.; Julthongpiput, D.; Huang, R. *Macromolecules* **2006**, *39*, 5095-5099.
34. Torres, J. M.; Stafford, C. M.; Vogt, B. D. *Polymer* **2010**, *51*, 4211-4217.
35. Torres, J. M.; Stafford, C. M.; Vogt, B. D. *ACS Nano* **2009**, *3*, 2677-2685.
36. Zhang Newby, B.-m.; Wakabayashi, K.; Composto, R. J. *Polymer* **2001**, *42*, 9155-9162.
37. O'Connell, P. A.; McKenna, G. B. *Science* **2005**, *307*, 1760-1763.
38. Huang, R.; Stafford, C. M.; Vogt, B. D. *J. Aerosp. Eng.* **2007**, *20*, 38-44.
39. Wang, X. P.; Xiao, X.; Tsui, O. K. C. *Macromolecules* **2001**, *34*, 4180-4185.
40. Paeng, K.; Ediger, M. D. *Macromolecules* **2011**, *44*, 7034-7042.
41. Paeng, K.; Swallen, S. F.; Ediger, M. D. *J. Am. Chem. Soc.* **2011**, *133*, 8444-8447.
42. Russell, T. P. *Annu. Rev. Mater. Sci.* **1991**, *21*, 249-268.
43. Green, P. F.; Palmstrom, C. J.; Mayer, J. W.; Kramer, E. J. *Macromolecules* **1985**, *18*, 501-507.
44. Vaia, R. A.; Giannelis, E. P. *MRS Bull.* **2001**, *26*, 394-401.
45. Gopakumar, T. G.; Lee, J. A.; Kontopoulou, M.; Parent, J. S. *Polymer* **2002**, *43*, 5483-5491.
46. Ji, S. X.; Liu, C. C.; Liu, G. L.; Nealey, P. F. *ACS Nano* **2010**, *4*, 599-609.
47. Binder, K.; Milchev, A.; Baschnagel, J. *Annu. Rev. Mater. Sci.* **1996**, *26*, 107-134.
48. Frank, B.; Gast, A. P.; Russell, T. P.; Brown, H. R.; Hawker, C. *Macromolecules* **1996**, *29*, 6531-6534.
49. Bae, S. C.; Wong, J. S.; Kim, M.; Jiang, S.; Hong, L.; Granick, S. *Philos. Trans. R. Soc. A-Math. Phys. Eng. Sci.* **2008**, *366*, 1443-1454.
50. Wong, J. S. S.; Hong, L.; Bae, S. C.; Granick, S. *Journal of Polymer Science Part B: Polymer Physics* **2010**, *48*, 2582-2588.

51. Sukhishvili, S. A.; Chen, Y.; Muller, J. D.; Gratton, E.; Schweizer, K. S.; Granick, S. *Macromolecules* **2002**, *35*, 1776-1784.
52. Manias, E.; Chen, H.; Krishnamoorti, R.; Genzer, J.; Kramer, E. J.; Giannelis, E. *P. Macromolecules* **2000**, *33*, 7955-7966.
53. Composto, R. J.; Mayer, J. W.; Kramer, E. J.; White, D. M. *Phys. Rev. Lett.* **1986**, *57*, 1312-1315.
54. Green, P. F.; Doyle, B. L. *Macromolecules* **1987**, *20*, 2471-2474.
55. Green, P. F.; Kramer, E. J. *Macromolecules* **1986**, *19*, 1108-1114.
56. Mills, P. J.; Green, P. F.; Palmstrom, C. J.; Mayer, J. W.; Kramer, E. J. *Applied Physics Letters* **1984**, *45*, 957-959.
57. Pu, Y.; Rafailovich, M. H.; Sokolov, J.; Gersappe, D.; Peterson, T.; Wu, W. L.; Schwarz, S. A. *Phys. Rev. Lett.* **2001**, *87*, 4.
58. van Alsten, J. G.; Sauer, B. B.; Walsh, D. J. *Macromolecules* **1992**, *25*, 4046-4048.
59. Yokoyama, H.; Kramer, E. J.; Rafailovich, M. H.; Sokolov, J.; Schwarz, S. A. *Macromolecules* **1998**, *31*, 8826-8830.
60. Zheng, X.; Sauer, B. B.; Vanalsten, J. G.; Schwarz, S. A.; Rafailovich, M. H.; Sokolov, J.; Rubinstein, M. *Phys. Rev. Lett.* **1995**, *74*, 407-410.
61. Deppe, D. D.; Dhinojwala, A.; Torkelson, J. M. *Macromolecules* **1996**, *29*, 3898-3908.
62. Dhinojwala, A.; Torkelson, J. M. *Macromolecules* **1994**, *27*, 4817-4824.
63. Kumar, S. K.; Vacatello, M.; Yoon, D. Y. *Journal of Chemical Physics* **1988**, *89*, 5206-5215.
64. Madden, W. G. *Journal of Chemical Physics* **1988**, *88*, 3934-3943.
65. Zheng, X.; Rafailovich, M. H.; Sokolov, J.; Strzhemechny, Y.; Schwarz, S. A.; Sauer, B. B.; Rubinstein, M. *Phys. Rev. Lett.* **1997**, *79*, 241-244.
66. Magde, D.; Webb, W. W.; Elson, E. *Physical Review Letters* **1972**, *29*, 705-&.

67. Casoli, A.; Schonhoff, M. *Biol. Chem.* **2001**, *382*, 363-369.
68. Cherdhirankorn, T.; Floudas, G.; Butt, H. J.; Koynov, K. *Macromolecules* **2009**, *42*, 9183-9189.
69. Cherdhirankorn, T.; Harmandaris, V.; Juhari, A.; Voudouris, P.; Fytas, G.; Kremer, K.; Koynov, K. *Macromolecules* **2009**, *42*, 4858-4866.
70. Masuda, A.; Ushida, K.; Okamoto, T. *J. Photochem. Photobiol. A-Chem.* **2006**, *183*, 304-308.
71. Zettl, H.; Hafner, W.; Boker, A.; Schmalz, H.; Lanzendorfer, M.; Muller, A. H. E.; Krausch, G. *Macromolecules* **2004**, *37*, 1917-1920.
72. Zhao, J.; Granick, S. *Macromolecules* **2007**, *40*, 1243-1247.
73. Van Keuren, E.; Schrof, W. *Macromolecules* **2003**, *36*, 5002-5007.
74. Tirrell, M.; Adolf, D.; Prager, S. *Lecture Notes in Mathematics* **1984**, *1063*, 37-45.
75. Hall, D. B.; Torkelson, J. M. *Macromolecules* **1998**, *31*, 8817-8825.
76. Pohl, D. W.; Schwarz, S. E.; Irniger, V. *Physical Review Letters* **1973**, *31*, 32-35.
77. Wang, C. H.; Xia, J. L. *Journal of Chemical Physics* **1990**, *92*, 2603-2613.
78. Tonge, M. P.; Stubbs, J. M.; Sundberg, D. C.; Gilbert, R. G. *Polymer* **2000**, *41*, 3659-3670.
79. Hamersky, M. W.; Tirrell, M.; Lodge, T. P. *Langmuir* **1998**, *14*, 6974-6979.
80. Cavicchi, K. A.; Lodge, T. P. *Macromolecules* **2004**, *37*, 6004-6012.
81. Axelrod, D.; Koppel, D. E.; Schlessinger, J.; Elson, E.; Webb, W. W. *Biophys. J.* **1976**, *16*, 1055-1069.
82. Zhang, F.; Schmidt, W. G.; Hou, Y.; Williams, A. F.; Jacobson, K. *Proc. Natl. Acad. Sci. U. S. A.* **1992**, *89*, 5231-5235.
83. Bulinski, J. C.; Odde, D. J.; Howell, B. J.; Salmon, T. D.; Waterman-Storer, C. M. *J. Cell Sci.* **2001**, *114*, 3885-3897.

84. Johnson, M. E.; Berk, D. A.; Blankschtein, D.; Golan, D. E.; Jain, R. K.; Langer, R. S. *Biophys. J.* **1996**, *71*, 2656-2668.
85. Smith, B. A. *Macromolecules* **1982**, *15*, 469-472.
86. Cicerone, M. T.; Blackburn, F. R.; Ediger, M. D. *Macromolecules* **1995**, *28*, 8224-8232.
87. Pinte, J.; Joly, C.; Ple, K.; Dole, P.; Feigenbaum, A. *J. Agric. Food Chem.* **2008**, *56*, 10003-10011.
88. Inoue, T.; Nemoto, N.; Kojima, T.; Kurata, M. *Polym. J.* **1988**, *20*, 869-874.
89. Hiemenz, P.; Lodge, T. P. *Polymer Chemistry*; 2nd ed.; CRC Press: Boca Raton, FL, 2007.
90. Forrest, J. A.; Dalnoki-Veress, K. *Advances in Colloid and Interface Science* **2001**, *94*, 167-195.
91. de Gennes, P. G. *Eur. Phys. J. E* **2000**, *2*, 201-203.
92. Ellison, C. J.; Torkelson, J. M. *Nat. Mater.* **2003**, *2*, 695-700.
93. Roth, C. B.; McNerny, K. L.; Jager, W. F.; Torkelson, J. M. *Macromolecules* **2007**, *40*, 2568-2574.
94. Russell, T. P.; Kumar, S. K. *Nature* **1997**, *386*, 771-772.
95. Ellison, C. J.; Kim, S. D.; Hall, D. B.; Torkelson, J. M. *Eur. Phys. J. E* **2002**, *8*, 155-166.
96. Priestley, R. D.; Mundra, M. K.; Barnett, N. J.; Broadbelt, L. J.; Torkelson, J. M. *Aust. J. Chem.* **2007**, *60*, 765-771.
97. Fukao, K.; Uno, S.; Miyamoto, Y.; Hoshino, A.; Miyaji, H. *Phys. Rev. E* **2001**, *64*, 11.
98. Hartmann, L.; Gorbatschow, W.; Hauwede, J.; Kremer, F. *Eur. Phys. J. E* **2002**, *8*, 145-154.
99. Beaucage, G.; Composto, R.; Stein, R. S. *J. Polym. Sci., Part B: Polym. Phys.* **1993**, *31*, 319-26.

100. Keddie, J. L.; Jones, R. A. L.; Cory, R. A. *Faraday Discuss.* **1994**, *98*, 219-230.
101. Grohens, Y.; Hamon, L.; Reiter, G.; Soldera, A.; Holl, Y. *Eur. Phys. J. E* **2002**, *8*, 217-224.
102. Kim, S.; Mundra, M. K.; Roth, C. B.; Torkelson, J. M. *Macromolecules*, *43*, 5158-5161.
103. Dalnoki-Veress, K.; Forrest, J. A.; Murray, C.; Gigault, C.; Dutcher, J. R. *Phys Rev E Stat Nonlin Soft Matter Phys* **2001**, *63*, 031801.
104. Roth, C. B.; Dutcher, J. R. *Eur. Phys. J. E* **2003**, *12*, S103-S107.
105. Granick, S.; Bae, S. C. *Journal of Polymer Science Part B: Polymer Physics* **2006**, *44*, 3434-3435.
106. Frankenburg, W. G. *Advances in catalysis and related subjects*; Academic Press: New York, New York, 1966.
107. McCafferty, E.; Wightman, J. P. *Surf. Interface Anal.* **1998**, *26*, 549-564.
108. Kim, S.; Hewlett, S. A.; Roth, C. B.; Torkelson, J. M. *Eur. Phys. J. E* **2009**, *30*, 83-92.
109. Priestley, R.; Mundra, M. K.; Barnett, N. J.; Broadbelt, L. J.; Torkelson, J. M. *Aust. J. Chem.* **2007**, *60*, 765-771.
110. Arbeloa, F. L.; Ojeda, P. R.; Arbeloa, I. L. *J. Lumines.* **1989**, *44*, 105-112.
111. Hamann, S.; Kiilgaard, J.; Litman, T.; Alvarez-Leefmans, F.; Winther, B.; Zeuthen, T. *Journal of Fluorescence* **2002**, *12*, 139-145.
112. Lakowicz, J. R.; Malicka, J.; D'Auria, S.; Gryczynski, I. *Anal. Biochem.* **2003**, *320*, 13-20.
113. Zhang, J. A.; Fu, Y.; Lakowicz, J. R. *J. Phys. Chem. C* **2007**, *111*, 1955-1961.
114. Smith, B. A.; Mumby, S. J.; Samulski, E. T.; Yu, L. P. *Macromolecules* **1986**, *19*, 470-472.
115. Tseng, K. C.; Turro, N. J.; Durning, C. J. *Polymer* **2000**, *41*, 4751-4755.

116. Crank, J. *Mathematics of Diffusion*; 2nd ed.; Oxford University Press: New York, 1975.
117. Bicerano, J. *Prediction of Polymer Properties*; 3rd ed.; Marcel Dekker, Inc.: New York, 2002.
118. Milhaupt, J. M.; Lodge, T. P.; Smith, S. D.; Hamersky, M. W. *Macromolecules* **2001**, *34*, 5561-5570.
119. Abramoff, M. D., Magelhaes, P.J., Ram, S.J. *Biophotonics International* **2004**, *11*, 36-42.
120. *Polymer Handbook*; Barandrup, J.; Immergut, E. H.; Grulke, E. A., Eds.; Wiley and Sons: Hoboken, New Jersey, 1999.
121. Desai, T.; Keblinski, P.; Kumar, S. K. *Journal of Chemical Physics* **2005**, *122*, 8.
122. Torres, J. A.; Nealey, P. F.; de Pablo, J. J. *Phys. Rev. Lett.* **2000**, *85*, 3221-3224.
123. Forrest, J. A.; Dalnoki-Veress, K. *Adv. Colloid Interface Sci.* **2001**, *94*, 167-196.
124. Jones, R. L.; Kumar, S. K.; Ho, D. L.; Briber, R. M.; Russell, T. P. *Nature* **1999**, *400*, 146-149.
125. Jones, R. L.; Kumar, S. K.; Ho, D. L.; Briber, R. M.; Russell, T. P. *Macromolecules* **2001**, *34*, 559-567.
126. Fu, G. D.; Xu, L. Q.; Yao, F.; Zhang, K.; Wang, X. F.; Zhu, M. F.; Nie, S. Z. *ACS Appl. Mater. Interfaces* **2009**, *1*, 239-243.
127. Jakubowski, W.; Min, K.; Matyjaszewski, K. *Macromolecules* **2006**, *39*, 39-45.
128. Matyjaszewski, K.; Jakubowski, W.; Min, K.; Tang, W.; Huang, J. Y.; Braunecker, W. A.; Tsarevsky, N. V. *Proc. Natl. Acad. Sci. U. S. A.* **2006**, *103*, 15309-15314.
129. Pintauer, T.; Matyjaszewski, K. *Chem. Soc. Rev.* **2008**, *37*, 1087-1097.
130. Jakubowski, W.; Kirci-Denizli, B.; Gil, R. R.; Matyjaszewski, K. *Macromol. Chem. Phys.* **2008**, *209*, 32-39.
131. Bardajee, G. R.; Li, A. Y.; Haley, J. C.; Winnik, M. A. *Dyes Pigment.* **2008**, *79*, 24-32.

132. Kalinina, O.; Kumacheva, E. *Macromolecules* **1999**, *32*, 4122-4129.
133. Hall, D. B.; Underhill, P.; Torkelson, J. M. *Polym. Eng. Sci.* **1998**, *38*, 2039-2045.
134. Spangler, L. L.; Torkelson, J. M.; Royal, J. S. *Polym. Eng. Sci.* **1990**, *30*, 644-653.
135. Beaucage, G.; Composto, R.; Stein, R. S. *J. Polym. Sci. Pt. B-Polym. Phys.* **1993**, *31*, 319-326.
136. Edelstein, A.; Amodaj, N.; Hoover, K.; Vale, R.; Stuurman, N. *Computer Control of Microscopes Using μ Manager*; John Wiley & Sons, Inc., 2001.
137. Evans, C. M.; Narayanan, S.; Jiang, Z.; Torkelson, J. M. *Physical Review Letters* **2012**, *109*, 038302.
138. Boucher, V. M.; Cangialosi, D.; Yin, H.; Schonhals, A.; Alegria, A.; Colmenero, J. *Soft Matter* **2012**, *8*, 5119-5122.
139. Gehlsen, M. D.; Bates, F. S. *Macromolecules* **1993**, *26*, 4122-4127.
140. Donth, E. *The Glass Transition: Relaxation Dynamics in Liquids and Disordered Materials*; Springer: Heidelberg, Germany, 2001.
141. Ndoni, S.; Papadakis, C. M.; Bates, F. S.; Almdal, K. *Review of Scientific Instruments* **1995**, *66*, 1090-1095.
142. Ho, C.-C.; Dai, C.-A.; Su, W.-F. *Journal of Applied Polymer Science* **2009**, *111*, 1571-1580.
143. Binder, W. H.; Sachsenhofer, R. *Macromolecular Rapid Communications* **2007**, *28*, 15-54.
144. McGill, N. W.; Williams, S. J. *J. Org. Chem.* **2009**, *74*, 9388-9398.
145. Rostovtsev, V. V.; Green, L. G.; Fokin, V. V.; Sharpless, K. B. *Angewandte Chemie International Edition* **2002**, *41*, 2596-2599.
146. Nie, Z.; Kumacheva, E. *Nature Materials* **2008**, *7*, 277-290.
147. del Campo, A.; Arzt, E. *Generating Micro- and Nanopatterns on Polymeric Materials*; 2 ed.; Wiley-VCH: Weinheim, 2011.

148. Bruning, J. H. *Proc. SPIE* **2007**, 6520, 652004.
149. Thompson, S. E.; Parthasarathy, S. *Mater. Today* **2006**, 9, 20-25.
150. Rogers, J. A.; Nuzzo, R. G. *Mater. Today* **2005**, 8, 50-56.
151. Xia, Y.; Whitesides, G. M. *Annu. Rev. Mater. Sci.* **1998**, 28, 153-184.
152. Kim, P.; Kwon, K. W.; Park, M. C.; Lee, S. H.; Kim, S. M.; Suh, K. Y. *BioChip J.* **2008**, 2, 1-11.
153. Whitesides, G. M.; Ostuni, E.; Takayama, S.; Jiang, X.; Ingber, D. E. *Annu. Rev. Biomed. Eng.* **2001**, 3, 335-373.
154. Bernard, A.; Renault, J. P.; Michel, B.; Bosshard, H. R.; Delamarche, E. *Adv. Mater.* **2000**, 12, 1067-1070.
155. Steiner, U. In *Nanoscale Assembly Chemical Techniques*; Huck, W. T. S., Ed.; Springer Science+Business Media, Inc.: New York, 2005, p 1-24.
156. Han, W.; Lin, Z. Q. *Angew. Chem.-Int. Edit.* **2012**, 51, 1534-1546.
157. Chou, S. Y.; Zhuang, L. *J. Vac. Sci. Technol. B* **1999**, 17, 3197-3202.
158. Schäffer, E.; Thurn-Albrecht, T.; Russell, T. P.; Steiner, U. *Nature* **2000**, 403, 874-877.
159. Oron, A.; Davis, S. H.; Bankoff, S. G. *Rev. Mod. Phys.* **1997**, 69, 931-980.
160. Craster, R. V.; Matar, O. K. *Rev. Mod. Phys.* **2009**, 81, 1131-1198.
161. Deegan, R. D.; Bakajin, O.; Dupont, T. F.; Huber, G.; Nagel, S. R.; Witten, T. A. *Nature* **1997**, 389, 827-829.
162. Choi, S.; Stassi, S.; Pisano, A. P.; Zohdi, T. I. *Langmuir* **2010**, 26, 11690-11698.
163. Zeng, H. B.; Kristiansen, K.; Wang, P.; Bergli, J.; Israelachvili, J. *Langmuir* **2011**, 27, 7163-7167.
164. Larson, R. G. *Angew. Chem.-Int. Edit.* **2012**, 51, 2546-2548.
165. Yunker, P. J.; Still, T.; Lohr, M. A.; Yodh, A. G. *Nature* **2011**, 476, 308-311.

166. Hu, H.; Larson, R. G. *J. Phys. Chem. B* **2006**, *110*, 7090-7094.
167. Truskett, V.; Stebe, K. J. *Langmuir* **2003**, *19*, 8271-8279.
168. Vakarelski, I. U.; Chan, D. Y. C.; Nonoguchi, T.; Shinto, H.; Higashitani, K. *Phys. Rev. Lett.* **2009**, *102*.
169. Yabu, H.; Shimomura, M. *Adv. Funct. Mater.* **2005**, *15*, 575-581.
170. Harris, D. J.; Hu, H.; Conrad, J. C.; Lewis, J. A. *Phys. Rev. Lett.* **2007**, *98*.
171. Xue, L. J.; Zhang, J. L.; Han, Y. C. *Prog. Poly. Sci.* **2012**, *37*, 564-594.
172. Cui, L.; Han, Y. C. *Langmuir* **2005**, *21*, 11085-11091.
173. Cui, L.; Li, B. Y.; Han, Y. C. *Langmuir* **2007**, *23*, 3349-3354.
174. Mitov, Z.; Kumacheva, E. *Phys. Rev. Lett.* **1998**, *81*, 3427-3430.
175. Bénard, H. *Rev. Gén. Sciences Pure Appl.* **1900**, *11*, 1261 - 1271.
176. Chou, S. Y.; Zhuang, L.; Guo, L. *Appl. Phys. Lett.* **1999**, *75*, 1004-1006.
177. Deshpande, P.; Chou, S. Y. *J. Vac. Sci. Technol. B* **2001**, *19*, 2741-2744.
178. Chen, L.; Zhuang, L.; Deshpande, P.; Chou, S. *Langmuir* **2005**, *21*, 818-821.
179. Deshpande, P.; Sun, X.; Chou, S. Y. *Appl. Phys. Lett.* **2001**, *79*, 1688-1690.
180. McLeod, E.; Liu, Y.; Troian, S. M. *Phys. Rev. Lett.* **2011**, *106*, 175501.
181. Peng, J.; Wang, H.; Li, B.; Han, Y. *Polymer* **2004**, *45*, 8013-8017.
182. Masclaux, C.; Gourgon, C.; Perret, C.; Labau, S. *Microelectron. Eng.* **2011**, *88*, 2048-2051.
183. Schäffer, E.; Harkema, S.; Roerdink, M.; Blossey, R.; Steiner, U. *Macromolecules* **2003**, *36*, 1645-1655.
184. Schäffer, E.; Harkema, S.; Roerdink, M.; Blossey, R.; Steiner, U. *Adv. Mater.* **2003**, *15*, 514-517.
185. Rayleigh, R. *Phil. Mag. Ser. 6* **1916**, *32*, 529-546.

186. Li, M.; Xu, S.; Kumacheva, E. *Macromolecules* **2000**, *33*, 4972-4978.
187. Xu, S.; Li, M.; Mitov, Z.; Kumacheva, E. *Progr. Org. Coatings* **2003**, *48*, 227-235.
188. Pease, L. F.; Russel, I. W. B. *The Journal of Chemical Physics* **2006**, *125*, 184716.
189. Nedelcu, M.; Morariu, M. D.; Harkema, S.; Voicu, N. E.; Steiner, U. *Soft Matter* **2005**, *1*, 62-65.
190. Schäffer, E.; Harkema, S.; Blossey, R.; Steiner, U. *Europhys. Lett.* **2002**, *60*, 255.
191. Dietzel, M.; Troian, S. M. *J. Appl. Phys.* **2010**, *108*, 074308.
192. Amundson, K.; Helfand, E.; Davis, D. D.; Quan, X.; Patel, S. S.; Smith, S. D. *Macromolecules* **1991**, *24*, 6546-6548.
193. Amundson, K.; Helfand, E.; Quan, X.; Smith, S. D. *Macromolecules* **1993**, *26*, 2698-2703.
194. Amundson, K.; Helfand, E.; Quan, X. N.; Hudson, S. D.; Smith, S. D. *Macromolecules* **1994**, *27*, 6559-6570.
195. Morkved, T. L.; Lu, M.; Urbas, A. M.; Ehrichs, E. E.; Jaeger, H. M.; Mansky, P.; Russell, T. P. *Science* **1996**, *273*, 931-933.
196. Venugopal, G.; Krause, S.; Wnek, G. E. *J. Polym. Sci., Part C: Polym. Lett.* **1989**, *27*, 497-501.
197. Venugopal, G.; Krause, S.; Wnek, G. E. *Chem. Mater.* **1992**, *4*, 1334-1343.
198. Wu, N.; Pease, L. F.; Russel, W. B. *Adv. Funct. Mater.* **2006**, *16*, 1992-1999.
199. Morariu, M. D.; Voicu, N. E.; Schaffer, E.; Lin, Z.; Russell, T. P.; Steiner, U. *Nature Materials* **2003**, *2*, 48-52.
200. Goldberg-Oppenheimer, P.; Kohn, P.; Langford, R. M.; Steiner, U. *Small* **2012**, *8*, 2595-2601.
201. Goldberg-Oppenheimer, P.; Steiner, U. *Small* **2010**, *6*, 1248-1254.

202. Voicu, N. E.; Harkema, S.; Steiner, U. *Adv. Funct. Mater.* **2006**, *16*, 926-934.
203. Voicu, N. E.; Ludwigs, S.; Steiner, U. *Adv. Mater.* **2008**, *20*, 3022-3027.
204. Wu, N.; Russel, W. B. *Nano Today* **2009**, *4*, 180-192.
205. Leach, K. A.; Gupta, S.; Dickey, M. D.; Willson, C. G.; Russell, T. P. *Chaos* **2005**, *15*, 047506.
206. Reddy, P. D. S.; Bandyopadhyay, D.; Sharma, A. *J. Phys. Chem. C* **2012**, *116*, 22847-22858.
207. Roberts, S. A.; Kumar, S. *Phys. Fluids* **2010**, *22*, 122102.
208. Amarandei, G.; Beltrame, P.; Clancy, I.; O'Dwyer, C.; Arshak, A.; Steiner, U.; Corcoran, D.; Thiele, U. *Soft Matter* **2012**, *8*, 6333-6349.
209. Dickey, M. D.; Collister, E.; Raines, A.; Tsiartas, P.; Holcombe, T.; Sreenivasan, S. V.; Bonnecaze, R. T.; Willson, C. G. *Chem. Mater.* **2006**, *18*, 2043-2049.
210. Dickey, M.; Raines, A.; Collister, E.; Bonnecaze, R.; Sreenivasan, S. V.; Willson, C. G. *J. Mater. Sci.* **2008**, *43*, 117-122.
211. Wu, N.; Pease, L. F.; Russel, W. B. *Langmuir* **2005**, *21*, 12290-12302.
212. Pease, L. F.; Russel, W. B. *J. Non-Newtonian Fluid Mech.* **2002**, *102*, 233-250.
213. Verma, R.; Sharma, A.; Kargupta, K.; Bhaumik, J. *Langmuir* **2005**, *21*, 3710-3721.
214. Gambhire, P.; Thaokar, R. M. *Phys. Rev. E* **2012**, *86*, 036301.
215. Deshpande, P.; Pease, L. F., III; Chen, L.; Chou, S. Y.; Russel, W. B. *Phys. Rev. E* **2004**, *70*, 041601.
216. Roberts, S. A.; Kumar, S. *J. Fluid Mech.* **2009**, *631*, 255-279.
217. Gambhire, P.; Thaokar, R. M. *Phys. Fluids* **2010**, *22*, 064103.
218. Lau, C. Y.; Russel, W. B. *Macromolecules* **2011**, *44*, 7746-7751.
219. Zhao, Y.; Xie, Z.; Gu, H.; Zhu, C.; Gu, Z. *Chem. Soc. Rev.* **2012**, *41*, 3297-3317.

220. Meuler, A. J.; McKinley, G. H.; Cohen, R. E. *ACS Nano* **2010**, *4*, 7048-7052.
221. Zawko, S. A.; Schmidt, C. E. *Lab on a Chip* **2010**, *10*, 379-383.
222. Grego, S.; Huffman, A.; Lueck, M.; Stoner, B. R.; Lannon, J. *Microelectron. Eng.* **2010**, *87*, 1846-1851.
223. Larson, R. G. *Angewandte Chemie International Edition* **2012**, *51*, 2546-2548.
224. Scriven, L. E.; Sternling, C. V. *Nature* **1960**, *187*, 186-188.
225. Thomson, J. *On certain curious motions observable at the surfaces of wine and other alcoholic liquors*, 1855.
226. Marangoni, C. *Sull'espansione delle gocce liquide*, 1865.
227. Bron, A. J.; Tiffany, J. M.; Gouveia, S. M.; Yokoi, N.; Voon, L. W. *Exp. Eye Res.* **2004**, *78*, 347-360.
228. Cazabat, A. M.; Heslot, F.; Troian, S. M.; Carles, P. *Nature* **1990**, *346*, 824-826.
229. Xia, Y. N.; Whitesides, G. M. *Annu. Rev. Mater. Sci.* **1998**, *28*, 153-184.
230. Briseno, A. L.; Mannsfeld, S. C. B.; Ling, M. M.; Liu, S.; Tseng, R. J.; Reese, C.; Roberts, M. E.; Yang, Y.; Wudl, F.; Bao, Z. *Nature* **2006**, *444*, 913-917.
231. Wu, H. K.; Odom, T. W.; Chiu, D. T.; Whitesides, G. M. *J. Am. Chem. Soc.* **2003**, *125*, 554-559.
232. Rolland, J. P.; Maynor, B. W.; Euliss, L. E.; Exner, A. E.; Denison, G. M.; DeSimone, J. M. *J. Am. Chem. Soc.* **2005**, *127*, 10096-10100.
233. Rajnicek, A. M.; Britland, S.; McCaig, C. D. *J. Cell Sci.* **1997**, *110*, 2905-2913.
234. Carman, M. L.; Estes, T. G.; Feinberg, A. W.; Schumacher, J. F.; Wilkerson, W.; Wilson, L. H.; Callow, M. E.; Callow, J. A.; Brennan, A. B. *Biofouling* **2006**, *22*, 11-21.
235. Schumacher, J. F.; Carman, M. L.; Estes, T. G.; Feinberg, A. W.; Wilson, L. H.; Callow, M. E.; Callow, J. A.; Finlay, J. A.; Brennan, A. B. *Biofouling* **2007**, *23*, 55-62.
236. Gallardo, B. S.; Gupta, V. K.; Eagerton, F. D.; Jong, L. I.; Craig, V. S.; Shah, R. R.; Abbott, N. L. *Science* **1999**, *283*, 57-60.

237. Grunze, M. *Science* **1999**, 283, 41-42.
238. Strawhecker, K. E.; Kumar, S. K.; Douglas, J. F.; Karim, A. *Macromolecules* **2001**, 34, 4669-4672.
239. Cai, Y.; Newby, B. M. Z. *J. Am. Chem. Soc.* **2008**, 130, 6076-6077.
240. Wong, S.; Kitaev, V.; Ozin, G. A. *J. Am. Chem. Soc.* **2003**, 125, 15589-15598.
241. Millan, M. D.; Locklin, J.; Fulghum, T.; Baba, A.; Advincula, R. C. *Polymer* **2005**, 46, 5556-5568.
242. Nagai, N.; Matsunobe, T.; Imai, T. *Polym. Degrad. Stabil.* **2005**, 88, 224-233.
243. Nurmukhametov, R.; Volkova, L.; Kabanov, S. *Journal of Applied Spectroscopy* **2006**, 73, 55-60.
244. Simons, J. K.; Chen, J. M.; Taylor, J. W.; Rosenberg, R. A. *Macromolecules* **1993**, 26, 3262-3266.
245. Zhang, D.; Dougal, S. M.; Yeganeh, M. S. *Langmuir* **2000**, 16, 4528-4532.
246. Mundra, M. K.; Ellison, C. J.; Behling, R. E.; Torkelson, J. M. *Polymer* **2006**, 47, 7747-7759.
247. Coates, J. In *Encyclopedia of Analytical Chemistry*; Meyers, R. A., Ed.; John Wiley & Sons Ltd.: Chichester, 2000, p 10815-10837.
248. Reichenbach, J.; Linde, H. J. *Colloid Interface Sci.* **1981**, 84, 433-443.
249. Weh, L. *Mater. Sci. Eng. C-Biomimetic Supramol. Syst.* **1999**, 8-9, 463-467.
250. Wu, K. H.; Lu, S. Y.; Chen, H. L. *Langmuir* **2006**, 22, 8029-8035.
251. *Polymer Handbook*; Brandrup, J.; Immergut, E. H.; Grulke, E. A., Eds.; Wiley and Sons: Hoboken, New Jersey, 1999.
252. Elman, J. F.; Johs, B. D.; Long, T. E.; Koberstein, J. T. *Macromolecules* **1994**, 27, 5341-5349.
253. Jalbert, C.; Koberstein, J. T.; Yilgor, I.; Gallagher, P.; Krukonis, V. *Macromolecules* **1993**, 26, 3069-3074.

254. Jeyaprakash, J. D.; Samuel, S.; Ruhe, J. *Langmuir* **2004**, *20*, 10080-10085.
255. Christensen, S. K.; Chiappelli, M. C.; Hayward, R. C. *Macromolecules* **2012**, *45*, 5237-5246.
256. Carroll, G. T.; Sojka, M. E.; Lei, X. G.; Turro, N. J.; Koberstein, J. T. *Langmuir* **2006**, *22*, 7748-7754.
257. Ubukata, T.; Yamamoto, S.; Moriya, Y.; Fujii, S.; Yokoyama, Y. *J. Photopolym Sci. Technol.* **2012**, *25*, 675-678.
258. Ubukata, T.; Moriya, Y.; Yokoyama, Y. *Polym. J.* **2012**, *44*, 966-972.
259. National Institute of Advanced Industrial Science and Technology. Spectral Database for Organic Compounds. <http://sdbs.riodb.aist.go.jp/sdbs/> (Accessed January 31, 2013).
260. Lee, L.-H. *Journal of Applied Polymer Science* **1968**, *12*, 719-730.
261. Okada, A.; Usuki, A. *Macromolecular Materials and Engineering* **2006**, *291*, 1449-1476.
262. Termonia, Y. *J. Polym. Sci. Pt. B-Polym. Phys.* **2010**, *48*, 687-692.
263. Nakatani, A. I.; Chen, W.; Schmidt, R. G.; Gordon, G. V.; Han, C. C. *Polymer* **2001**, *42*, 3713-3722.
264. Papon, A.; Montes, H.; Hanafi, M.; Lequeux, F.; Guy, L.; Saalwachter, K. *Physical Review Letters* **2012**, *108*, 5.
265. Gam, S.; Meth, J. S.; Zane, S. G.; Chi, C. Z.; Wood, B. A.; Seitz, M. E.; Winey, K. I.; Clarke, N.; Composto, R. J. *Macromolecules* **2011**, *44*, 3494-3501.
266. Janes, D. W.; Moll, J. F.; Harton, S. E.; Durning, C. J. *Macromolecules* **2011**, *44*, 4920-4927.
267. Moll, J.; Kumar, S. K. *Macromolecules* **2011**, *45*, 1131-1135.
268. Sangani, A. S.; Yao, C. *J. Appl. Phys.* **1988**, *63*, 1334-1341.
269. Wool, R. P. *Macromolecules* **1993**, *26*, 1564-1569.
270. Reiter, G. *Macromolecules* **1994**, *27*, 3046-3052.

271. Si, L.; Massa, M. V.; Dalnoki-Veress, K.; Brown, H. R.; Jones, R. A. L. *Phys Rev Lett* **2005**, *94*, 127801.
272. Golovin, A. A.; Volpert, V. A. *Physics of Fluids* **2007**, *19*, 122104.
273. Golovin, A. A.; Volpert, V. A. *Mathematical Modelling of Natural Phenomena* **2008**, *3*, 27-54.
274. Madou, M. J. *Fundamentals of Microfabrication: The Science of Miniaturization*; Second Edition ed.; CRC Press: Boca Raton, Florida, 2002.
275. Emmony, D. C.; Howson, R. P.; Willis, L. J. *Applied Physics Letters* **1973**, *23*, 598-600.
276. Siegrist, M.; Kaech, G.; Kneubuhl, F. K. *Applied physics* **1973**, *2*, 45-46.
277. Young, J. F.; Preston, J. S.; van Driel, H. M.; Sipe, J. E. *Physical Review B* **1983**, *27*, 1155-1172.
278. Bolle, M.; Lazare, S.; Leblanc, M.; Wilmes, A. *Applied Physics Letters* **1992**, *60*, 674-676.
279. Kim, D. Y.; Tripathy, S. K.; Li, L.; Kumar, J. *Applied Physics Letters* **1995**, *66*, 1166-1168.
280. Frechet, J. M. J.; Eichler, E.; Ito, H.; Willson, C. G. *Polymer* **1983**, *24*, 995-1000.
281. *Advanced Nanomaterials*; Geckeler, K. E.; Nishide, H., Eds.; Wiley-VCH: Weinheim, Germany, 2010.
282. Pujari, S.; Keaton, M. A.; Chaikin, P. M.; Register, R. A. *Soft Matter* **2012**, *8*, 5358-5363.
283. Gupta, V. K.; Krishnamoorti, R.; Chen, Z. R.; Kornfield, J. A.; Smith, S. D.; Satkowski, M. M.; Grothaus, J. T. *Macromolecules* **1996**, *29*, 875-884.
284. Tornøe, C. W.; Christensen, C.; Meldal, M. *The Journal of Organic Chemistry* **2002**, *67*, 3057-3064.
285. Mantovani, G.; Ladmiral, V.; Tao, L.; Haddleton, D. M. *Chemical Communications* **2005**, *0*, 2089-2091.

286. Schwindeman, J. A.; Granger, E. J.; Quirk, R. P.; Hall, R. W.; Letchford, R. J. *Protected amine initiators and polymers derived therefrom*, WO2000050479A1 2000.
287. Canalle, L. A.; van Berkel, S. S.; de Haan, L. T.; van Hest, J. C. M. *Advanced Functional Materials* **2009**, *19*, 3464-3470.

Vita

Joshua Max Katzenstein was born in Detroit, Michigan and was raised in the suburb of Beverly Hills, Michigan. After completing high school at Wylie E. Groves High School in Birmingham, Michigan in 2004 he enrolled at The University of Michigan. During his time here Josh was an undergraduate research assistant for Prof. Richard Laine and completed internships at IBM in environmental programs and GE-Lighting in new product development. After graduation with a B.S.E. in chemical engineering in 2008 he began his Ph.D. studies at The University of Texas at Austin with Prof. Christopher Ellison. After completing his Ph.D. Josh will join Dow Coating Materials (part of The Dow Chemical Company) in Midland, Michigan.

PUBLICATIONS AND PATENTS

- Janes, D.W.; **Katzenstein, J.M.**; Shanmuganathan, K.; Ellison, C.J. “Directing Convection to Pattern Thin Polymer Films” *Journal of Polymer Science Part B: Polymer Physics* **2013**, *51*, 535-545.
- **Katzenstein, J.M.**; Janes, D.W.; Cushen, J.D.; Hira, N.B.; McGuffin, D.L.; Prisco, N.A.; Ellison, C.J. “Patterning by Photochemically Directing the Marangoni Effect”, *ACS Macro Letters* **2012**, *1*, 1150-1154.
- Provisional Patent Application: **Katzenstein, J.M.**; Janes, D.W.; Ellison, C.J. Method for Creating Topographical Patterns in Polymers via Surface Energy Patterned Films and the Marangoni Effect” Filed 8/22/12.
- **Katzenstein, J. M.**; Janes, D. W.; Hocker, H. E.; Chandler, J. K.; Ellison, C. J. “Nanoconfined Self-Diffusion of Poly(isobutyl methacrylate) in Films with a Thickness-Independent Glass Transition” *Macromolecules* **2011**, *45*, 1544-1552.
- Bates, C. M.; Strahan, J. R.; Santos, L. J.; Mueller, B. K.; Bamgbade, B. O.; Lee, J. A.; **Katzenstein, J. M.**; Ellison, C. J.; Willson, C. G. “Polymeric Crosslinked Surface Treatments for Controlling Block Copolymer Orientation in Thin Films” *Langmuir* 2011, *27*, 2000-2006.

Permanent e-mail: jkatzens@gmail.com

This dissertation was typed by the author.